Progress in Materials Science 94 (2018) 462–540

Contents lists available at ScienceDirect

Progress in Materials Science

journal homepage: www.elsevier.com/locate/pmatsci

Review on superior strength and enhanced ductility of metallic nanomaterials

I.A. Ovid'ko [a,b], R.Z. Valiev [b,c,*], Y.T. Zhu [d,e]

[a] Research Laboratory for Mechanics of New Nanomaterials, Peter the Great St. Petersburg Polytechnic University, St. Petersburg 195251, Russia
[b] Department of Mathematics and Mechanics, St. Petersburg State University, St. Petersburg 199034, Russia
[c] Institute of Physics of Advanced Materials, Ufa State Aviation Technical University, 12 K. Marx str., Ufa 450008, Russia
[d] Department of Materials Science and Engineering, North Carolina State University, Raleigh, NC 27695, USA
[e] Nano and Heterogeneous Materials Center, Nanjing University of Science and Technology, Nanjing, China

ARTICLE INFO

Article history:
Received 13 November 2016
Received in revised form 28 December 2017
Accepted 3 February 2018
Available online 5 February 2018

In memory of our co-author, dedicated scientist, colleague, friend – Prof. Ilya A. Ovid'ko

Keywords:
Strength
Ductility
Nanostructured materials
Metals
Deformation
Fracture
Dislocations
Grain boundaries
Twins
Heterostructure

ABSTRACT

Nanostructured metallic materials having nanocrystalline and ultrafine-grained structures show exceptional mechanical properties, e.g. superior strength, that are very attractive for various applications. However, superstrong metallic nanomaterials typically have low ductility at ambient temperatures, which significantly limits their applications. Nevertheless, several examples of nanostructured metals and alloys with concurrent high strength and good ductility have been reported. Such strong and ductile materials are ideal for a broad range of structural applications in transportation, medicine, energy, etc. Strong and ductile metallic nanomaterials are also important for functional applications where these properties are critical for the lifetime of nanomaterial-based devices. This article presents an overview of experimental data and theoretical concepts addressing the unique combination of superior strength and enhanced ductility of metallic nanomaterials. We consider the basic approaches and methods for simultaneously optimizing their strength and ductility, employing principal deformation mechanisms, crystallographic texture, chemical composition as well as second-phase nano-precipitates, carbon nanotubes and graphene. Examples of achieving such superior properties in industrial materials are reviewed and discussed.

Contents

1. Introduction 463
2. Plastic deformation and fracture processes in metals: grain size effects 464
3. Dominant deformation mechanisms in metallic nanomaterials 469

Abbreviations: APT, atom probe tomography; bcc, body-centered cubic; CNT, carbon nanotube cold rolling; ECAP, equal-channel angular pressing; fcc, face-centered cubic; GB, grain boundary; GP, Guinier-Preston; hcp, hexagonal close-packed; HPT, high-pressure torsion; HRTEM, high-resolution transmission electron microscopy; MD, molecular dynamics; NC, nanocrystalline; NS, nanostructured; RT, room temperature; SEM, scanning electron microscope; SPD, severe plastic deformation; ST, solution-treated; TEM, transmission electron microscopy; TKD, transmission Kikuchi diffraction; UFG, ultrafine-grained; UTS, ultimate tensile stress; YS, yield stress.

* Corresponding author at: Institute of Physics of Advanced Materials, Ufa State Aviation Technical University, 12 K. Marx str., Ufa 450008, Russia.
E-mail addresses: ovidko@nano.ipme.ru (I.A. Ovid'ko), ruslan.valiev@ugatu.su (R.Z. Valiev), ytzhu@ncsu.edu (Y.T. Zhu).

https://doi.org/10.1016/j.pmatsci.2018.02.002
0079-6425/

3.1. Deformation by perfect dislocations . . . 469
3.2. Partial dislocation emission from grain boundaries . . . 472
3.3. Deformation twinning . . . 473
3.4. Grain boundary sliding . . . 476
3.5. Rotational deformation mode . . . 481
3.6. Stress-driven migration of grain boundaries . . . 484
3.7. Deformation mechanism maps . . . 490
3.8. Interaction between deformation mechanisms . . . 493
3.9. Crack nucleation and growth processes . . . 495
4. Key factors affecting the ductility of metallic nanomaterials . . . 496
4.1. Structure of grain boundaries (GBs) in NS materials . . . 497
4.2. Nanotwins in metallic nanomaterials . . . 499
4.3. Segregations in nanostructured SPD-processed alloys . . . 500
4.4. Precipitations of second phases during and/or after SPD . . . 501
5. Basic strategies for improving ductility of metallic nanomaterials . . . 503
5.1. Grain boundary processes and enhancement of ductility . . . 503
5.1.1. Enhanced ductility of NC metals . . . 503
5.1.2. Enhanced ductility of NS SPD-processed metals . . . 506
5.2. Superior strength and good ductility of nanotwinned, ultrafine-grained metals . . . 509
5.3. Deformation of ultrafine-grained metals at cryogenic temperatures . . . 512
5.4. Using stacking faults to enhance ductility . . . 515
5.5. High strength and good ductility of heterostructured metallic nanomaterials . . . 516
5.5.1. Gradient structured materials . . . 517
5.5.2. Heterogeneous lamella materials . . . 518
5.5.3. Other types of heterostructured materials . . . 519
5.6. Improving strength and ductility by precipitation-hardening . . . 520
5.7. Optimizing the strength and ductility of nanostructured metallic composites containing carbon nanotubes and graphene sheets/nanoplatelets . . . 521
6. Superior strength and ductility in industrial alloys and steels . . . 525
7. Structural stability of metallic nanomaterials . . . 528
8. Summary and future directions . . . 529
Acknowledgements . . . 529
References . . . 530

1. Introduction

Nanostructured metallic materials with nanocrystalline (NC) and ultrafine-grained (UFG) structures demonstrate unique mechanical, chemical and physical properties that are of utmost interest for a wide range of applications; see, e.g., reviews [1–18] and books [19–23]. These properties occur in nanostructured metallic materials (hereinafter called metallic nanomaterials) owing to their specific structural features such as nanoscale and ultrafine grains as well as exceptionally large amounts of grain boundaries (GBs). In particular, metallic nanomaterials typically show superior strength, superior hardness and enhanced wear resistance due to the nanoscale and interface effects [1–14,20–23]. Superstrong metallic nanomaterials are very promising for structural and functional applications. First of all, high strength is always desired for structural materials for transportation vehicles and other engineering applications where light weight improves their energy efficiency. Besides, superstrong metallic nanomaterials with outstanding physical and chemical properties have the potential to significantly enhance the lifetime and performance of nanomaterial-based devices in diverse functional applications.

In addition to high strength, good ductility and toughness are also required for engineering materials to prevent catastrophic failure during service. However, most metallic nanomaterials possess superior strength but low ductility, which severely limits their practical utility. Thus, despite of their high strength, low ductility poses a bottleneck that limits the application of metallic nanomaterials in many advanced technologies.

In general, the trade-off between strength and ductility is a traditional problem in materials science and engineering. These two properties are generally mutually exclusive. For centuries, engineers have been forced to choose either strong or ductile material, not both as desired.

Nevertheless, several research groups reported on metallic nanomaterials with good ductility and high-strength at ambient temperatures and superplasticity at high temperatures; see, e.g., reviews [24–29]. The unique combination of high strength and good ductility exhibited by nanostructured metals make them "dream engineering materials" for structural and functional applications in transportation, medicine, energy, etc. To develop the field of nanostructured metals, it is critically important to reveal the underlying mechanisms that can produce high ductility and to analyze the approaches to obtain excellent ductility.

This article presents an overview of experimental and theoretical studies addressing the outstanding combination of superior strength and ductility of metallic nanomaterials. Special attention is paid to the basic strategies for simultaneously

optimizing their strength and ductility, employing fundamental deformation mechanisms, structural architecture on single or multiple length scales, texture, chemical composition as well as second-phase precipitates, carbon nanotubes and graphene. We will focus on general effective strategies that can be widely used in material nanotechnologies. In addition, we will present the examples of achieving superior properties in industrial materials using the discussed strategies.

It should be noted that several short reviews [24–29] on similar topics have been published previously. However, all these reviews report only on certain experimental data and focus on partial problems in the areas under discussion. This paper presents a comprehensive review addressing all key problems related to optimizing strength and ductility of metallic nanomaterials. Both experimental data and theoretical concepts will be thoroughly overviewed.

In this paper, we consider deformation behaviors exhibited by metallic nanomaterials with NC and UFG structures. Here, NC materials are defined as metals and alloys consisting of grains with sizes d below 100 nm. UFG metallic materials are conventionally defined as metals and alloys that consist of submicron grains - crystallites with size d ranging from 100 nm to 1 μm. UFG metals and alloys usually contain nanoscale structural elements with sizes below 100 nm, such as dislocation cells, subgrains, nanoscale twins, nanoparticles and nanoscale compositional non-homogeneities, see, e.g., [21,23,30]. Therefore, both NC and UFG metals and alloys are typically called referred to as nanostructured (NS) metallic materials or, in short, metallic nanomaterials. With nanoscale and ultrafine grains inherent in the structure of metallic nanomaterials, they demonstrate unique mechanical properties that are very different from those of coarse-grained polycrystalline metals.

It should be noted that ductility is measured by tensile test only, and can be considered as tensile plasticity. In the literature and practice, ductility has been defined in two ways: uniform elongation or elongation to failure. Uniform elongation is defined as the strain at the maximal loading, or at the highest stress in the engineering stress-strain curve, after which necking occurs. This value denotes the deformation stage related to the onset of plastic flow localization. Elongation to failure stands for total elongation during tensile tests. It includes both the uniform elongation and the necking segment. For conventional materials tested using large standard specimens, the uniform and total elongations are quite close, but they can be significantly different for small specimens, which is often the case for nanomaterials. It is found that the uniform elongation is not affected much by the sample geometry and size [28,31,32], and therefore is more suitable for use as a measure of ductility for nanostructured materials where small samples with various geometries are often used. Therefore, the data on both uniform and total elongation measurements are presented herein with the corresponding comments.

In conclusion of the introductory section we also consider the processing of NS materials. It is known that the approaches to process bulk NS materials have been classified into two categories: «top - down» and «bottom - up» [21,23]. The "bottom-up" approach produces NS materials by building up from individual atoms or nanoparticles. The "top-down" approach produces ultrafine grains through grain refinement with the application of severe plastic deformation (SPD). In this article special attention is paid to NS materials produced by SPD techniques.

2. Plastic deformation and fracture processes in metals: grain size effects

In search for strategies to enhance the ductility of metallic nanomaterials without dramatic loss of their strength, it is critical to understand how plastic deformation and fracture processes are related to their structure. The basic (generic) structural features of metallic nanomaterials are the presence of nanoscale/ultrafine grains and extremely high density of GBs. In the first approximation, these features can be quantified by the mean grain size d. In addition to the basic structural features, there are special structural features that can vary in different nanomaterials with the same mean grain size and are sensitive to both materials characteristics and synthesis/processing history. Examples of the special features include grain shapes, grain size distribution, dominant types and structures of GBs, single-phase/composite structure, second-phase geometry, fabrication-induced flaws, nano-twins, and compositional inhomogeneity.

Before discussing the deformation mechanisms of metallic nanomaterials and their relationships with structural features and properties, we present in this section the general observations of plastic deformation and fracture processes in metallic materials as a function of grain size. In particular, metallic materials are classified into coarse-grained (CG), UFG and NC categories according to their grain sizes (Section 1). In this section, we will discuss the general structural features of CG, UFG and NC metallic materials as well as effect of grain size on mechanical properties. The specific structural features and their effects on strength and ductility of nanometals will be considered in following sections.

Let us begin by briefly describing some definitions and approaches underlying the basis of this review. First, it is well known that in addition to grains, grain boundaries (GBs) and triple junctions of GBs represent essential structural elements for metallic materials. Each grain has a specific crystal orientation and neighboring grains share a GB area with a thickness of ~0.5 nm, which can be considered as a layer accommodating orientation mismatch between them (Fig. 1) [33,34]. GBs in nanomaterials have atomic structures and properties that can be different from those of CG materials; see, e.g., [2,4,20–23,33,35]. In particular, the structure of GBs in nanomaterials fabricated by severe plastic deformation and other nonequilibrium methods is strained with high densities of disorderedly arranged GB dislocations [20,23]. These extrinsic defects change the structure of GBs and can considerably increase the rate of GB diffusion; see, e.g., [36,37].

GBs triple junctions have a tube-like geometry with diameters of 1–2 nm. Structures and properties of triple junctions differ from those of GBs [38–43]. Grain interiors, GBs and their triple junctions play different roles in plastic deformation and fracture processes, and this difference provides basis for the grain size effects on their mechanical properties.

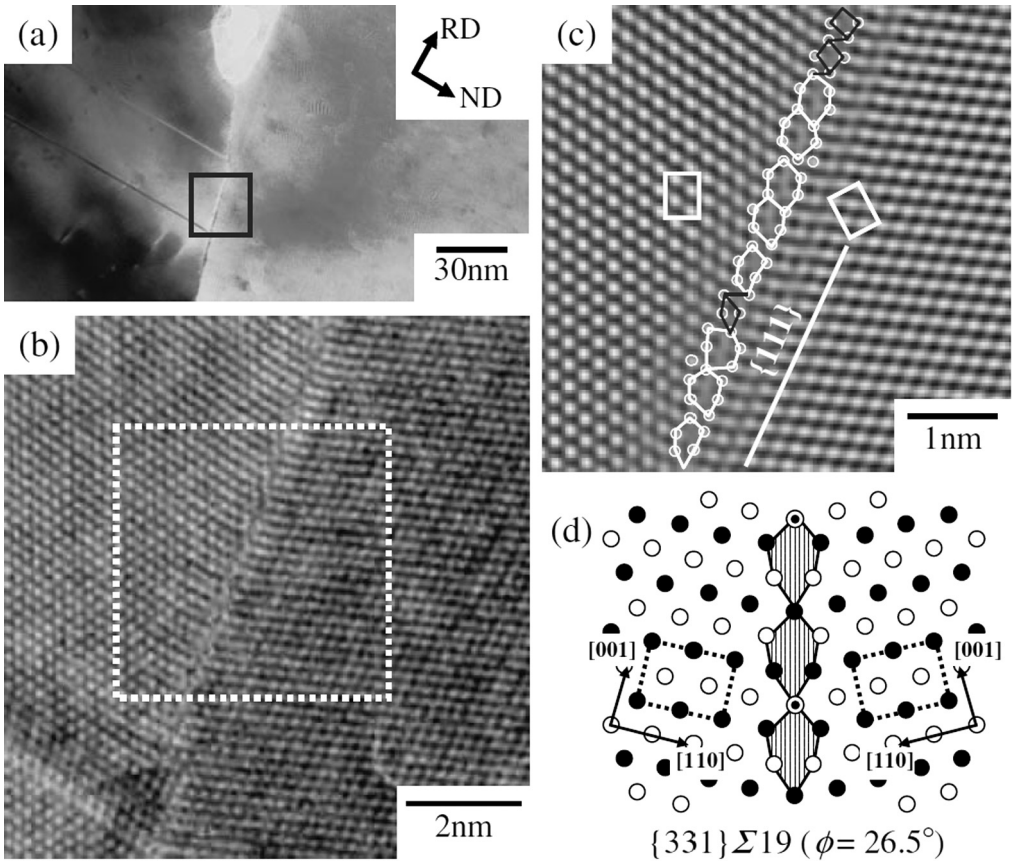

Fig. 1. (a) TEM image and (b) HRTEM image of a high angle grain boundary close to Σ19 ATGB in 2cARB-Cu, (c) the FFT image of the dotted square region in (b) and (d) the atomic structure of the {3 3 1} Σ19 STGB obtained by MD simulation [34].

To understand the grain size effects on plastic deformation and underlying mechanisms, it is important to note that GBs serve as effective obstacles for dislocations, the basic carriers of plastic flow in most metals. This role of GBs manifests itself in the relationship of yield stress τ_y with grain size d in NC, UFG and coarse-grained metals, for a review, see [10]. For d above a critical value $d_c \approx 10$–30 nm, depending on the material and its microstructure, it follows the classic Hall–Petch relationship:

$$\tau_y \approx \tau_0 + kd^{-1/2} \tag{1}$$

where τ_0 and k are material parameters that related to the friction resistance for dislocation glide in grain interiors and transmission of plastic flow across GBs, respectively.

The Hall-Petch relationship and its interpretation based on the role of GBs as obstacles of dislocation slip explains well the fundamental origin of superior strength and hardness exhibited by nanomaterials. Indeed, the yield stress, strength and hardness increases with decreasing grain size, reaching ultrahigh values at very small grain sizes, mostly due to suppression of dislocation slip by GBs.

In the range of ultra-small grain sizes, $d < d_c$, the GB area per unit volume is so large (Fig. 2) [44] that dislocation generation in the grain interior is severely or even completely suppressed, and GBs become structural elements that can mediate or at least effectively assist plastic flow. This is demonstrated by significant deviation from the Hall-Petch relationship at $d < d_c$. Specifically, in this grain size range, NS metals after heat treatment typically show an inverse Hall-Petch relationship, while the as-fabricated NS metals often show a reduced Hall–Petch slope or a constant strength with decreasing grain size d; see, e.g., [10,45,46]. These behaviors are influenced by GB deformation mechanisms that effectively contribute to plastic flow or even dominate plastic flow at grain sizes below d_c at room temperature [10]. Hereinafter such NS materials will be called (NC) metals with finest grains in order to differentiate them from metallic nanomaterials with fine grains (having sizes from d_c to 1 μm) where the lattice dislocation slip typically dominates.

Grain size dramatically influences the ductility of metallic materials. In order to understand this phenomenon better, let us consider the mechanics of uniform tensile deformation in metals as well as plastic flow and fracture instabilities suppressing ductility in metallic nanomaterials. As well known, ductility is tensile plasticity [30,47], which is governed by the

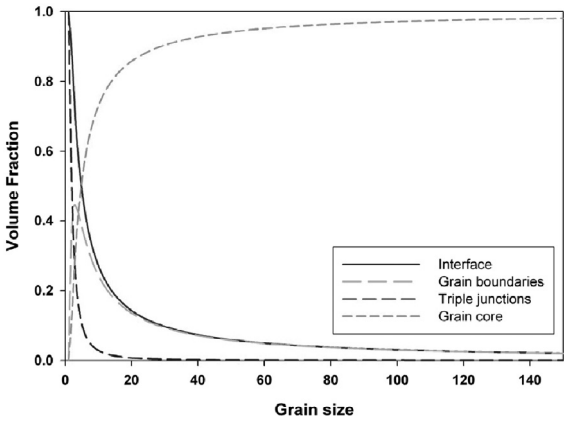

Fig. 2. Evolution of volume fractions of interface, grain boundaries, triple junctions, and grain cores with the grain size in nm [44].

interplay between plastic flow and failure as well as by the ability to suppress strain instability associated with macroscopic necking. Plastic deformation in most metallic materials is commonly mediated by the dislocation slip [48,49].

Fracturing is a multi-stage process involving nucleation, propagation and convergence of cracks and/or voids, which cause the disintegration of a solid into separate pieces. Fracture can be classified into ductile facture and brittle fracture. Ductile fracture is typically associated with necking and mediated by dislocation activities. It involves relatively slow nucleation, growth and coalescence of voids (Fig. 3a–d), where dimples are observed on fracture surfaces.

Brittle fracture is characterized with fast nucleation of cracks, followed by their convergence and/or growth to form a large catastrophic crack without perceptible plastic deformation (Fig. 3e and f). These processes are also called crack nucleation and propagation instabilities. The brittle behavior is due to low plasticity and results in low ductility, which is generally undesired in materials for structural and other applications.

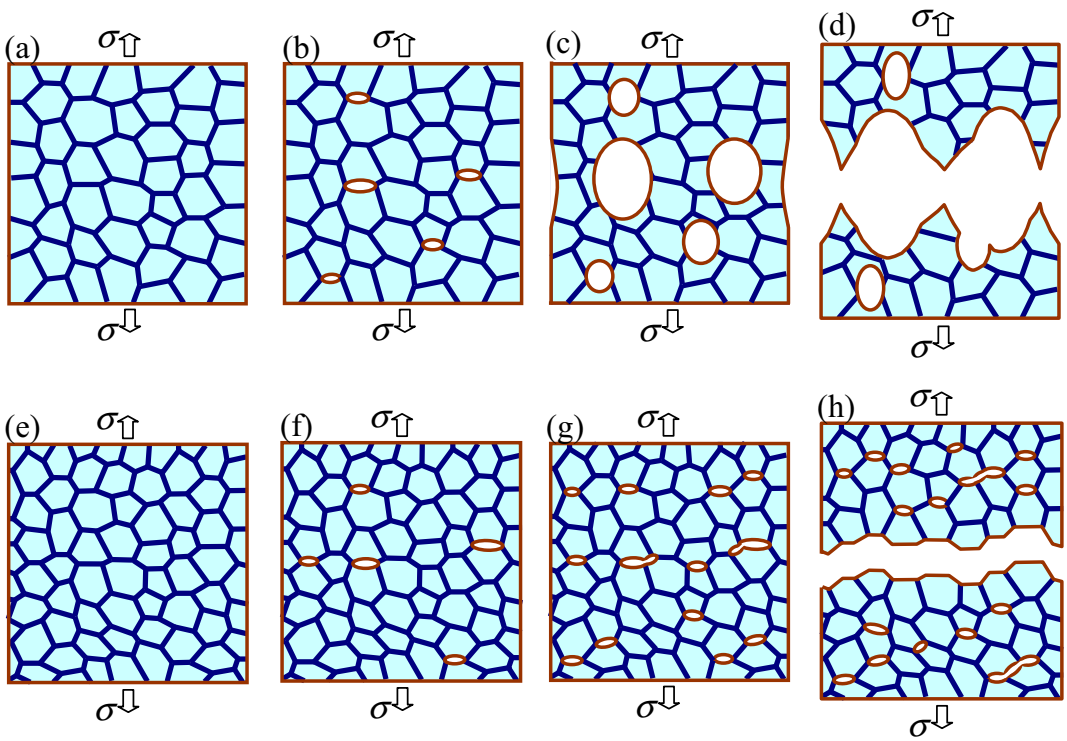

Fig. 3. (a–d) Ductile fracture occurs through a relatively slow nucleation, growth and coalescence of voids. Neck formation, after extended homogeneous deformation, may accompany growth and coalescence of voids. (e–h) Brittle fracture in nanocrystalline specimen occurs through fast nucleation of nanoscale flat cracks, their convergence and/or growth along grain boundaries.

In general, the intrinsic brittle versus ductile behavior of a single crystal is controlled by competition between cleavage fracture by atomic decohesion and plastic deformation by dislocation generation and motion at stress sources and concentrators, first of all, crack tips; for details, see [50–52]. In single crystalline metals, dislocations are easily generated and emitted from crack tips and other stress sources/concentrators, because metals have comparatively low energy barriers for glide and nucleation of dislocations [48–52]. Consequently, crack tips are rapidly blunted, weakening the stress concentration. Therefore, crack growth and generation are effectively suppressed. The same is true in CG metals where GBs occupy negligibly small volume fractions and thus weakly influence dislocation nucleation at crack tips (Fig. 4a).

Below we discuss another factor influencing ductility, namely the resistance to deformation localization, i.e. necking. In contrast with the slow ductile fracture (Fig. 3a–d), fast ductile fracture processes associated with plastic flow localization can occur in solids under tensile load. In this situation, uniform deformation is unstable, leading to local reduction in cross-sectional area (necking) of a plastically deforming specimen (Fig. 5) [53,54]. The necking is followed by both stress concentration and fast ductile fracture through fast nucleation, growth and coalescence of voids within the neck region. When necking occurs at an early stage of deformation, a solid exhibits low ductility characterized by low uniform elongation, although local plastic strain in the neck region is comparatively large, and dimpled structures are observed at fracture surfaces. Unfortunately, this is often the mechanical behavior of metallic nanomaterials.

The resistance to necking is determined by strain hardening θ and strain rate sensitivity m [24,26,53,54]. These parameters are defined as

$$\theta = \sigma^{-1}(\partial\sigma/\partial\varepsilon)_{\dot{\varepsilon}} \tag{2}$$

$$m = (\partial \ln\sigma/\partial \ln\dot{\varepsilon})_{\varepsilon} \tag{3}$$

where σ denotes flow stress, ε true strain, and $\dot{\varepsilon}$ strain rate. Higher strain hardening θ and/or higher strain rate sensitivity m produces larger uniform elongation. Note that θ is the slope of the true stress-strain curve normalized by the flow stress. According to Hart criterion, under a constant extension rate, uniform tensile deformation is stable if [24,26,53,54]

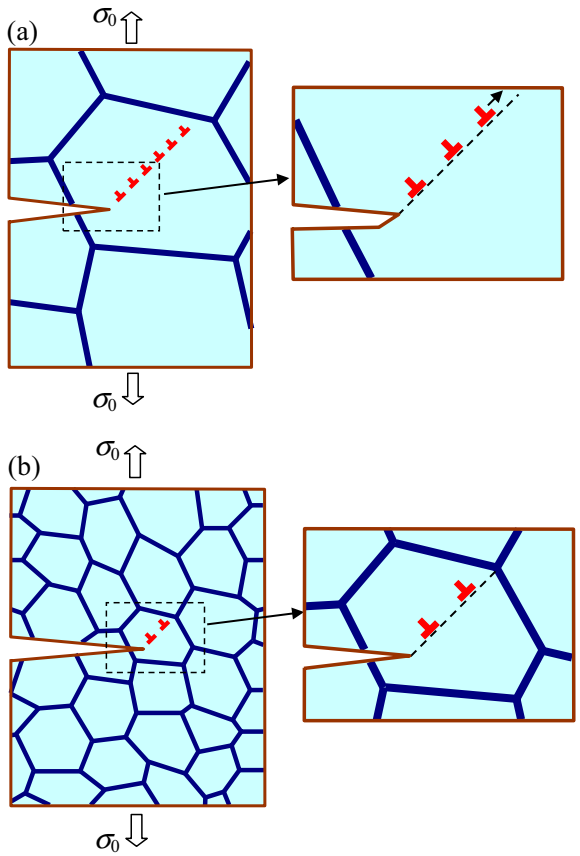

Fig. 4. (a) Crack blunting in coarse-grained metals effectively occurs through emission of lattice dislocations from crack tip (schematically). (b) Crack blunting in nanocrystalline metals. Dislocation emitted from crack tip stops at the nearest grain boundary. Its stress field hinders subsequent dislocation emission owing to dislocation repulsion. As a result, the dislocation emission from crack tip and thereby crack blunting are suppressed in nanocrystalline specimen.

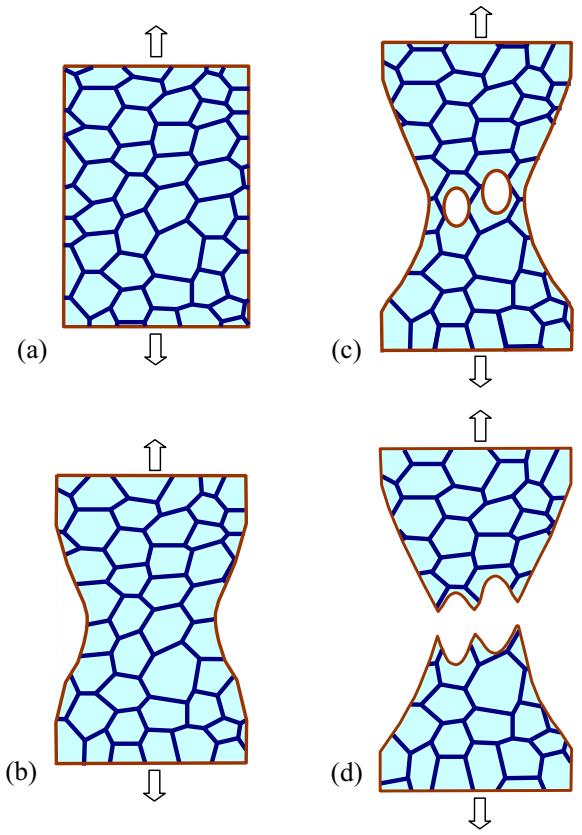

Fig. 5. Necking in metallic specimen under tensile load (schematically).

$$\theta + m > 1. \tag{4}$$

In CG metals under tensile load at room temperature, strain hardening provides the main contribution to the stability of uniform plastic deformation, while the effect of strain rate sensitivity is negligible because $m \ll 1$. In this case, the Hart criterion is reduced to the Considère criterion [55], which has the form $\theta > 1$.

At room temperature, high strain hardening in CG metals is associated with deformation-induced generation and accumulation of dislocations with increasing plastic strain [48,49]. At high homologous temperatures, strain rate sensitivity could become high, e.g. $m > 0.33$, which is typical for diffusion-controlled GB sliding. This could significantly improve stability of uniform deformation, leading to superplasticity [56–59].

Early necking is responsible for low ductility in metallic nanomaterials. Since their strain rate sensitivity m is typically low ($m \ll 1$) at room temperature, strain hardening θ is the primary factor that determines uniform elongation [60,61]. In general, strain hardening is produced by the accumulation of crystalline defects such as dislocations, twins, etc. during plastic deformation. In CG metals, dislocations are generated at conventional dislocation sources such as Frank-Read sources [48,49]. With increasing plastic strain, these dislocations are effectively accumulated in the form of dislocation cells and subboundaries in large grains [35,62]. Annihilation of lattice dislocations conventionally involves their climb with rate governed by slow bulk diffusion. This provides a pronounced strain hardening and thereby suppresses deformation instability in CG metals up to large plastic strains.

In metallic nanomaterials, dislocation sources are reduced or may longer exist in grain interior when the grain sizes are very small [13,63–65] (see also Section 3.1). Dislocations often are generated at GBs, glide across the grain and then disappear at GBs without accumulation in grain interior. Also, the recovery process is enhanced due to the size and GB effects [24] (see also the Section 3.1). Therefore, strain hardening θ in nanomaterials is usually low or even approaches 0. As a consequence, mechanical instability (necking) usually occurs at a low strain, leading to low uniform elongation (ductility) (Fig. 5).

In NC metals with finest grains ($d < d_c$), the strain rate sensitivity will become higher at finest grains [60,61], which helps with improving ductility, but this is usually not enough to offset the effect of the reduction in strain hardening. In addition, there are two additional grain size effects that reduce ductility. The first is associated with extremely high flow stress. As shown in Eq. (2), higher flow stress leads to lower normalized strain hardening θ. In addition, the high applied stress could reach values close to the threshold stress for initiating cracks near stress concentrations and sustain crack growth. These stress concentrations can occur at flaws formed during fabrication. The second effect of finest grains on ductility is related

to the fact that standard toughening mechanisms, such as emission of dislocations by cracks, are suppressed in nanoscopic grains and thereby are not effective in hindering crack propagation [66,67]. More specifically, GBs effectively prevent dislocations from emitting from a crack tip and thus prevent crack blunting, especially in NC metals with finest grains (Fig. 4b). As a result, crack growth is enhanced in NC metals with finest grains, as observed in numerous experiments; see a review article [68] and references therein.

Both of the aforementioned factors operate in NS metals with fine grains in the range of d_c to around 1 μm. However, their flow stresses are lower, and their reduction of fracture toughness (due to the suppression of dislocation emission from crack tips) is less pronounced than that in NC metals with finest grains.

Therefore, grain size is a key structural parameter that renders the high strength and typically low ductility of metallic nanomaterials. As mentioned earlier, there are also special structural features that can be different in different NS materials with the same mean grain size and are caused by both intrinsic material properties and extrinsic processing parameters. In general, it is possible to manipulate the structural features to enhance ductility of superstrong metallic nanomaterials [26,28,29,69,70]. Within the discussed approaches, it is crucially important to identify and describe plastic deformation mechanisms that operate in NS materials and reveal the critical parameters for their activation. This will be done in next section.

3. Dominant deformation mechanisms in metallic nanomaterials

As discussed in previous sections, deformation mechanisms in NS metals are significantly influenced by GBs, which constitute a large volume fraction in such metals. In general, GB-mediated deformation mechanisms can be divided into two basic categories: (1) "pure" GB mechanisms by the motion of GBs themselves, and (2) GB-mediated mechanisms associated with dislocation emission from GBs [1–14,20–23]. The "pure" GB mechanisms include GB sliding, stress-driven GB migration, grain rotations mediated by GB dislocations, GB and triple junction diffusional creep. These mechanisms can significantly contribute to plastic deformation in NC metallic materials having finest grains. GB-mediated mechanisms include twinning, perfect and partial dislocations emitted at GBs. GB-mediated mechanisms are typically dominant in metallic nanomaterials with fine grains. Below we will consider GB-mediated mechanisms (Sections 3.1,3.2,3.3) and "pure" GB mechanisms (Sections 3.4,3.5,3.6,3.7), along with their synergies (Section 3.8), in metallic nanomaterials.

3.1. Deformation by perfect dislocations

In conventional CG metals, the dominant deformation mechanism is usually the slip of dislocations in grain interior. The dislocations are generated and stored mostly in the grain interior during plastic deformation. We now discuss conventional processes of the dislocation generation and storage in CG metals as well as their specific features in metallic nanomaterials.

Dislocations in CG metals are believed to be generated at Frank-Read sources (Fig. 6), especially those formed due to double cross slip [48,49]. A Frank-Read source (Fig. 6) operates at the shear stress $\tau_{F\text{-}R} \approx Gb/L$, where G denotes the shear modulus, b the magnitude of Burgers vector, and L the source size, that is, the distance between two pinning points for the initial gliding dislocation segment [48,49] (Fig. 6).

For geometric reasons, the maximum size L_{max} of a conventional Frank-Read source that can operate in a grain of size d is estimated as $L_{max} \approx d/3$ [71]. Therefore, in order to activate a Frank-Read source, one needs to apply a critical minimum shear stress of

$$\tau_{F\text{-}R} \geqslant 3Gb/d \tag{5}$$

This stress rapidly increases with decreasing grain size d. According to Eq. (5), the critical stress for activating a Frank-Read source can be increased to unrealistically huge values of $G/40$-$G/10$ in NC metals with grains sizes of 10–30 nm or smaller. Therefore, dislocation generation via Frank-Read sources in metallic nanomaterials is significantly hampered, or even completely suppressed when the grain size decreases to the order of 10 nm.

Dislocations are effectively accumulated in the interiors of coarse grains as plastic deformation progresses, which is responsible for the pronounced strain hardening and consequent high ductility. Strain hardening in pure metals is related

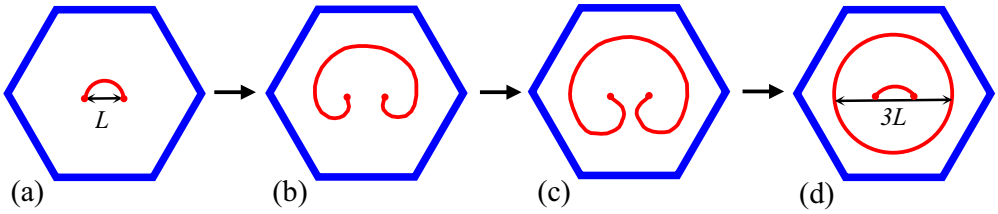

Fig. 6. Schematics of Frank-Read source of size L operating in a grain.

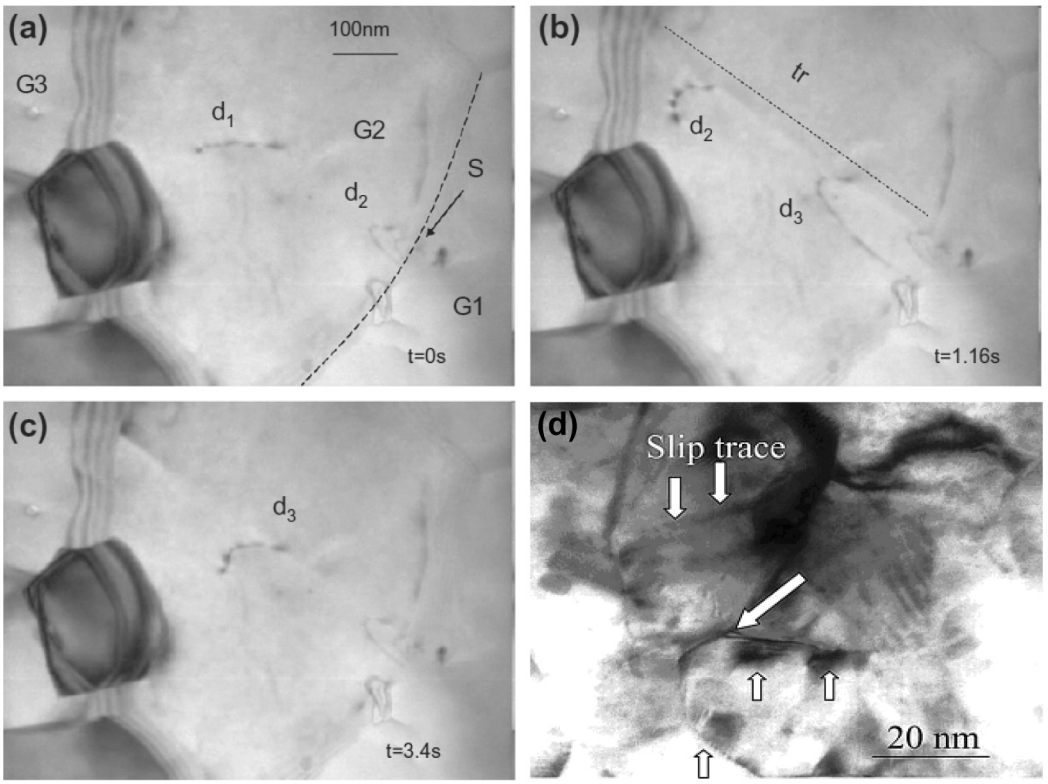

Fig. 7. (a–c) Intragranular dislocation activity at above 2% total strain during in situ TEM straining. The sequence shows a source S, located in the grain boundary GB12 (marked by a dashed line) emitting intragranular dislocations d1_3 in the plane delimited by its trace tr towards the interface GB23 [77]. (d) A bright field TEM image of nc-Ni following cold-rolling, showing slip traces indicated by downward-pointing arrows, a triple junction nanovoid, and semicircular strain contrast at grain boundaries indicated by upward-pointing arrows that suggest dislocation emission [75].

to the interactions among dislocations whose density ρ increases due to the generation of dislocations by conventional dislocation sources.

Dislocation-dislocation interactions significantly affect the flow stress and thereby strain hardening in CG metals at the main extended stage of its plastic deformation, which largely corresponds to the deformation stage III in single crystalline metals [72]. To a good approximation, the flow stress σ of a polycrystalline metal usually has the following relationship with dislocation density ρ [72]:

$$\sigma = \alpha G b \rho^{1/2} \tag{6}$$

where α is a constant related to material, temperature, strain rate and dislocation arrangement. Eq. (6) holds for pure fcc metals, where the lattice friction to dislocation motion is negligibly small. It is also valid for hcp and bcc metals at relatively high temperatures where the Peierls barrier is weak in resisting dislocation slip [72].

According to the Eq. (6), the strain hardening is controlled by the evolution of dislocation density ρ with increasing plastic strain ε. In a first approximation, the dislocation density evolution can be represented in its simplest, yet rather general, form [72,73]:

$$d\rho/d\varepsilon = k_1/b\Lambda - k_2\rho \tag{7}$$

where Λ denotes the dislocation mean free path, k_1 is a constant or a slowly varying quantity, and k_2 is a positive parameter determined by strain rate and temperature. The term $k_1/b\Lambda$ in Eq. (7) represents the rate of athermal accumulation of dislocations generated at dislocation sources during plastic deformation, and the term $-k_2\rho$ represents dynamic recovery that depends strongly on temperature and to a less extent on strain rate [72]. Both of these processes are active in the entire extended deformation stage. The first term dominates at low strains, providing high strain hardening. The contribution of the second mechanism gradually increases with plastic strain, leading to decreases in strain hardening. Nevertheless, in most cases, the strain hardening is high enough to maintain uniform tensile deformation at the main extended deformation stage [72]. The strain hardening from the first process is offset by that from the second at large strains, leading to the end of the extended deformation stage.

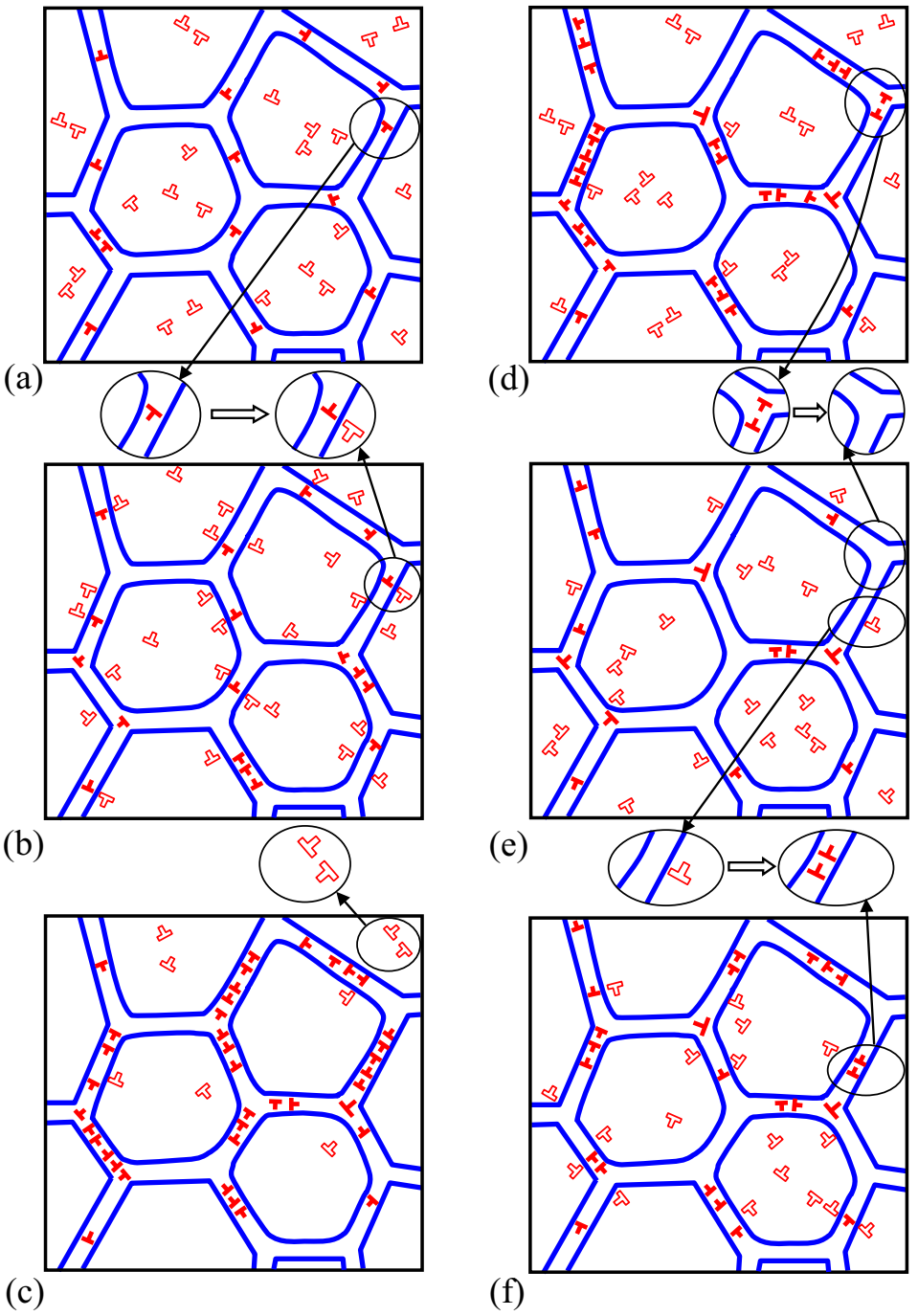

Fig. 8. (a–f) Schematics of evolution of lattice and grain boundary dislocation structures in NS materials with fine grains during plastic deformation. Generation of lattice dislocations concurrently occurs at grain boundaries and at Frank-Read Sources in grain interiors. The generated lattice dislocations move across grain interiors and are absorbed by grain boundaries where they are trapped and split into grain boundary dislocations. In turn, grain boundary dislocations either annihilate with grain boundary dislocations of opposite Burgers vectors or undergo other transformation to generate lattice dislocations at grain boundaries. Both the dislocation splitting and annihilation processes at GBs are fast, since their rates are controlled by GB diffusion, which is much faster than the bulk diffusion. Typical elementary processes inherent to evolution of dislocation structures in NS materials with fine grains are schematically illustrated in magnified insets. The magnified insets in (a) and (b) show grain boundary dislocation (a) whose transformation results in the generation of its antipode - sessile grain boundary dislocation with opposite Burgers vector – and a mobile lattice dislocation that moves in the adjacent grain (b). The magnified inset in (c) schematically shows generation of a lattice dislocation dipole (corresponding to a lattice dislocation loop in 3D material) at a Frank-Read source in grain interior. The inset in (d) and the upper inset in (e) show a dipole of grain boundary dislocations (d) that annihilate at grain boundary (e). The bottom inset in (e) and the inset in (f) show a lattice dislocation (e) that moves towards a grain boundary where this dislocation is absorbed and splits into two grain boundary dislocations (f).

In metallic alloys and composites, the strain hardening is also influenced by impurities, compositional inhomogeneities and second-phase inclusions, which hinder dislocation motion. These effects will be discussed in next sections with particular attention on their effects on ductility in metallic nanomaterials.

The deformation behavior discussed above is typical for CG metals. When grain size decreases, dislocation slip demonstrates different behavior owing to both the nanoscale and GB effects. Indeed, in metallic nanomaterials, dislocation sources in grain interiors are limited or no longer exist due to small grain sizes [13,71], and GBs become effective dislocation sources and sinks; see, e.g., [20–23,74–81]. Emission of dislocations from GBs has been experimentally documented in metallic nanomaterials with fine grains (Fig. 7a–c) [74,77] and NC metals with finest grains (Fig. 7d) [64,75,82–84].

In nanomaterials, dislocations glide across grain interior and are absorbed by GBs where they may be trapped and split into GB dislocations (Fig. 8). In turn, these GB dislocations may be annihilated with other GB dislocations with opposite Burgers vectors or undergo other transformation to produce lattice dislocations at grain boundaries (Fig. 8). Both the dislocation splitting and annihilation processes at GBs are fast, since their rates are controlled by GB diffusion, which is much faster than the bulk diffusion. With both the high rates for dislocation annihilation and inhibition of conventional dislocation sources, dislocation cannot accumulate to produce strain hardening. Consequently, necking occurs at low strains (Fig. 5), leading to low ductility. This behavior is typical for metallic nanomaterials with fine grains where dislocations are emitted and annihilated at GBs (Fig. 8) during plastic deformation.

3.2. Partial dislocation emission from grain boundaries

As discussed above, for CG metals, there exist dislocation sources in the grain interior. The best-known dislocation source is the Frank-Read source [48]. However, there are also arguments that Frank-Read source has not been observed experimentally [85]. Theoretically, any dislocation segment that can slip but have two ends pinned can act as a Frank-Read source. Considering that dislocations slip on different slip systems often interact with each other to form dislocation jogs and networks, it is reasonable to assume that the Frank-Reed source can easily form in the interior of coarse-grains.

When grains are refined to a critical size below 100 nm, dislocations often no longer exist in the grain interior. Although trapped dislocations have been observed in grains much smaller than 100 nm, and even down to 5 nm [86–88], these are exceptions in a small fraction of grains instead of typical cases. Shown in Fig. 9 is hierarchy and size ranges of different structural features of nanostructured Ti, which was processed by severe plastic deformation (SPD) [13,65]. As shown, the interiors of grains or sub-grains smaller than 100 nm are largely dislocation free.

Without dislocations in the interior of nanometer-sized grains, the conventional dislocation sources that operate in coarse-grained metals no longer work. GB plays a critical role in the deformation of nanocrystalline metals in two different ways: (1) GB acts as the dislocation source and sink [6,13,63,64,82,83,89–102], (2) GB sliding and grain rotation [87,101–116]. Below we will discuss the partial dislocation emission from GBs because this becomes a prevalent phenomenon in NC fcc metals.

Partial dislocation emission from GBs was first observed by molecular dynamic (MD) simulations [83,95,102,117], and later verified experimentally under high-resolution electron microscopy (HRTEM) [82,92,93]. The slip of a partial dislocation leaves behind a stacking fault, which is often the first step to the nucleation of deformation twins. When the grain size is below a critical size, it becomes easier to emit partial dislocations than full dislocations [63,64,83,94]. It is found that in nanocrystalline Ni full dislocations on the non-equilibrium GBs are often dissociated into two partials with a wide stacking

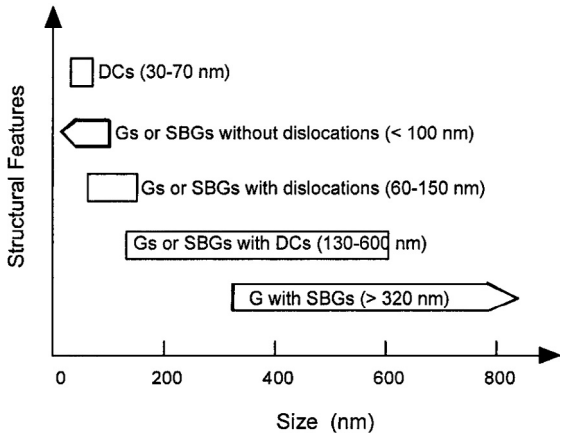

Fig. 9. Hierarchy and size ranges of different structural features in nanostructured Ti processed by severe plastic deformation. Grains and subgrains are largely dislocation free in their interior when their sizes are reduced to below 100 nm [65]. The acronyms are G – grains, SBG – subgrains, DC – dislocation cells.

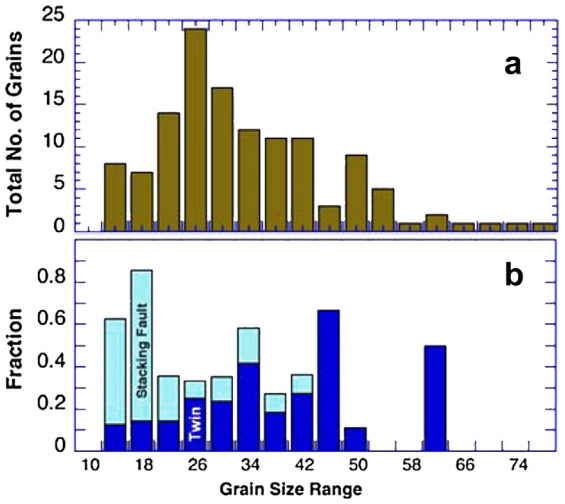

Fig. 10. (a) Grain size distribution of nanocrystalline Ni. (b) The fraction of grains containing stacking faults and twins in Ni after tensile testing at liquid nitrogen temperature. The two highest blue bars should be disregarded because they are statistically abnormal due to the small number of grains sampled. Because a stacking fault has to be formed first before forming a twin, the total bar height (twin + stacking fault) can be regarded as fraction of grains that produced stacking fault, which apparently increased with decreasing grain size. In contrast, there is an optimum grain size for twinning.

fault in-between. These partials can readily slip into the grain interior under appropriate local stress [89]. In other words, there are partial dislocation sources on GBs that are readily available to glide into grain interior.

Another reason for the observation of partial-slip-generated stacking fault is due to the large splitting distance between the leading and trailing partials of a full dislocation [63,64,83]. Due to the orientation difference between the Burgers' vectors of the leading and trailing partials, the applied stress may drive the two partials further apart. When the splitting distance is larger than the grain size, the trailing partial will not have the opportunity to be emitted from the GB and the leading partial produces a stacking fault across the grain. Since smaller grains have higher flow stress, the splitting distance between the leading and trailing partials will be larger in smaller grains, which, coupled with the smaller grain size, makes it easier to produce stacking fault in smaller grains.

From the above discussion, it is not surprising that there is grain size effect on formation of stacking faults by the slip of partial dislocations. It has been observed that stacking fault is formed more frequently with decreasing grain size in nanocrystalline Ni (see Fig. 10) [118].

The emission and slip of partial dislocations from GBs leave behind stacking faults. This will have effect on the mechanical properties in three potential ways. First, the formation of stacking fault is the first step to nucleate a deformation twin. Twins have been reported to be able to simultaneously increase strength and ductility of nanometals [13]. Second, the accumulation of stacking faults will increase the strain-hardening rate to help with increasing ductility. Third, stacking faults can interact with gliding dislocations in a way similar to twin boundaries to help with dislocation accumulations, which will increase the strain hardening. This is especially important for hexagonal close-packed (hcp) metals, in which deformation twinning is suppressed when the grain size is small [119–121]. For example, it has been reported that high density of stacking faults can significantly enhance the strength while maintaining good ductility in ultrafine-grained Mg [122–126].

3.3. Deformation twinning

Twinning is one of the most important deformation mechanisms in metallic materials, especially at low temperatures, high strain rates and in materials with low stacking fault energy [13,127,128]. Deformation twinning in nanocrystalline fcc metals are very important because it is one of a few mechanisms that can simultaneously increase their ductility and strength [13,128,129]. Therefore, it is of critical importance to study the deformation twinning in NS metals.

The mechanisms for the nucleation and growth of twins in NS fcc metals are usually very different from those in CG metals [13,128,130–132]. For CG metals twinning mechanisms proposed in the literature include the pole mechanism [133], the prismatic glide mechanism [134], the faulted dipole mechanism [135], and others [136–138]. These mechanisms involve dislocation sources in grain interior, and the partials to produce a twin have the same Burgers vector. In other words, each layer of the twin plane shifted toward to the same direction to produce a shear strain. In contrast, for NC fcc metals and alloys, GBs become the primary source for partial emissions to produce twins, because it is largely dislocation free in their grain interior. Consequently, the twin morphologies in NC fcc metals are very different from those in CG fcc metals [127].

Twinning mechanisms observed and proposed in NC fcc metals by both MD simulations [84,95] and HRTEM [13] include homogeneous nucleation by the coincidental overlapping of two stacking fault ribbons formed by dissociated lattice dislocations [82], grain boundary splitting and migration [91], overlapping of a stacking fault from the grain boundary with a

dissociated lattice dislocation [89], partial dislocation emission from the GBs [92,139–141], cross-slip of twinning partials [130,142], the dislocation rebound at GB [130,143], etc. The primary mechanism for the formation of deformation twins in NC fcc metals is partial dislocation emission from GBs. A partial multiplication mechanism on the GB has been proposed to explain why partials can be emitted from every slip plane to form a deformation twin [144]. Multiple twins intersecting each other have also been observed and their formation mechanisms by dislocation reactions have also been proposed [130,145].

Most deformation twins in NC fcc metals are found to no longer produce macroscopic strain, as they usually do in conventional CG metals [127]. This is a unique phenomenon observed in NC fcc metals and alloys [127]. Two mechanisms have been proposed based on experimental observations for the formation of such type of twins. The first is random activation of partials (RAP) from GBs [127]. For fcc metals, twins can be produced by the slip of partials on successive slip planes even when the Burger's vector of these partials are different. There are three possible Burgers vectors for partial dislocations on a slip plane. The slip of a partial dislocation produces a stacking sequence change of A → B, B → C, C → A for all of the three Burgers vectors. Since the sum of the three Burgers vectors equal zero, i.e. $\mathbf{b_1} + \mathbf{b_2} + \mathbf{b_3} = 0$, the sum of the Burgers vectors of all partials that form a twin should be approximately zero in the RAP mechanism, in which the total numbers of partials from all Burgers vectors are about the same.

The other mechanism that can produce a twin without macroscopic strain is the cooperative slip of three partials (CSTP) [141,146–150], in which the sum of their Burgers vectors equaling zero, generating twins with zero-macrostrain. Specifically, a group of three partials with Burgers vectors of $\mathbf{b_1}$, $\mathbf{b_2}$, $\mathbf{b_3}$ slip together under an applied load. When one or two of the three partials are driven forward by the applied stress, stacking fault(s) will be generated, which will drive the partial (s) left behind to move forward to reduce the stacking fault energy. These two types of mechanisms, namly RAP and CSTP, can be differentiated under HRTEM basing on the morphology of their incoherent twin boundary (see Fig. 11 [151]). These two mechanisms are found to be almost equally significant in the formation of twins with zero strain [146]. Alloying element is also found to affect the CSTP mechanism via changing the stacking fault energy [151,152]. It should be noted that this mechanism can also leads to detwinning when the applied stress is reversed [153–155].

Deformation twinning has been found significantly affected by grain size. As illustrated in Fig. 12, CG metals become more difficult to deform by twinning with decreasing grain size, which is a trend observed experimentally for metals with fcc, bcc and hcp crystal structures [128,156]. For NS metals, the grain size effect becomes very different. As shown in Fig. 12, for fcc metals, with decreasing grain size in the NC range, twinning first becomes easier, reaches an optimum grain size for twinning, and then becomes more difficult [13,128]. This phenomenon was first predicted by an analytical model with the assumption that all dislocations are emitted from GBs [63,64]. This assumption was based on the experimental observation of the lack of dislocation source in the interior of nano-sized grains [65] as well as the observation of partial dislocation emission from the GB by MD simulations [83,95,102,117] and HRTEM observations [82,92,93]. The unique grain size effect on deformation twinning for NC fcc metals was verified later experimentally (see Fig. 10) [118,157].

The optimum grain size for twinning shown in Fig. 12 is very important in designing NS fcc metals for high strength and high ductility [13]. NS metals typically have very low ductility, which severely limit their structural applications. Deformation twinning has been found to be able to increase not only the strength, but also the ductility at the same time, while most other approaches for increasing ductility often sacrifice the strength [13,128,129]. Therefore, for NS fcc metals, their grain size should match the optimum grain size for twinning to obtain the high ductility as well as high strength. The optimum grain size for twinning can be estimated as

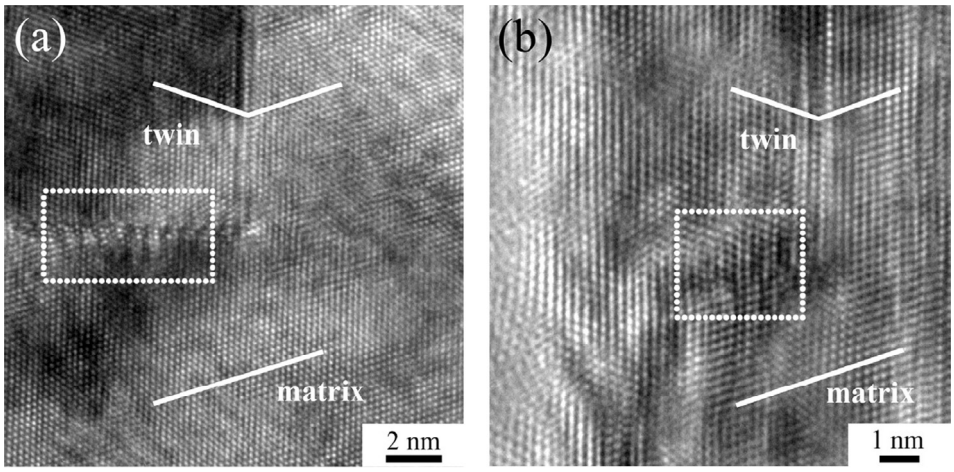

Fig. 11. Two mechanisms for producing twins with zero macroscopic strain [151]. (a). The cooperative slip of three partials (CSTP), (b) The random activation of partials (RAP) mechanism.

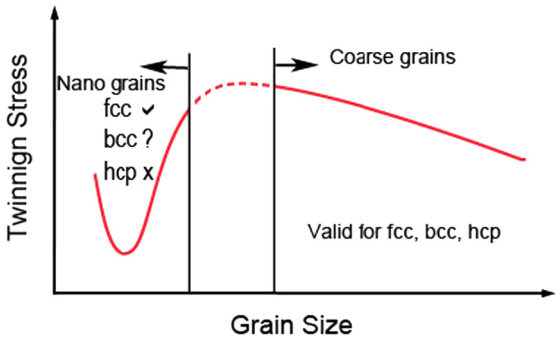

Fig. 12. Schematics of the grain size effect on deformation twinning for fcc, bcc, and hcp metals.

$$\frac{d_m}{\ln(\sqrt{2}d_m/a)} = \frac{9.69 - \nu}{253.66(1-\nu)}\frac{Ga^2}{\gamma} \tag{8}$$

where d_m is the optimum grain size for twinning, a is the lattice parameter, ν is the Poisson's ratio, G is the shear modulus, and γ is the stable stacking fault energy [13].

The optimum grain size for deformation twinning in fcc metals was further demonstrated in a report on the detwinning-twinning process in Ni-20 (wt%) Fe alloy thin film with an average grain size about 20 nm. The sample initially had 30% of its grains containing growth twins (Fig. 13a). Under high-pressure torsion (HPT) [158], detwinning occurred because the grain sizes were smaller than the optimum grain size for twinning, which is around 70 nm (Fig. 13b). The grain size increased with increasing HPT strain, and when the grain size matched the optimum grain size for twinning, deformation twins reappeared (Fig. 13c). When the grain size grew further to larger than the optimum grain size, the detwinning occurred again to reduce the fraction of grains containing twins (Fig. 13d).

The above observations demonstrate the importance of designing NS fcc metals and alloys to have the optimum grain sizes. The twins are not stable in grains out of the optimum grain size range. Detwinning is usually caused by the interaction between the dislocations and twin boundaries [159].

It should be noted that the Eq. (8) was derived for pure metals where the ratio of stacking fault energy to twin boundary energy is about 2. For alloys, this assumption may not be valid, and consequently the predicted optimum grain size may deviate from the experimental observation [152]. In addition, deformation parameters such as strain rate and temperature

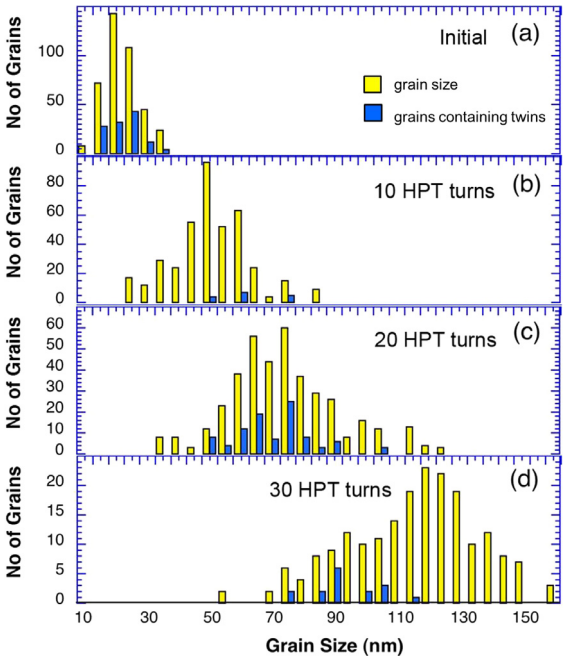

Fig. 13. The distributions of grain size (yellow bar) and grains containing twins (blue bar) in (a) as-synthesized Ni-20 (wt%) Fe alloy film, (b) after processing for 10 HPT turns, (c) after processing for 20 HPT turns, and (d) after processing for 30 HPT turns.

may also influence twinning [118]. Nevertheless, the Eq. (8) provides an estimate of the optimum grain size, which is useful for designing NS fcc alloys.

The grain size effect for twinning is not clear for NC bcc metals [13]. Further studies are needed. For CG hcp metals, deformation twinning is usually activated due to the lack of five slip systems that are required for continuous deformation without producing voids according to the von Mises criterion [160]. However, twinning becomes more difficult with decreasing grain size all the way to the nanocrystalline range [13,119,161]. The reason for the observation is not clear. Basing on indirect evidence from the literature and on extensive discussions with many colleagues, we rationalize the following hypothesis. First, the nucleation of a deformation twin is much more difficult and requires much higher applied stress than the slip of dislocations. In a large hcp grain, dislocation pileup at grain boundaries or other obstacles produces high local stress concentration, and the lack of slip systems makes it more difficult to activate other slip systems to relieve the stress concentration. Therefore, it has high statistical probability that the stress concentration becomes high enough to nucleate a deformation twin. However, when the grain size becomes too small, the probability for large dislocation pileups decreases, which decreases the probability for the stress concentration to reach the critical stress for twin nucleation. In addition, when the grain sizes reach ultrafine grain and nanocrystalline range, GB related processes such as grain rotation and grain boundary sliding become active to accommodate and coordinate inter-grain deformation, which further relieves the stress concentration and decreases the twinning probability. Therefore, with decreasing grain size, although the global flow stress increases, it becomes less likely to build up local stress concentration high enough to nucleate deformation twins. The above hypothesis, although logically reasonable, still needs to be further studied and verified. It is unfortunate that deformation twinning cannot be activated as an effective mechanism to improve the strength and ductility in NS hcp metals and alloys.

3.4. Grain boundary sliding

We now consider GB sliding as a deformation mechanism in NS metals under certain conditions. GB sliding means a relative shear of neighboring grains across the GB [162]. GB sliding conventionally occurs in high-angle GBs in CG and NS materials at elevated temperatures [74,112,162–164], although there are examples of enhanced GB sliding in NS metals at room temperature; see, e.g., [109,165–168]. In particular, in addition to intragranular dislocation slip, GB sliding was found to significantly contribute to plastic flow of UFG aluminum processed by equal channel angular pressing at room temperature [109].

Theoretically, GB sliding occurs by generation and motion of GB dislocations. Such dislocations by definition are line GB defects that violate GB symmetry in translation. GB dislocations are specified by Burgers vectors with small magnitudes ranging approximately from $a/5$ to $a/3$, where a is the lattice parameter [33]. Slip of GB dislocations having Burgers vectors parallel to a GB boundary plane leads to GB sliding. The dislocation mode of GB sliding is described in terms of the dislocation theory in solids; see, e.g., [169].

In CG and NS metals, GB sliding occurs along GBs that join at triple junctions and form complicated configurations with non-trivial geometry (Fig. 14a). In addition, even individual GBs are often not flat, but contain facets and ledges. With non-trivial geometry of GBs and their ensembles, GB sliding is different from "ideal" sliding along a flat GB in a bi-crystal. There are geometrical obstacles for GB sliding along curved GBs. In the case of NC materials, especially those with finest grains, GBs are very short, and the density of triple junctions are very high. In these materials, GBs change orientations of their planes at triple junctions, which serve as major geometrical obstacles for GB sliding. Therefore, accommodation of GB sliding at triple junctions is critical for GB sliding in NC materials (Fig. 14). The same is true for microcrystalline materials exhibiting superplasticity whose dominant deformation mechanism is GB sliding.

GB sliding in NS materials can be effectively accommodated by transformations of defects at triple junctions and local migration of GBs (Fig. 14b–e), emission of dislocations from triple junction to adjacent grains (Fig. 14f and g), diffusion-controlled rotational deformation (Fig. 14i and h) and other local diffusion processes. Also, elastic straining slightly contributes to accommodation. We now consider the first two processes (Fig. 14b–g) as basic accommodating mechanisms for GB sliding.

In microcrystalline metals, emission of dislocations from triple junctions to grain interior is conventionally viewed as the dominant accommodation mechanism for GB sliding (Fig. 14f and g). There are two scenarios for dislocation slip to accommodate GB sliding (Fig. 15) [162,168]. First, when subgrains exist (Fig. 15a), dislocations emitted from a triple junction pile up at the first subgrain boundary at B in the adjacent grain (Fig. 15a). Second, when no subgrains exist (Fig. 15b), dislocations emitted from a triple junction pile up at the opposite GB (Fig. 15b).

Strain rate serves as a key characteristic parameter for GB sliding accommodated by dislocation emission in both its variants shown in Fig. 15. The process controlling the strain rates is dislocation climb from the pile-up heads B and D. In the first situation, dislocations from the pile-up heads are removed by dislocation climb controlled by relatively slow bulk (lattice) diffusion. The strain rate $\dot{\varepsilon}_{gbs(d>\lambda)}$ that from GB sliding can be described as [162]:

$$\dot{\varepsilon}_{gbs(d>\lambda)} = \frac{A' D_{bulk} G b}{k_B T} \left(\frac{b}{d}\right) \left(\frac{\sigma}{G}\right)^3 \tag{9}$$

where A' denotes a dimensionless constant, D_{bulk} bulk diffusion coefficient, k_B the Boltzmann constant, d grain size, T absolute temperature, and σ applied stress.

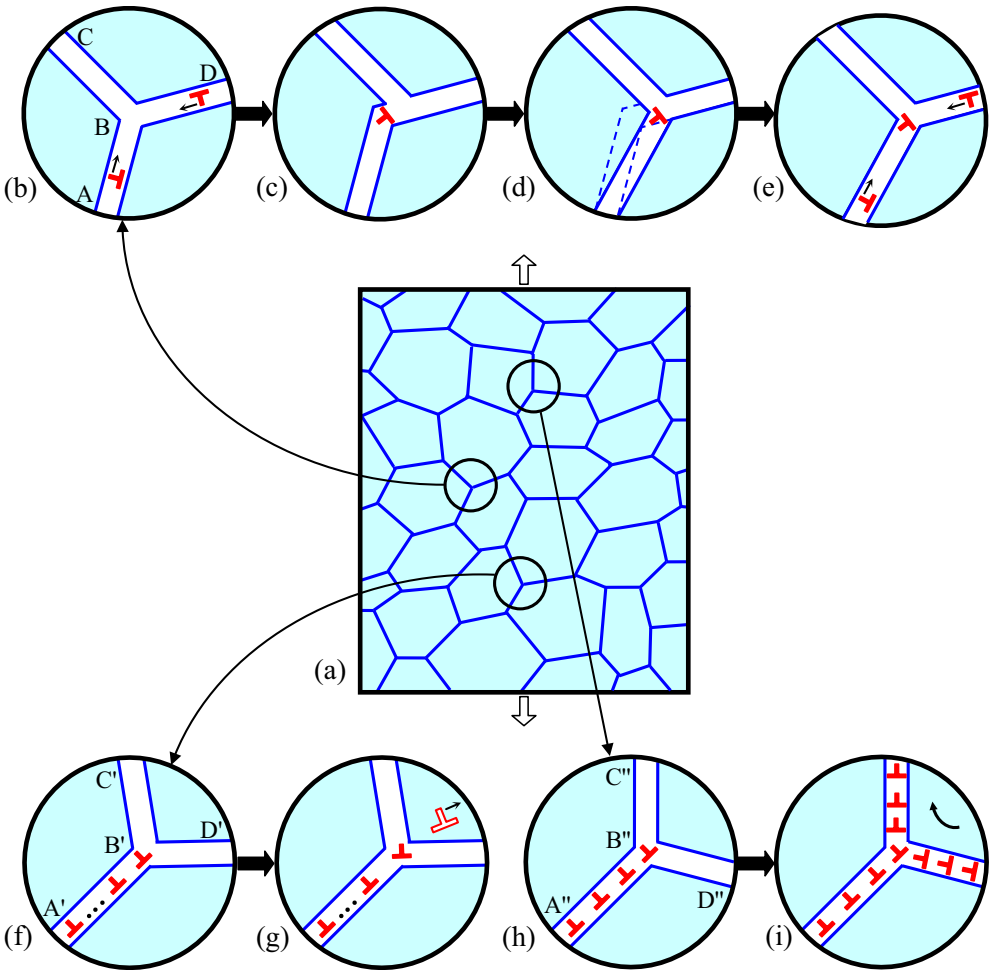

Fig. 14. Grain boundary sliding and its basic accommodation mechanisms in NS materials. (a) Nanocrystalline or ultrafine-grained specimen under tensile load (a schematic general view). Magnified insets (b–i) illustrate accommodation mechanisms. (b–e) Accommodation through transformations of defects at triple junctions and local migration of grain boundaries. (f and g) Accommodation through emission of lattice dislocations from triple junction to adjacent grain. (i and h) Accommodation through diffusion-controlled rotational deformation.

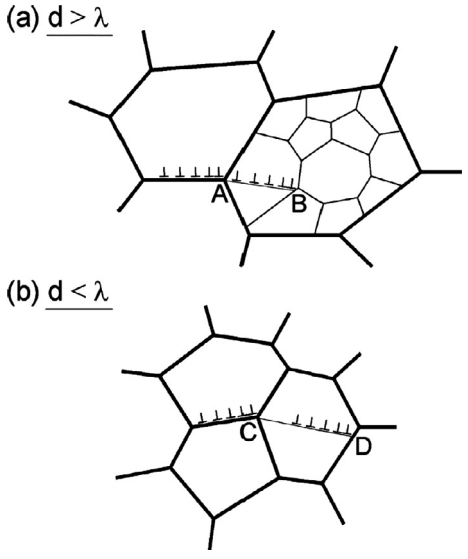

Fig. 15. A unified model for Rachinger GBS under (a) conventional creep conditions when $d > \lambda$ and (b) superplastic conditions when $d < \lambda$ [162].

In the second scenario, dislocations from the pile-up heads are located at GBs, and they are removed by GB dislocation climb processes controlled by comparatively fast GB diffusion. In these circumstances, the strain rate $\dot{\varepsilon}_{gbs(d<\lambda)}$ that specifies GB sliding is as follows [162]:

$$\dot{\varepsilon}_{gbs(d<\lambda)} = \frac{A'' D_{gb} G b}{k_B T} \left(\frac{b}{d}\right)^2 \left(\frac{\sigma}{G}\right)^2 \tag{10}$$

where A'' denotes a dimensionless parameter ($\approx$10), and D_{gb} the GB diffusion coefficient ($D_{gb} \gg D_{bulk}$).

With Eq. (3) for strain rate sensitivity m and the strain rate in Eqs. (9) and (10), one finds the parameter m = 0.33 and 0.5 for the microstructures with and without subgrains, respectively. The value of m = 0.5 corresponds to superplastic deformation regime in microcrystalline materials with stable grain sizes in the range from 2 to 10 μm at and temperatures above $0.5T_m$, where T_m is the melting temperature [162,168]. Conventional superplasticity in microcrystalline materials is featured by low strain hardening, which makes large strain rate sensitivity crucial for stable superplastic tensile deformation.

Superplastic deformation in NS metals can occur at lower temperatures and higher strain rates than that in microcrystalline metals with the same chemical compositions [112,163,164,170–172]. This is caused by smaller grain sizes and enhanced diffusion figuring in the strain rate Eq. (10) for metallic nanomaterials. In addition, superplastic deformation in metallic nanomaterials is typically characterized with high flow stresses and pronounced strain hardening (without steady state flow), in contrast to superplasticity in microcrystalline materials; see, e.g., (Fig. 16 [163]). These observations indicate unique GB sliding and superplasticity in NS metallic materials at elevated temperatures.

Superplastic deformation in metallic nanomaterials is accompanied with grain growth that contributes to strain hardening. However, as noted by Mukherjee [74], grain growth alone is not able to cause all of the strain hardening in these materials. For example, during the superplastic deformation of Ni_3Al alloy at 650 °C and at 1×10^{-3} s^{-1} strain rate, the grain size change contributed to a flow stress increase by a factor of 2 [74]. However, the flow stress actually increased by a factor of ~5.

In order to explain the observed unusual strain hardening in superplastic metallic nanomaterials, it is important to identify and describe the processes occurring at triple junctions due to GB siding. In particular, one should consider unique mechanism accommodating GB sliding in metallic nanomaterials, which could be different from dislocation slip in adjacent grains.

First, it is worth noting that accommodation of GB sliding is affected by the geometry of triple junctions where the sliding processes occur. Some triple junctions allow GB sliding at realistic stress levels while others not. For instance, let us consider GB sliding along a GB A′B′ where maximum or nearly maximum shear stress operates (Fig. 14f). Shear stresses are low in GBs C′B′ and D′B′ adjacent to the junction B' so that GB sliding stops at this junction. Its accommodation is conventionally believed to occur through emission of either perfect or partial dislocations in the adjacent grain (Figs. 14g and 21) [173]. Conventional superplasticity theory for microcrystalline materials focuses on dislocations emissions from triple junctions; see Refs. [162,164,168] and our previous discussion (Fig. 15). However, GB-sliding-induced transformations of triple junctions themselves are also important, and these transformations are of crucial significance in NS materials, which have very high density of triple junctions.

Following [174–176], when GB sliding is accommodated by dislocation emission into grain interior, it produces dipoles of wedge disclinations at and near triple junctions (Fig. 17). Each disclination is defined as a rotational linear defect at either a GB or a triple junction and specified by the rotational misfit called its strength [177–179]. In particular, a triple junction disclination is characterized with strength being a triple junction angle gap, that is, a non-zero sum of tilt misorientations that specify GBs adjacent to the junction [177–179]. A disclination at a tilt GB represents the line shared by two adjacent GB segments having difference in their tilt misorientations, which plays the role of disclination strength. Fig. 17b–d

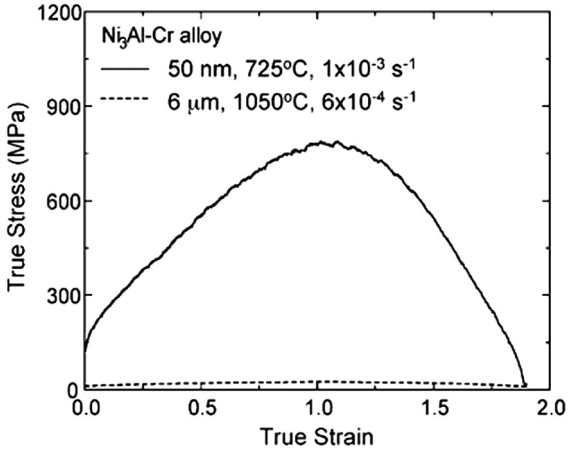

Fig. 16. Tensile curves for Ni_3Al for superplastic deformation under different conditions [163].

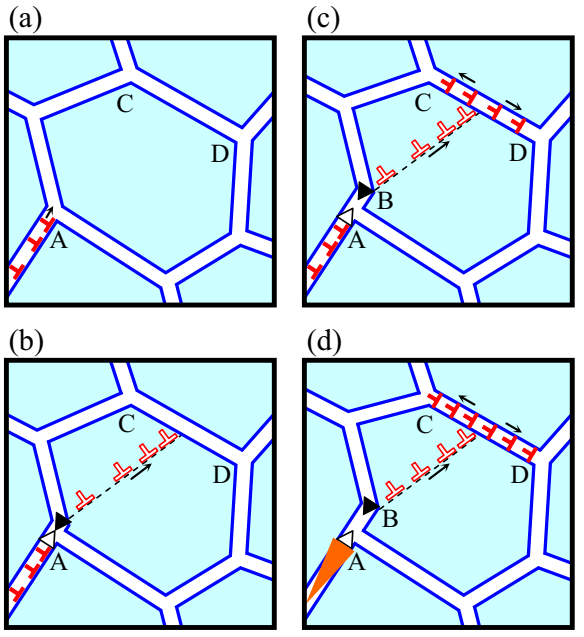

Fig. 17. Grain boundary sliding and its accommodation through lattice dislocation emission from triple junctions. (a) Grain boundary sliding occurs through the movement of grain boundary dislocation along a grain boundary. Grain boundary dislocations are accumulated near triple junction A. (b) Grain boundary sliding leads to splitting of the initial triple junction A into two double junctions, A and B, of grain boundaries. Grain boundary dislocations transform into lattice dislocations that are emitted from junction B and glide within grain I. These processes are accompanied by formation of dipole of wedge disclinations (full and open triangles) at junctions A and B. (c) The lattice dislocations glide towards grain boundary CD where they transform into grain boundary dislocations climbing along this grain boundary. The distance between wedge disclinations A and B increases due to grain boundary sliding. (d) The distance between wedge disclinations A and B increases more due to grain boundary sliding. Nanocrack (elongated orange triangle) nucleates in the stress field of the dipole of wedge disclinations A and B.

schematically shows nucleation of disclination dipole owing to GB sliding in a NC metallic specimen. Such disclination dipoles create high internal stresses, and their formation provides both significant contribution to the flow stress and pronounced strain hardening in NS materials where plastic flow involves GB sliding [174–176]. So, the disclination-dipole-induced contribution τ_d to the overall flow stress is as follows [176]:

$$\tau_d = \frac{G\omega^2\varepsilon}{2\pi(1-\nu)f_{gbs}}\left(\ln\frac{R_s f_{gbs}}{\varepsilon d}+1\right), \tag{11}$$

where G denotes the shear modulus, ω the disclination strength, ε the plastic strain, ν the Poisson ratio, f_{gbs} the fraction of GBs that mediate GB sliding, R_s the mean screening length for stress fields created by a disclination dipole, and d the mean grain size.

According to Eq. (11), τ_d rapidly increases with ε, if $\varepsilon < R_s f_{gbs}/d$, providing pronounced strain hardening associated with nucleation of GB disclination dipoles. The strain hardening in question occurs intensively in NS materials with high densities of GBs and triple junctions. Following estimation in paper [176] for NC copper and nickel, the formation of GB disclinations due to GB sliding (Fig. 17b and c) gives rise to significant strain hardening and thus delays plastic instabilities in NC metals. However, cracks can be nucleated in stress fields of disclination dipoles and thereby diminish ductility in metallic nanomaterials (Fig. 17d). These competing effects of GB disclination dipoles on ductility of metallic nanomaterials deformed by GB sliding will be discussed in detail in Section 5.1.

We now consider triple junctions with geometry that allow GB sliding in two adjacent GBs in NS materials (Fig. 18). In this case, high shear stresses operate in two GBs adjacent to a triple junction so that GB sliding occurs in these two GBs, transmits across the triple junction and induces transformations of both the junction and the GBs. For instance, following Ref. [180], let us examine a model configuration of GB dislocations that mediate GB sliding in the vicinity of a triple junction (Fig. 18b). In the initial state, there are two GB dislocations located in GBs adjacent to the triple junction. They are specified by Burgers vectors $\boldsymbol{b}_1$ and $-\boldsymbol{b}_2$ parallel to those GB planes. Hereinafter, the dislocations under consideration will be called the $\boldsymbol{b}_1$- and $-\boldsymbol{b}_2$-dislocations, respectively. The dislocation configuration undergoes transformations driven by shear stress τ. More precisely, the $\boldsymbol{b}_1$- and $-\boldsymbol{b}_2$-dislocations are stopped near the triple junction at comparatively low stress $\tau < \tau_1^{crit}$ (Fig. 18b). These dislocations glide over short distances and converge, if the stress increases so that it achieves value of τ_1^{crit} (Fig. 18c). As a result of the convergence, a sessile GB $\boldsymbol{b}$-dislocation is generated, which has Burgers vector $\boldsymbol{b} = \boldsymbol{b}_1 - \boldsymbol{b}_2$ (Fig. 18c). Along with the formation of the $\boldsymbol{b}$-dislocation, the triple junction moves over a short distance owing to GB sliding

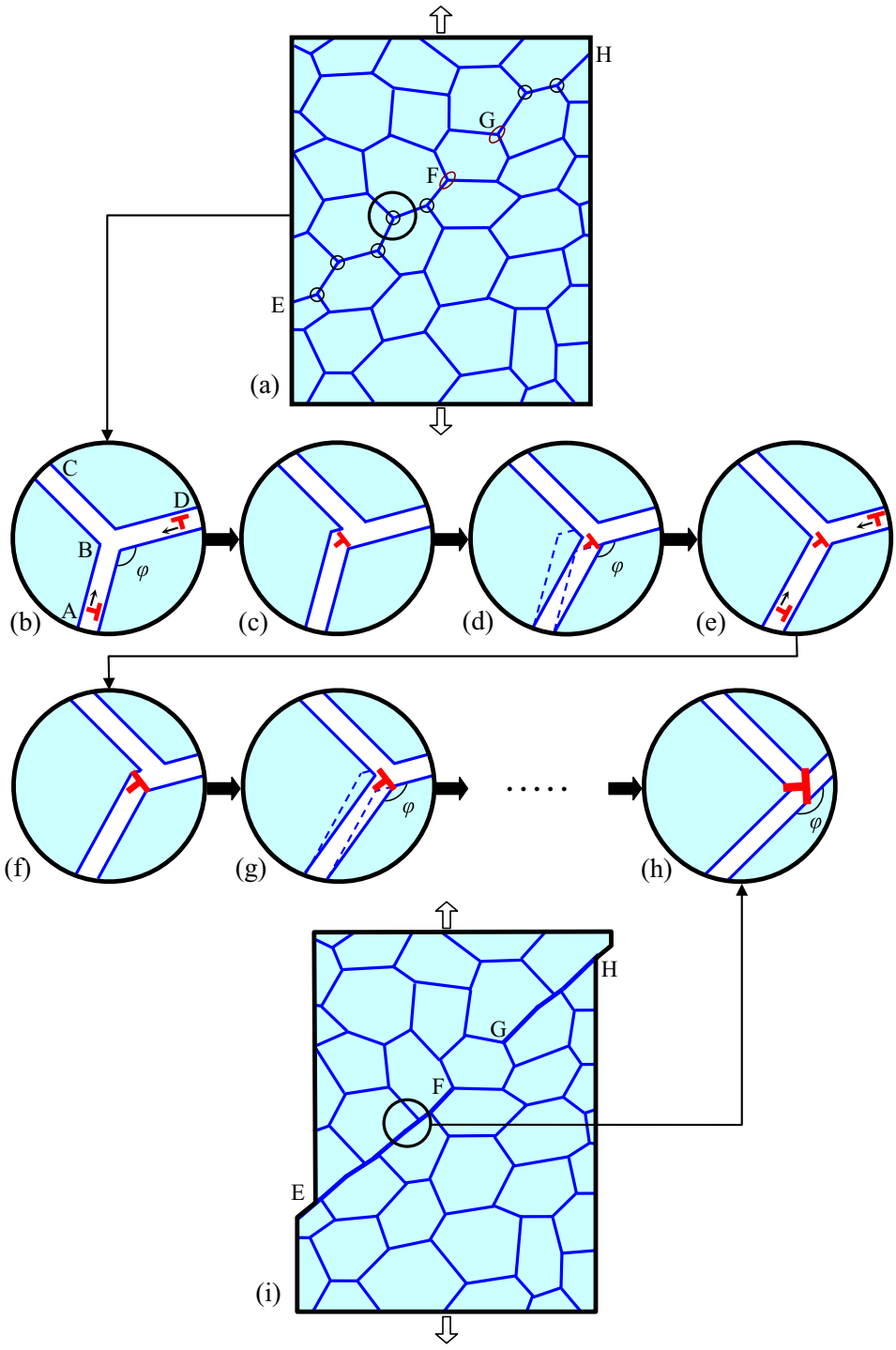

Fig. 18. Formation of mesoscopic sliding surface in a metallic nanocrystalline specimen deformed by grain boundary sliding. (a) Nanocrystalline specimen under tensile load (a schematic general view in 2D). Triple junctions F and H (marked by small ellipses) do not transmit grain boundary sliding, because the two grain boundaries adjacent to each of these junctions are highly misoriented relative to the maximum shear stress direction (that makes a 45° angle with the tensile load direction). Other triple junctions (marked by small circles) at grain boundary chain EH effectively transfer grain boundary sliding at realistic stress levels. Magnified insets (b)-(h) illustrate accommodation of grain boundary sliding through transformations of defects at triple junction B and local migration of adjacent grain boundary AB. These processes lead to gradual increase of the triple junction angle φ so that φ becomes close to 180° after transmission of pronounced gain boundary sliding across triple junction B; see figure (h). The same processes occur at other triple junctions (marked by small circles) that effectively transfer grain boundary sliding and belong to the grain boundary chain EH. As a result, mesoscopic sliding surface EH is formed; see figure (i). In doing so, grain with triple junctions F and H obstructs grain boundary sliding along the mesoscopic sliding surface. Accommodation of grain boundary sliding at this grain can occur by lattice slip (Figs. 20f and g and 21) or rotational deformation (Fig. 20h and i). In this case, the accommodation mechanism controls rate of grain boundary sliding along the mesoscopic sliding surface.

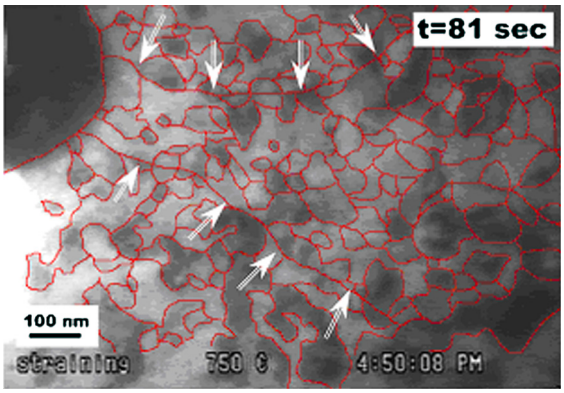

Fig. 19. TEM images taken just after cooperative grain boundary sliding. Arrows show mesoscopic sliding surfaces [163].

(Fig. 18c [180]). The triple junction displacement is accommodated by local migration of the adjacent GB (Fig. 18d). The driving force for the migration process represents a decrease in proper energy of the GB whose length is reduced owing to the local migration.

After the transformation of $\boldsymbol{b}_1$- and $-\boldsymbol{b}_2$-dislocations (Fig. 18b–d), GB sliding continues to proceed near the triple junction through nucleation and glide of new GB dislocations (Fig. 18 e). The glide of the new dislocations is hampered by their elastic interaction with the $\boldsymbol{b}$-dislocation. With the hampering effect, one needs to increase the applied stress to sustain GB sliding. That is, a new critical value $\tau_2^{crit} > \tau_1^{crit}$ should be applied in order to move the new GB dislocations towards the triple junction where they converge with the sessile $\boldsymbol{b}$-dislocation (Fig. 18f). As a result of the convergence transformation, the new sessile dislocation is formed whose Burgers vector magnitude increases as compared to b (Fig. 18f). Besides, local accommodating GB migration occurs as shown in Fig. 18g.

The transformations of GB dislocations repeatedly occur, resulting in growth of both the Burgers vector magnitude that specifies the sessile dislocation and, consequently the stress needed to sustain GB sliding. According to the theoretical analysis presented in Ref. [176], the increase in the flow stress due to transformations of GB dislocations near triple junctions contributes significantly to the strain hardening experimentally observed [171,172] in NS materials at the first extended stage of superplastic deformation; see also a discussion in paper [163].

The transformations also give rise to transfers of triple junctions and accommodating GB migration processes (Fig. 18 [180]). Due to such processes, the triple junction angle φ grows (Fig. 18) which specifies the role of such a junction in hampering the GB sliding. Thus, when the GB sliding progresses, the angle φ increases, which is accompanied by diminishing strain hardening caused by the triple junction. At late stages of GB sliding, the triple junction angle φ approaches 180°, in which case planes of GBs adjacent to the triple junction form one extended plane (Fig. 18h).

In addition, GB dislocations gliding along GBs AO and OB (Fig. 18) elastically interact. More precisely, there is the elastic attraction between them, which grows with rising triple junction angle φ [180]. This causes a negative contribution to the flow stress needed to sustain the GB sliding. Thus, as the GB sliding progresses, the angle φ increases leading to two negative contributions to the flow stress: one contribution is from triple junction geometry decreasing its hampering effect on GB sliding, the other is due to enhancement of the attraction force between GB dislocations moving towards triple junction. Consequently, transformations of GBs near triple junctions during the GB sliding (Fig. 18) can serve as dynamic recovery processes that reduce the strain hardening in NS materials. The strain hardening effect related to GB dislocation storage at triple junctions competes with the dynamic recovery related to GB migration in vicinities of triple junctions. With the competition, one logically explains the typical character inherent to "stress–strain" curves (see, e.g., Fig. 16) in NS materials exhibiting high strain-rate superplasticity [163,180]. Briefly speaking, during the initial long-stage superplastic deformation, the strain hardening dominates, whereas the dynamic recovery processes become dominant at the late superplastic deformation stage.

Also, the model [180] (Fig. 18) effectively explains the formation of mesoscopic sliding surfaces – planar arrays of GBs - experimentally observed in NS materials at the second stage of superplastic deformation at elevated temperatures (Fig. 19 [163]) [112,163] and at cold rolling at ambient temperatures [166]. The formation of such surfaces is treated as a unique feature of superplasticity [112,163,181].

To summarize, GB sliding represents a deformation mechanism that effectively operates in microcrystalline metallic materials and NS metals with fine grains at elevated temperatures. In NC metals with finest grains and some UFG metallic materials produced by severe plastic deformation, GB sliding can occur at even room temperature [109,166,168].

3.5. Rotational deformation mode

We now consider the rotational deformation mode – plastic flow accompanied by rotations of crystal lattices – in NS metallic materials. Both post deformation and in situ TEM experiments indicate an essential role played by the rotational

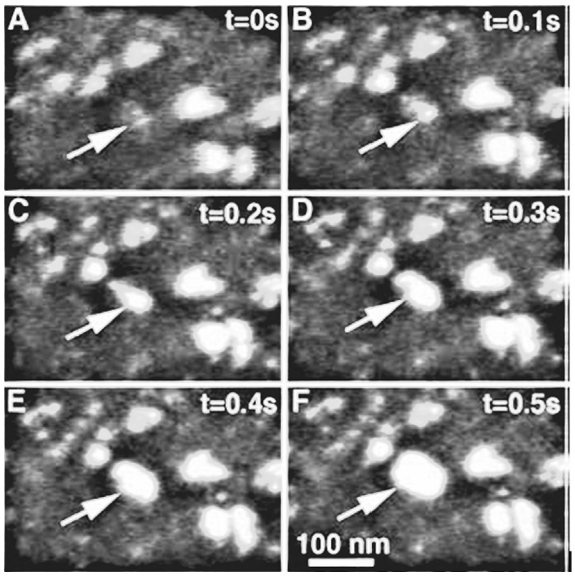

Fig. 20. Dark-field TEM observation of the rapid genesis of an agglomerate (e.g., white arrow) depicted by individual still frames extracted from a dynamic video sequence. (A) At $t = 0$ s, no grains in the strong diffraction condition are near the white arrow. (B) At $t = 0.1$ s, a grain in the strong diffraction condition with a size of about 6 nm is visible. (C) At $t = 0.2$ s, a group of grains in bright contrast with a size of about 28 nm is visible. (D) At $t = 0.3$ s, the group of grains has a nearly elliptical shape, with dimensions of 60 by 35 nm. (E) At $t = 0.4$ s and (F) $t = 0.5$ s, the size of the group of grains increases to maximum dimensions of about 80 by 60 nm [87].

deformation mechanism in NC materials [87,114–116,182–186] (as with CG metals under severe deformation; see reviews [177,179]). For instance, in the dark field in-situ TEM experiment, Shan and co-workers [87] observed crystal lattice rotations in individual grains and grain agglomerates in plastically deformed NC nickel film having an average grain size of 10 nm (Fig. 20 [87]). With in-situ HRTEM, Murayama and co-workers [182] observed nanoscale crystal lattice rotations mediated by a disclination dipole in iron under plastic deformation by mechanical milling. Wang and co-workers [187] recently observed grain rotation in thin nanocrystalline Au films. Also, molecular dynamics simulations have revealed crystal lattice rotations in plastically deformed NC metals; see, e.g., [188,189].

Recently, Izadi et al. [190] observed grain rotations during tensile deformation of a free-standing, ultrafine-grained Al film with a mean grain size of 180 nm and thickness of 200 nm using in-situ TEM straining with automated crystal orientation mapping. A large fraction (52%) of grains also experienced rotations during unloading. Interestingly, 15% of grains did not rotate during the loading-to-unloading transition. Although the grain size of 180 nm is much larger than characteristic grain sizes (below 10–30 nm) at which diffusion-assisted deformation mechanisms are commonly active in metals at room temperature, here the loading and unloading were performed at a very low strain rate (below 10^{-5} s^{-1}), which could enable diffusion-assisted grain rotation. Also, GB and triple junction diffusion that accompanied grain rotations could create a spatially inhomogeneous stress distribution in the film and thus lead to the forward rotations of a part of the grains during unloading. In addition to grain rotations, Izadi et al. [190] observed in some cases GB migration and detwinning during both loading and unloading.

Rotational deformation in CG, UFG and NC solids is often mediated by dipoles of GB disclinations whose motion along GBs induces local rotations of crystal lattice [177,179,191]. Fig. 21 schematically presents an exemplary case of the rotational deformation during development of a misorientation band. The band in its initial state is bounded by two parallel GBs (Fig. 21a). The final state of the band (Fig. 21f) is characterized by crystal lattice orientation (Fig. 21a). It is energetically unfavorable to change the initial lattice orientation (Fig. 21a) to the final one (Fig. 21f) in one step. Instead, the rotational deformation occurring through multi-stage displacement of a GB disclination dipole and successive changes in lattice orientation within the misorientation band is energetically preferred (Fig. 21a–f). In doing so, a dipole of GB disclinations (Fig. 21a–f) with the interspacing h between the disclinations carries plastic deformation equivalent to that mediated by a superdislocation with Burgers vector magnitude [177,179]:

$$B \approx 0.5h \tan(\omega/2) \tag{12}$$

When GB disclinations move, for geometric reasons, they either absorb pre-existing dislocations [177,179,191,192], or emit new dislocations into grain interiors [193,194]. The disclination motion accompanied by dislocation emission serves as a good example of interaction between various deformation mechanisms, in which the rotational deformation mediated by GB disclinations is accommodated by emission of dislocations from GBs and slip in grain interiors.

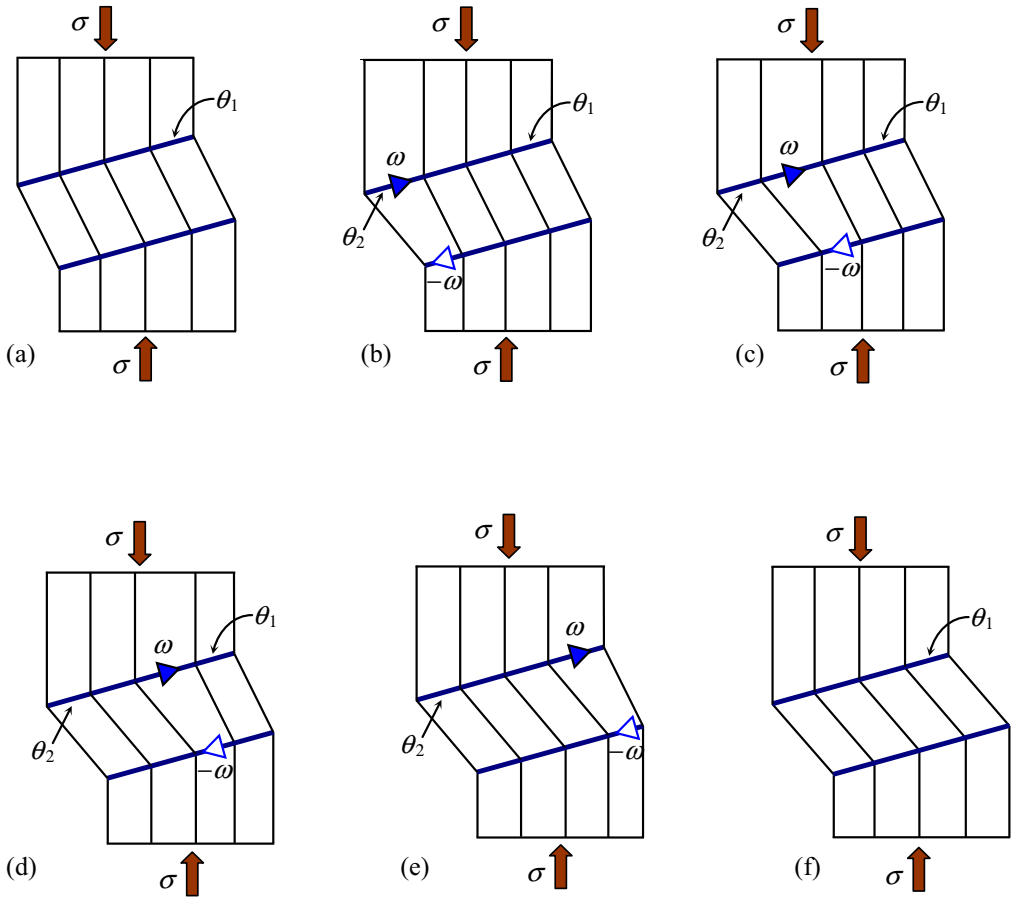

Fig. 21. Misorientation band in a crystal under stress (schematically). Disclinations (triangles) are generated at grain boundaries and compose a dipole configuration. Their motion along grain boundaries mediates plastic flow associated with crystal lattice rotation within the misorientation band.

In addition, the rotational deformation can effectively occur in NS materials as a unique GB deformation mode mediated by GB dislocations [108,195–197]. It has been demonstrated in experiments [115,186] that the rotational deformation mediated by GB dislocations (in agreement with theoretical models presented in Refs. [108,195,196]) significantly contributes to plastic flow in Pt films with a thickness around 10 nm and grain size around 6 nm (Fig. 22 [115]).

It is important to note that rotational deformation mediated by GB dislocations can effectively accommodate GB sliding in nanomaterials. Following Ref. [108], we now discuss the geometry of this rotational deformation. For simplicity, we will focus on a two-dimensional grain structure containing a hexagonal nanograin (Fig. 23). As discussed in Section 3.4, triple junctions geometrically hinder glide of GB dislocations, carriers of GB sliding. In this case, glide of GB dislocations can be transformed at a triple junction into their climb (along adjacent GBs) through the splitting of gliding dislocations into climbing ones (Fig. 23). Successive splitting transformations give rise to the formation of two finite walls of climbing GB dislocations (Fig. 23). Lattice rotations occur owing to climb-controlled extension of GB dislocation walls. Thus, successive splitting transformations provide the crossover from the GB sliding to rotational deformation. That is, the rotational deformation mediated by GB dislocations effectively accommodates GB sliding. This statement is consistent with experimental data [166,198], which indirectly indicating concurrent GB sliding and grain rotations in plastically deformed metallic nanomaterials.

In general, dislocations climbing along GBs also mediate grain rotations that are not related to plastic flow [199]. Grain rotations are driven by a decrease in GB energy and can induce grain coalescence in materials under thermal treatment [199,200]. Grain rotations driven by a decrease in the GB energy can contribute to transformations of GBs in NS materials during their plastic deformation, which in turn enhances such rotations. Indeed, geometrically necessary dislocations trapped by GBs during plastic deformation in NS materials induce changes in GB energies, and may facilitate grain rotations. This statement is supported by experimental data [201] showing that grain rotations transform some high-angle GBs into low-angle ones in NC Ni-Fe alloy, and eventually the GB disappeared, leading to grain coalescence [201]. Thus, grain rotation in NS metals can occur through slip of dislocations emitted from low-angle GBs.

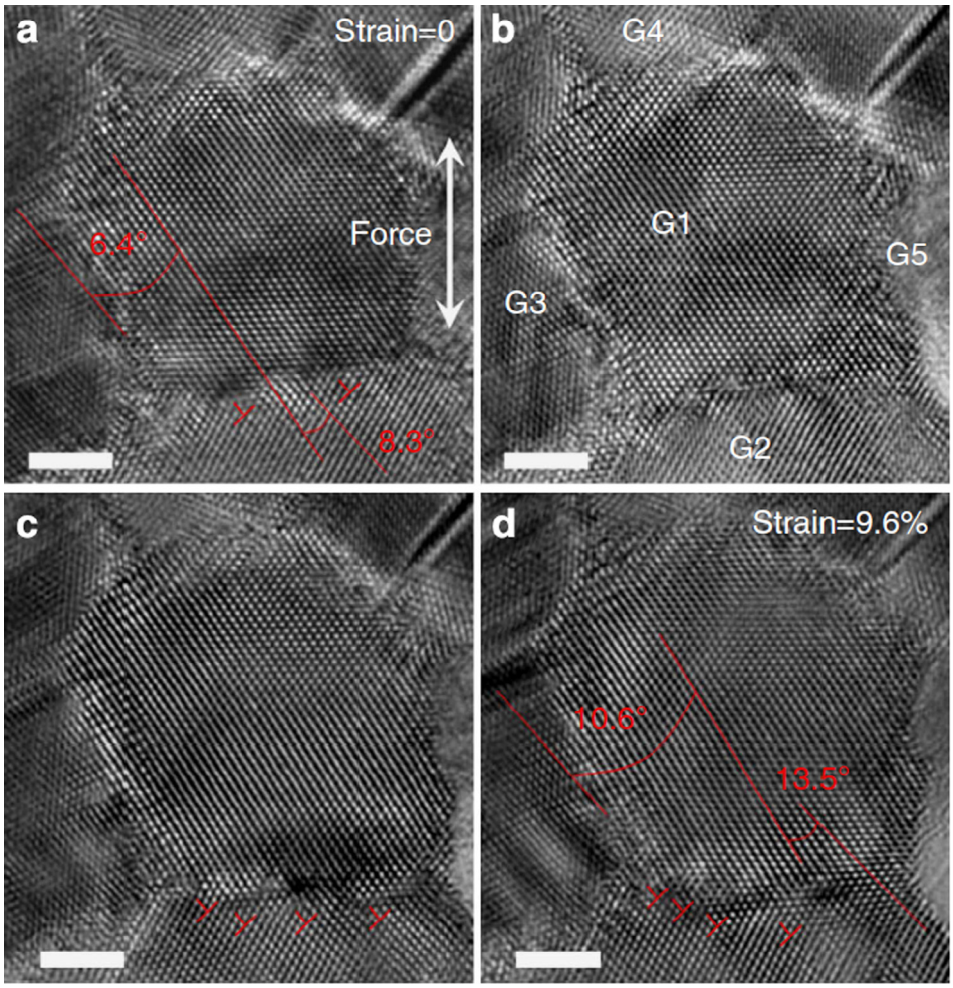

Fig. 22. HRTEM images taken at different points of time showing the GB dislocation-mediated grain rotation. (a) Two GB dislocations (as marked with 'T') at GB_{1-3}. (b–d) During straining, the number of the dislocations increased, leading to the GB angle at G_{1-2} increasing from 8.3° to 13.5°. Scale bars, 2 nm. [115].

3.6. Stress-driven migration of grain boundaries

Stress-driven migration of GBs serves can contribute to both plastic flow and grain growth in NS materials [107,183,202–226], as with their CG counterparts; see, e.g., [227–236]. In particular, grain growth mediated by GBs migration can result in nano-to-CG transformation, which causes strain softening.

Following experimental observations [183,187,202–205,208–215,218–222] and computer simulations [206,207,216,223], GB migration and grain growth extensively occur in NS metals deformed at high stresses. GB migration and grain growth in UFG Al and Al-Mg films was observed under in-situ indentation under TEM [202,203] at room temperature (Fig. 24 [202]). Stress-driven migration of GBs was identified as an important deformation mechanism in UFG metals subjected to high stresses during indentation at room temperature [202,203].

It was reported [209] that NC Al film has significant grain growth at room temperature during tensile tests at high stresses. The yield stress (91–116 MPa) and the ultimate strength (149–190 MPa) measured in these tests [209] are much higher than those of CG Al. It is important to note that substantial grain growth was observed exclusively in regions with high local stresses. Specifically, grain growth occurred in vicinities of crack tips serving as effective stress concentrators. Stress-driven GB migration is believed occurred, leading to grain growth.

In recent study [183,187,202–205,208–215,218–222] concurrent GB migration and grain rotation in thin nanocrystalline Au films with a thickness of 10 nm and average grain size of 18 nm was observed in situ at room temperature using a TEM (Fig. 25 [187]). Fig. 25a displays a TEM image before the deformation, and Fig. 25b presents an enlarged view of Fig. 25 at atomic resolution, where five grains (G1 to G5) are highlighted. Before deformation the grain size of G1 is approximately 14 nm and the GB angle of GB1–3 is 18.52° (Fig. 25a). With increasing strain (Fig. 25b–d), GB1–3 and GB3–4 move toward the interior of G3, while the angle of GB1–3 decreases from 18.52° to 10.77°. With a further increase in strain (Fig. 25d–f)

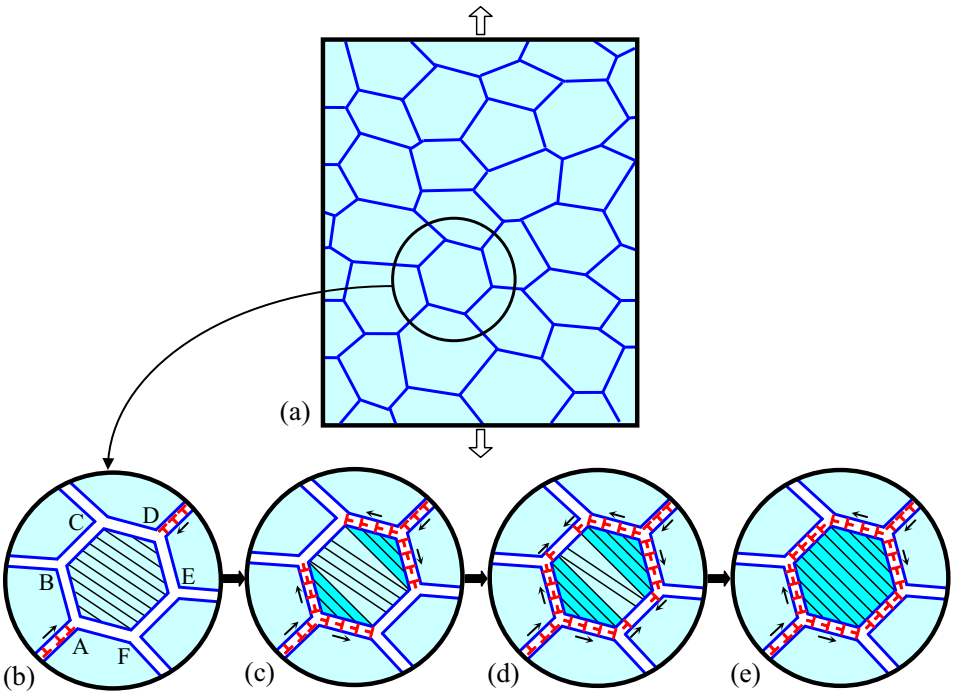

Fig. 23. Grain boundary sliding and its accommodation through rotational deformation whose rate is controlled by grain boundary diffusion. (a) Nanocrystalline or ultrafine-grained specimen under tensile load (a schematic general view). Magnified insets (b–e) illustrate accommodation of sliding along grain boundaries adjacent to triple junctions A and D through rotational deformation within grain ABCDEF (schematically). The rotational deformation is mediated by diffusion-controlled climb of grain boundary dislocations.

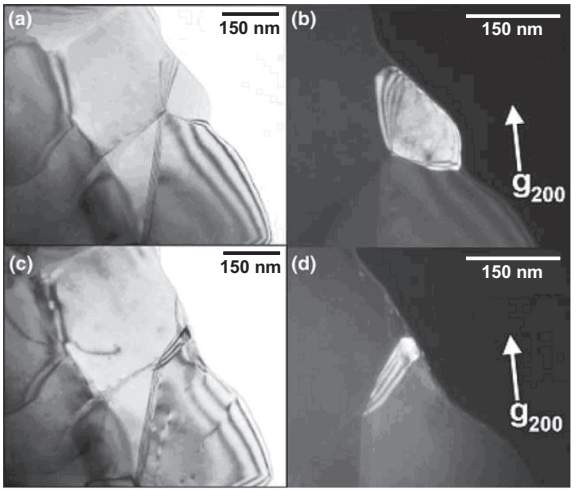

Fig. 24. (a) Bright-field image before the indentation; (b) dark-field image of the middle small grain before the indentation; (c) bright-field image after the indentation; (d) dark-field image of the middle small grain after the indentation [202].

GB1–2 and GB3–2 migrate, and the GB angle of GB1–3 continues to reduce from 10.77° to 7.98°. The mechanism of grain rotation can be seen more clearly in Fig. 25g and h, which show enlarged HRTEM images of the yellow-framed regions in Fig. 25b and f, respectively. As seen in Fig. 25g, the low-angle grain boundary GB1–3 contains an array of lattice dislocations. During the deformation, some dislocations leave the GB. As a result, the number of dislocations at GB1–3 decreases, and the average spacing of the dislocations increases from 0.8 to 1.4 nm, leading to a reduction in the GB misorientation angle.

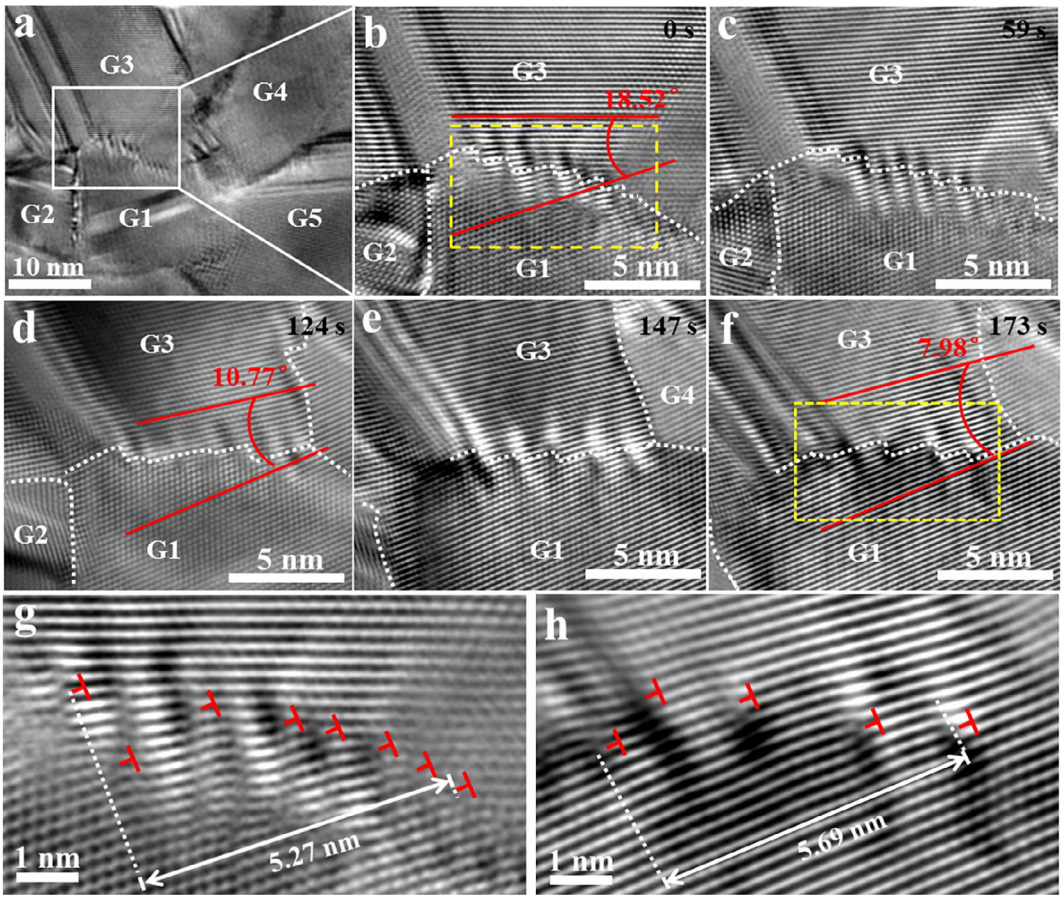

Fig. 25. (a–f) HRTEM images showing GB migration and grain rotation in nanocrystalline Au films. (g and h) show enlarged views of the yellow dotted boxes in (b) and (f) [187].

The authors of [187] observed GB migration more frequently that grain rotation and attributed the GB migration to enhanced diffusion in the ultrathin nanocrystalline film, which could activate the Coble creep with a strain rate of 10^{-3} s^{-1}. In turn, the diffusion-assisted Coble creep led to the GB migration.

GB migration was also observed in MD simulations. In particular, the simulations [207] give evidence for stress-driven GB migration in NC nickel with a very small grain size d of 5 nm at room temperature. The deformation mediated by GB migration was observed for tests specified by a rather large stress 2.5 GPa. The simulations [207] show that GB migration in NC metals with finest grains occurs at high stresses. In these simulations, GBs migrated over distances up to $d/2 \approx 2.5$ nm.

Thus, stress-driven migration of GBs represents a deformation mechanism operating in metallic nanomaterials at high stresses. The stress-driven GB migration in NS metals has similarities with GB migration in bicrystalline metals [227–233]. When a GB migrates under stress in a bicrystal, the migration process is often coupled to shear. For example, such a migration process has been experimentally observed in Al bicrystals at very low applied stresses (<1 MPa) [228,229]. Some time ago, Cahn and co-workers [235,234,236] theoretically described GB migration coupled to shear in bicrystalline solids. This description is consistent with results of experiments [229,230,233,227,228,231,232] and computer simulations [235,236] addressing the migration of tilt GBs in bicrystals.

In bicrystals, GB migration coupled to shear has the specific geometric features that differentiate this deformation mode from that operating in CG and NS materials. The fact is that the shear easily changes the bicrystal geometry when a GB migrates under stress. In this case, accommodation of the stress-driven GB migration occurs through an unconstrained change in the shape of a bicrystalline specimen. Consequently, the flow stress that drives GB migration coupled to shear is low. In contrast, in a NS specimen, GBs typically migrate under stress in internal grains surrounded by other grains that hinder the shears coupled to GB migration (Fig. 26 [217]). That is, the shears are constrained in NS materials and thereby require comparatively high stresses to drive GB migration processes coupled to such shears.

Following Refs. [107,217], we now briefly discuss the geometry of stress-driven GB migration in NS metallic materials. Let us examine an arrangement of rectangular grains having low-angle tilt boundaries, including a vertical grain boundary, a finite wall of periodically spaced perfect dislocations, with ends at points A and B as shown in Fig. 27a and b (left figures).

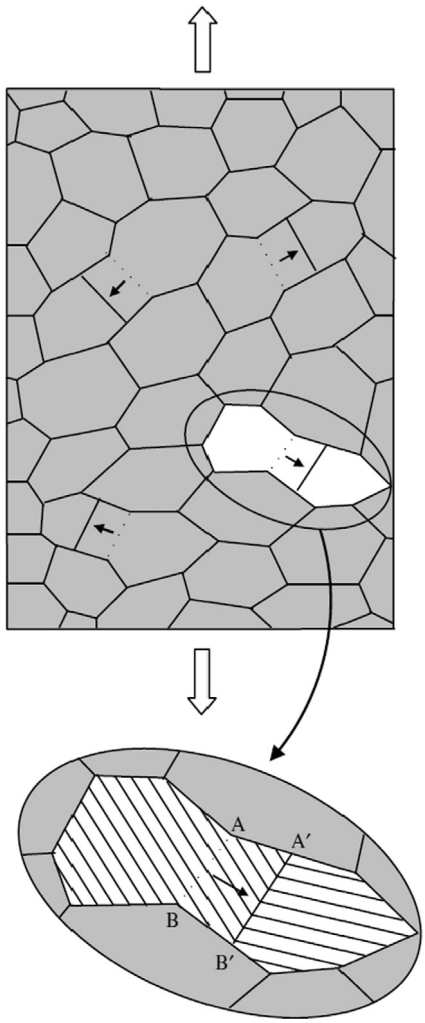

Fig. 26. Stress-driven migration of grain boundaries in a deformed nanocrystalline specimen. The shear coupled to migration is hampered by surrounding grains. The magnified inset highlights the geometry of a nanograin group hampering shear coupled to grain boundary migration [217].

When a shear stress τ is applied, the vertical tilt boundary *AB* migrates to its new position where it ends at points *A*′ and *B*′ as shown in Fig. 27a and b (right figures). As a result, within the region *ABB'A'* swept by the vertical tilt boundary during its migration, slip of lattice dislocations (structural elements of the vertical boundary) causes plastic flow, and crystal lattice rotates by the tilt misorientation angle ω that specifies the migrating GB (Fig. 27a and b (right figures)).

In the initial state (Fig. 27a and b (left figures)), there are triple junctions *A* and *B* connected by GB *AB*. We assume that the junctions *A* and *B* do not create stresses in the initial state, because they are characterized by zero-angle gaps. It means that the sums of misorientation angles that specify tilt boundaries adjacent to these junctions are equal to 0. Migration of the vertical tilt boundary *AB* to its new position where it ends at points A′ and B′ violates balance of misorientation angles at points (GB junctions) *A*, *B*, *A*′ and *B*′ (Fig. 27b). More precisely, the vertical tilt boundary having the tilt misorientation ω moves away from the junctions *A* and *B* so that they become geometrically uncompensated by angle gaps $-\omega$ and $+\omega$ (Fig. 27b, right figure), respectively. Besides, the vertical tilt boundary in in its new position form new junctions *A*′ and *B*′ with horizontal tilt boundaries. The junctions *A*′ and *B*′ are geometrically unbalanced, because they acquire angle gaps $+\omega$ and $-\omega$, respectively, owing to adjoining of the vertical tilt boundary to them [107,217] (Fig. 27b, right figure). In the defect theory, geometrically unbalanced junctions *A, B, B*′ and *A*′ represent disclinations having strengths $\pm\omega$ [169,177–179]. Motion of the disclinations produces plastic deformation [169,177–179,191]. To summarize, stress-induced GB migration mediates plastic flow and gives rise to nucleation of disclination quadrupole (Fig. 27b) [107,217]. Here we considered this statement in the case of low-angle tilt boundaries. In general, the statement is valid for high-angle GBs, too (Fig. 27c and d); for details, see [217].

Gutkin and Ovid'ko [107] have calculated the characteristic stress $\tau = \tau_{c1}$ at which stable migration of GBs mediating plastic flow starts to occur. This stress can be described as:

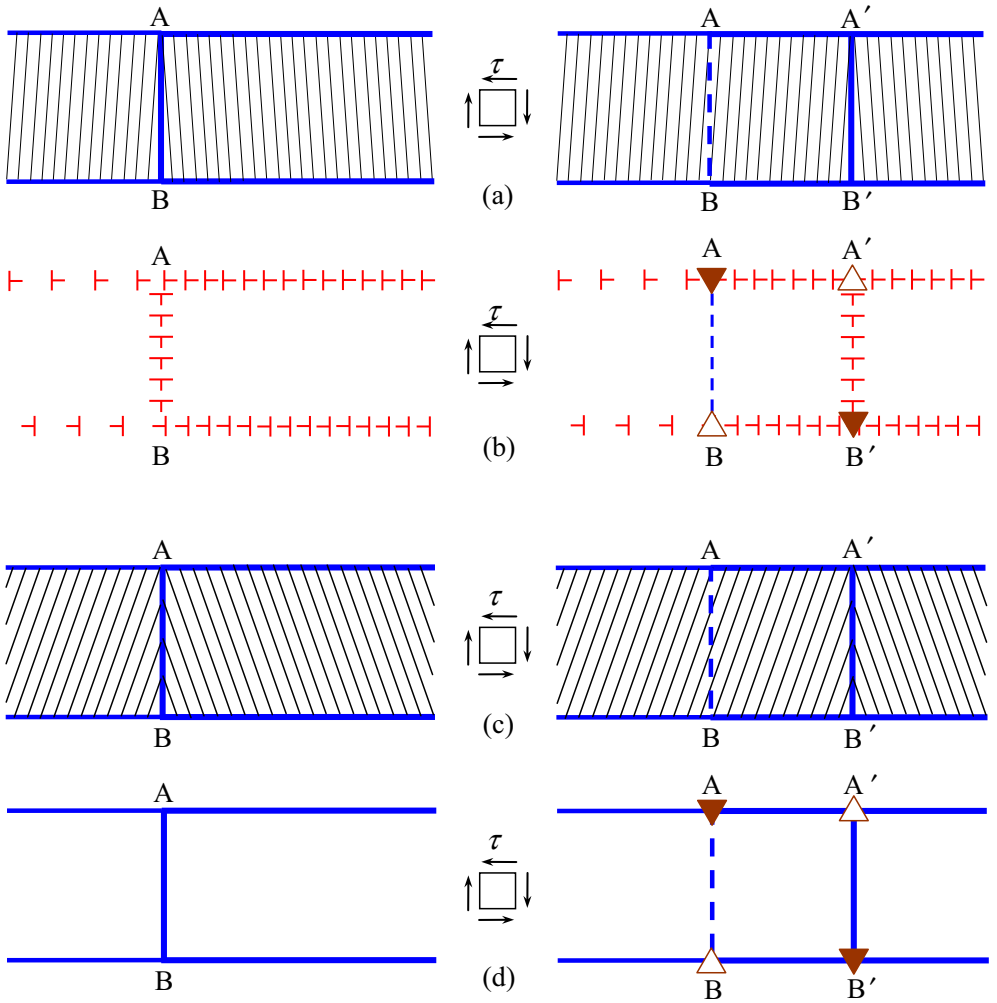

Fig. 27. Stress-induced migration of a low-angle (a, b) or high-angle (c, d) grain boundary from position AB to position A′B′ as a mechanism of rotational deformation realized through the glide of a wall of lattice dislocations (b) or motion of a dipole of wedge disclinations (d), respectively (see the text for comments).

$$\tau_{c1} \approx \frac{D\omega a}{d} \ln\frac{d}{a} \tag{13}$$

where $D = G/2\pi(1-\nu)$, G denotes the shear modulus, a the crystal lattice parameter, and ν the Poisson ratio.

Dao and co-workers [9] exploited Eq. (13) in order to estimate the critical stress τ_{c1} for the onset of stress-driven migration of tilt GBs in NC metals. They found that, for the disclination strengths in the range $5^\circ \leqslant \omega \leqslant 30^\circ$ and for grain sizes ranging from 10 to 30 nm, Eq. (13) gives τ_{c1} in the range 20–300 MPa. Dao and co-workers [9] noted that this theoretical estimate is consistent with experimentally documented stresses for many fcc metals with grain sizes ranging from 10 to 30 nm.

According to Eq. (13), the stress τ_{c1} decreases with increasing grain size d so that stress-driven GB migration in CG metals occurs at lower stresses as compared to that in NS metals. However, in CG metals, stress-driven GB migration competes with conventional lattice slip, which needs even lower stresses and thereby typically dominates.

It is important to note that the disclination strength ω appearing in Eq. (13) is equal to the tilt GB misorientation angle only for low-angle GBs, where the misorientation of the crystal planes of neighboring GBs is created by a wall of dislocations with identical Burgers vectors, as shown in Fig. 27b. For high-angle GBs the relation between the GB misorientation angle and the disclination strength ω is much more complicated and depends on the structure of a specified GB. For example, incoherent twin boundaries in fcc metals can be modeled as arrays of Shockley partials with the zero total Burgers vectors [127] (see Section 3.3). Evidently, for such boundaries, we have: $\omega = 0$. Recent experiment [237] and computer simulation [238] also demonstrated that the migration of another kind of GBs, namely $\Sigma 7$ {1 3 2}/{1 3 2} GBs in Al, produces no strain, which

means that such GBs are also characterized by $\omega = 0$. For general tilt high-angle GBs the disclination strength should lie in the range $0 \leqslant \omega \leqslant \theta$, where θ is the GB misorientation angle.

Also, Eq. (13) provides only sufficient conditions for the onset of GB migration, as it considers only the initial and final locations of the GB atoms (after the GB has migrated). However, in reality, high-angle GBs do not migrate as a whole. Their migration starts at certain GB regions due to the local atomic motion, whose activation may require higher stress than the migration of a GB as a whole.

Stress-driven GB migration as a unique deformation mechanism effectively operates in metallic nanomaterials due to their unique structural features, including extremely small grain sizes and high density of GBs. Subsurface areas of bulk NS materials often play an important role in deformation and fracture processes, because conditions for generation and evolution of defects mediating such processes are different from those in bulk areas. This is related to the free surface effects operating in subsurface areas. Of high significance, the effects under consideration are in NC solids having nanoscopic sizes, for instance, in nano- and micropillars, free-standing nanowires, and films with nanoscopic thicknesses. In such solids, the NC structure and free surface effects provide unique arena for operation of new deformation modes. Recently, in Ref. [104], one of such new modes – the stress-driven rotations of GBs – near free surfaces in NC materials has been suggested and theoretically described.

This deformation mechanism being a "cousin" of stress-driven GB migration operates in a NC specimen is schematically presented in Fig. 28 [104], which shows a 2D section of the NC specimen and magnified insets of its sub-surface region where stress-driven GB rotation occurs. More precisely, the specimen contains a low-angle tilt boundary AB in the vicinity of its free surface (Fig. 28b). This boundary forms the junction A with static GBs CA and DA (Fig. 28b). The GB junction A is geometrically balanced in its initial state, that is, it does not create internal stresses. According to the description [104], external stress induces rotation of the tilt boundary AB (Fig. 28c). As a result of the rotation, plastic flow occurs in the area swept by the rotating tilt boundary, and the GB junction A becomes geometrically unbalanced (Fig. 28c). The latter leads to an increase in the elastic energy.

The free surfaces effects on GB rotations are as follows. First, stresses created by the unbalanced GB junction A are effectively screened by the free surface. Second, the low-angle tilt boundary AB can decrease its length (and thereby energy) during its rotation when some of its intrinsic dislocations enter the surface and disappear at it (Fig. 28b and c). This enhances GB rotations near free surfaces in NS materials [104]. At the same time, the free surface effects under discussion are absent in the bulk, in which case GB rotations are comparatively difficult to drive by stresses.

In subsurface regions of NC solids, GB rotations are more likely than in their coarse-grained counterparts, because NC structures have very high density of GBs. In CG solids, where GB density is low, and dislocation slip typically dominates, GB rotations are not intensive in even subsurface regions.

It was theoretically shown [104] that GB rotations driven by high stresses can effectively occur in NC nickel. Each GB is quantitatively characterized by a rotation angle φ_{eq} corresponding to the equilibrium, low-energy state of the defect system examined. The angle φ_{eq} is sensitive to characteristics of the defect system and can be up to tens of degrees. In doing so, φ_{eq}

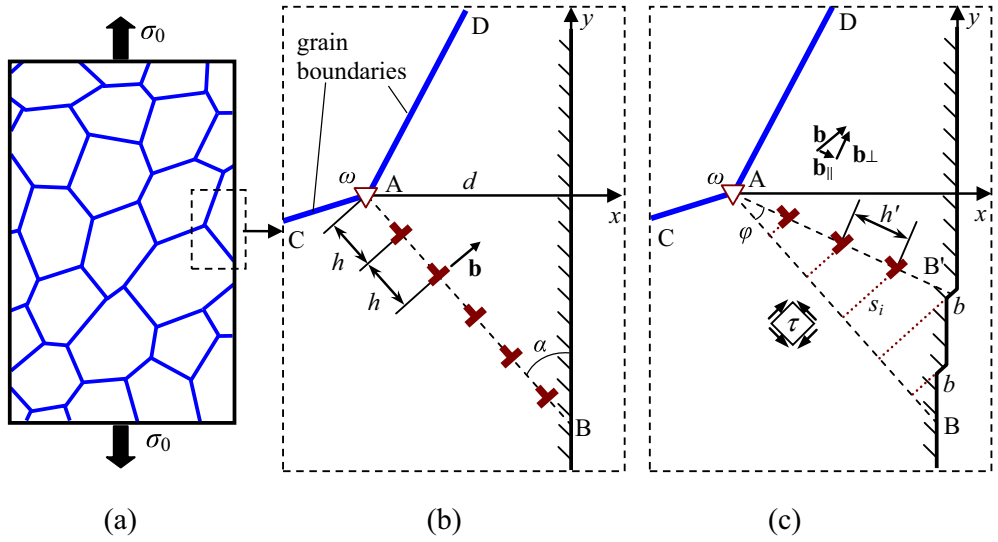

Fig. 28. Geometry of grain boundary rotation near free surface. (a) General view of nanocrystalline specimen. (b and c) Magnified inset of the subsurface region where stress-driven rotation of a tilt grain boundary occurs. (b) Initial state. A low-angle symmetric tilt boundary AB - a wall of periodically spaced edge dislocations - is located near the free surface and forms a triple junction A with two static symmetric tilt boundaries AC and AD. (c) Stress-driven cooperative motion of GB dislocations occurs which results in tilt boundary rotation (by angle φ) from its initial location AB to a new location AB'. Also, grain boundary rotation leads to the disappearance of several grain boundary dislocations at the free surface and associated formation of free-surface steps [104].

grows with increasing external stress, shows a weak sensitivity to the tilt boundary length, and diminishes with increasing GB tilt misorientation. Theory [104] predicting a new deformation mechanism through stress-driven GB rotations agrees well with data of the experiment [184]. In this experiment addressing plastic deformation of a nickel nanopillar with the NC structure, GB rotations were observed near the nanopillar free surface [184] (Fig. 29).

3.7. Deformation mechanism maps

In previous sections, we have considered basic deformation mechanisms operating in metallic nanomaterials. It is important to note that different deformation mechanisms can be dominant in a NS material, depending on its grain size, temperature, stress and strain rate. This variation can be reflected in the form of deformation mechanism map for a material. For instance, a deformation mechanism map in the grain size – strain rate coordinates, based upon available experimental observations and computer simulations for NS palladium, was proposed in the paper [71] (Fig. 30). In particular, this map shows that Coble creep operates at very small strain rates and grain sizes. When the strain rate increases, Coble creep in NS palla-

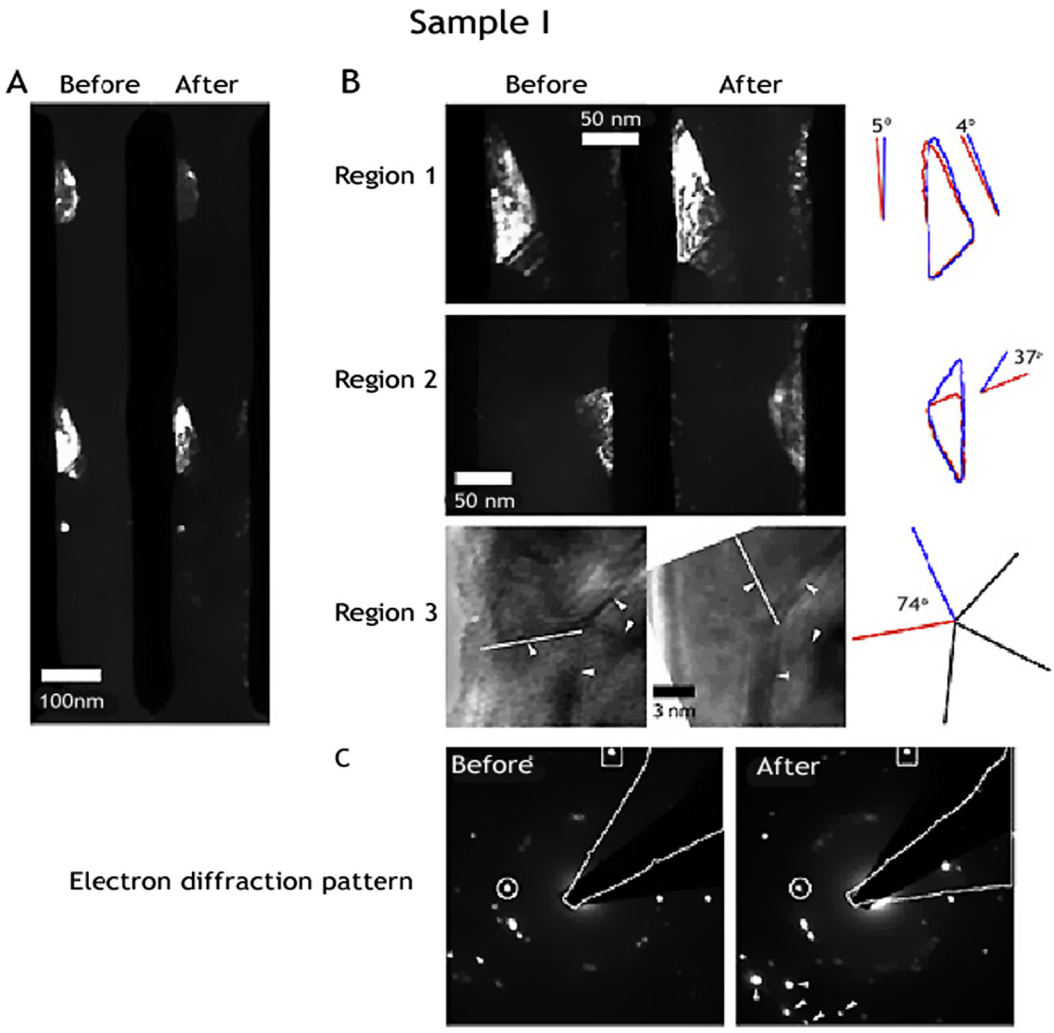

Fig. 29. (A) Dark-field TEM images showing a pillar (sample I) before and after deformation. (B) Zoomed-in dark-field (regions 1 and 2) and high-resolution (region 3) images of three different regions within the pillar shown in (A), and (third column) outlines of grain boundaries to highlight the grains' shape change. (C) The electron diffraction patterns before and after deformation (sample I). The diffraction spots within the circles were used to image (A) and region I of (B). Those within the squares were used to image region II in (B). The new diffraction spots, indicated by arrows in the post-deformation pattern, are from the non-gauge section areas, which were not included within the selective area aperture in the pre-deformation pattern. (D) Dark-field images showing another pillar (sample II) before and after deformation. The white box in the postdeformation image indicates a strip-like feature formed by deformation. (E) Zoomed-in bright-field image of the region within the box in (D). Two solid lines indicate the orientation of lattice planes. (F) Zoomed-in high-resolution image of the region within the box in (E). The solid lines indicate the orientation of the lattice planes, and the arrows point out the location of twin boundaries. (G) The electron diffraction patterns before and after deformation (sample II). The diffraction spots within the circles were used to image (D) [184].

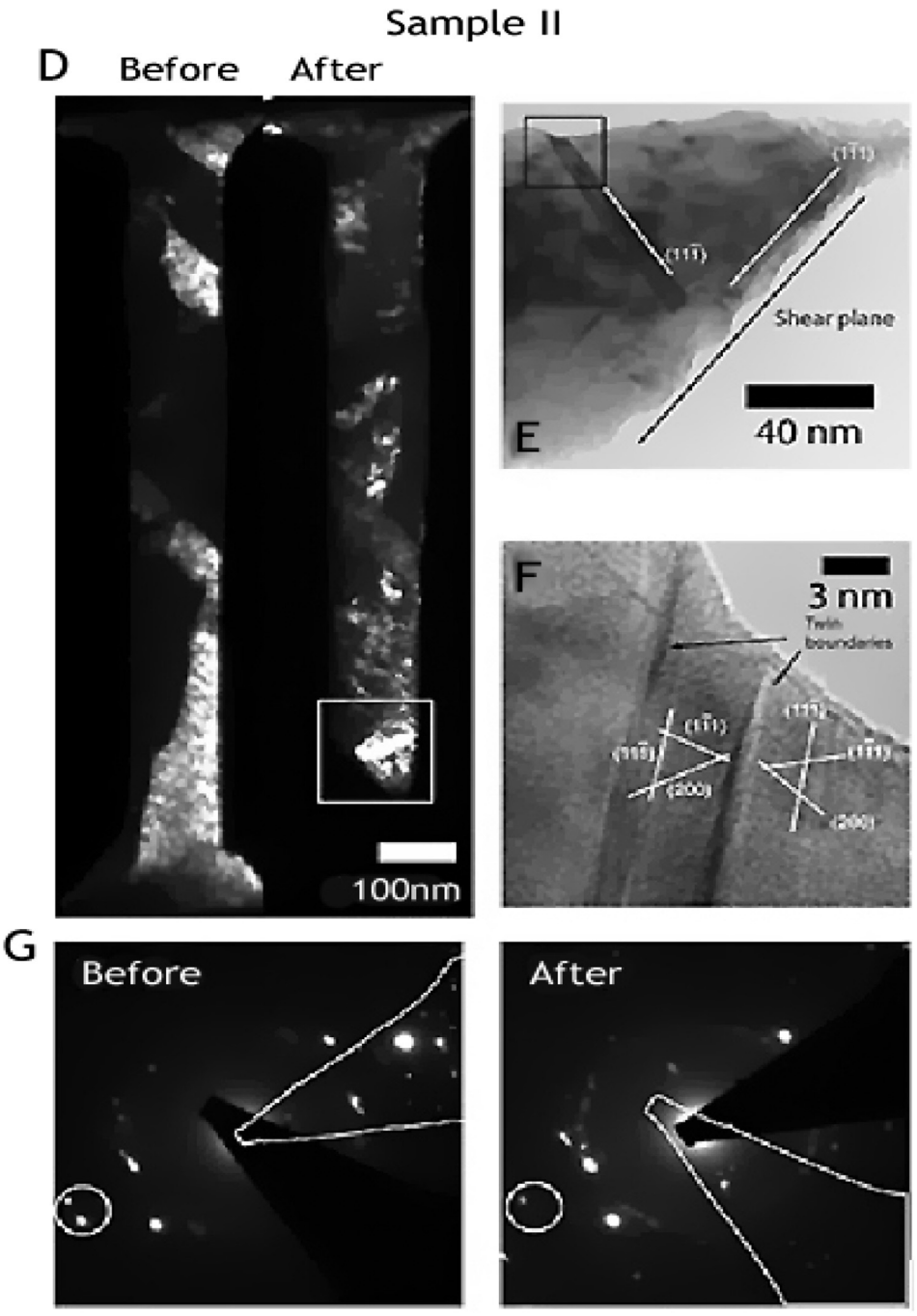

Fig. 29 (*continued*)

dium is followed by the combination of partial dislocation slip, GB sliding and grain rotations, and then by the combination of co-planar twinning, GB sliding and grain rotations (Fig. 30). In the case of very high strain rates, GB sliding is dominant at small grain sizes, while plastic deformation mediated by twin networks occurs at larger grain sizes (Fig. 30). Coarse-grained palladium deforms by conventional dislocation slip.

Another deformation mechanism map, based on the experimental study of nanocrystalline Au films, was constructed in paper [187] (Fig. 31). In this study, plastic deformation mechanisms acting in over 50 grains (with grain size from 5 to 45 nm) were monitored. Four deformation mechanisms were observed in NC Au films: GB migration, grain rotation, the motion of partial dislocations and the motion of full dislocations across grains. Fig. 31 shows the dependences on grain size of the fraction of grains in which a specified mechanism is activated, for the four deformation mechanisms. One can see that at the

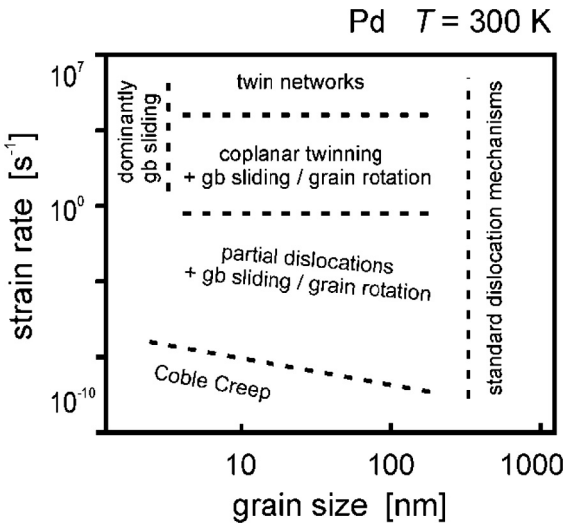

Fig. 30. Tentative deformation mechanism for Pd at small grain size [71].

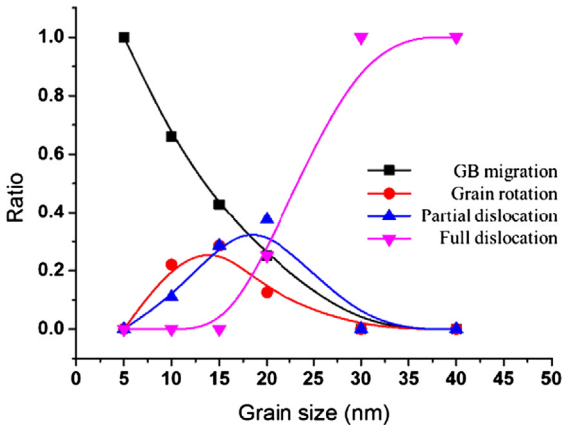

Fig. 31. Statistical distributions of the probability for the action of deformation mechanisms in grains of NC Au films as functions of grain size [187].

grain size below 20 nm, the dominant deformation mechanism is GB migration. The frequency of GB migration monotonously decreases with grain size. Also, grain rotation and partial dislocation motion contribute to plastic deformation of the grains with the size below 20 nm. At the grain size above 20 nm, the dominant deformation mechanism is the motion of full dislocations across grains.

Kawasaki and Langdon reported a deformation mechanism map for UFG Zn-22%Al processed by HPT at 473 K at which superplastic deformation occurs at appropriate stress and strain rates [239,240]. As shown in Fig. 32, Coble creep [241] occurs at low applied stress and small grain sizes because of high GB area per unit volume. At large grain sizes and low applied stresses, Nabarro-Herring [242,243] creep prevails. The Region II represents intermediate strain rates with a strain rate sensitivity $m \sim 0.5$, where maximum superplastic deformation can be obtained. The Region I and II represent lower and higher strain rates, respectively, with m in the range of 0.1–0.3. Note that the deformation mechanism map in Fig. 32 is only for elevated temperatures.

For deformation mechanism at room temperature, we propose a new deformation mechanism map that combines the features in both Fig. 30 [71] and Fig. 31 [187], as well as the grain size effect on deformation twinning and partial dislocation emission (Fig. 12) [13,118,128]. As schematically shown in Fig. 33 with both grain size (x-axis) and strain rate (y-axis) plotted in a logarithmic scale, coble creep plays a dominant role at very low strain rate. This is because of the high GB area per unit volume. At higher strain rate, with decreasing grain size the deformation mechanism(s) changes from full dislocation slip to deformation twinning + partial dislocation slip, to deformation twinning + partial dislocation slip + grain rotation, to partial dislocation slip + grain rotation + GB migration, to grain rotation + GB migration, to GB migration. Note that twinning occurs only in a grain size range, which becomes larger with increasing strain rate, because high strain rate promotes

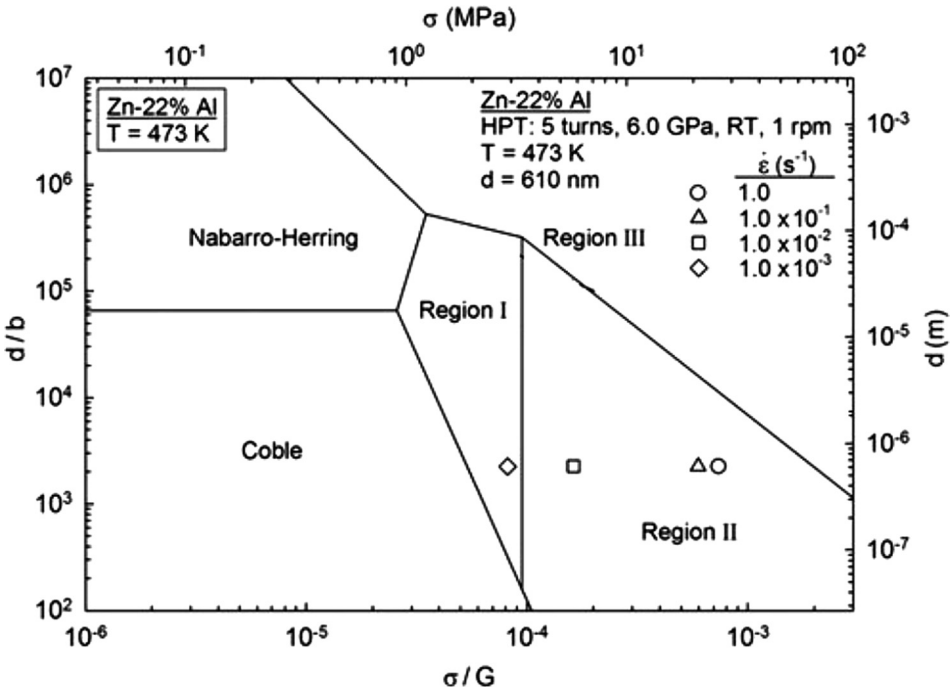

Fig. 32. Deformation mechanism map for UFG Zn-22%Al alloy processed by HPT [239,240].

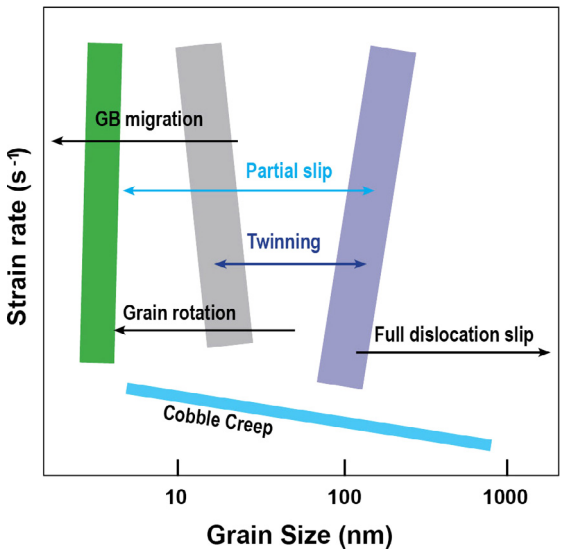

Fig. 33. Schematic deformation mechanism map for nanostructured fcc metals with medium to high stacking fault energy at room temperature. The wide boundary line is because the deformation mechanisms usually have an overlapping grain size range.

twinning [13,118,128]. Fig. 33 can be valid for nanocrystalline and UFG fcc metals with medium to high stacking fault energies. For fcc metals and alloys with very low tacking fault energies, deformation twinning could occur in CG grains. For metals with bcc and hcp structures, the deformation mechanism could be very different [13].

3.8. Interaction between deformation mechanisms

In general, various deformation modes can concurrently operate and significantly affect each other in NS materials with NC and/or UFG grains. In particular, various deformation mechanisms accommodate each other in NS metals, so that there exists effective interaction between such mechanisms [5,20]. The interaction is of crucial importance in NS metallic materials demonstrating superplastic deformation which, as shown experimentally [74], occurs through several basic

deformation mechanisms that significantly affect each other. These mechanisms include GB sliding, rotational deformation and dislocation slip. In the context discussed, the combined actions of interacting deformation modes should be definitely taken into account in optimizing strength and ductility.

Let us briefly discuss several important examples of interacting deformation mechanisms (in particular, those considered in previous sections) in metallic nanomaterials. As noted in Section 3.4, dislocation slip effectively accommodates GB sliding through emission of dislocations from triple junctions that stop GB sliding (Figs. 14f, g and 15). At the same time, GB sliding itself can be stimulated by slip. Dislocations that slip in the grain interior reach GB regions and undergo splitting transformations [1]. As a result of such transformations, GB dislocations are formed whose motion leads to GB sliding. Thus, the dislocation slip and GB sliding sustain/accommodate each other, providing effective concurrent operation in NS metals.

In addition, there are other scenarios where transformations of gliding GB dislocations – carriers of GB sliding - lead to dislocation emission and nanoscale twins in NS metals [244–246]. However, following theoretical estimates [244–246], such transformations need very high stresses to be realized so that they are not typical in NS metals in conventional deformation regimes.

Also, in Sections 3.4 and 3.5, we examined the situation where GB sliding and rotational deformation concurrently occur in NS metallic materials (Figs. 14i, h and 29). This interaction between GB sliding and rotational deformation modes plays a significant role in superplastic deformation in NS metallic materials.

Cooperative GB sliding and migration (GBSM) process (Fig. 34 [103]) represents another good example of interacting deformation mechanisms in NS metals [103,247]. Let us consider, following Ref. [103], the specific geometric features of GB sliding and cooperative GBSM processes in a NS metallic specimen under plastic deformation (see a 2D illustration in Fig. 34). The external stress induces GB sliding to occur, in which case the starting GB configuration I (Fig. 34b) transforms

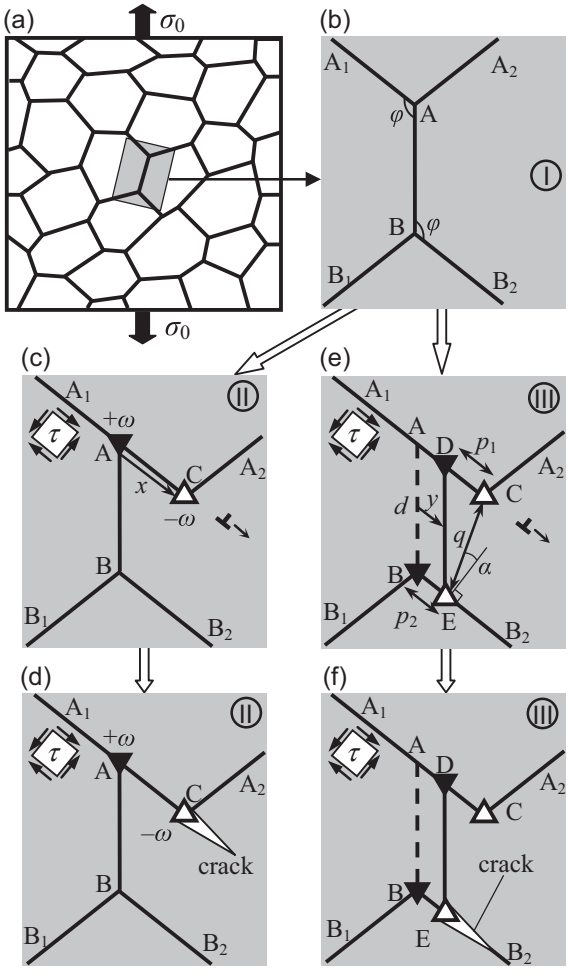

Fig. 34. Grain boundary deformation processes in nanocrystalline specimen: (a) General view. (b) Initial configuration I of grain boundaries. (c) Configuration II results from "pure" grain boundary sliding. Dipole of disclinations AC is generated due to grain boundary sliding. (d) Crack forms and grows into the grain interior. (e) Configuration III results from cooperative grain boundary sliding and migration process. Two disclination dipoles CD and BE are generated due to this cooperative process. (f) Crack forms and grows along grain boundary fragment EB_2 [103].

into configuration II (Fig. 34c). GB junction geometrically stops GB sliding whose accommodation is realized through dislocation emission from the junction (Fig. 34c). In addition, as it has been demonstrated in [174,176], a dipole of disclinations A and C is formed owing to GB sliding (Fig. 34c). In general, local stresses created by the disclination dipole are capable of initiating a crack (Fig. 34d).

Along with GB sliding, GB migration under stress can occur as an effective deformation mechanism in NS metals [107,183,202–226]. Following [103], stress-driven GB sliding and migration can cooperatively occur as one process mediating plastic flow in NS metals (Fig. 34). During such a cooperative operation, mutual accommodation of defects generated owing to GB sliding and those generated owing to GB migration comes into play. The cooperative GBSM process serves as a special deformation mode that is more energetically favored then "pure" GB sliding. Theoretical results [103,247] are consistent with experimental observations [112,163] of concurrent GB sliding and grain growth in plastically deformed NS materials.

Plastic deformation processes may compete with fracture processes in NS metals with relatively low plasticity. In this circumstance, interaction between deformation mechanisms – mutual accommodation of concurrently operating mechanisms – enhances plasticity of NS metals. More precisely, when deformation mechanisms accommodate each other, plastic strain inhomogeneities are effectively smoothed, which alleviates as "dangerous" stress sources capable of initiating crack generation. For instance, GB sliding creates defects at triple junctions, and cracks can be nucleated by high local stresses of these defects [248]. However, accommodation of GB sliding through emission of lattice dislocations from defected GB segments at and near GB junctions releases, in part, the high local stresses [249], in which case crack nucleation is suppressed. This situation will be discussed in detail in Section 5.1.

Another example is the cooperative GBSM process in NS metals. Following theoretical analysis [103], a NS metallic specimen, where plastic deformation through cooperative GBSM is dominant, shows enhanced ductility, as compared to that where pure GB sliding is dominant.

3.9. Crack nucleation and growth processes

Metallic nanomaterials may exhibit either brittle or ductile fracture behavior, which is sensitive to their microstructure and loading condition. For instance, several groups published experimental reports on NS metals having an average grain size larger than 20 nm that exhibit slow ductile fracture characterized with dimpled fracture surface and necking [75,86,250–255]. The dimples have sizes significantly exceeding the grain size, which is attributed to coalescence of microvoids.

At the same time, there are NC metals and alloys exhibiting the brittle fracture. For instance, intergranular brittle fracture occurs in NC Ni-15%Fe alloys and NC nickel with a mean grain sizes of 9 and 30 nm [250,254,256]. In the examples discussed, nucleation and convergence of numerous intergranular cracks led to the formation of main brittle cracks.

Fracture of metallic nanomaterials is critically influenced by their structural features: ultra small grain sizes and high density of GBs. Indeed, since GBs have low atomic densities and weak interatomic bonds, compared to those in grain interiors, cracks tend to nucleate and grow at GBs. Besides, GBs enhance diffusion-controlled growth and coalescence of microvoids mediating ductile fracture in NS metallic materials. GBs also have extra energy (as compared to the bulk phase), which enhances GB crack nucleation and growth. In contrast, NC metals with finest grains, GBs are extremely short and curved at numerous triple junctions. In this case, geometry of GB arrangement hinders intergranular fracture processes.

Plastic deformation in NC metals with finest grains occurs at very high stresses, and GB sliding represents one of effective deformation mechanisms. In this case, following experiments, computer simulations and theoretical models, crack nucleation and growth processes are critically influenced by GB sliding. In particular, it was theoretically revealed that the enhanced generation of nanocracks in deformed NC metals with finest grains can occur at triple junctions containing defects formed due to GB sliding, such as dislocations [248,257], disclination dipoles [174,176] (Fig. 17d) and dislocation-disclination configurations [175]. Also, nanocracks at GB triple junctions have been in situ observed by Kumar et al. in experiments addressing plastic deformation of electrodeposited NC nickel with a mean grain size of 30 nm [75] (Fig. 7). Besides, molecular dynamics simulations [258] demonstrate that nanocracks are nucleated at triple junctions near long cracks in NC nickel having grain size in the range 5–12 nm. The discussed experimental data, computer simulations and theoretical results indicate that triple junction nanocracks represent typical carriers of fracture in NC metals with finest grains.

Crack growth also has unique features in NS metals due to the grain size and GB effects. In most cases, high-strength NS metals are characterized with low ductility and low fracture toughness at room temperature. At the same time, the damage tolerance, as quantitatively characterized by the product of strength and toughness, could be remarkably high in NS metallic materials [253]. In particular, some fcc metallic materials having the NC structure show a ductile-to-brittle transformation with decreasing grain size [250,254]. At the same time, fcc metallic materials having the CG structure exhibit good ductility which is mostly related to suppression of crack propagation through enhanced crack blunting by dislocation emission from crack tips. As briefly discussed in Section 2, the sensitivity of crack blunting processes to the grain size is responsible for different fracture behaviors demonstrated by NS and CG fcc metallic materials. Following [66,67], GBs block dislocations emitted from crack tips, and this process in fact determines if cracks are blunted. In these circumstances, in a polycrystal with large grains, when dislocations are emitted from the crack, they slip over large distances before being stopped by GB (Fig. 5). Consequently, they are not effective in hindering emission of new dislocations, new dislocations are effectively emitted from the crack and then slip along a crystal plane, inducing pronounced crack blunting. As shown in [51,52], crack

growth is hindered by substantial crack blunting, which thereby gives the material higher toughness. In NC metals with finest grains, when a dislocation is emitted from a crack, it stops at the GB spaced closely to the crack tip (Fig. 6). Even one such a dislocation prevents new dislocation emission events owing to elastic repulsion between dislocations [66,67]. Therefore, dislocation emission cannot be activated to induce significant crack blunting. As a consequence, the NC metal tends to exhibit low resistance to crack growth.

On the other hand, it is also reported that [259] NC nickel with grain size of ≈20 nm has higher crack growth resistance than its CG counterpart. Similar observations [260–263] on enhancing fracture toughness are also reported on NC ceramics. These observations indicate [217,264–271] that unique toughening mechanisms can operate in NC materials, which are not effective in CG materials. Examples include stress-driven GB migration [217], nanoscale deformation twinning [272], Ashby-Verall creep [270,271], GB sliding [264], nucleation of nano grains [265], rotational deformation [266,267], and GB rotations [268] near crack tips. In recent years, it has been proposed that interacting deformation modes cooperatively operate near crack tips and affect crack growth processes and thus can enhance fracture toughness in NC materials [247,273–279].

Thus, in metallic nanomaterials having fine grains, dislocation slip is often dominant at room temperature. Due to very small grain sizes and high density of GBs in these materials, they typically exhibit low strain hardening and thereby low ductility. In NC metallic materials with finest grains ($d < d_c$) and very high density of GBs, GB-mediated deformation effectively contribute to plastic flow. These mechanisms, including GB sliding, deformation twinning, partial dislocation emission from GBs, rotational deformation and stress-driven migration of GBs, are characterized with very high flow stresses being near the critical stresses for crack nucleation. In addition, NC metallic materials having finest grains have extremely high density of GB junctions at which plastic deformation mediated by GB mechanisms is hampered. Consequently, plastic strain inhomogeneities and associated stress concentration are rapidly created at GB junctions as plastic deformation progresses.

4. Key factors affecting the ductility of metallic nanomaterials

The key factors that determine the ductility of NS materials include:

1. Testing conditions (temperature, strain rate, specimen geometry for small non-standard samples).
2. Microstructures, which are determined primarily by processing history.

Concerning the testing conditions, it is well known [171,280,281] that under certain temperature and strain rate conditions, NS materials can display enhanced ductility and even exhibit superplasticity, i.e. demonstrate tensile uniform elongation to failure of more than 400% and show increased strain rate sensitivity. Superplasticity of NS materials usually occurs at lower temperatures and/or higher strain rates than their CG counterparts. The superplasticity of NS materials has been discussed in several recent reviews [281,282]. In Section 3.4 we briefly analyzed GB sliding as the main mechanism of superplasticity. However, detailed examination of this issue is beyond the scope of this work, as superplastic flow is usually demonstrated at elevated temperatures, although recently a number of works have been published on superductility and superplasticity of NS alloys even at room temperature [165,283].

Below we discuss in more detail the structural features of NS materials and their influences on ductility at ambient and lower temperatures. For illustrative purposes special attention will be paid to NS materials produced by consolidation of nanoparticles [284,285] as well as by SPD techniques that over the last two decades have attracted extensive interest according to the growing number of publications with top citation index [286] as well as numerous subject-related conferences, seminars and symposiums (www.nanospd.org).

As noted above, application of SPD, in which very large plastic deformation is used under high pressure with accumulated strains ε exceeding ~4–6 [1,21,23,287], allows producing ultrafine grains (UFG) of submicron sizes and even nano-size (<100 nm).

The pioneer works on fabrication of UFG materials by SPD were performed in the end of 80th – beginning of 90th by Valiev et al. [170,288] (see also recent reviews on nanoSPD history) [281,289] and to date the SPD processing has become a major approach for producing metals with ultrafine and nanosized grains [47,281]. Several different SPD techniques for fabricating nanomaterials have been developed [21,23,287,282], among which equal-channel angular pressing/extrusion (ECAP/ECAE) [23,290] is the most successful to date. High-pressure torsion (HPT) [1,291] is another extensively studied technique. These methods were proposed and used in earliest works to produce UFG materials [1,170]. HPT is particularly promising for fundamental studies since it can refine grains to below 100 nm and form high-angle grain boundaries [292–294]

SPD can also lead to unusual phase transformation such as a dissolution or formation of second phases, disordering, amorphization, providing different nanostructures such as nanotwins, non-equilibrium GBs, dislocation cells, solute clusters and segregations [30,295,296]. Such changes in material structure can affect the mechanisms of deformation and fundamentally modify the material properties. Consequently, SPD processing has enabled the development of structural and functional metals and alloys with superior and exceptional properties [13,23,30,70,73,129,293–298].

Below we outline four key nanostructural attributes in SPD-processed metals [1,30,295,296], which are the basis for their remarkable mechanical and functional properties and the discovery of which was made possible through the application of new and modernized imaging and characterization techniques over the past decade.

4.1. Structure of grain boundaries (GBs) in NS materials

NS materials have a very high density of GBs, which renders them unique and new properties. Therefore, NS materials may be considered as interface-controlled materials [1,23,299].

Gleiter and co-workers performed pioneering work on NC materials, in which it was assumed that GBs can have unique atomic structures that are different from GBs in conventional CG materials [2,299]. Particularly, this is important for NS materials processed by SPD methods [23].

GBs of various kinds can be generated in NS materials processed by SPD (large and small-angle, special and random, equilibrium and non-equilibrium GBs with containing extrinsic dislocations) [1,81,295,296] and this is the basis for GB engineering of NS materials, i.e. controlling their properties by varying GB structure using different SPD routes and regimes [23,300].

"Non-equilibrium GBs" was suggested for the first time in the late eighties [301] and [302] according to interactions between high-angle GBs and lattice dislocations. Following [1,302], three main features can be distilled out in the formation of non-equilibrium GBs: the excessive elastic energy, increased free volume and the existence of long-range elastic stresses (Fig. 35). The increase in excess of free energy and long-range lattice distortions in vicinity of non-equilibrium GBs can be described in terms of dislocations captured by GBs and incorporated into their structure. Such "uncommon" GBs were called "non-equilibrium", however, as a matter of principle, all GBs can be considered as non-equilibrium if not taking into account the effects of segregation (see Section 4.3). In this paper we use this term for characterizing the GBs with strain-distorted structure as non-equilibrium GBs [81] because it has been admitted and used by the SPD-related association.

Nazarov, Romanov and Valiev created a model for such non-equilibrium GBs in a number of works [303,304] dealing with GBs behavior and formation. Dislocations formed while gliding toward high-angle GBs and then, after having been captured by a boundary, form specific configurations of "extrinsic GB dislocations," meaning the dislocations which locally modify the initial (pre-deformation) misorientation of the two adjacent grains, but collectively does not contribute to the overall misorientation across the GB. Random GBs populated by those extrinsic GB dislocations are characterized by excess energy as well as by significant microdeformation related to the GB region [303], as a combined effect. Recently this approach has been further developed by Romanov et al. [305].

Previous investigations of GBs in NS materials processed by SPD, used various, often complementary, characterization methods: TEM, XRD, Mössbauer spectroscopy, dilatometry, differential calorimetry, etc. (see, e.g. [1]). It was revealed that

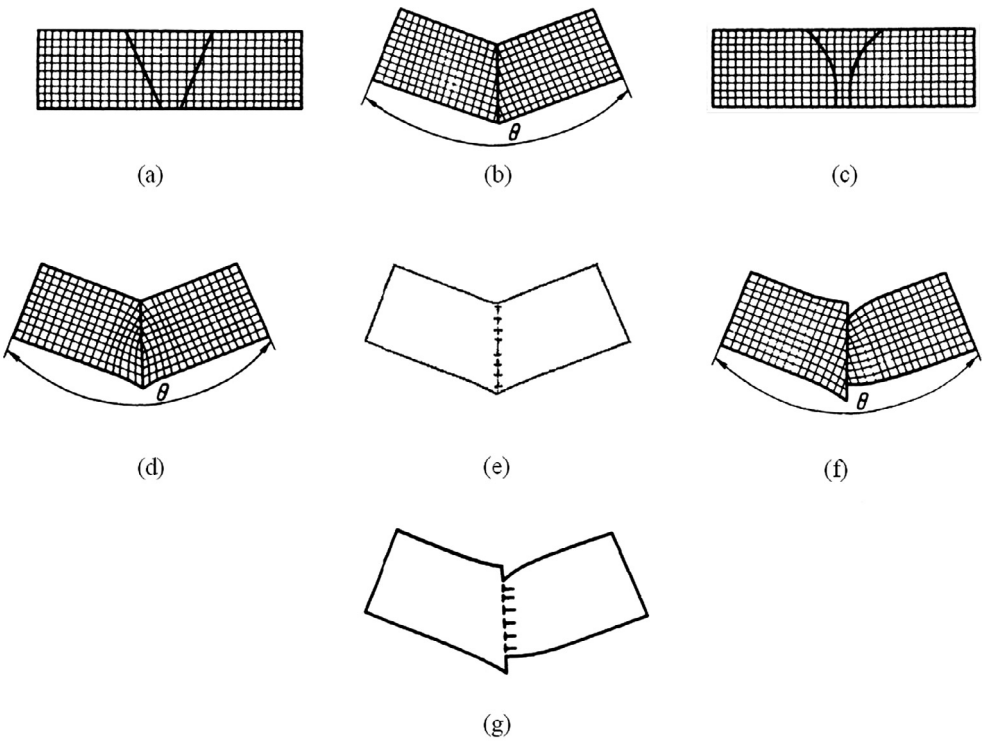

Fig. 35. Schemes of two types of grain boundaries by thought cuts: a → b perfect equilibrium grain boundary; c → d and a → f non-equilibrium, strain-distorted grain boundaries; e and g GB dislocation complexes illustrating the same elastic distortions as in (d) and (f) [302].

high-angle GBs in materials produced by advanced SPD techniques have particular non-equilibrium structures. Afterwards, structure sensitive probes were used to study atomic structure transformations, such as GB diffusion measurements or high-resolution TEM studies, to determine and describe modifications of GB structure in relation to SPD processing.

For instance, extremely high dislocation density combined with facets and steps at GBs was revealed in NS Al-3% Mg alloy subjected to HPT [306] resulting in non-equilibrium GBs with a crystalline lattice distortion area of ~5–7 nm [1,23], which significantly affects the properties of the alloy. HRTEM was also applied for studying the origin of GBs in Ni_3Al subjected to severe deformation and annealing [172]. The micrograph of a boundary segment in sample subjected to annealing at 650 °C is demonstrated in Fig. 36a. The GB line looks highly distorted. One can observe a few zones, where (1 1 1) lattice fringes are absent, or are resolved, assuming local distortions of crystal lattice. This fits to another HRTEM observation of metals after HPT [306] that showed non-equilibrium GB structure in these materials. Another grain boundary in the same sample that was parallel-oriented to the incident beam is demonstrated in Fig. 36b. The GB is sharp being less than 0.5 nm in thickness, which is equivalent to a few interatomic distances. Interestingly, the boundary is still wavy but the lattice fringes are complete through the boundary. Termination points of lattice fringes are indicated as ⊥. These features are associated with additional planes, which can be interpreted as GB dislocations. The study of several GBs in UFG Ni_3Al with the following annealing at 650 °C showed that these boundaries still preserve their non-equilibrium state, being relaxed only partially. Huang et al. compared the HRTEM images of GBs with those of simulated GBs with the same misorientation in NS copper processed by SPD, and found that excessive extrinsic dislocations indeed exist in GB segments, which renders the GB higher energy and make there GB segments non-equilibrium [35].

Earlier studies [1,306] revealed serrated contrast character by TEM and HRTEM analyses, which indicates high local density of dislocations in non-equilibrium GBs. Due to the possible Moiré effect near interfaces and taking into account delocalization of information due to aberrations of HRTEM electromagnetic lens system these findings required further clarification, which became possible in Cs-corrected TEM. Fig. 37a demonstrates an HRTEM micrograph of GB in Pd90Ag10 alloy, which was subjected to severe deformation by numerous rolling and folding [307], a process similar to an earlier scheme [308,309]. The GB was shown in a non-equilibrium state with respect to interpretations provided in [1]. It was represented by faceted (Fig. 37a) interface between two neighboring grains, oriented along ⟨1 1 0⟩ direction. Such GBs are typically observed in SPD materials [1,23,310].

To establish whether the image of the observed distorted grain boundaries is in non-equilibrium state, the local microdistortions of crystal lattice at GB area (Fig. 37a) were calculated by geometric phase analysis (GPA), which makes it possible to calculate relative magnitudes of in-plane components of strain tensor as well as of rigid body rotation tensor as for reference lattice, basing on the intensity distribution in HRTEM [307,311]. The HRTEM analysis can be found in [312]. Fig. 37b partly shows this analysis in the capacity the rigid body rotation. Further to disorientation of two adjusting grains, distinct and considerable color variation designating variation of lattice relative rotations becomes evident in area near the boundary. It is important to emphasize that the bright spots ("hot spots") in Fig. 37b relate to the areas with occurrences of discontinuity in transmitted phase of electron wave, in other words core region positions of full or partial dislocations are designated with these spots. In addition to this, local structures within distorted GB region which demonstrate local reorientation of crystal lattice regions may as well contribute to these bright characters in deformation maps, considering that linear density of hot spots (roughly measured as 10^9 m^{-1}) is clearly excessively high for correlation with only extrinsic GB dislocations.

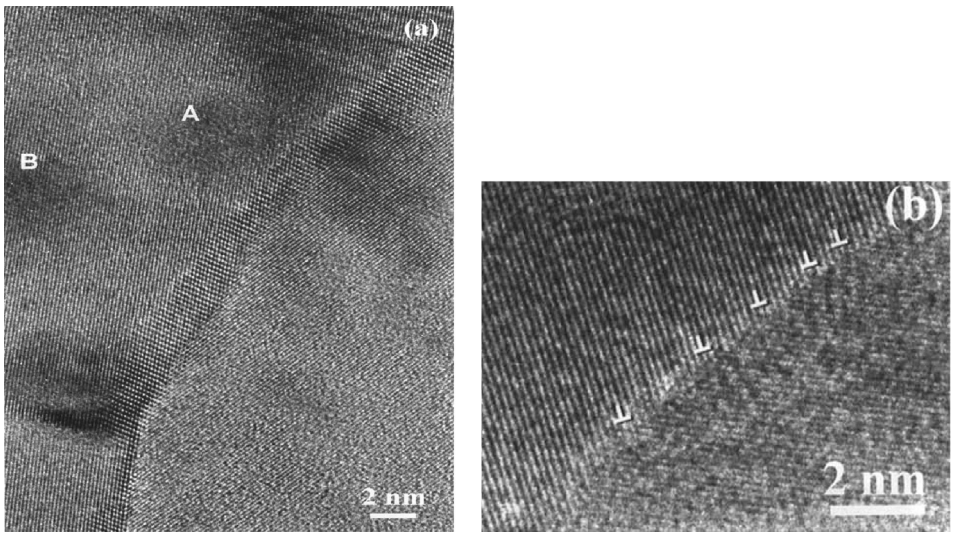

Fig. 36. Grain boundaries in nanocrystalline Ni_3Al annealed at 650 °C for 30 min: (a) The boundary is wavy and corrugated in the regions A and B, the (1 1 1) lattice fringes are weakly defined, illustrating local distortions of crystal lattice. In (b), steps or ledges are shown for another GB containing dislocations marked by ⊥ [172].

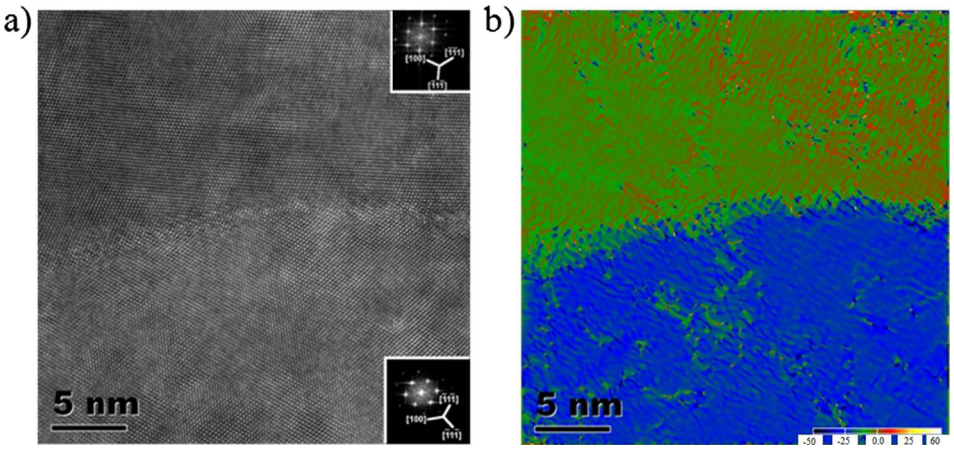

Fig. 37. (a) HRTEM image illustrating two grains in nanocrystalline Ag10Pd90 alloy, which are rotated by an angle of 23.7°. The grain boundary is wavy and faceted. Fourier transformations of micrographs are presented as inserts. (b) Deformation map demonstrating in-plane rigid body rotation xy (rotations on a scale from −50° to +60° (anticlockwise positive) are seen). Hot spots in bright yellow color, which are discernible at high density along the GB, are classified as dislocation cores. Greenish color of upper grain corresponds to a zero rotation taken in capacity of Ref. [307].

Thus, taking into account that the GB structure dominates in UFG materials, it is possible to draw the following conclusions from recent studies:

- UFG materials contain non-equilibrium GBs with strain-distorted structure, which have excessive Gibbs free energy, enhanced free volume and enhanced stresses associated with the distortions of near-boundary region due to high density of GB dislocations.
- The structural width of such non-equilibrium GBs is of the order of few nanometers, which is significantly larger than that of the relaxed high-angle GBs in annealed CG materials. This conclusion correlates well with the recent data of theoretical analysis [226,305,313].

4.2. Nanotwins in metallic nanomaterials

A high density of SPD-produced nanotwins was found in different NS metals and alloys. Fig. 38 demonstrates twins with typical spacing of 10–20 nm revealed by TEM in UFG Cu produced by SPD processing and rolling at cryogenic temperatures [129]. Deformation twinning can be promoted by decreasing stacking fault energy value by alloying, deformation at either high strain rate or low homologous temperature [13]. There is an optimum grain size for deformation twinning [13,118,128,314]. This optimum grain size is can be calculated from the following equation [13]:

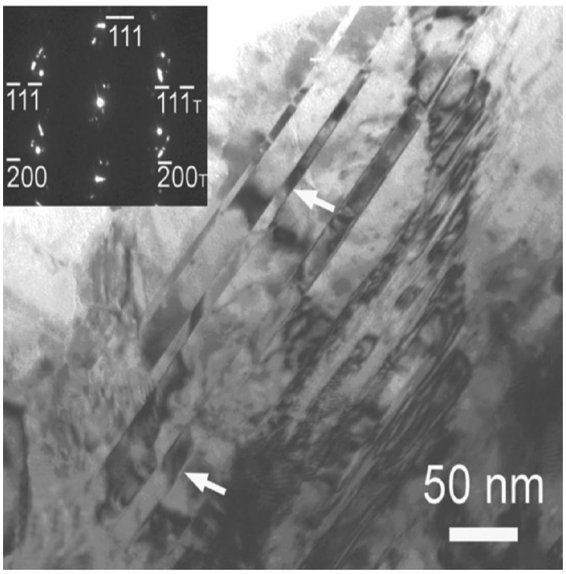

Fig. 38. BF TEM image of the typical grain with deformation nanotwins in UFG copper produced by ECAP and cryogenic rolling [129].

$$\frac{d_m}{\ln\left(\frac{\sqrt{2d_m}}{a}\right)} = \frac{9.69 - \upsilon}{253.66(1-\upsilon)}\frac{Ga^2}{\gamma} \tag{14}$$

where d_m is the optimum grain size, γ denotes the value of stacking fault energy, a - lattice parameter, ν - Poisson's ratio, and G - the shear modulus.

Experiments and molecular dynamics simulations have also found that mechanisms for deformation twinning in nanocrystalline metals can be changed from those governing twinning in coarse-grained materials (see Section 3.2). This leads to the observation of different types of strain-induced twins in NS metals [13]. Also, it has been well illustrated that the formation of deformation twins can improve both the strength and ductility of nanostructured materials (see also Section 5).

4.3. Segregations in nanostructured SPD-processed alloys

A few cases of indirect evidence of GB segregation has been reported in SPD-processed NS materials, where thermal stability was studied as function of impurity level in nickel [315] or Sb concentration in copper [316]. Nevertheless, only lately direct proof of GB segregation in different UFG materials subjected to SPD has been reported, mostly on the basis of atomic scale specification taking into account atom probe tomography (APT) [317–320]. The method offers only very limited crystallographic data and the GB misorientation commonly remains uncertain. Furthermore, it is possible to investigate only small GB areas, which makes it difficult to obtain sufficient statistical data. Meanwhile, it was confirmed that SPD-induced segregation at GBs is not a crucial character and can be noticed in various alloys.

In particular, 3D atom probe tomography (APT) was applied to establish that SPD can interfere with precipitate formation in age-hardening alloys rather than contributing to clustering and segregation of alloying elements [295,317–322]. For example, the data in Fig. 39 [319] demonstrate that segregations at GBs generate clusters of ~3–5 nm width in age-hardening 7075 Al alloy. Furthermore, concentration of alloying elements at GBs can be one order of magnitude larger than in grain interior [317,319,321].

It has been suggested [295,296,321] that non-equilibrium GB can include a greater number of segregating atoms than relaxed interfaces. APT data demonstrated as well that GB segregation is inhomogeneous and Mg concentration in solid solution can considerably differ from grain to grain [319,321]. These observations indicate that local GB configuration and particularly dislocations lying at or near boundaries may affect distribution of solute elements.

To further study this important point, a systematic investigation to unveil the microstructure modification of a low-alloying Al–Mg–Si Al alloy (AA6060) processed by HPT at different temperatures was performed in [322]. Transmission

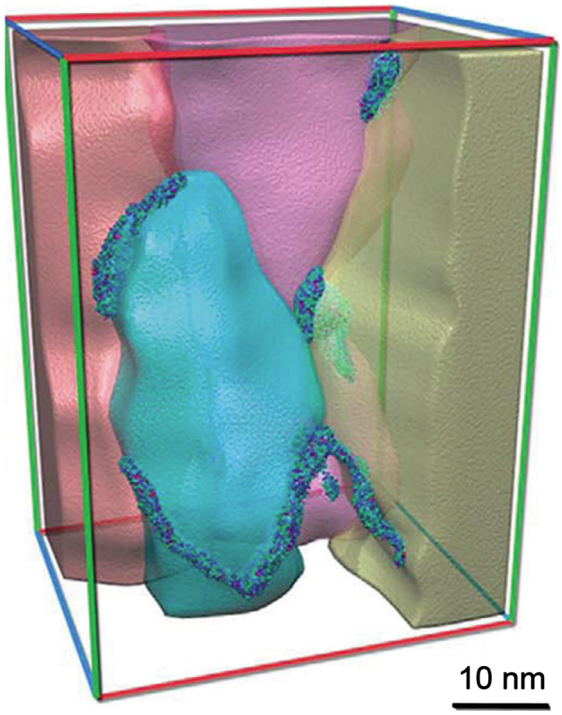

Fig. 39. The APT image of UFG 7075Al alloy. Grain boundary segregations of alloying elements and their view at triple junctions are shown [319].

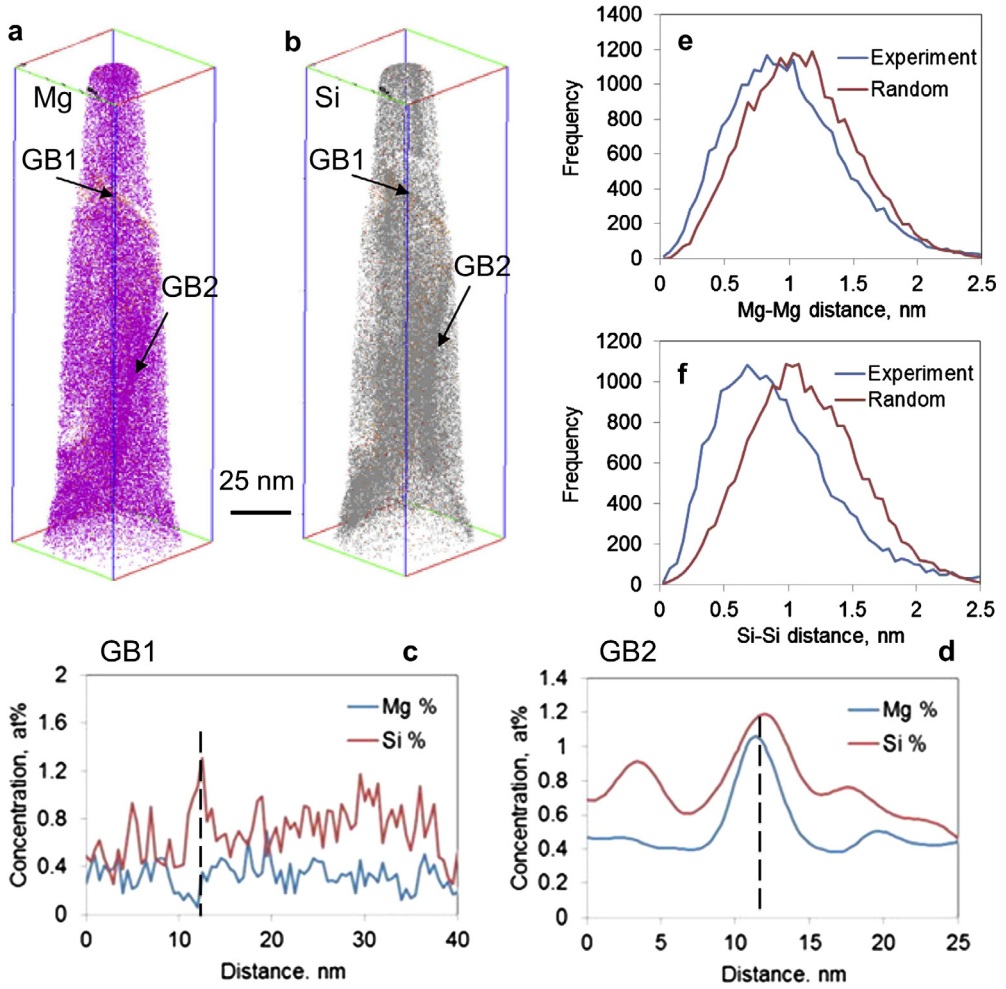

Fig. 40. Typical atom maps of AA6060 alloy processed by HPT at RT with ten revolutions: Mg map (a), Si map (b), composition profiles across GB1 (c), composition profiles across GB2 (d), nearest-neighbour distribution of Mg **(e)** and nearest-neighbour distribution of Si (f) [283]

Kikuchi diffraction (TKD) in SEM [323] was employed to reveal ultrafine grains and the texture of the alloy. APT was used to examine the distribution of solute atoms.

Fig. 40 [322] shows atom maps of a sample after ten-revolution HPT processing at RT. The analyzed volume contains two GBs (GB1 and GB2) enriched with Si as shown in Fig. 40b. The composition profiles across GB1 and GB2, as shown in Fig. 40c and d, respectively, indicate that GB1 is only enriched with Si, but shows no clear segregation of Mg. In contrast, GB2 is enriched in both Si and Mg. This points that GBs may have various segregation features according to the origin of each GB. GB1 had weak solute segregations with Mg and Si. In contrast, GB2 had strong solute segregations. The nearest-neighbour analysis of Mg and Si, as shown in Fig. 40e and f, confirmed that Si atoms developed more inhomogenous distribution than Mg atoms. Inhomogeneous distribution of GB segregations was also observed in the alloy after HPT at 100 °C. At the same time their cluster distribution becomes more visible.

It is also important to note that the UFG alloys with GB segregations exhibit a very high yield stress after HPT processing, which in many cases considerably exceeds that predicted by the Hall–Petch law [319,321]. These results clearly indicate that grain boundary segregations can considerably influence on strain mechanisms (dislocation nucleation and glide) in nanostructured SPD-processed materials (see also Section 6).

4.4. Precipitations of second phases during and/or after SPD

SPD processing affects not only the segregation of solutes at GBs, but also the precipitation behavior. Several mechanisms have been reported responsible for the SPD-induced modification of precipitate microstructure: (i) the fragmentation and dissolution of pre-existing precipitates due to high strain applied by the processing [324–326]; (ii) accelerated precipitation, which is observed in alloys processed by SPD due to dynamic aging [318,327–329]; (iii) changing in the orientation of

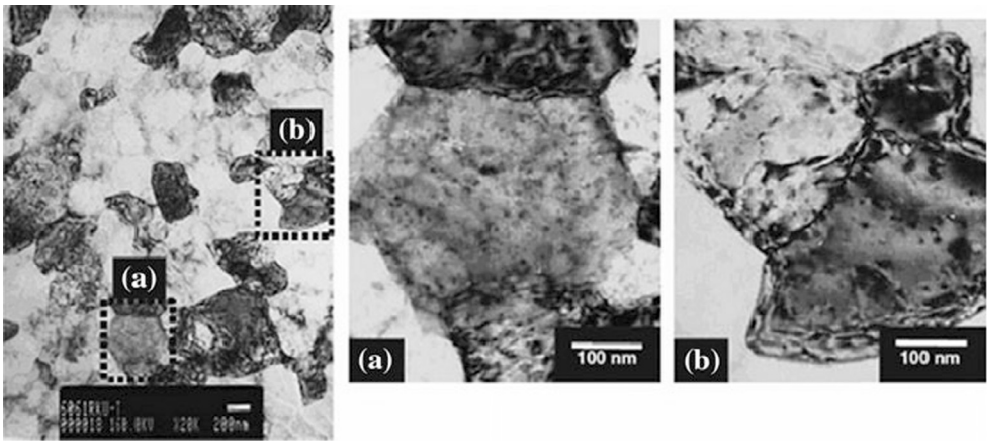

Fig. 41. TEM picture of UFG AA6061 alloy produced by ECAP with parallel channels: The nanosized precipitations can be observed inside the grain due to dynamic aging in areas A and B [330].

precipitates in the matrix, which leads to isotropic growth of the precipitates into a spherical morphology due to the loss of the low-energy interface between the precipitates and the matrix [318].

Formation of precipitates was noticed in various SPD-processed alloys after solution quenching [23,296]. Fig. 41 provides the instance of these nano-particles with dimensions ~10–20 nm precipitated in UFG AA6061 after ECAP-PC [330]. The nano-particles nucleated via dynamic aging contribute to precipitation hardening. Nevertheless, dimension and morphology of precipitates are commonly highly dependent on SPD processing regimes (temperature, applied strain, pressure, etc). Recently, the approach was employed to develop a novel way for producing NS Al alloys for new generation conductors [296,331]. The strategy proceeds from combination of strengthening mechanisms of together with electrical conductivity factors through formation of required UFG states by SPD at room temperature followed by SPD or heat treatment at elevated temperatures to decompose the oversaturated solid solution into nanoscale precipitates due to dynamic aging. The UFG microstructures with second-phase nanoprecipitates may exhibit enhanced mechanical strength as a result of grain boundary strengthening and precipitation hardening. Decreasing the concentration of alloying elements and suppressing formation of Guinier-Preston zones in the grain interior considerably improved electrical conductivity. As an experiment, AA6201 was selected as a material commonly utilized for electrical conductors [331]. The alloy were treated for solid solution and processed by means of HPT with unconstrained anvils [291]. Three temperatures of treatment were selected: room temperature (RT), with subsequent deformation at 130 °C, 180 °C and 230 °C.

TEM revealed very uniform UFG microstructure with an average grain dimension of ~130 nm [331]. The grain interior is characterized with low density of lattice dislocations. At the same time, high residual stresses resulting from the non-equilibrium GBs with extrinsic dislocations were indicated by spots propagation on a chosen region of electron diffraction patterns and extinction lines inside grains [295,306].

The UFG microstructure can be further affected by straining at elevated temperatures. Table 1 contains the results of microstructural characterization of the AA6201 alloy after HPT. The presence of spherical second-phase nanoprecipitates is a considerable feature of such microstructures. The mean dimension of second-phase precipitates grows with increasing HPT temperature. At 130 °C the precipitate size is 10 nm, increasing processing temperature to 230 °C increased g the size to 50 nm (Table 1). Those nanoprecipitates were identified as β-Mg2Si, which are commonly formed due to dynamic aging during SPD processing of Al–Mg–Si alloys at elevated temperatures [320,332,333]. Such nanoprecipitates are noted to have a different morphology in contrast to the needle-shaped nanoprecipitates formed during static aging. X-ray measurements clearly indicate considerable reduction in lattice parameter of the Al matrix after HPT processing (Table 1), thus demonstrating the strong decomposition of oversaturated solid solution. That is consistent with recent observations by the 3D APT

Table 1
Microstructure and mechanical properties of the AA6201 alloy in the studied conditions [331].

Processing	Microstructure	a [Å]
Solid solution treated	CG, d = 65 μm	4.0526
T81	CG, d = 65 μm	4.0512
HPT at room temperature	UFG, d = 130 nm	4.0521
HPT at room temperature + HPT at 130 °C	UFG, d = 280 nm, d_p = 10 nm	4.0509
HPT at room temperature + HPT at 180 °C	UFG, d = 440 nm, d_p = 30 nm	4.0505
HPT at room temperature + HPT at 230 °C	UFG, d = 960 nm, d_p = 50 nm	4.0500

d grain size; d_p size of second-phase precipitates; a lattice parameter.

technique [295,331]. The occurrence of ordinary banded diffraction contrast at GBs points to substantial recovery of non-equilibrium GBs while HPT at elevated temperatures [1,331].

The above results indicate that SPD processing is a powerful tool for modifying nanostructures in metallic materials. In principle, different microstructural parameters (grain size, GB state, density of dislocations, segregations of solute atoms, etc.) may be obtained in materials subjected to SPD to engineer their mechanical and functional properties. Next Chapter reports several bright examples of the influence of grain refinement on the ductility of metallic nanomaterials.

5. Basic strategies for improving ductility of metallic nanomaterials

As already discussed in previous sections, in order to enhance the ductility of metallic nanomaterials without dramatic loss of their strength, it is necessary to suppress both plastic strain instability and crack nucleation/growth instabilities. In metallic nanomaterials with fine grains, dislocation slip is dominant at room temperature, and plastic strain instability (necking) is typically responsible for low ductility; for details, see Section 2. In short, the instability often occurs at low plastic strain in NS metals because dislocation generation and slip are different in NS metals as compared to ductile CG metals. During the deformation of CG metals, dislocations are intensively generated and stored within large grains, producing strain hardening. In NS metals dislocations are mostly generated, stored and annihilated at/near GBs, especially when the grains are very small and GB area per unit volume is very large. After some initial stage of deformation, the GB-controlled dislocation activities in metallic nanomaterials gives rise to a dynamic equilibrium, i.e. a dynamic balance between an increase in the dislocation population through their nucleation at GBs and its decrease through annihilation of dislocations at GBs, a fast process controlled by fast diffusion along GBs [24]. Strain hardening is absent in the dynamic equilibrium, leading to early plastic instability during tensile tests (Section 2). Since the ductility can be regarded as the tensile plasticity, the early plastic instability during tensile test leads to low ductility [30,47].

Following the above discussion, we can list several general principles that can be used to enhance ductility in NS metals with fine grains:

Principle I: Disrupt the balance between the dislocation storage and the dislocation annihilation at GBs in NS metals. Strategies are elaborated, based on the formation of deformation-distorted GBs in NS metals (for details; see Section 5.1) and deformation of such metals at cryogenic temperatures (Section 5.3).

Principle II: Relocate the storage of dislocations from GBs to the interiors of ultra small grains, where dislocations are annihilated slowly owing to slow bulk diffusion. Strategies developed based on this principle include the formation of nanotwinned structures (Section 5.2); tailoring stacking fault energy via alloying (Section 5.4); precipitation-hardening (Section 5.6); and insertion of carbon nanotubes into NS metal matrixes (Section 5.7).

Principle III: Architecture a heterostructure consisting of grains of various scales, in which mechanical incompatibility between heterogeneous domains causes back stress hardening to increase the strength and ductility. The mechanical incompatibility leads to strain gradient near the boundaries of heterogeneous domains, which has to be accommodated by geometrically necessary dislocations and consequently produces large back stress hardening and back–stress strain hardening. Strategies developed using this principle include heterogeneous lamella structures (Section 5.5) and gradient-structured metals (Section 5.6). Note that the principle III is also applicable for ductility enhancement in NC metals having finest grains, where GB deformation mechanisms effectively operate and create defects at triple junctions of GBs.

Principle IV: Smooth (in a controlled, optimized way) plastic strain inhomogeneities at triple junctions that serve as dangerous stress concentration sites during the deformation of NS metals with finest grains. With this principle, one prevents or at least delays nucleation of triple junction cracks and provides a moderate strain hardening that suppresses plastic strain instability (Section 5.1). A strategy using this principle is fabrication of deformation-distorted GBs characterized by high diffusivity to enhance stress-releasing diffusion.

5.1. Grain boundary processes and enhancement of ductility

5.1.1. Enhanced ductility of NC metals

Although most metallic nanomaterials exhibit disappointingly low ductility, there are several experimentally documented examples of good ductility at room temperature. Of special interest are experimental data [86,252] on single-phase NS metals without artifacts, which are characterized by narrow grain size distributions and demonstrate enhanced ductility.

In the experiments [86,252], NS copper and Al-5%Mg alloy having mean grain sizes of 23 and 26 nm, respectively, were fabricated by in-situ consolidation during ball milling. These NS materials demonstrated both ultrahigh strength and good ductility [86,252] (Fig. 42). They show strain hardening and ductile fracture with dimples on the fractured surfaces. Also, dislocation slip was observed to be active in these Cu and Al-5%Mg alloy. Based upon these experimental data, Youssef and co-workers [86,252] attributed both the strain hardening and thereby the enhanced ductility to dislocation storage in the grain interior. However, this explanation does not address the microscopic mechanisms responsible for the generation and storage of dislocations in the interiors of nanoscale grains. The dislocation behavior is of critical importance, because, in most cases, the lattice dislocation generation and storage in nanoscale grains are very limited or even completely

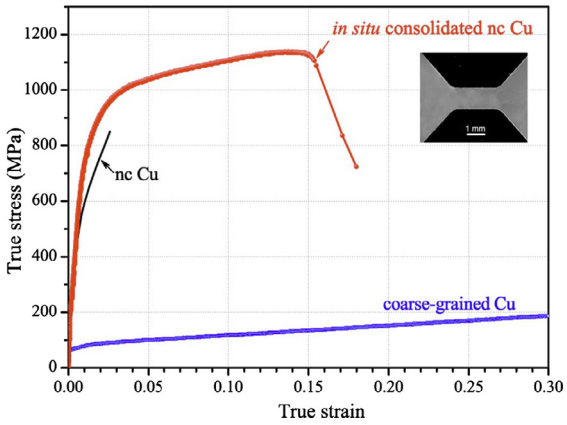

Fig. 42. A typical tensile stress-strain curve for the bulk in situ consolidated nanocrystalline Cu sample in comparison with that of a coarse-grained polycrystalline Cu sample (an average grain size larger than 80 μm) and a nanocrystalline Cu sample prepared by an inert-gas condensation and compaction technique (with a mean grain size of 26 nm) [86].

suppressed. Conventional dislocation sources (like Frank-Read ones) no longer exist in nanoscale grains (see Section 5), and, even if dislocations are generated, they tend to be attracted to GBs, where these dislocations are absorbed due to the image forces [334–336].

The experimental data [86,252] on simultaneously high strength and good tensile ductility of NS metals with narrow grain size distributions are logically explained using the concept [5,337] on interaction of deformation modes, with optimization of GB sliding and diffusion processes [176] taken into account. Following Ref. [176], let us consider this explanation in detail. GB sliding in metals is often accommodated by emission of dislocations from triple junctions and produces wedge disclination dipoles at these junctions [174,176] (Fig. 17). The wedge disclination dipoles provide significant strain hardening in NS metallic materials. The theoretically estimated strain hardening [174,176] is so high that it leads to the experimental values of the flow stress at very small values of plastic strain (for instance, 0.01–0.02, for Ni, and less than 0.01, for Cu). Although plastic instability is effectively suppressed by such a pronounced strain hardening related to GB sliding, the hardening also typically promotes crack nucleation and growth, which cause early fracture. However, in the observed good ductility [86,252] in NS metallic materials, the moderate strain hardening can be logically attributed to effectively accommodate GB sliding. For instance, GB diffusion in NS metals is capable of dramatically decreasing or even completely removing both the stresses and strain hardening created by disclination dipoles. Following [176], in certain conditions that optimize GB sliding and diffusion processes, GB diffusion can suppress crack nucleation and growth, resulting in good ductility of NC metals. In addition, the GB sliding mechanism should also have relatively high strain rate sensitivity, which helps with improving ductility. The optimization means that the diffusion rate is low enough to suppress strain instability but, at the same time, high enough to reduce strain hardening and suppress nucleation of cracks, for a specific strain rate. Besides, for a specific strain, one can distinguish some interval of temperatures and strain rates at which a NS metallic specimen is stable to delay both necking and catastrophic fracture (Fig. 43) [176].

In this situation, the Hart criterion (4) for stability of tensile deformation relative to localization can be re-written in terms of the strain rate sensitive and insensitive parts as [176]:

$$h_0 + h_{dif} + m > 1 \tag{15}$$

In Eq. (15), the strain rate insensitive term h_0 is controlled by the applied stress when GB diffusion is absent. This positive term h_0 is associated with the strain hardening produced by disclinations. In Eq. (15), h_{dif} and m are sensitive to strain rate. The second term – the conventional strain rate sensitivity m defined by formula (3) - is always positive. The h_{dif} is always negative, which describes the effect of diffusion on the strain hardening. Estimates given in Ref. [176] show that h_{dif} is much larger than m. As a consequence, the sum $(h_{dif} + m)$ of the terms sensitive to strain rate is negative. Also, following Ref. [176], in the situation where diffusion is fast enough and the strain rate is substantially low, the sum $(h_{dif} + m)$ can significantly diminish the effective strain hardening presented in the left-hand side of formula (15). For example, in the case of NC copper with grain size $d = 10$ nm at $T = 330$ K and plastic strain $\varepsilon = 0.05$, for plastic strain rate $\dot{\varepsilon} = 10^{-4}$ s^{-1}, one finds $h_0 = 11.5$ and $h_{dif} + m = -8.2$. At the same time, for the same values of d, T and ε as well as for $\dot{\varepsilon} = 10^{-2}$ s^{-1}, we have $h_0 = 11.5$ and $h_{dif} + m = -0.6$, respectively. Thus, the effective strain hardening $h_0 + h_{dif} + m = 3.3$ and 10.9, for $\dot{\varepsilon} = 10^{-4}$ s^{-1} and 10^{-2} s^{-1}, respectively. This indicates a trend that strain hardening increases with rising strain rate.

In the situation under discussion, the effective strain hardening diminishes due to GB diffusion. For instance, the effective strain hardening decreases owing to GB diffusion down to values that allow plastic instability to occur in a NC metal in tensile test. For example, in the case of NC copper with grain size $d = 10$ nm at $T = 330$ K and plastic strain $\varepsilon = 0.1$, for plastic strain rate $\dot{\varepsilon} = 10^{-4}$ s^{-1}, one obtains $h_0 = 5.89$ and $h_{dif} + m = -5.04$, so that the effective strain hardening has value of 0.85. For this value, according to the Hart criterion (15), plastic flow is unstable.

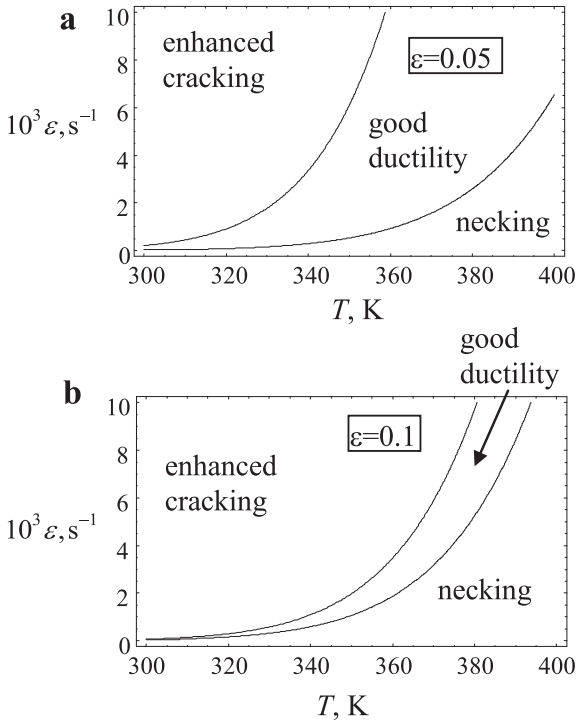

Fig. 43. Ductility maps of nanocrystalline Cu with the grain size d = 15 nm in the coordinates $(T, \dot{\varepsilon})$, for $\varepsilon = 0.05$ (a) and $\varepsilon = 0.1$ (b) [176].

To summarize, following analysis given in Ref. [176], fast diffusion can significantly diminish strain hardening, thereby leading to necking. On the other hand, when diffusion rate is low, the flow stress can increase up to levels at which cracks are intensively generated and grow, resulting in the catastrophic fracture of a NC specimen. In these circumstances, for a specified plastic strain, a range of strain rates and temperatures exists in which a NC metallic solid is stable (Fig. 43) [176]. With increasing strain, the range in question shrinks. The range can even disappear, when strain reaches its critical value. In this case, the optimization of conditions (strain rate, temperature) for tension of a NC metallic specimen becomes useless for its ductility enhancement through suppression of necking and brittle fracture.

For instance, Fig. 43 presents the ductility maps for NC copper in coordinates T and $\dot{\varepsilon}$, for ε = 0.05 (Fig. 43a) and ε = 0.1 (Fig. 43b). The curves in Fig. 43 separate the parameter regions where NC copper under tensile load is stable at a given strain ε from the regions where it is unstable (either necking or fracture). As it follows from Fig. 43, NC copper can exhibit substantial ductility over a certain range of strain rates $\dot{\varepsilon}$ and temperatures T. With increasing plastic strain ε, the middle parameter region in the maps (where NC copper demonstrates ductile behavior) shrinks (Fig. 43), and this region completely disappears at some critical plastic strain ε_c that does not depend on T. In the case of NC copper with the parameter values specified above, one has: $\varepsilon_c \approx 0.15$ [176].

The maps in Fig. 43 are not quantitatively accurate due to approximate calculations and uncertain values of several parameters, which are sensitive to the fabrication history and structural characteristics of a specimen in its initial, predeformation state. Nevertheless, the maps show the existence of a range for deformation parameters with which NC metals are intrinsically ductile owing to optimization of GB sliding and diffusion. With rising plastic strain, the range shrinks, and at critical plastic strain ε_c the NC metal becomes unstable to failure at any strain rate $\dot{\varepsilon}$ and temperature T.

Finally, notice that dislocations are emitted from triple junctions in order to accommodate GB sliding (Figs. 15 and 17). These dislocations have the following two effects. First, dislocations are absorbed by GBs where they glide and climb, enhancing GB sliding and producing GB vacancies and interstitial atoms that enhance GB diffusion [5,168]. Second, dislocations emitted from triple junctions can be stored in grain interiors, due to interactions with other dislocations and GB defects. In these circumstances, the experimentally observed dislocations, as noted by Youssef et al. [86], can contribute to the strain hardening and thus improve ductility. However, in the experiments [86], dislocations were observed by TEM near growing crack tips where extremely high local stresses operate, and the stress screening effects of crack free surfaces are pronounced. With these factors, conditions for dislocation generation and storage in vicinities of crack tips are much softer compared to those in nanoscale grain interiors located far from crack tips. Therefore, dislocation activity can be suppressed in regions far from crack tips, and its real contribution to the strain hardening of NC metals with narrow grain size distributions can be insignificant.

Thus, the concept [5,337] on interaction of deformation modes in NC metallic materials with smallest grain sizes, taking into account optimization of GB sliding and diffusion processes [176], gives at least semi-quantitative explanation of the

experimentally observed [86,252] good tensile ductility of NC metallic materials that do not contain artifacts are characterized by narrow grain size distributions at low temperatures. Representations of this concept may be also relevant in description of other experimentally observed examples of enhanced ductility shown by NS materials at room temperature.

5.1.2. Enhanced ductility of NS SPD-processed metals

The ductility of NS materials produced by SPD is usually rather limited under normal testing conditions [28,168]. It is found [338] that strength and ductility usully trade off with each other [4,339].

In 2002 a pioneer study by Valiev et al. [338] reported on a new trend in the field which got a name "the paradox of strength and ductility". In Fig. 44 a plot for relation between strength and ductility is drawn. One can see that majority of metals (Al, Cu, Co, Mg, etc.) obeys the general trend to sacrifice the ductility for the sake of strength and their plotted values lie below an approximating curve [338]. However the data related to NS Ti, produced by HPT as well as for NS Cu, produced by multi-pass ECAP are situated far beyond this curve, revealing an extraordinary strength coupled with good ductility. In order to achieve this combination one should subject the material to high-strain SPD and produce UFG metals with high-angle GBs promoting GB sliding which boosts up the strain rate sensitivity value [338]. Lately, similar trend was reproduced for the case of Cu [340], an Al–3%Mg alloy [341]. These results open an intriguing new possibility to enhance strength and ductility by SPD processing.

Indeed, as shown below, a number of strategies have been suggested to improve the ductility in NS metals with fine grains while retaining their strength, including the introduction of nanotwins, formation of second-phase particles and others. However, they are all based on strain hardening increase, leading to the deterring of strain localization and consequently, enhancement of ductility (see Section 3). On the other hand, the variation of SPD processing parameters may increase strain rate sensitivity through control of GB structure leading to enhanced GB sliding.

Several recent publications reported a rather general and relatively simple strategy to enhance the ductility of UFG metals fabricated by SPD. It involves conducting conventional SPD processing, say, by either ECAP or HPT, to very high strains [164,340–342]. For instance, Mungole with co-workers revealed the role of HPT processing strain on strength and ductility in a cast Al–7% Si hypoeutectic alloy [342]. The alloy was processed by HPT for different numbers of turns at room temperature. The number of turns was chosen as N = 0, 1/4, 1, 5, and 10, corresponding to the estimated average strains for the HPT disks as 0, ≈2.3, ≈9.2, ≈46.2, and ≈92.5, respectively [342]. Tensile tests were performed at 298 K and a strain rate of 10^{-3} s^{-1}, and the stress-strain curves are shown in Fig. 45 [342]. It should be noted that due to small sample size, the elongation to failure presented in this figure and others reported in the literature may be significantly over-estimated [31,32]. Fig. 45 shows that, with increasing number of HPT turns, the yield stress (YS), ultimate tensile stress (UTS) and strain to failure increases.

Similar results were obtained for tension tests at 298 K and other strain rates ranging from 10^{-4} to 10^{-2} s^{-1}. All the results are summarized in Fig. 46 [342] that presents plots in three different forms. Fig. 44a shows the normalized YS *vs*. normalized elongation to failure. The former is calculated as the measured YS normalized by YS of the as-cast specimen. The normalized elongation to failure is calculated as the measured elongation to failure normalized by that of the as-cast specimen. Fig. 46b and c present the dependences of the normalized UTS on the normalized elongation to failure and the normalized uniform elongation, respectively.

Data in Fig. 46 are presented in the two areas divided by the vertical and horizontal dashed lines at which the normalized quantities under discussion have value of 1 [342]. In this representation, the experimental data that correspond to conven-

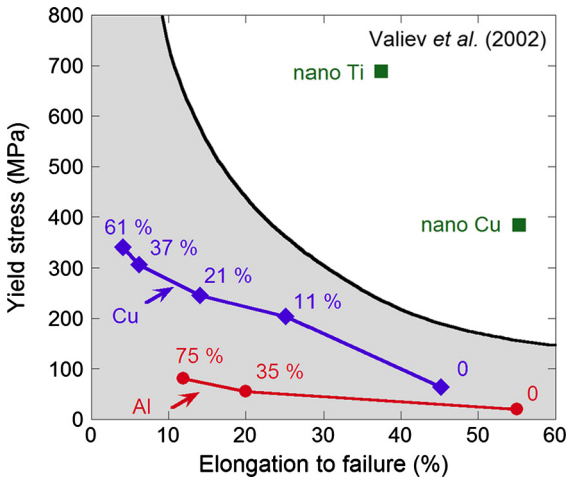

Fig. 44. Conventional plot of yield stress against elongation to failure illustrating the paradox of strength and ductility: almost all UFG metals lie in the shaded area below the solid curve but the two points labeled nano Ti and nano Cu are exceptions to the rule where nanostructures were achieved by using SPD processing to impose very large strains [338].

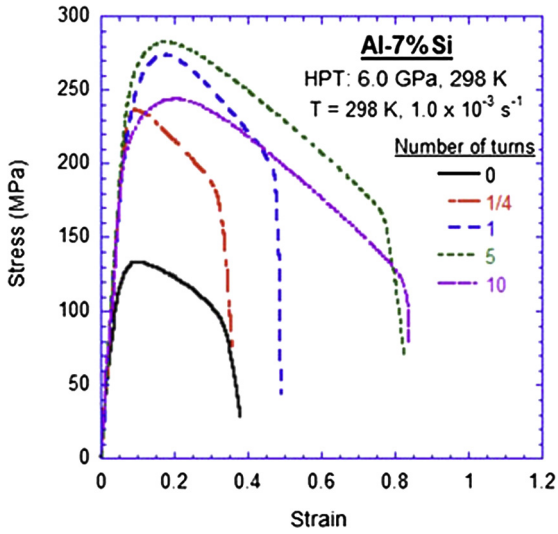

Fig. 45. Representative plots of engineering stress versus engineering strain for samples tested under tension in the unprocessed condition and after processing by HPT at 298 K: the tensile testing was conducted at 298 K under an initial strain rate of 1.0×10^{-3} s^{-1} [342].

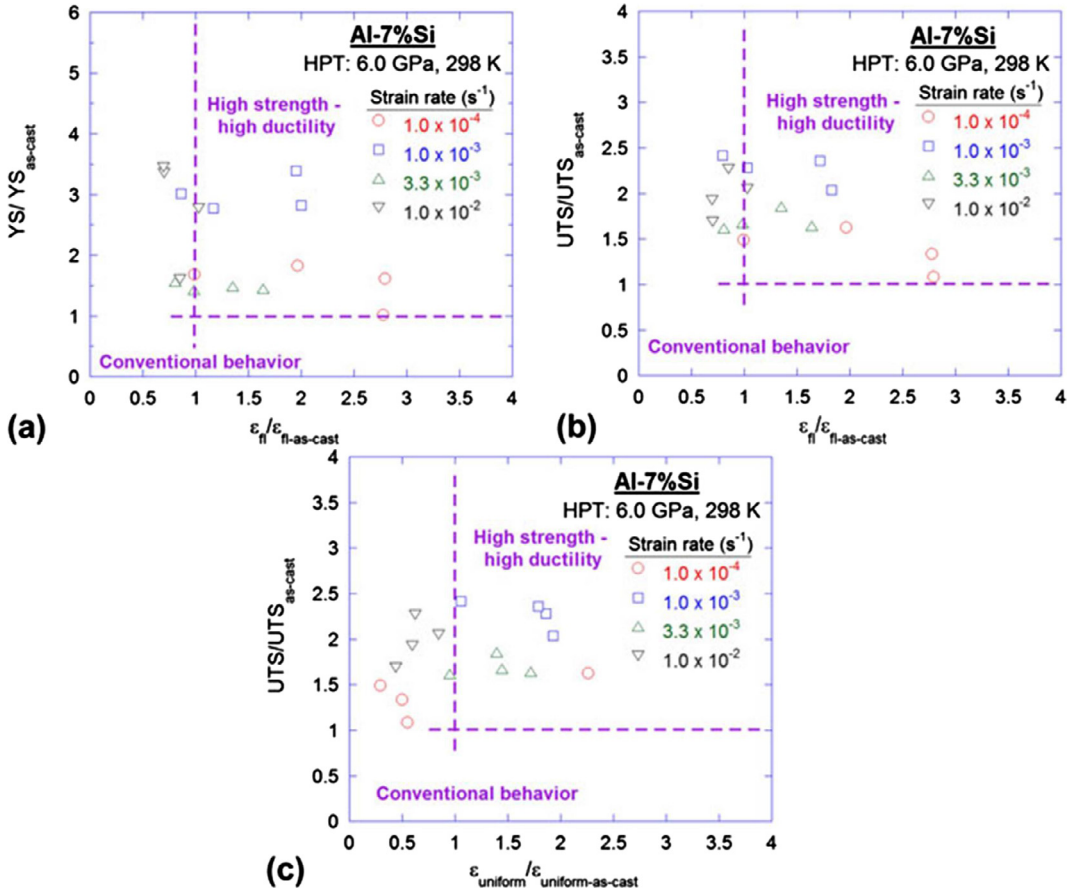

Fig. 46. Variation of (a) the normalized YS and (b) the normalized UTS with the normalized elongation to failure and (c) the variation of the normalized UTS with the normalized uniform elongation corresponding to the strain at UTS for samples processed by HPT at 298 K: data falling above the broken horizontal line and to the right of the broken vertical line display a simultaneous increase in strength and ductility compared to the as-cast material and this is designated the high strength–high ductility region whereas conventional behavior denotes an increase in ductility at the expense of strength or an increase in strength at the expense of ductility [342].

tional deformation behavior exhibiting concurrently high strength and low ductility, or conversely good ductility and low strength, are shown as points in the area to the left and below the dashed lines. The unusual deformation behavior of NS metals demonstrating concurrently enhanced strength and ductility corresponds to the points located within the large rectangular areas (Fig. 46a–c) each is bounded by the two dashed lines. Within these areas, both the normalized strength and the corresponding elongation have values >1. These areas in Fig. 46a–c are designated as the regions of high strength–high ductility.

From a microscopic viewpoint, the experimental observation of simultaneous high strength and reasonable ductility in metals processed through SPD to extremely large strains is attributed to activation of GB sliding [168,338,342]. Note that GB sliding is typically operative in metals at elevated temperatures nearly and above $0.5T_m$, where T_m is the melting temperature. Following [28,168,342], in NS metals subjected to high SPD strains, GB sliding substantially contributes to plastic flow at comparatively low temperatures due to a large population of non-equilibrium (deformation-distorted) GBs with high-angle misorientations and high diffusivity. This explanation is consistent with the experimentally observation [342] that the Al–7% Si alloy specimens tested at the slow and intermediate strain rates (10^{-4}, 10^{-3}, $3.3{\cdot}10^{-3}$ s^{-1}) exhibit a more pronounced tendency to have both high strength and good ductility, as compared to those tested at the highest strain rate (10^{-2} s^{-1}). This tendency indicates that one should use comparatively low strain rates to obtain concurrently high strength and good ductility under tension at ambient temperatures [168,342].

Note that the nature of enhanced ductility exhibited by strong NS metals subjected to high SPD plastic strains is not fully understood and definitely needs further investigation. Specifically, there exist the following experimental facts [342] that represent highly important and intriguing subjects for further examinations:

(i) With only a few exceptions, the UFG metallic specimens demonstrating an increase in both strength and ductility also exhibit enhancement in both uniform and total elongations. At the same time, the UFG metallic specimens showing conventional deformation behavior with high strength and limited ductility are characterized by larger decrease in the uniform elongation, as compared to the total elongation.
(ii) The relative improvement in both strength and ductility is more pronounced for the specimens processed at the lower temperature.
(iii) The number of HPT turns and associated plastic strain substantially influence the strain rate sensitivity m for the UFG metals in tension tests at room temperature. The as-cast specimen exhibited an $m \approx 0.03$, the specimens after 1/4 and 1 HPT turn have $m \approx 0.02$, and the specimens after 5 and 10 HPT turns have $m \approx 0.12$ and ≈ 0.14, respectively. Strain rate sensitivity m with comparatively high values of ~ 0.12 and ≈ 0.14 can enhance the ductility of UFG metals. However, this contribution is not very significant, as compared to that of strain rate sensitivity to superplasticity of UFG and conventional microcrystalline metals at elevated temperatures, in which case $m > 0.33$ (often $m \approx 0.5$).

Note that, in parallel with very high SPD plastic strains, short-term anneal after SPD can also enhance ductility at low temperatures [167,168,343–347]. For instance, the HPT-processed titanium with a mean grain size of 120 nm in room temperature tension tests exhibits YS > 800 MPa, UTS = 980 MPa and elongation to failure = 12% [167]. Short anneal treatment exerts rather significant effects on its mechanical properties in tension at room temperature. In particular, it was revealed that both strength and ductility are highly sensitive to anneal temperature T and demonstrate their maximum values in the range of T from 250 to 300 °C (see also Section 6.

Although grain growth can often mask or even suppress the effects of short term anneal on mechanical properties of NS metals, there are experimental data indicating ductility enhancement due to short-term annealing associated with grain growth. For instance, Andreau with co-workers [346] examined influence of short (10 min) anneal on strength and ductility of a HPT-processed Al–1.0% Mg solid solution alloy with a pre-anneal mean grain size of around 200 nm. Following HPT, the alloy specimens were subjected to 10 min annealing at some temperatures within the range 373–523 K and demonstrated an increase in grain size. More precisely, there is no visible grain growth at 373 K. However, grain growth occurs and results in grain size ~360 nm, ~940 nm and ~1.98 μm at 432, 473 and 523 K, respectively. The structural evolution involving both grain growth and changes in dislocation ensemble characteristics leads to corresponding changes in engineering stress-strain curves for room temperature tensile tests with initial strain rate values of 10^{-4} and 10^{-2} s^{-1} (Fig. 47a and b, respectively). In particular, the NS specimens processed by 10 turns with no subsequent thermal treatment exhibit high stresses, but low ductility, while, after a 10 min annealing at 423, 473 or 523 K, the stresses become lower, and ductility becomes remarkably higher (Fig. 47).

Thus, the unique combination of superior strength and enhanced ductility can be achieved in metallic nanomaterials through SPD-processing to very high strains and/or short-term anneal after such a processing. In NS metals subjected to high SPD strains, GB sliding substantially contributes to plastic flow even at comparatively low temperatures due to a large amount of non-equilibrium (deformation-distorted) high-angle GBs and high diffusivity. At the same time, the nature of enhanced ductility exhibited by SPD-processed NS metals is not fully understood and definitely needs further investigation. In particular, it is important to pay attention to GB structure, which may vary significantly depending on the SPD processing regimes (see Section 4), which have significant influence on GB sliding and as a result, on the ductility of NS materials. Particularly, recent studies [165,283] demonstrated that existence of GB segregations in SPD-processed NS alloys make it possible to significantly activate GB sliding and give effect to very high tensile ductility of samples already at room temperature.

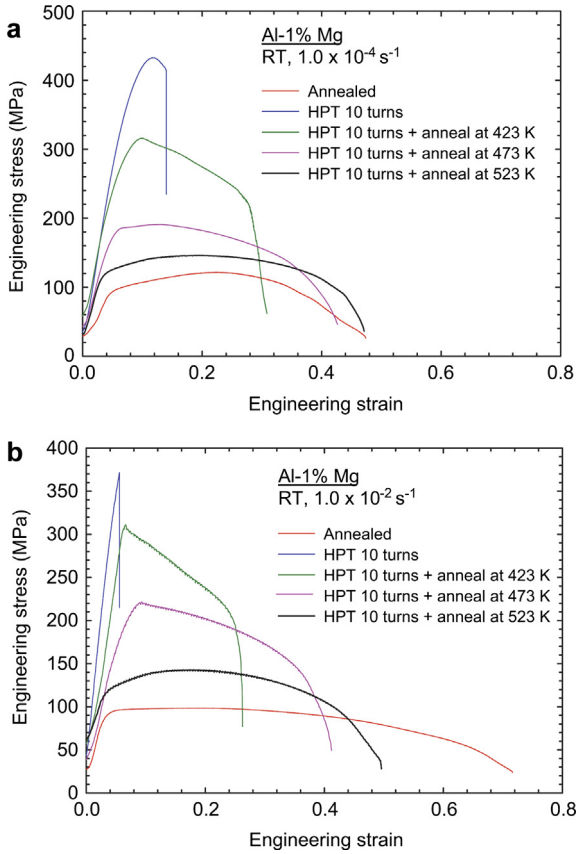

Fig. 47. Stress–strain curves at room temperature for the annealed material, after HPT through 10 turns and after HPT through 10 turns and annealing at 423, 473 and 523 K at (a) 1.0×10^{-4} and (b) 1.0×10^{-2} respectively [346].

5.2. Superior strength and good ductility of nanotwinned, ultrafine-grained metals

As discussed above in Section 3, when the grain size is very small, GBs may act as the dislocation source and sink without accumulation in the grain interior [6,13,63,64,82,83,89–102], which leads to low strain hardening rate. To solve this problem, twin boundaries can be engineered into the grain interior as dislocation barriers and accumulation sites. When dislocations glide to a twin boundary, they can accumulate at the twin boundary if the applied stress is not very high [159,348,349]. When the applied stress is sufficiently high, dislocations can interact with the twin boundary in a number of ways including transmission across the twin boundary [159,314,350–353], and detwinning [159,314,351]. In addition, twin boundaries have also been observed to act as a dislocation source if there are steps on them [140]. These interactions between dislocations and twin boundaries will help with dislocation activities and accumulation. Therefore, an ultrafine-grained metal containing a high density of twin boundaries is predicted to be very effective to produce strain hardening, which consequently helps with improving ductility. The blocking of dislocations by the twin boundaries and the high stress needed for dislocation to react with the twin boundaries is expected to increase the strength.

- From the above discussion, it is desired to engineer a high density of twin boundaries into the interior of ultrafine/nanostructured metals to produce both high strength and high ductility. Twins can be produced by either growth or by deformation. For example, nanostructured Cu film produced by electrodeposition has been reported to have high density of growth twins [348,354,355]. The Cu film exhibited much higher strength and ductility than nanocrystalline Cu without twins (see Fig. 48a). TEM micrograph after tensile test shows dislocations deposited at the grain boundaries (see Fig. 48b). The twin boundaries were very clean and sharp before the tensile testing [348]. These results clearly show that twins can simultaneously increase the strength and ductility of NS metals. Nanotwinned thin film can also be prepared by Magnetron-sputter deposition [356], pulsed laser deposition [146,357] and other thin film techniques. These twins are normally considered growth twins, but high internal stress may exist to produce deformation twins [146]. However, thin films are usually slow to grow and expensive, and usually not practical or useful for structural applications, where the strength and ductility are critically needed.

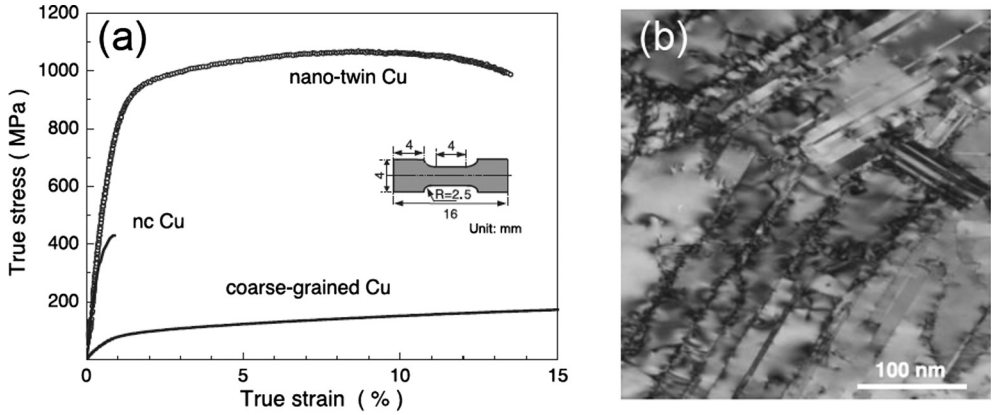

Fig. 48. (a) High strength and high ductility of electrodeposited nano-twin Cu as compared with nanocrystalline (nc) Cu without twin. (b) Dislocation accumulations at twin boundaries after tensile testing [348].

Preexisting twins can also be formed by deformation, which can be used to process bulk materials large enough for practical structural applications. For example, high density of twins was produced in NS Cu by means of ECAP followed by cryogenic drawing and cryogenic rolling (see Fig. 49a) [129]. As shown, the deformation twins look different from growth twins because they are formed by the slip of partial dislocations, and simultaneously interact with other dislocations. Therefore, deformation twins usually contain dislocations at twin boundaries and interior, so that they look "messy" due to the strain field caused by dislocations. It should be noted that these twins were formed during the cryogenic deformation, and were preserved to the room temperature. ECAP at room temperature only refined the grain size to ultrafine grain size but did not produce twins in Cu because their grains sizes were still too large to produce deformation twins at room temperature [13]. These preexisting twins formed by cryogenic deformation were found effective in simultaneously increase the strength and ductility of NS Cu, as shown in Fig. 49b.

The best way to utilize deformation twinning to increase the strength and ductility is for the NS metal to deform by twinning and dislocation slip during the tensile deformation. This can be achieved by lowering the stacking fault energy (SFE) to make twinning occur at room temperature and quasi-static strain rates that are typical of a normal tensile test [297,358,359]. For example, Zhao et al. found that NS Cu-10%Zn alloy has both higher strength and higher ductility than NS Cu processed by HPT (see Fig. 50). This was attributed to the lower SFE (22 mJ/m^2) of the Cu-10%Zn alloy as compared to Cu (41 mJ/m^2). This trend was also observed later in the Ni-Co alloy system [360]. It was found that in the NS Cu-10% Zn alloy both deformation twins and dislocations accumulated during the tensile test, which produced high strain hardening to enhance ductility [297]. In contrast, in the NS Cu only dislocation accumulation was observed and the dislocation density increase was not as high as in the NS Cu-Zn alloy.

From the above discussion, a NS fcc metal can be designed to activate deformation twinning to obtain both high strength and high ductility. However, as discussed earlier, the grain size of a NS metal needs to be near the optimum grain size for twinning to utilize this mechanism [13]. This optimum grain size can be calculated using Eq. (14), and is significantly affected by SFE. In addition, alloying may affect the ratio of the SFE to the twin fault energy, which also affects the optimum grain size [152,361]. There may be an optimum SFE for the best ductility (see Fig. 51) [358]. Zhao et al. observed that in the

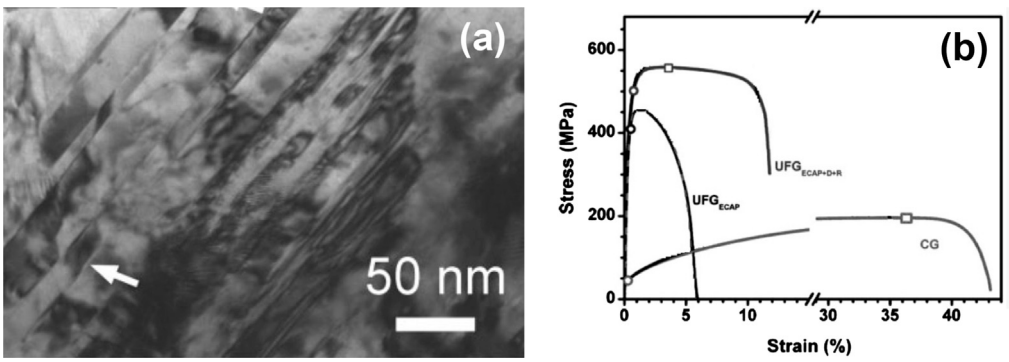

Fig. 49. (a) Twins introduced into the nanostructured Cu during the cryogenic extrusion and rolling [129]. (b) Tensile engineering stress-strain curves indicate that introduction of twins during the cryogenic extrusion and rolling after ECAP significantly increased the ductility and also improved the strength of the nanostructured Cu.

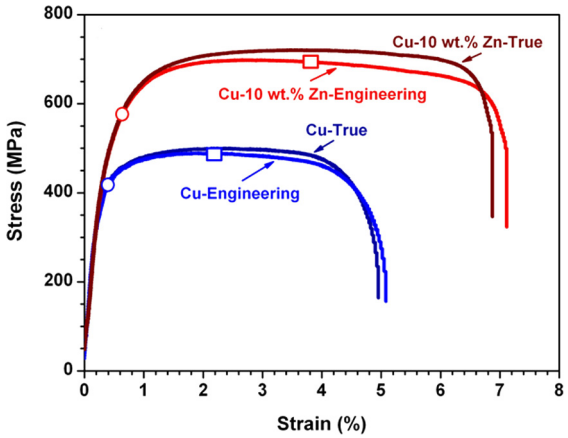

Fig. 50. Stress-strain curves of nanostructured Cu and Cu-10%Zn alloy processed by HPT for 5 revolutions at room temperature under a pressure of 6 GPa [297].

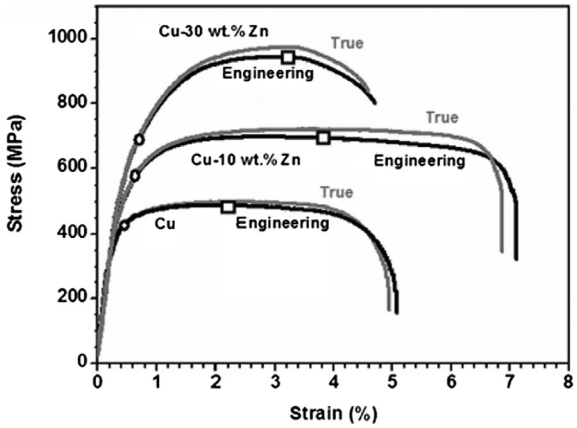

Fig. 51. Engineering and true stress-strain curves for nanostructured Cu, Cu-10 wt%Zn, and Cu-30 wt%Zn with stacking fault energies of 41 mJ/m^2, 22 mJ/m^2, and 7 mJ/m^2, respectively. All samples were processed by HPT for 5 revolutions at room temperature under a pressure of 6 GPa [358].

NS Cu-Zn metal and alloys processed by HPT, when the SFE decreased from 41 mJ/m^2 (Cu) to SFE = 22 mJ/m^2 (Cu-10%Zn alloy) to SFE = 7 mJ/m^2 (Cu-30%Zn alloy), the ductility first increased and then decreased (see Fig. 51). It appears that the Cu-10%Zn alloy with an intermediate SFE has the highest ductility. However, it should be noted that the Cu-10%Zn sample has an average grain size of 110 nm, while the Cu-30%Zn sample has a grain size of only 10 nm. It is known that smaller grain size has lower ductility for NS metals [69]. Therefore, it is highly possible for the Cu-30%Zn sample to have higher ductility than the Cu-10%Zn sample if they both have similar grain size around 100 nm. This needs to be clarified through further study.

An ideal NS/UFG structure for high strength and high ductility may possess the following features/deformation behaviors [362]: (1) high-density of twin boundaries to increase the strength and to provide locations for dislocation accumulation, (2) low initial dislocation density so that more room is available for dislocation accumulation and strain hardening, (3) deformation by twinning during the tensile testing to effectively accumulate twins, stacking faults and dislocations, i.e. low stacking fault energy plus appropriate grain size for twinning. Such an ideal structure was reported in ultrafine-grained 304L stainless steel produced by reverse transformation of deformation-induced martensite (see Fig. 52a). As shown, ultrafine grains that are largely free of dislocations but contain growth twins with straight, clean twin boundaries were produced. After tensile tests for a strain of 28%, dislocations were accumulated inside the grains (Fig. 52b). Dislocations interacted with twin boundaries, which became sites for dislocation accumulation, and stacking faults also formed and accumulated between twin boundaries (Fig. 52c). The combination of these factors produced a combination of high strength and very good ductility (Fig. 52d).

It should be noted that for fcc metals with very low SFE hierarchical twin structures with primary, secondary and even tertiary twins have been engineered to further increase the strength and ductility [363–366].

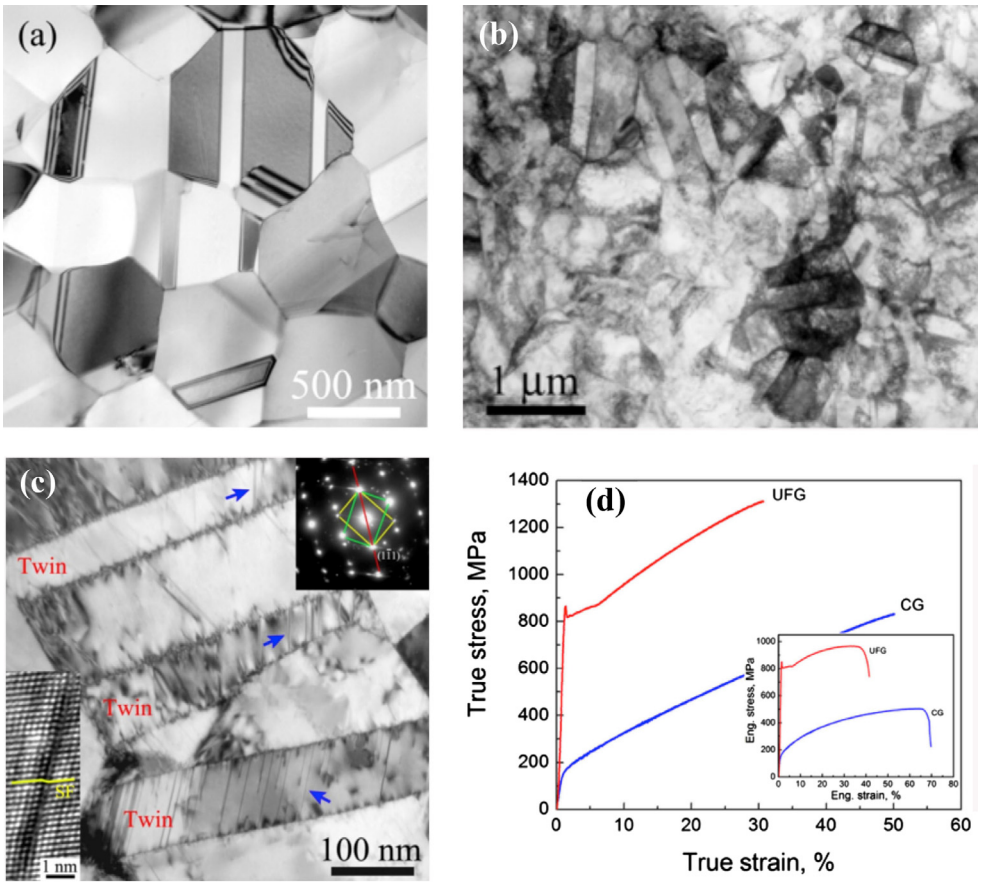

Fig. 52. (a) An ideal UFG structure in 304L stainless steel produced by reverse transformation of deformation-induced martensite [362]. (b) TEM micrograph after tensile test for 28% strain. (c) Dislocation interaction with twin boundaries and stacking faults. (d) Tensile mechanical behavior.

5.3. Deformation of ultrafine-grained metals at cryogenic temperatures

The cryogenic behavior of NS materials is a relatively novel subject. Meanwhile, there are still a few publications demonstrating that the cryogenic properties of NS materials could exceed those of corresponding CG materials or materials subjected to cold rolling or other conventional deformation-processing. For example, in the study [367] excellent mechanical properties were observed in bulk NS metals at cryogenic temperatures. Three metals, Ti, Fe and Cu, were produced via severe plastic deformation using ECAP followed by cold rolling. This treatment allowed refinement of the grain structure of Cu down to the average grain sizes of about 190–300 nm. For the case of Ti the final grain size amounted to 260 nm and for Fe it was possible to reach the value of 200 nm. At room temperatures the NS metals demonstrated enhanced strength during tensile tests, however stress-strain curves exhibited fast localization of strain and corresponding necking to occur at early deformation stage (see curve A in Fig. 53 for the case of Cu).

Curve B in Fig. 53 illustrates that for the same ECAP-processed Cu this plastic instability problem lessens at liquid-nitrogen temperature (77 K). There is enhanced uniform tensile deformation as well as increased value for elongation to failure (%EL). On the true stress-strain diagram one can see the distinct strain hardening region at the corresponding curve [368].

Besides improved ductility, Fig. 53 shows higher yield stress (~500 MPa) at the cryogenic temperature, significantly exceeding the value corresponding to RT. Such significant temperature dependence has been observed as well in the hardness data of a NC Cu [369]. As well known, CG fcc metals possess limited sensitivity of yield stress to the temperature (as well as for the strain rate) [370,371] thanks to the fact that for dislocation slip low thermal activation is needed to move through such obstacles as different configurations of internally stored dislocations. The NS fcc metals have enhanced temperature sensitivity at RT and therefore, at cryogenic temperatures NS fcc metals will possess higher yield strength, as demonstrated in Fig. 53.

Increasing strain rate has similar effect on strain hardening as lowering the temperature [371], which is true for conventional metals. In Fig. 53, Curves from B to D show that the ultimate tensile stress [368], elongation (especially uniform one) and the strain hardening tend to increase simultaneously when the strain rate is increased.

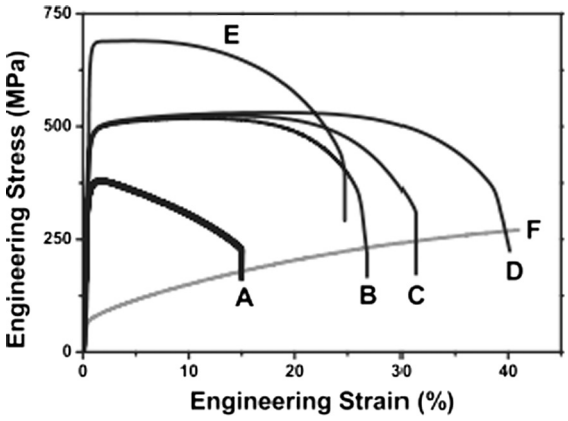

Fig. 53. Engineering stress–strain curves of nanostructured Cu. Curve A is for ECAP Cu tested at RT at a strain rate of 1×10^{-4} s^{-1}. Curves B–D are for the same ECAP Cu tested at 77 K, for strain rates of 1×10^{-4} s^{-1}, 1×10^{-3} s^{-1}, and 1×10^{-1} s^{-1}, respectively. Curve E is for the 190 nm Cu (see text) tested at 77 K at a strain rate of 1×10^{-1} s^{-1}. For comparison, Curve F shows the behavior of coarse-grained Cu over the first 40% of strain at 77 K and 1×10^{-4} s^{-1}.

ECAP processing of Cu with subsequent cold rolling combined with low-temperature thermal treatment, resulted in additional decreasing of grain sizes down to ~190 nm [372]. Fig. 53 also illustrates the tensile curve obtained at 77 K for this material (curve E) with yield stress of ~700 MPa, which is considerably higher than the value typical for RT [372]. At the same time, the material retains some strain hardening as well as uniform elongation region and reasonable ductility of about 25%. It should be noted that such level of ultimate tensile stress can hardly be reached in Cu nanostructured by the other techniques [373,374] and in the case it is achieved the elongation to failure drops to less than 3% [373,375].

In Fig. 54 the tensile engineering stress–strain curves are drawn for the Ti (260 nm) specimen [65,376] tested at 77 K. According to Curve A, the Ti demonstrates some ductility and a small uniform elongation at RT, whereas at 77 K a drastic increase in strength up to ~1.4 GPa is observed. Fig. 54 indicates a simultaneous growth of%EL, which increases with strain rate up to a maximum of ~20% rather than a reduction in ductility. The results obtained for strength and ductility in this study exceed or are at the same level typical for the highly alloyed Ti [371,377]. The mechanical response (strain hardening rate) at the cryogenic temperature was shown recently to be considerably enhanced by the 20% compression strain test [377]. This allowed avoiding early necking, which is untypical for such strong materials.

Bcc metals are known for their yield stress dependency on temperature and at cryogenic temperatures it should be notably increased [371,378]. According to Fig. 55, a huge increment in ultimate tensile strength could be achieved in NS Fe (as compared to CG one - see Curve A) when the grain size is decreased down to 200 nm. The high strength (more than 1.6 GPa) provided by the additional athermal grain boundary strengthening can be comparable to some high-strength steels [368]. It is even more impressive that the ductility of NS Fe at 77 K exceeds the ductility of Fe in CG state. Fig. 56a and b demonstrate that the materials are tested under the same conditions. The NS Fe in Fig. 56a has the ductile features on the fracture surface as compared to CG Fe in Fig. 56b with its cleavage features. The nanostructuring advantages for bcc materials at cryogenic

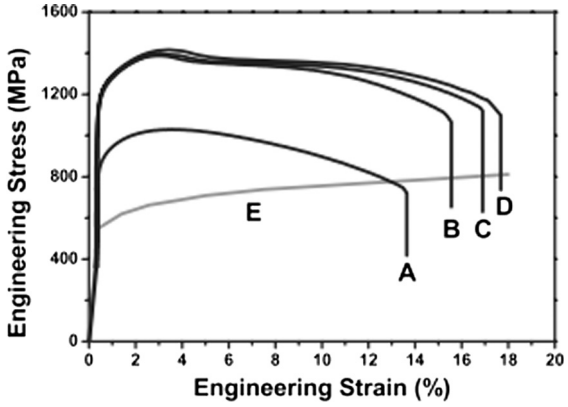

Fig. 54. Engineering stress-strain curves of nanostructured Ti. Curve A is obtained from RT testing at strain rate of 1×10^{-3} s^{-1}. Curves B–D are for the same Ti tested at 77 K, for strain rates of 1×10^{-3} s^{-1}, 1×10^{-2} s^{-1}, and 1×10^{-1} s^{-1}, respectively. For comparison, Curve **F** shows the behavior of Ti over the initial 18% of strain at 77 K.

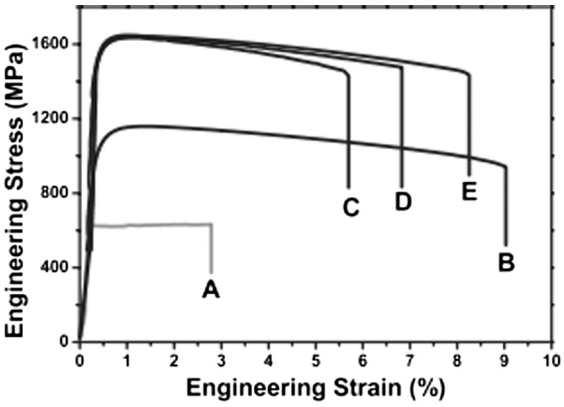

Fig. 55. Engineering stress-strain curves of nanostructured Fe. Curve B is obtained from testing at RT at strain rate of 1×10^{-4} s^{-1}. Curves C–E are for the same Fe tested at 77 K, for strain rates of 1×10^{-4} s^{-1}, 1×10^{-3} s^{-1}, and 1×10^{-1} s^{-1}, respectively. Curve A is for a coarse-grained Fe tested at 77 K and 1×10^{-4} s^{-1}, used here as a comparison to show its inferior strength and ductility.

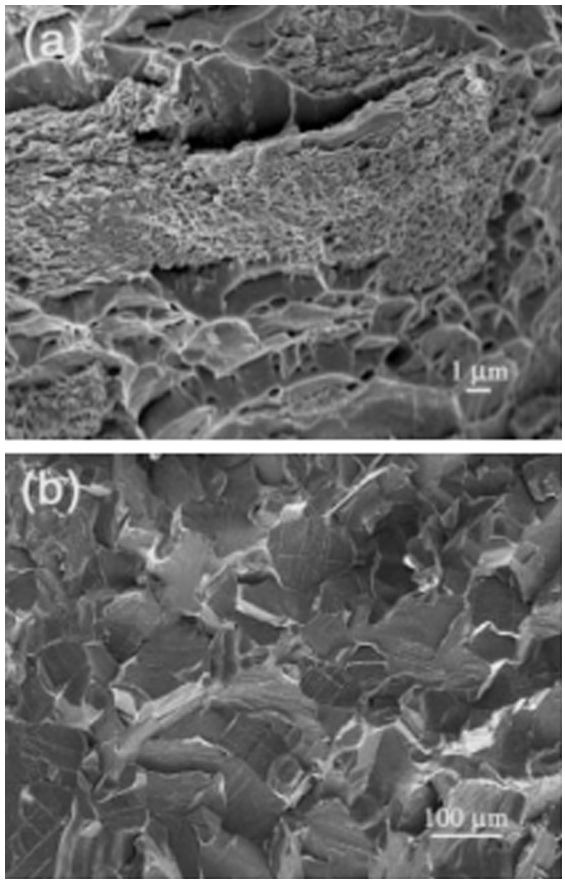

Fig. 56. Scanning electron micrographs of the fracture surfaces. (a) Nanostructured Fe after tensile test at 77 K and 1×10^{-2} s^{-1} shows ductile features on a fine scale, in contrast with the cleavage fracture features in (b) for coarse-grained Fe tested under the same conditions.

temperatures are also worth mentioning. The difference of bcc materials from hcp or fcc ones is that the strain hardening behavior does not significantly depend on temperature or strain rate effects [378].

The above reported results have demonstrated that the combination of drastically enhanced strength and reasonable ductility make the NS materials promising candidates for low-temperature applications regardless of their crystal lattice type.

5.4. Using stacking faults to enhance ductility

For fcc metals with very low SFE, large quantity of stacking faults will be generated during plastic deformation via slip of partial dislocations or dissociation of full dislocations. One example is shown in Fig. 52c in which high density of stacking faults were formed between twins [362]. Some of the stacking faults may be converted into thin twins when another partial dislocation glides on an adjacent slip plane. The stacking faults increase strain hardening by several mechanisms. First, the accumulation of stacking faults will increase the strain hardening in the same way as the accumulation of dislocations. In other words, high density of stacking faults makes it more difficult for partial dislocations to slip to form more stacking faults. Second, stacking faults are planar defects and can effectively block dislocations from different slip systems, forcing them to interact with the stacking faults, which requires higher applied stress. Note that some partial dislocations can effectively cut a stacking fault, which produces two partials to slip to eliminate the stacking fault just like what occurs in detwinning [13,159,314]. It should also be noted that in fcc metals stacking faults are not as effective as twins in blocking and accumulating dislocations. Third, stacking faults from different slip systems may interact with each other and divide the large grains into smaller domains. It has been reported that in low SFE 304 stainless steel, partial slips may be accompanied with martensitic phase transformation, which forms parallelepiped domain walls to block the slip of other dislocations [379,380].

More importantly, when a dissociated dislocation meets another one, a Lomer-Cottroll lock might form. For example, as shown in Fig. 57, a dislocation with Burgers vector **BD** glides on slip plane BCD is dissociated into two partials, **BD** → **Bα** + **αD**, with a stacking fault ribbon between them. Another dissociated dislocation **BA** → **Bδ** + **δA** is on the ABC plane. When the leading partial **Bα** of the dislocation **BD** meets the stacking fault ribbon of the dislocation **BA**, it may react with the stacking fault and cross-slip to the ABC plane under appropriate applied stress: **Bα** → **Bδ** + **δα.** Partial **Bδ** slips to the left to erase the stacking fault and to form a dissociated dislocation **BA**, while a Lomer-Cottroll lock is formed, as shown in the right part of Fig. 57c. Lomer-Cottroll locks are stationary and can act as effective barriers to block and accumulate dislocations. For example, high density of Lomer-Cottroll locks have been believed responsible for the observed strong strain hardening in cold-rolled nanocrystalline Ni [381], which should result in enhanced ductility.

It should be noted that there is so far very little report on how the stacking faults affect the strength and ductility of nanostructured fcc metals. This is because in fcc metals, the formation of stacking faults are often accompanied with the formation of deformation twins and it is impossible to clearly differentiate their individual contributions. Therefore, the observed mechanical behaviors are often attributed to deformation twins. However, according to the above discussion,

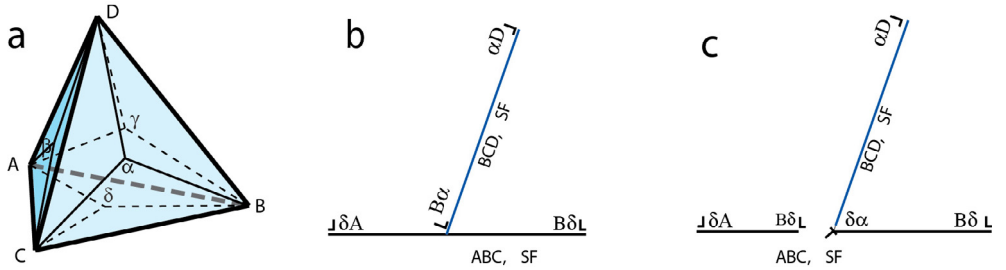

Fig. 57. (a) Thompson Tetrahedron for an fcc metal. (b) A dissociated dislocation BD on the BCD plane meets the stacking fault ribbon of BA on the ABC plane. (c) A Lomer-Cotroll lock is formed after the partial Bα interacts with BA stacking ribbon and cross-slip onto the ABC plane.

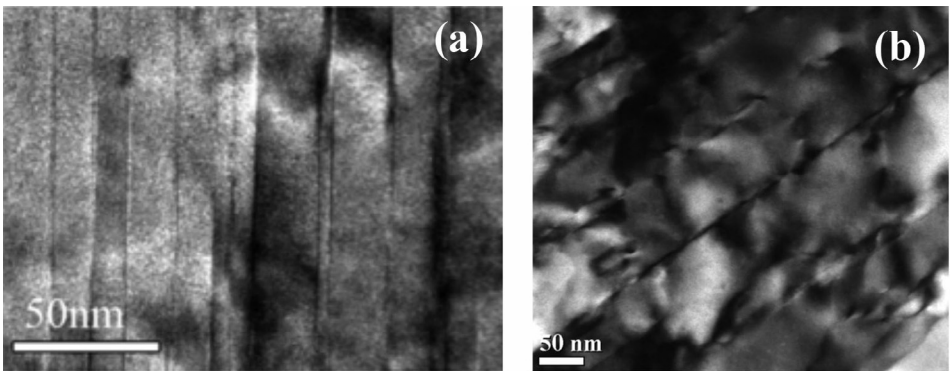

Fig. 58. (a) TEM image of high density of stacking faults on the basal plane in a Mg alloy. (b) After tensile deformation, dislocations are accumulated at stacking faults [122].

stacking faults should in no doubt have positive effect on the strength and ductility of NS metals and alloys. As discussed below, the effect of stacking faults on the strength and ductility is clearly demonstrated in NS hcp metals.

For CG hcp metals, deformation twinning is usually activated when the plastic strain reaches a certain critical value, due to the lack of sufficient slip systems [13]. However, as the grain size becomes smaller, twinning becomes more difficult [13,119,161]. Therefore, deformation twinning, which is effective in simultaneously increasing the strength and ductility of NS fcc metals, is not available for NS hcp metals. Fortunately, it was found in an UFG Mg alloy that stacking faults are effective in blocking and accumulating dislocations (see Fig. 58), which are similar to twin boundaries. The high density of stacking faults consequently produced high strength and good ductility [122,123]. The key to producing high density of stacking faults is to lower the SFE on the basal plane. For Mg, some alloy elements, such as Y, Fe, Gd, are effective in reducing SFE according to *ab initio* calculation [126].

5.5. High strength and good ductility of heterostructured metallic nanomaterials

NS metals and alloys have been studied for over thirty years since it is first proposed conceptually by Gleiter in 1981 [299]. NS metals typically have very high strength as compared to their CG counterparts, but their low ductility has been a major challenge to overcome although various strategies have been developed to improve the ductility, as discussed in other sections of this paper.

In our textbooks and in practice, it is often desired to have a relatively uniform microstructure in metals and alloys. For example, abnormal grain growth where some grains grow much larger during the recrystallization of cold-worked metals is considered bad for mechanical properties. Recently, it was found that microstructure heterogeneity could have surprising advantages. For example, heterostructured materials with NS and CG domains can have a strength and ductility combination that is not obtainable by homogeneous materials [366,382–386]. The length scale of the heterogeneity could be in the micrometer range or in some cases could be comparable to the component dimensions. The high mechanical incompatibility between domains leads to strain gradient near their interfaces/domain boundaries, which need to be accommodated by geometrically necessary dislocations [387,388]. Geometrically necessary dislocations have the same Burgers vector and will produce a long-range stress field, i.e. back stress, which leads to back stress hardening to increase yield strength. In addition, the back stress may increase with strain, i.e. back stress strain hardening, to produce higher ductility. Therefore, heterostructures may produce a combination of high strength and good ductility. The back stress in heterostructured materials can be best calculated from unloading/reloading curves (see Fig. 59) using the following equation:

$$\sigma_b = \frac{\sigma_r + \sigma_u}{2} \tag{16}$$

where σ_u and σ_r are the unloading and reloading yield stresses, respectively, as defined in Fig. 59. The σ_u and σ_r can be determined by a preset derivation of the slope from the linear apparent Young's modulus ($E_u = E_r$) [388].

Heterostructured materials can be further classified into different types according to their micro and macro structural features, including gradient structure, heterogeneous lamellar structure, laminate structures, harmonic structures, etc. Below we will discuss the gradient structures and heterogeneous lamella structure in details and also other heterostructures briefly. The common fundamental thread of these heterostructures is the mechanical incompatibility between different heterogeneous domains. Their differences are in their sizes, geometries and distribution of the heterogeneous domains.

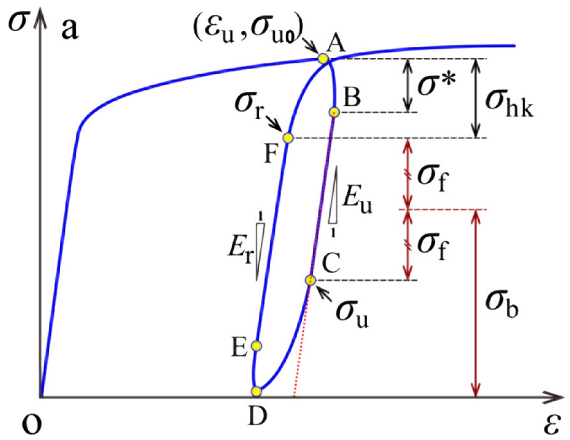

Fig. 59. The Schematic of the unloading-reloading for defining the unload yielding σ_u, reload yielding σ_r, back stress σ_b and frictional stress σ_f, effective unloading Young's modulus of E_u, effective reloading Young's modulus of E_r.

5.5.1. Gradient structured materials

One type of heterostructures is gradient structure, which is characterized with a macroscopic structural gradient from the sample surface along the depth. The structural features that exhibit gradients at macroscopic scale could be grain size, density of crystalline defects such as dislocations, twins and stacking faults, second-phase particles, texture or a combination of them. Fig. 60 shows a grain size gradient typically produced by surface mechanical attrition treatment (SMAT) [389]. Importantly, the SMAT approach is conducive to large-scale industrial production, which makes it relevant to real world applications. SMAT also produces a texture gradient although its effect on mechanical properties is not well studied [389].

The gradient structured materials have a built-in intrinsic mechanical incompatibility during deformation. The deformation of a gradient-structured sample during a tensile testing can be classified into three stages. In Stage I**,** the gradient-structured sample will deform elastically when the applied strain is very small, as illustrated in Fig. 61A. With increasing applied strain, the coarse-grained central layer starts to deform plastically (Stage II, Fig. 61B), in which the plastically deforming central layer and the elastically deforming nanostructured layers co-exist. The plastically deforming layer has an apparent Poison's ratio of 1/2, while the elastic layer has a Poison's ratio of ~1/3 for most metals. In other words, the plastically deforming central layer will contract laterally more than the elastically deforming outer layers. This causes incompatibility in the lateral direction (x-direction) to convert the applied uniaxial stress into bi-axial stresses. Logically, there exist two elastic/plastic interfaces, which dynamically move toward the sample surface with increasing applied strain. Note that the applied strain is uniform across the sample thickness. However, there exists a stress gradient in the plastically deforming zone because of variation in strength and flow stresses in different layers. This stress gradient should contribute to higher yield strength and consequently produce a synergetic strengthening [383,390,391]. In addition, strain gradient exists at least in the lateral direction, which should cause back stress to raise the yield strength [387,388].

In Stage III the whole sample deforms plastically. It is well known that nanostructured materials have low mechanical stability, which usually start necking at very low plastic strain [1,7,129,165,281,287,290,297,299,360,376,392–400]. As discussed earlier, necking is caused largely by the low strain-hardening in nanostructured materials [13,69,70,129,297,358,376,381,395,401,402]. The surface layers of sample undergo unstable necking first, which makes them contract quickly in the lateral direction (see Fig. 61C). However, the necking is constrained by the stable coarse-grained central layer, which develops another type of internal mechanical incompatibility. A steep strain gradient develops near the interfaces of the unstable necking layers and the central stable layer [382,383]. This will promote the accumulation of geometrically necessary dislocations and the development of back stress [403–408], which consequently increases strain hardening. In addition, the two necking/stable interfaces dynamically migrate from the sample surfaces toward the central layer, leaving in its wake high density of dislocations. This causes a steep upturn in strain hardening rate and consequently higher ductility in the gradient structured metal.

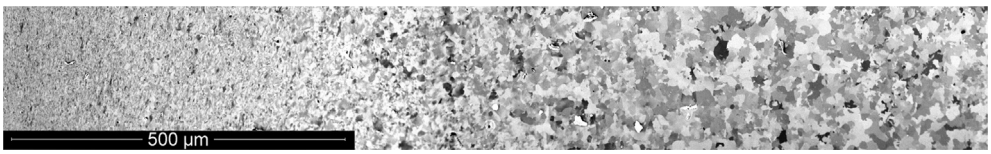

Fig. 60. Schematic illustration of microstructural characteristics along the depth in the surface layer subjected to SMAT.

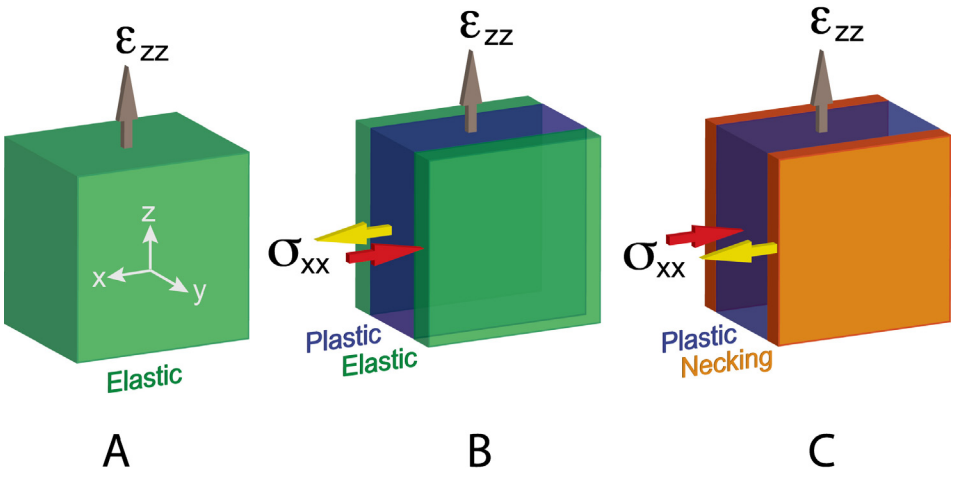

Fig. 61. Schematic of the change of stress state during tensile testing of graded structure. (A) Stage I; (B) Stage II; (C) Stage III. The yellow and red arrows represent tensile and compressive stress in the x direction, respectively.

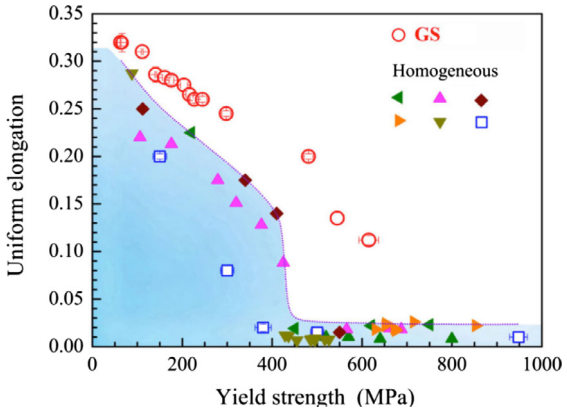

Fig. 62. Strength and ductility in the gradient structured (GS) IF steel as compared with their homogeneous counterparts.

The gradient structure has been found to be capable of producing high strength with good ductility that is not obtainable by homogeneous structures (see Fig. 62) [382]. As shown, when the homogeneous IF-steel is deformed to increase strength, its ductility drops dramatically, especially when the strength is above 400 MPa [409–413]. In contrast, the gradient-structured (GS) sample has much higher ductility than homogeneous nanograined structures in the strength range of 450–600 MPa.

In addition, gradient structures can also be combined with other strategies such as the twinning induced plasticity (TWIP) effect [366] and transformation induced plasticity (TRIP) effect to further improve the strength and ductility [414].

5.5.2. Heterogeneous lamella materials

Although gradient metals have superior combinations of strength and ductility (see Fig. 62), there is still a tradeoff between the strength and ductility. In other words, the strength of a gradient material is lower than its UFG counterpart, and its ductility is lower than its CG counterpart. It has been a dream for materials scientists and engineers to avoid this strength-ductility tradeoff, which is believed impossible according to our textbook and literature data.

At room temperature, most metals and alloys have low strain rate sensitivity and strain hardening is the primary factor in determining the uniform ductility according to the Considère criterion: $d\sigma_t/d\varepsilon_t \geqslant \sigma_t$, where σ_t is the true stress and ε_t is the true strain. This equation means that metals with high strength need high strain hardening to prevent unstable deformation (necking). However, as discussed earlier, NS metals have lower strain hardening due to their small grain sizes. Therefore, it has been believed hopeless and impractical to produce high ductility in NS metals comparable with that of their CG counterparts [30,387].

It was reported recently that heterogeneous lamella (HL) Ti can have the strength of UFG Ti and the ductility of CG Ti (see Fig. 63a) [387]. As shown, all HL Ti samples have significantly higher strength than the CG Ti and also to different extent higher ductility, which is unprecedented. Furthermore, as shown in Fig. 63b, the strain hardening in the HL60 sample is higher than that in the CG Ti, which is the reason for its high ductility. UFG and NS metals usually have much lower strain hardening than their CG counterparts [69,387]. These observations contradict our conventional understanding on the strength and ductility of metals and alloys.

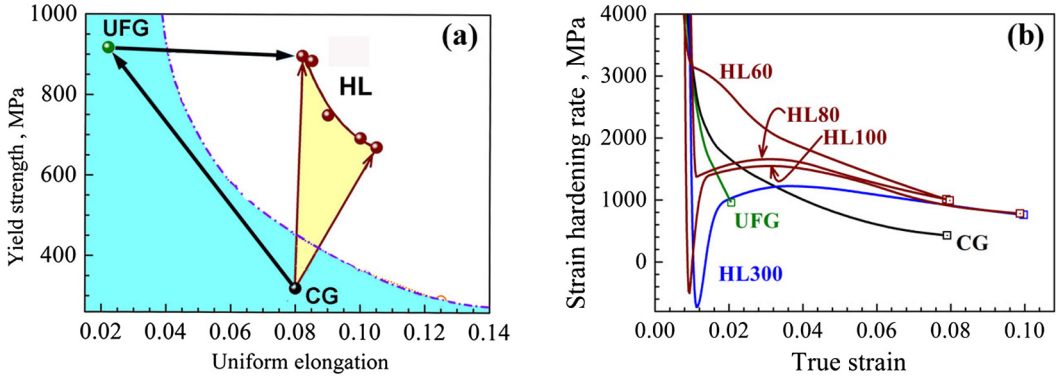

Fig. 63. (a) Heterogeneous lamella (HL) Ti has both the high strength of ultrafine grained (UFG) Ti and the ductility of coarse-grained (CG) Ti. (b) HL Ti shows higher strain hardening than the CG Ti after some plastic strain or even in the entire strain range (HL60).

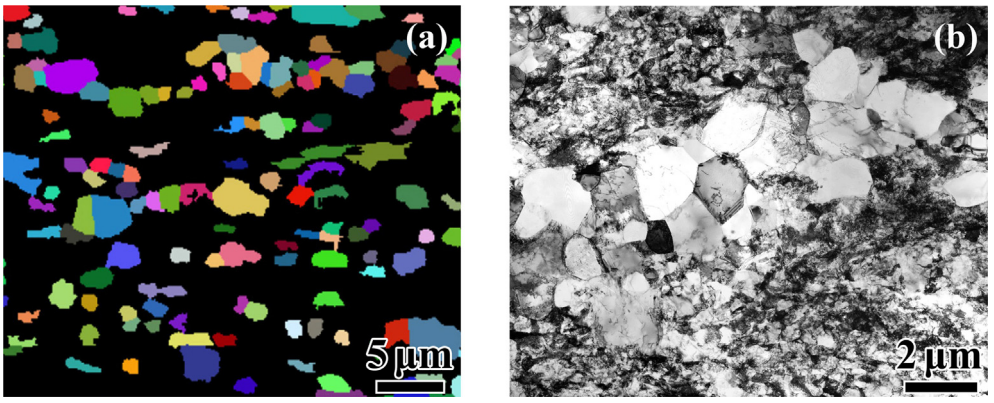

Fig. 64. (a) EBSD image of recrystallized grains (average diameter = ~4 μm) embedded in the UFG matrix with grain sizes below 1 μm, which is blackened out). (b) TEM micrograph of typical interfaces between the recrystallized grain lamellae and the UFG matrix.

The HL60 sample contains 25 vol% of large recrystallized grains with an average diameter of ~4 μm, which are embedded in the UFG grain matrix (see Fig. 64) [387]. The question arises why adding 25 vol% of larger grains into the strong UFG matrix does not lower its strength. This was attributed to the high back stress caused by the unique structure in which the softer recrystallized lamellae are totally surrounded by the hard matrix and therefore cannot deform freely until they build up enough back stress to force the harder matrix to deform together with them. In other words, the unique structure makes the softer lamellae almost as strong as the harder matrix. In addition, during the subsequent plastic deformation, the softer lamellae sustained much higher plastic strain than the harder matrix, i.e. there is a significant strain partitioning. This consequently causes significant strain gradient near the lamella interfaces, which is accommodated by geometrically necessary dislocations to build up back-stress hardening, especially in the early stage of plastic deformation. This back-stress hardening is higher than the conventional work hardening caused by the accumulation of forest dislocations and is primarily responsible for the observed extraordinarily high strain hardening and the high ductility [387]. These new fundamental understanding provides a new paradigm in designing metals and alloys for high strength and high ductility.

5.5.3. Other types of heterostructured materials

There are several other types of heterostructured materials that exhibit superior strength and ductility due to the mechanical incompatibility, including the harmonic-structured materials in which the CG core are separated and surrounded by NS shells as schematically illustrated in Fig. 65 [415–417], dual phase steel [418–423], laminate structured materials [424,425], bi-modal and multi-modal structured materials [24,373,401,426,427], hybrid materials [428–431], etc. Although not explicitly stated in most of the original publications, the common feature of these materials is that there exist domains with very different flow stresses (mechanical incompatibility). These domains are forced to coordinate with each other to deform together, which produces a large strain gradient across their boundaries. These cause the pile up of geometrically necessary dislocations, which produce a high back stress. During the plastic deformation, strain partitioning happens where

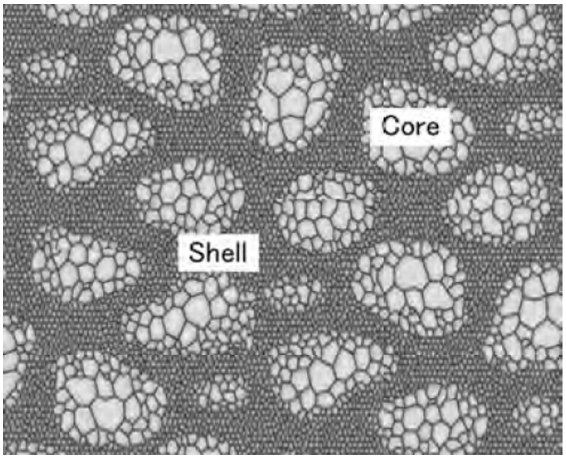

Fig. 65. Schematic illustration of the harmonic structure [415].

the softer domains sustain much higher plastic strain, which in turn produces larger strain gradient with increasing applied strain and consequently back-stress strain hardening to enhance ductility.

It can be argued that the conventional composite materials are also heterostructured materials. If the composite is metal based, they can indeed be considered in the scope of the heterostructured materials discussed here. Otherwise, they are beyond the scope of the heterostructured materials discussed here.

5.6. Improving strength and ductility by precipitation-hardening

Considering the low strain hardening in NS materials is originated from limitation to accumulate dislocations and other defects, the strategy is based on introduction of the nanostructural elements to increase accumulation of dislocations [432]. This phenomenon was observed in the UFG Al–10.8Ag (wt%) alloy [394] produced by ECAP and additional thermal treatment. Fig. 66 demonstrates application of this strategy for the alloy, where the Vickers microhardness is shown as function of the aging time at 373 K for the samples treated to solid solution (ST) and processed by ECAP and by rolling at RT [394]. The initial hardness in ST state value was relatively low, however aging lead to the increase is observed with the maximal value corresponding to aging for 100 h. After cold rolling, one could observe increase in hardness which insignificantly changed after aging. The ECAP-processed specimens demonstrated even higher hardness, which gradually elevated with aging with a maximal value corresponding to 100 h. The studies have shown that the relatively lower values of hardness registered after cold rolling as compared to ECAP result from relatively less values of strain ($e \sim 1.4$ and 8 respectively) providing less effective microstructural refinement. The microstructure after rolling was formed mostly by subgrains and cells divided by low-angle boundaries. Using scanning transmission electron microscopy (STEM), the reason for the maximum hardness observed after ECAP followed by 100 h of aging was provided by intensive precipitation processes. The intragranular spherical precipitates with the diameter of about 10 nm represented by η-zones and elongated γ′ particles 20 nm long were observed. Further aging up to 300 h gave raise to γ″ precipitates while the fraction of η-zones decreased. This process lead to decreasing hardness with the aging performed for over 300 h (see Fig. 66). Mechanical properties are also subject to change due to annealing after ECAP (see Fig. 67), where the tensile stress-strain curves for the specimens processed by ECAP, ST, cold rolling and ECAP followed by aging are given [394]. One can see that ST and artificial aging give an enhanced tensile strength and reasonable uniform elongation while cold rolling followed by aging provides essential strength growth but the ductility parameters are poor. ECAP without aging also resulted in high strength but no visible strain hardening and reduced uniform elongation. In distinction from that, the material subjected to ECAP and subsequent aging for 100 h demonstrates high yield stress, marked strain hardening region and reasonable elongation to failure. Indeed, the specimens produced by ECAP and aging are characterized by similar level of uniform deformation exhibited by those produced by ST and aging as well as the total elongation to fracture. It testifies that the strength and ductility of precipitation-hardened alloys can be considerably enhanced by SPD and post-deformation heat treatment. Moreover, despite the fact that the results presented in Figs. 66 and 67 were reported for a model Al–Ag alloy, one may assume that it is possible to obtain similar results in commercial alloys for engineering applications where the aging treatments are generally well documented. As it will be shown in Section 6, this approach was similarly successful when applied to commercial Al alloys, i.e. AA7075 [29,70,433], AA2024 [434] and others [28].

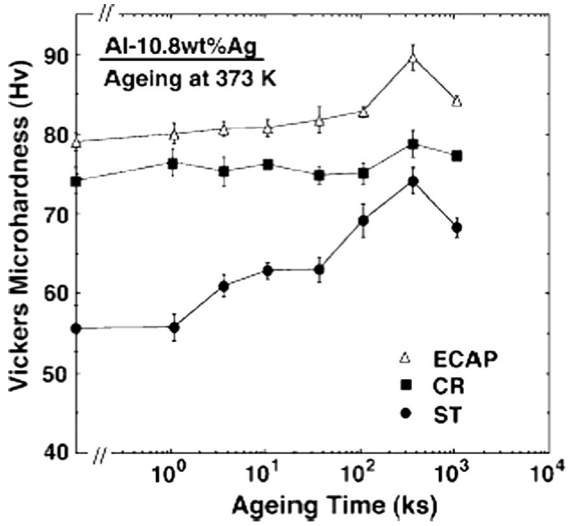

Fig. 66. Dependence of the Vickers microhardness as function of aging time for the Al–10.8% Ag alloy after solution treatment (ST), cold-rolling (CR), and ECAP [394] .

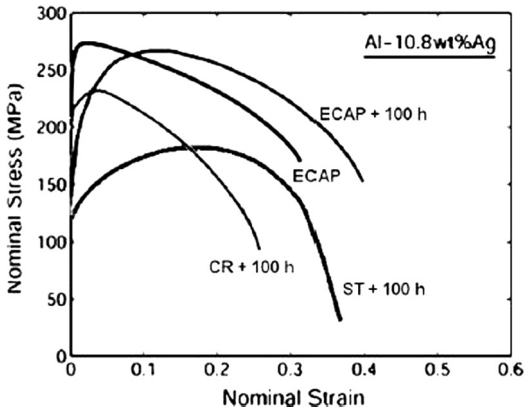

Fig. 67. Nominal stress-strain curves at room temperature for the Al–10.8% Ag alloy after solution treatment (ST), cold-rolling (CR) with aging at 373 K for 100 h, ECAP without subsequent aging and ECAP with aging at 373 K for 100 h [394].

5.7. Optimizing the strength and ductility of nanostructured metallic composites containing carbon nanotubes and graphene sheets/nanoplatelets

NS-metal-matrix nanocomposites containing carbon nanotubes (CNTs) and graphene nanoinclusions have been recently reported effective in improving the strength and ductility of NS materials. The rationale behind this strategy is that CNTs and graphene have very high tensile strength and elastic moduli [435–437] so that their presence in low quantities can significantly increase the strength through load transfer from the matrix to reinforcement. The load transfer mechanism, in parallel with Orowan looping of lattice dislocations at CNTs and their stoppage at graphene nanoinclusions, can significantly enhance strength in conventional CG metal-matrix nanocomposites containing CNTs and graphene nanoinclusions; see, e.g., reviews [438–441]. Besides, carbon nanoinclusions are often located at GBs in metal matrixes where these nanoinclusions impede GB migration/grain growth during material synthesis [439–441]. In contrast, pure metals fabricated in the same conditions can exhibit a substantial grain growth accompanied by a decrease in their strength. Thus, the materials can retain fine grains due to CNTs and graphene nanoinclusions. In addition, thermal mismatch between the metal matrix and reinforcement can generate geometrically necessary dislocations whose stress fields can contribute to strengthening.

Note that, with the afore-discussed hindering effects of CNTs and graphene on dislocation slip in the metal matrix, the reinforcement of CG metals through insertion of CNTs and graphene nanoinclusions typically leads to a significant decrease in ductility [438–441]. At the same time, lattice dislocation slip is limited in NS metals so that the suppressing effects of Orowan looping of dislocations at CNTs and their stoppage at graphene nanoinclusions on dislocation-mediated plasticity are expected to be limited in NS-metal-matrix nanocomposites reinforced by CNTs and graphene. In these circumstances, CG- and NS-metal-matrix nanocomposites reinforced by carbon nanostructures have difference in the deformation behavior, and NS-metal-matrix nanocomposites may exhibit a good combination of strength and ductility.

Li et al. [442,443] reported high strength and enhanced compressive plasticity of NC Cu reinforced by multi-walled CNTs. This nanocopper-CNT nanocomposite was fabricated through ball milling, powder consolidation and HPT. The resultant nanocomposite has a NC copper matrix with an average grain size ≈22 nm and contains 1 wt% CNTs. CNTs are observed in both GB regions and grain interiors. Under nanopillar compression tests (effectively exploited in mechanics of metallic nanopillars; see, e.g., [444,445]), the nanocomposite demonstrates high plasticity with fracture strain $\varepsilon_f \approx 0.29$, pronounced strain hardening and a large strength ≈1700 MPa. The nanocomposite containing 1 wt% CNTs shows substantially enhanced strength and almost the same plasticity, as compared to those of its unreinforced counterpart.

From a microscopic viewpoint, Li and co-workers [442,443] revealed the two main enhancing effects of CNTs on strength of the nanoCu-CNT composite. First, CNTs hinder motion of dislocations in nanograins (whose sizes are typically larger than $d_c \approx$ 10–15 nm in Cu, in which case the dislocation slip is dominant in these Cu nanograins). Second, CNTs modify dislocation-controlled grain refinement processes in HPT-processed Cu and suppress GB migration so that a mean grain size ≈22 nm in the nanoCu-CNT composite is significantly smaller than that (≈29 nm) in its unreinforced counterpart.

Strain hardening can be responsible for good plasticity demonstrated by the nanoCu-CNT composite, although its effect is not pronounced in compressive load. The role of CNTs in strain hardening is logically attributed to the fact that dislocations are blocked and thereby intensively accumulated at Cu-CNT interfaces. The stress fields of such blocked dislocations contribute to strain hardening.

We now discuss ductility of NS-metal-matrix nanocomposites with multi-walled CNTs. The experimental data in this area vary rather widely [446–448]. Asgharzadeh et al. fabricated Al - 3 vol pct CNT nanocomposites with Al grain size ≈65 nm, using room-temperature HPT consolidation of Al/CNT powders initially processed by mechanical milling [447]. In tensile test, this nanocomposite demonstrated a considerable increase (by tens of percent) in strength and hardness at the expense of a drastic (by nearly 10 times) reduction in fracture strain, as compared to its pure Al counterpart. Asgharzadeh et al.

attributed the low ductility to the role of CNTs and especially their agglomerates as stress concentrators initiating intensive strain localization and crack nucleation [447].

In the experiment [448], UFG Ni-CNT nanocomposites were fabricated using spark plasma sintering of Ni-CNT powders. Tensile tests showed comparable fracture strengths between the Ni–CNT nanocomposites and the unreinforced UFG Ni, whereas the former exhibited smaller fracture strain than the latter [448].

Thus, the experiments [447,448] revealed no advantages of CNT reinforcement for optimization of strength and ductility of NS metals under tensile load. More promising results have been obtained by Choi with co-workers [446]. With hot rolling of ball milled composite powders, they fabricated nanocomposites that are reinforced by CNTs and have Al matrixes characterized with various grain sizes, namely composites A, B, C and D having average grain sizes ≈65, 73, 150 and 250 nm, respectively. In tensile tests, the nanocomposites A, B, C and D exhibit both increase in strength and decrease in fracture strain with increasing volume fraction of CNTs; see stress-strain dependencies in Fig. 68. For comparison, Fig. 68 presents also the stress-strain curve of the un-milled monolithic Al consolidated under the same rolling condition as the composite C with an average grain size of 150 nm. At the same time, for several nanocomposites under examination, values of fracture strain are in the functional range (>5%) for engineering materials under tension (Fig. 68). For instance, the nanocomposites D with the CNT fractions 1.5 and 3% are characterized by a rather good fracture strain ≈ 13% and ultimate stress values ≈ 350 and 460 MPa, respectively (Fig. 68d). The nanocomposite D with the CNT fraction 4.5% have both a functional fracture strain ≈7% and remarkable high ultimate stress ≈500 MPa (Fig. 68d). The latter value is nearly 2.5 times larger than that of unreinforced Al.

In the situation under discussion, the key strengthening mechanisms are suggested as the load transfer and grain size strengthening [446]. The nanocomposites C and D with comparatively large grain sizes ≈150 and 250 nm, respectively, show higher ductility than the nanocomposites A and B with very small grain sizes (Fig. 68), because the dislocation accumulation and thereby strain hardening occur more easily in large grains.

Thus, using CNTs as reinforcing elements in NS-metal-matrix nanocomposites can be effective in achieving both high strength and functional ductility [442,446]. At the same time, in addition to CNTs, other nanoinclusions can be exploited in enhancement of the mechanical properties of metals. In search for reinforcing fillers in metal-matrix nanocomposites, one can list the following key requirements [441]:

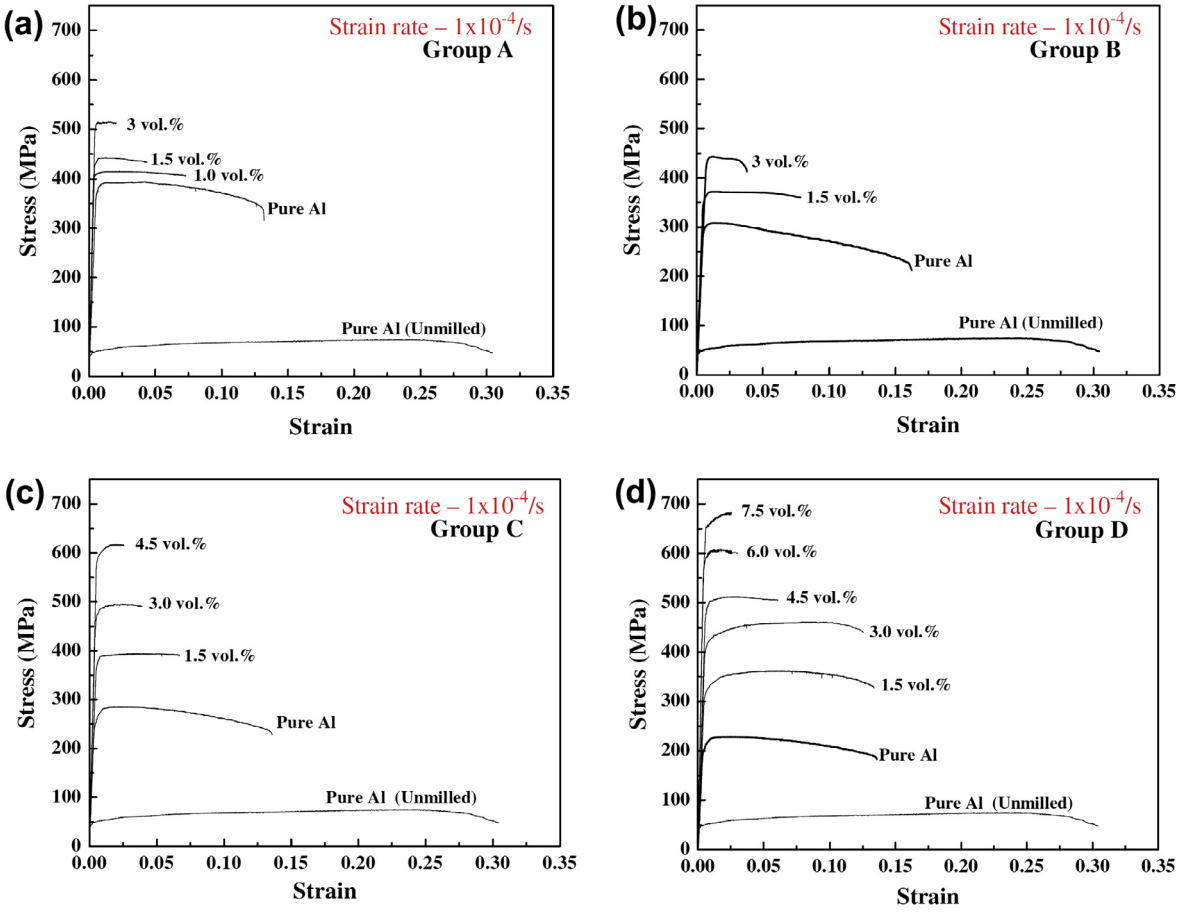

Fig. 68. Tensile true stress–true strain curves of a NS-metal-matrix nanocomposite specimens [446].

(i) Reinforcing inclusions should have high strength and Young modulus.
(ii) Inclusions should be characterized with high aspect ratio and high surface area.
(iii) Inclusions and metal matrix should have strong bonding.
(iv) Inclusions should be homogeneously dispersed, and their agglomeration should be prevented.

Graphene is a very promising candidate to serve as a reinforcing material in metal-matrix nanocomposites, because of its superior strength ≈130 GPa and huge Young modulus $Y \approx 1$ TPa [436,437], in addition to its 2D geometry responsible for maximum surface-to-volume ratio and typically high aspect ratio. Besides, graphene is cheaper than CNTs having similarly superior mechanical properties. With all these factors, in recent years, a rapidly growing interest has been attracted to fabrication of metal-graphene composites and examinations of their mechanical characteristics; see, e.g., [441,449–458]. However, most attentions have been devoted to nanocomposites with CG metal matrixes. At the same time, there is an impressive example where a NS metallic composite exhibits remarkable mechanical characteristics.

Specifically, with chemical vapour deposition method, Kim and co-workers [459] fabricated Cu- and Ni-graphene nanolayered composites with both superior strength characteristics and substantial plasticity demonstrated in nanopillar compression tests. The composites had the nanolayered structure consisting of metallic (copper or nickel) layers and monolayer graphene between them. Copper-graphene composite solids with metallic (Cu) layer thicknesses $\lambda = 70$, 125 and 200 nm as well as nickel-graphene composites characterized by $\lambda = 100$, 150 and 300 nm were synthesized. With focused ion beam milling, nanopillars having height of 400–600 nm and diameter of 200 nm were fabricated from these composites and subjected to compressive load (Fig. 69).

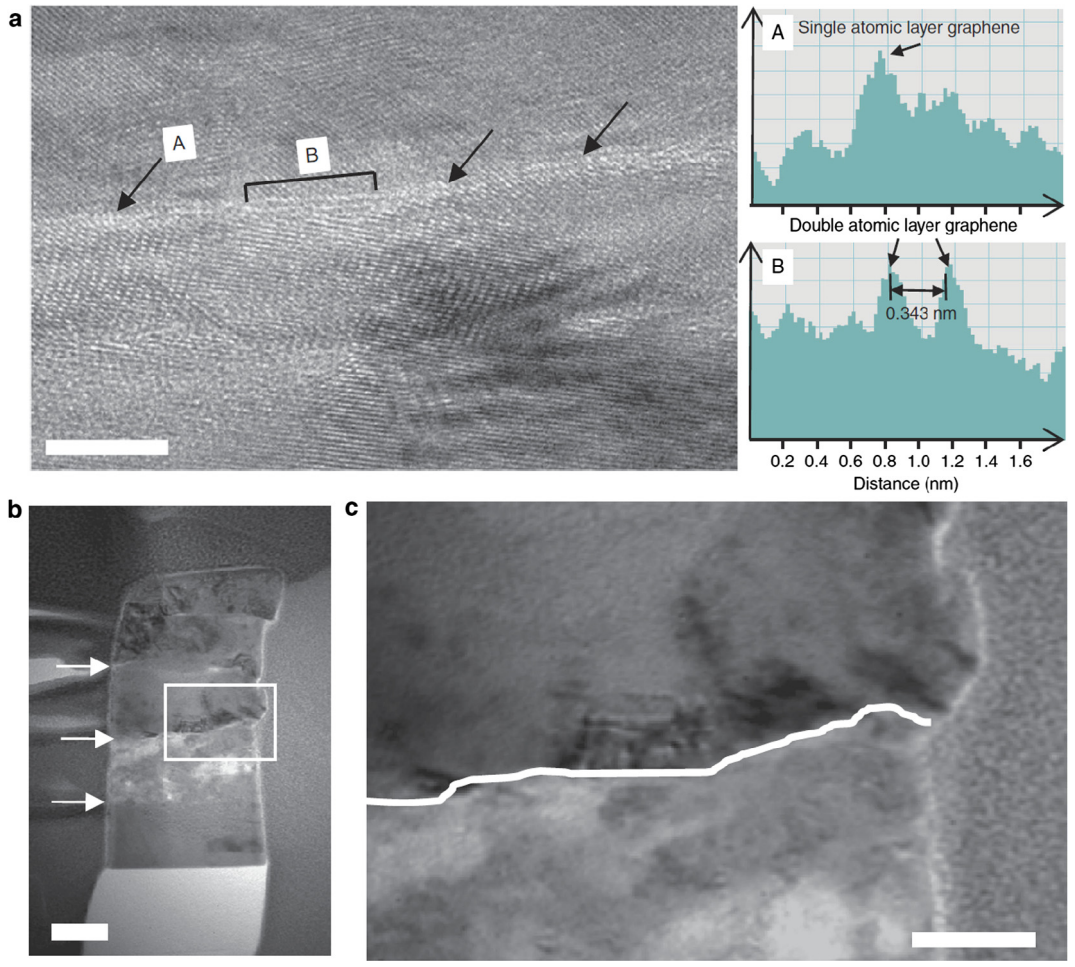

Fig. 69. TEM analysis of the Cu–graphene nanolayered composite. (a) TEM image of a metal–graphene interface that shows mostly single layers with some double layers. Scale bar, 5 nm. (b) TEM image of a Cu–graphene nanopillar with 125-nm repeat layer spacing at a low magnification after deformation. Scale bar, 100 nm. (c) TEM image of a Cu–graphene nanopillar after deformation that shows a higher density of dislocations above the graphene interface. Scale bar, 50 nm [459].

In the nanopillar compression tests, Cu-graphene composites with repeat layer thickness $\lambda = 70$ nm and Ni-graphene composites with $\lambda = 100$ nm showed strengths of 1.5 and 4.0 GPa, respectively [459]. The strengths under consideration are highest for metal-graphene composites.

Typical stress-strain curves for nanopillar compression tests of the Ni- and Cu-graphene composites with various values of λ are presented in Fig. 70a and b. Also, the flow stress at 5% plastic strain as a function of λ, for the Ni- and Cu-graphene composites, is presented in Fig. 70c and d, respectively. These figures show the trend that the flow stress and fracture strain increase in an approximately linear way with diminishing the metal layer thickness λ. In particular, the flow stress has its maximum values of 1.5, for Cu-graphene composite characterized by $\lambda = 70$ nm, and 4.0 GPa, for Ni-graphene composites having $\lambda = 100$ nm [459]. These values are highest for fabricated metal-graphene composites. In particular, the Ni-graphene composite with $\lambda = 100$ nm is characterized by the stress of 4.0 GPa being nearly 52% of the theoretical strength for Ni.

In addition to graphene interfaces, both the nanolayered structure and the nanopillar geometry can significantly contribute to an increase in the flow stress of the composite materials. Kim et al. [459] estimated the strengthening effects of the nanolayered structure and the nanopillar geometry in the case of metal-graphene nanolayered composites on the basis of the corresponding experimental data reported in the literature. He concluded that the strengthening effect of graphene interfaces in the metal-graphene composites is much more significant than the combined effects of both the nanolayered structure and the nanopillar geometry.

The superior strength is inherent to the metal-graphene composites with the nanolayered structure because graphene layers effectively block dislocation slip [459]. This view was supported by the experimental observations of a high density of dislocations that are present in a plastically deformed layer and do not penetrate across a graphene interface between this layer and its neighboring layer free from dislocations in a Cu-graphene nanolayered nanopillar (Fig. 69c).

Thus, the new and effective approach to create metallic nanomaterials with high strength and good ductility (or compressive plasticity) is to implant either CNTs or graphene nanoinclusions in NS metallic matrices. In particular, there are several examples of nanometal-CNT and nanometal-graphene nanocomposites exhibiting enhanced strength and substantial ductility. Note, however, that fabrication of these nanocomposites is in its infancy especially in the case of nanometal-graphene nanocomposites. It is expected that rapid progress will be made in synthesis, fundamental research and technological applications of these nanocomposites.

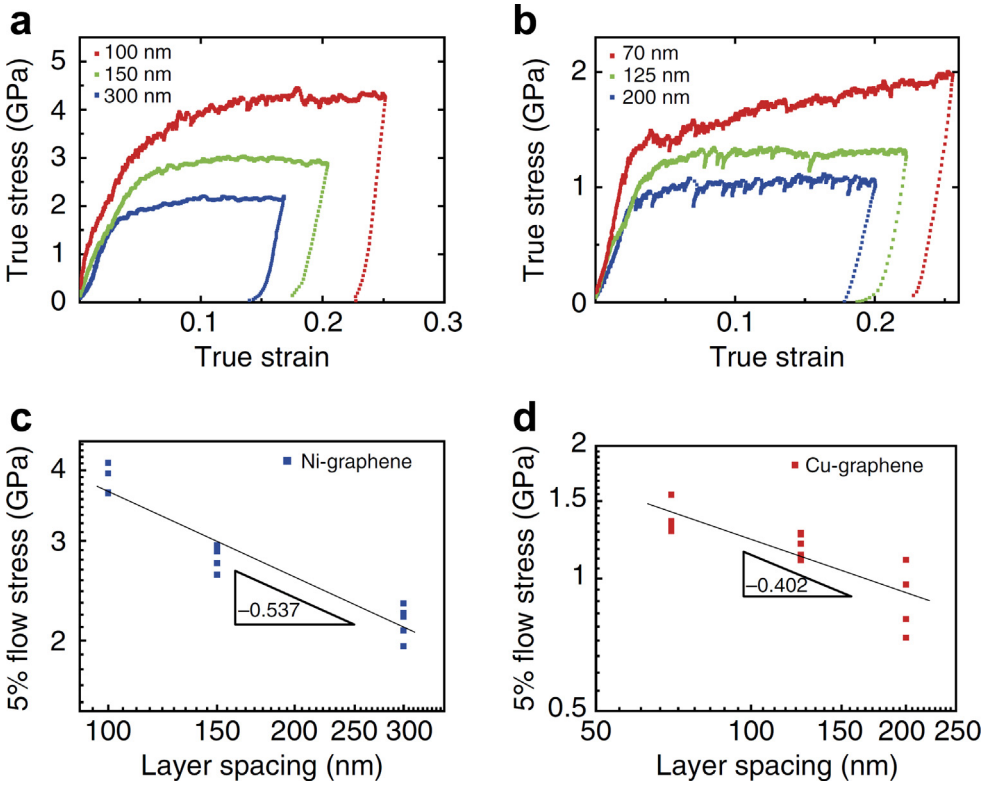

Fig. 70. Results of nanopillar compression test. Stress versus strain curves for (a) Ni–graphene and (b) Cu–graphene of various repeat metal layer spacings. The flow stresses at 5% plastic strain versus repeat layer spacing plots for (c) Ni–graphene and (d) Cu–graphene nanolayered composites [459].

6. Superior strength and ductility in industrial alloys and steels

The aforementioned key strategies for improving the strength and ductility of metallic nanomaterials were generally proposed and developed in pioneering works [29,69,70,129,338,339,348,373] on pure metals and model alloys. In recent years however their successful application was demonstrated on a number of industrial alloys and steels. A few recent examples are presented below in more detail.

The first example is the application of ECAP to obtain high strength and ductility in different Al alloys [394,460]. Kim et al. reported the improvement of the yield strength up to ~630 MPa in the 2024 Al alloy while keeping the considerable ~15% fracture elongation, which was made possible through combination of solid solution treatment, ECAP and post-ECAP low-temperature aging. The influence of aging at low-temperature after ECAP on tensile characteristics of Al–10.8 wt%Ag was studied by Horita et al. [394]. It was demonstrated by HRTEM analysis that work hardening may be improved through the formation of the so-called fine "ŋ-zone" precipitate particles of <50 nm in size, such particles being dispersed in grain interior.

What is common for the above-cited studies is that the second-phase particles were generally or entirely dissolved into a matrix for the oversaturated solid solution, which can be undesirable with a number of Al alloys [434]. For instance, large concentrations of alloying elements in 2024 aluminum alloy lead to a very brittle behavior if all particles of the second-phase (T-phase) are dissolved into matrix, thus grain refinement in the alloys becomes difficult or nearly impossible through SPD processing such as cryo-rolling or ECAP. Moreover, some second-phase particles, if left undissolved, may contribute to dislocation accumulation and grain refinement during SPD. This may in turn increase the strength and ductility via resistance to dislocation slip and trapping due to precipitation of nano-sized second-phase particles in the process of aging.

The above arguments are supported by a study to develop a better procedure for simultaneous increase of strength and ductility in the age-hardening 2024 Al alloys [434], in which the second-phase particles were only partially dissolved while

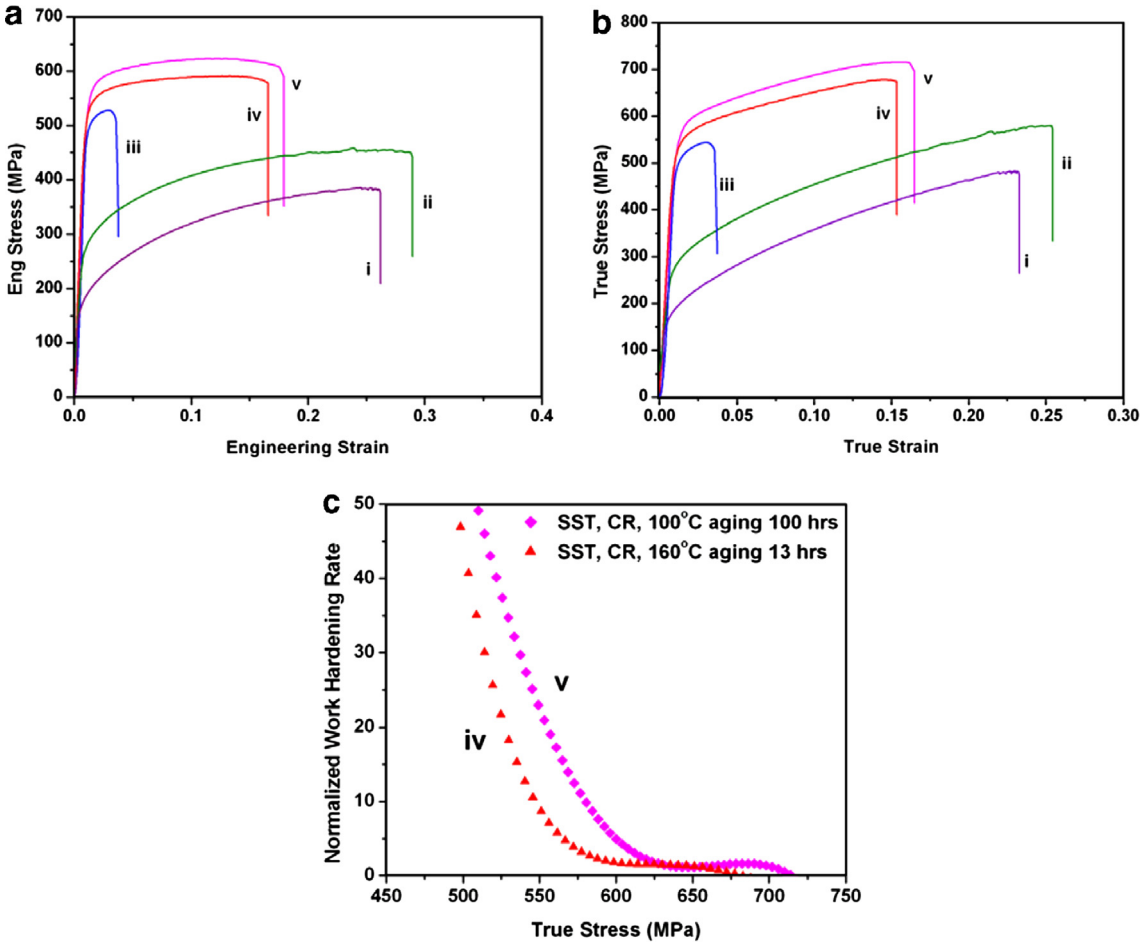

Fig. 71. (a) Ordinary tensile engineering and (b) respective real stress–strain curves of 2024 aluminum alloy under various treatment conditions. (c) Comparison of strain-hardening rate curves of specimens of two kinds. The curves various specimen treatment states: (i) SST at 493 °C; (ii) SST + aging at 160 °C for 10 h; (iii) SST + CR; (iv) SST + CR + aging at 160 °C for 13 h; (v) SST + CR + aging at 100 °C for 100 h [434] .

solution treatment to upgrade processing qualities and promote precipitation of nanoscale second-phase particles. Fig. 71 [434] demonstrates the ordinary tensile stress–strain curves for 2024 aluminum alloy under various treatment states. In accordance to engineering stress–strain curves (Fig. 71a), the specimen has the yield stress value about 150 MPa, and the UTS about 380 MPa. The total elongation consisted of 26% (curve i) after solution treatment at 493 °C for 10 h. SST of specimen (10 h of annealing at160 °C) led to increasing of both the yield stress and the elongation (curve ii). Rolling of a specimen after SST at cryogenic temperature (SST + CR) considerably improved strength, but ductility was reduced to less than 5%, which is ordinary for CR metals (curve iii). Significantly, heating the SST + CR state largely enhanced ductility, whereas subsequent strength enhancement was quite modest (curves iv and v). Heating for 100 h at 100 °C clearly resulted in simultaneous increase in UTS and total elongation (curve v) than aging at higher temperature – for 13 h at 160 °C (curve iv). Yield stress corresponding to curve (v) consists of about 580 MPa, which is three times higher than in the curve (i) and approximately two times higher than in the curve (ii). In addition, the total elongation for the curve (v) measured for the SST + CR + aging at 100 °C state consists of 18% with 13% corresponding to uniform elongation. These values by far exceed those of SST + CR specimens that constitute 3.8% and 3.2%, correspondingly.

SST + CR + aging specimens (curves iv, v) have obvious strain hardening (Fig. 71b) unlike most pure NS metals that frequently demonstrate weak work hardening or even work softening [461–463]. The normalized work-hardening rate, Θ, $\Theta = \frac{1}{\sigma}\frac{d\sigma}{d\varepsilon}$, is plotted as a function of real stress in Fig. 71c. A specimen aged at 100 °C is seen to have higher Θ than that in a specimen aged at 160 °C, thus providing explanation for the higher ductility of the former.

The observed mechanical behaviors were tailored by the 2024 Al alloy microstructures at different processing states. The authors [434] presented systematic precise TEM analyses of the specimens after various treatments to establish the peculiarities of the microstructure including precipitation evolution and precipitation-dislocation interactions to correlate the observed mechanical behaviors with microstructures.

The microstructures after different processing procedures are summarized in Table 2.

The mechanical characteristics of 2024 Al alloys with fine structures at different treatment states are similar to 7075 Al alloy in respective conditions [70,129]. Nevertheless, precipitation strengthening proved to be more efficient to increase the mechanical properties, especially the ductility, in the 2024 alloy than in 7075 alloy. In particular, 2024L alloy when used in case of SST + CR + aging at 100 °C exhibited increased yield strength by SST + CR 2024 alloy sample by 12.4% due to precipitation hardening that is slightly higher than 12% achieved in 7075 alloy [70].

Thus, this study has demonstrated that high density of nanoscale second-phase precipitates as well as low dislocation density are desirable for concurrently achieving high strength and high ductility. The remaining second-phase particles were crucial for producing the high dislocation density in the process of cryo-rolling that consequently contributed to the high density of nanoscale second-phase precipitates. This strategy should be applicable for other precipitation-hardened alloys.

Similar tendency has been revealed in [464], where the aging behavior of 6060 Al alloy was studied in broad ranges of temperature, time, and ECAP strain, the alloy being subjected to ECAP at RT and previously treated in solid solution. High-temperature and short-time aging are shown to be most efficient in simultaneous enhancement of strength and ductility. In contrast to CG material subjected to aging, UTS and homogeneous elongation were increased by ~35% after one extrusion and aging at 170 °C during 18 min. Concurrent recovery and precipitation produce noticeable effect on the ductility enhancement in Al–Mg–Si alloys.

There are also a number of publications on enhancement of strength and ductility in commercially pure (CP)-Ti and its alloys through their nanostructuring by SPD techniques.

In particular, HPT-processed Ti showed the possibility to increase the overall ductility by subjecting an SPD processed sample to a very short-term anneal [167]. The reason for this is that the short-term annealing puts into order interface defect structures, thus making them more equilibrium without any considerable increase in grain size. Furthermore, annealing can also reduce dislocations density in grain interior of a material processed by SPD, therefore suggesting more room for efficient dislocation storage. An enhanced storage capability may increase strain hardening and result in increased ductility. Subsequently, similar results were reported for Ti subjected to ECAP and drawing [343] and Ti after ECAP-Conform and drawing [344].

Table 2
Summary of processing states and microstructures of 2024 Al alloys.

Aging	Al matrix		Precipitates	
	Shape and state	Grain/subgrain size	Small needles and plates	S′: interparticle spacing/density
160 °C, 10 h	Lamellar grains, dislocation recovery	400 nm 800 nm	Al_2CuMg S′ phase, orthorhombic, high density	20 nm/2–2.5 × 10^{15} m^{-2}
160 °C, 13 h	Equiaxed grains, recrystallization	1 μm	Less high density S′ phase	30 nm/1 × 10^{15} m^{-2}
100 °C, 100 h	Large equiaxed grains, recrystallization and grain growth	800 nm 1.5 μm	Higher density S′ phase	1015 nm/4 × 10^{15} m^{-2}

All samples were solution-treated at 493 °C for 10 h and cryo-rolled; all contains remnant orthorhombic T-phase ($Al_{20}Cu_2Mn_3$).

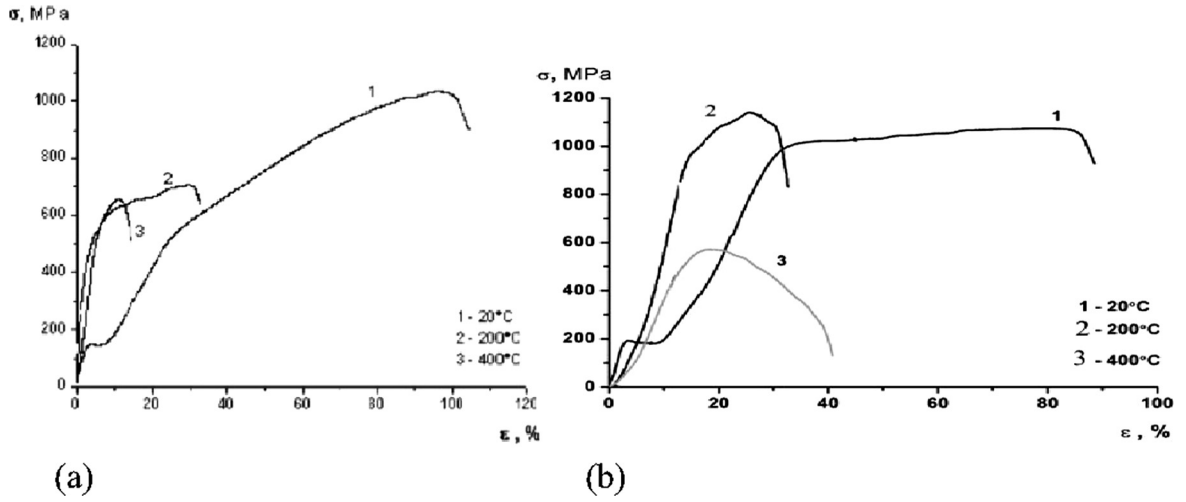

Fig. 72. Engineering stress-strain tensile curves for $Ti_{49.4}Ni_{50.6}$ at different temperatures: (a) CG state; (b) NS state, produced by ECAP [466].

Another example is TiNi alloys, which has exceptional properties including high strength, corrosion resistance, superelasticity and shape-memory effect. Such alloys are especially promising for numerous structural and functional applications in medicine and engineering. Their superelasticity and shape-memory effect are due to B2 to B19′ martensitic transformations (MT) and numerous fundamental investigations have been focused on the study of these two unique properties. At the same time, superior properties of TiNi would be very desirable for various advanced applications due to necessity for product miniaturization and improvement of their functional characteristics. Recent works revealed the efficiency of nanostructuring by SPD processing to enhance the properties of TiNi alloys [465,466].

Fig. 72 shows engineering stress-strain curves of CG and NS $Ti_{49.4}Ni_{50.6}$ alloy measured at different testing temperatures [466]. The stress-strain curves for RT of CG and NS TiNi are most unique with extensive homogenous deformation up to 70–80% but the yield stress values noticeably varies. Furthermore, in both alloys there is the so-called "plateau" credited to MT caused by stress but the stress value (σ_m) of pseudo-yield for NS TiNi notably exceeds those for the CG alloy. Yield stress of NS alloy at 200 °C also exceeds that of the CG alloy by almost twice. The strength of the NiTi in CG and NS states is considerably reduced at 400 °C. Tensile straining of alloy at above 200 °C appears to have not induced martensitic transformation as shown by curves $\delta(\varepsilon)$ of both alloys, without pseudo-yield phase stage. The strengthening stage for both states at 200 and 400 °C is rapidly replaced by a softening and neck-formation stages. Consequently, the total strain to failure for both CG and NS alloys is dramatically reduced.

Unique relationship of high strength with UTS $\geq$ 1200 MPa and high ductility at RT is demonstrated for NS alloy. The results reveal that such ductility is related to the martensitic transformation induced by stress, whereas the increase of strain temperature, while suppressing the martensitic transformation, brings about a considerable decrease of ductility.

Reducing grain size down to nanometer range and controlling the development of martensitic transformation opens up an opportunity for major improvement of both mechanical and functional properties in TiNi alloys that are very promising for applications in medicine and engineering.

Regarding steels, rather interesting investigation was carried out on the microstructure and mechanical properties of T91 steel (modified 9Cr-1Mo steel) subjected to different thermomechanical treatments (TMTs) [467]. ECAP was implemented at different temperatures. Mechanical strength of the steel improves due to ECAP at RT with sacrifice in ductility. Unlike this, the hot ECAP process makes the hardening less pronounced whereas the ductility and work hardening ability are retained. Microstructure analyses show a noticeable reduction of the mean grain size after cold ECAP, whereas hot-ECAP is more efficient to refine and homogenously redistribute the carbide nanoprecipitates. As a result of post-ECAP heat treatment (500 °C/10 h), secondary carbide precipitation is observed in the alloys treated by cold-ECAP, while hot-ECAP processed samples maintain smaller nanoscale carbide precipitates and homogenous microstructure. Such phenomenon was found to explain the evolution of precipitates with the reference to TMT influence.

The above results indicate that the enhanced mechanical strength of ECAP-processed T91steel arises primarily from grain refinement and precipitation hardening. At the same time hot ECAP enables TMT to be a promising method for production of ultrafine-grained steels with high strength and ductility for advanced structural applications.

Another recently developed approach implies multilayer steels for a better combination of high strength and ductility [468]. Multilayer steels have been proposed in response to the demand for a novel route to producing steels with high performance by using steels of high-strength and high-ductility alternatively in a layered structure. The multilayers can be considered as a type of heterostructures [469]. In the corresponding study [468], their development history, design, production, properties and applications are presented. Multilayer steels possess higher combinations of strength and ductility in contrast

to the present monolithic steels and also demonstrate exceptional deformation characteristics under high-strain-rate deformation together with decent formability. Such excellent characteristics in multilayer steels are possible to achieve through enhanced interfacial toughness among layers and reduced thickness of brittle steel layers in accordance with high brittle steel strength and the enhanced fracture toughness of the ductile steel. By varying the combinations of components offers an opportunity to extend the concept of multilayer steels for different types of nanomaterials.

In summary, the results presented in this section testify to the fact that many key strategies of enhancement of strength and ductility can be as well applied to industrial alloys and steels, which confirms that superior mechanical properties can be achieved for these structural materials as well.

7. Structural stability of metallic nanomaterials

Metallic nanomaterials are structurally unstable due to their high GB area per unit volume [299,470]. The ratio of GB area to volume is proportional to 1/d, where d is the grain size. Consequently, with decreasing grain size the total GB energy per unit volume quickly increases in nanomaterials, leading to thermodynamic instability as well as mechanical instability. For example, we have observed grain growth in high-purity Cu processed by ECAP at room temperature. This thermal instability is the reason why the grains of most pure metals such as Al, Cu, Ni and Ti cannot be refined to below 100 nm by SPD techniques such as ECAP. This is because the SPD is a top-down approach, which refines grains from bulk, which can avoid the contamination of the materials. As a result, the GBs are free of impurity to lower the GB energy and to pin the GBs, making the grain growth easy [30]. In contrast, NC metals produced by bottom-up approaches such as consolidation of nano-sized powders synthesized by inert gad condensation (IGC) [2,299,471,472] and electrodeposition [118,385] usually contain impurities such as oxygen and nitrogen which can either separate to GBs or to form oxides/nitrides to stabilize the NC structure.

There are two issues concerning the stability of nanostructures. The first issue is thermally driven grain growth at elevated temperatures, which limits the application temperature of metallic nanomaterials. Their high GB area per unit volume provides high driving force for grain growth, which makes nanomaterials very unstable at elevated temperatures.

Two fundamental approaches have been proposed and studied to stabilize the nano grain structures. The first is thermodynamic approach, in which solute atoms are segregated to the GBs to lower the GB energy [473]. It is theorized that when appropriate solute atoms segregate to the GB, it is possible to reduce the GB energy to 0, so that the driving force for grain growth will be eliminated and the nanostructure will be stabilized. Atoms with large atomic size misfit is especially effective in this stabilization [473]. In addition, the solute atoms on the GBs also act to kinetically stabilize the GBs by solute drag, which will be discussed later. Thermodynamic models have been developed on the thermodynamic stabilization of metallic nanomaterials [474–486], and stability maps have been proposed [484–486]. There are some cases where the model predictions agrees reasonably well with experimental observations for thermodynamic stabilization, while there are also alloy systems where no effective thermodynamic stabilization can be achieved [473]. Alloy systems reported with full thermodynamic stabilization include Ti-W and Al-Pb [484,487]. The stability map also predicted other W alloy systems that could be stabilized thermodynamically [484]. The details of these models and their evolutions can be found in a recent review by Saber et al. [473] and is beyond the scope the current review paper.

The second approach to stabilize metallic nanomaterials is via kinetic stabilization by second-phase particle pinning, solute dragging, and solute ordering to reduce GB mobility [473]. In the binary phase diagrams, only a few alloy systems are isomorphous with no solubility limit. This means that second-phase precipitation may occur before thermodynamic stabilization is reached. Indeed, many nanostructured alloy systems with high thermal stability reported in the literature are stabilized by both the thermodynamic mechanism (GB segregation) and the kinetic mechanism (second-phase particle pinning) [488–495]. In some cases, the kinetic stabilization played the primary role [495].

The second issue is the mechanically driven grain growth, which directly affects the mechanical behavior. In an early report, it was found that the superplastic deformation of NS materials at relatively low temperature was accompanied with grain growth, which exhibited unusual superplastic behaviors [171]. Stress-driven grain growth was first observed by Wolf et al. by MD simulations in 2001 and 2003 [496,497]. Two grain-growth mechanisms were observed: grain rotation and GB migration. Grain rotation led to the conversion of high-angle GBs to low-angle GBs and eventual coalescence of the adjacent grains. High-angle GBs were found to have higher mobility and therefore migrate faster than low-angle GBs. The stress-driven grain growth was later unequivocally verified by Zhang et al. [205] in nanocrystalline Cu, which exhibited rapid grain growth under indentation at the liquid nitrogen temperature, which avoids the conventional diffusion controlled GB migration. Liao et al. found that NC Ni started grain growth when the applied stress is above a critical value under HPT, and grain rotation happened during the grain growth process [211,498]. They also found that there is a maximum grain size for this stress-driven grain growth, which is related to the deformation parameters [211,498]. HPT process is characterized with very large plastic strain and high stress. Fan et al. reported the observation of grain growth in NC metals and alloys during compression [213], tension [499–501] at low strain rate. Grain growth in UFG Mg was also found under high strain rate [502,503]. Stress driven grain growth has been found in many metals and alloys under various testing conditions [116,201,202,206,209,210,218,219,502–506], ands are verified by in-situ TEM observations [507,508]. These observations of stress-induced grain growth raise a concern on the structural stability of metallic nanomaterials under stress during service and how to stabilize the structure. Recently, Lu reported that impurity segregation to the grain boundary can help with stabilizing the nano grains and push the critical grain size for inverse Hall-Petch relationship to smaller grain sizes and higher stresses during tensile testing [509].

8. Summary and future directions

In this review strategies to increase the strength and ductility in the metallic nanomaterials with nanocrystalline (NC) and ultrafine-grained UFG) structures are deliberated with both theoretical analysis and experimental observtions of deformation mechanisms. Metallic nanomaterials typically exhibit high strength but low ductility owing to their very small grains and very large GB areas per unit volume. These structural features critically affect plastic deformation and fracture processes in NS materials. In NS metals having fine grains with an average size $d > d_c$, dislocation slip is dominant and plastic deformation mediated by dislocations is typically characterized with low strain hardening and thereby low ductility.

In NS metals having finest grains with $d < d_c$, volume fractions occupied by GBs are extremely large, and GB-assisted and mediated deformation mechanisms are dominant. These mechanisms – GB sliding, deformation twinning, partial dislocation emission from GBs, rotational deformation and stress-driven migration of GBs - are characterized with very high flow stresses being near the critical stresses for crack nucleation. In addition, NC metallic materials having finest grains are characterized with extremely large quantities of GB junctions at which plastic deformation mediated by GB mechanisms is hampered. Consequently, plastic strain heterogeneities and associated stress concentration points (that initiate either plastic flow localization or cracks) are rapidly created at GB junctions as plastic deformation progresses in such materials. Therefore, the ductility of NS metals with finest grains is suppressed by either plastic strain instability and/or crack growth instability.

In order to enhance the ductility of metallic nanomaterials without loss of their strength, a number of key strategies were suggested, which mostly involves manipulating their microstructures and phase compositions on the nanoscale by optimizing regimes and parameters of their fabrication and processing. From the principle of flow stability during tensile tests, ductility can be enhanced by higher strain hardening and/or strain rate sensitivity. Here we have discussed recent works on enhancement of ductility through optimization/acceleration of GB sliding and diffusion processes by SPD processing to very high plastic strains and/or by giving the material a short-term anneal immediately after processing. At the same time, special attention is paid to the strategies on enhancing ductility by increasing strain hardening through the formation of nanotwins, structurally heterogeneous and gradient structures; deformation at cryogenic temperatures; tailoring stacking fault energy; precipitation-hardening; and incorporation of carbon nanotubes and graphene nanoinclusions in NS metal matrixes. Although these strategies are effective in providing concurrently high strength and high ductility in a large number of NS metallic materials, large-scale production of superstrong NS materials with good ductility for various structural applications is still a challenge. Indeed, presently there are not many reports on NS materials with high strength and good ductility as well as other service properties required for their structural use, in particular, fatigue strength, fracture and impact toughness [510,511], etc. Therefore, with available knowledge on the existing approaches addressing the unique combination of superior strength and enhanced ductility, new research efforts in this area are definitely needed.

In summary, we outline the key points that are of particular interest for future research on ductility of high-strength NS metals and alloys:

(1) Further examinations of previously developed strategies (see Section 5), including experimental identification, computer simulations and theoretical description of ductility enhancement mechanisms operating in NS metallic materials. With knowledge of these mechanisms, systematic fabrication of simultaneously strong and ductile NS metallic materials can be studied using designed processing strategies.
(2) Experimental identification, computer simulation and theoretical description of new mechanisms for plasticity, suppression of crack nucleation and growth instabilities in NS metallic materials with finest grains.
(3) Research efforts addressing novel nanocomposites with optimized mechanical characteristics. Of particular interest are metal-matrix nanocomposites containing nanoinclusions of graphene and other nano types of nano-phases.
(4) Experimental identification, computer simulations and theoretical description of nanostructural fetures (parameters) from phase transformations induced by fabrication/processing in metallic materials, in particular, alloys. Development of nanostructural design of NS materials with superior strength and ductility.
(5) Research efforts addressing combinations of high strength, good ductility and excellent functional properties (biocompatibility, electronic, thermal, energy-storage and -harvesting properties, etc.).
(6) Identification of structural characteristics and fabrication/processing parameters that control and optimize strength and ductility of NS metallic materials having various structures and chemical compositions.

Successfully addressing these important issues will make a large impact on fundamental nanomaterials science and advance the fabrication/processing of super strong NS metallic materials with good ductility for a wide range of technological applications.

Acknowledgements

We would like to sincerely thank all our colleagues who provided support, comments, discussions and allowed us to cite their publications during the work on this paper and apologize to all collaborators whose contributions we may have overlooked. Their comments on this paper will always be welcome and highly appreciated.

The completion of this Review article was made possible with assistance of Prof. Ovid'ko's colleagues from the Institute of Problems of Mechanical Engineering, Russian Academy of Sciences (Saint Petersburg, Russia) – Drs. Alexander Sheinerman and Sergey Bobylev and we would like to express our sincere gratitude for their support, discussions and useful remarks.

This work was supported in part (for I.A.O.) by the Russian Science Foundation (Grant 14-29-00199), in part by the Russian Federal Ministry for Education and Science (through R.Z.V. Grant No. 14.B25.31.0017), and in part by the U.S. Army Research Office (W911 NF-17-1-0350), and the National Key R&D Program of China (2017YFA0204403).

References

[1] Valiev RZ, Islamgaliev RK, Alexandrov IV. Bulk nanostructured materials from severe plastic deformation. Prog Mater Sci 2000;45:103–89.
[2] Gleiter H. Nanostructured materials: basic concepts and microstructure. Acta Mater 2000;48:1–29.
[3] Kumar KS, Van Swygenhoven H, Suresh S. Mechanical behavior of nanocrystalline metals and alloys. Acta Mater 2003;51:5743–74.
[4] Valiev RZ. Nanostructuring of metals by severe plastic deformation for advanced properties. Nat Mater 2004;3:511–6.
[5] Ovid'ko IA. Deformation and diffusion modes in nanocrystalline materials. Int Mater Rev 2005;50:65–82.
[6] Wolf D, Yamakov V, Phillpot SR, Mukherjee A, Gleiter H. Deformation of nanocrystalline materials by molecular-dynamics simulation: relationship to experiments? Acta Mater 2005;53:1–40.
[7] Meyers MA, Mishra A, Benson DJ. Mechanical properties of nanocrystalline materials. Prog Mater Sci 2006;51:427–556.
[8] Koch CC. Structural nanocrystalline materials: an overview. J Mater Sci 2007;42:1403–14.
[9] Dao M, Lu L, Asaro RJ, De Hosson JTM, Ma E. Toward a quantitative understanding of mechanical behavior of nanocrystalline metals. Acta Mater 2007;55:4041–65.
[10] Pande CS, Cooper KP. Nanomechanics of Hall-Petch relationship in nanocrystalline materials. Prog Mater Sci 2009;54:689–706.
[11] Aifantis EC. Deformation and failure of bulk nanograined and ultrafine-grained materials. Mater Sci Eng A 2009;503:190–7.
[12] Greer JR, De Hosson JTM. Plasticity in small-sized metallic systems: intrinsic versus extrinsic size effect. Prog Mater Sci 2011;56:654–724.
[13] Zhu YT, Liao XZ, Wu XL. Deformation twinning in nanocrystalline materials. Prog Mater Sci 2012;57:1–62.
[14] Valiev RZ, Sabirov I, Zhilyaev AP, Langdon TG. Bulk nanostructured metals for innovative applications. JOM 2012;64(10):1134–42.
[15] Mishnaevsky L, Levashov E, Valiev RZ, Segurado J, Sabirov I, Enikeev N, et al. Nanostructured titanium-based materials for medical implants: Modeling and development. Mater Sci Eng R 2014;81:1–19.
[16] McHenry ME, Willard MA, Laughlin DE. Amorphous and nanocrystalline materials for applications as soft magnets. Prog Mater Sci 1999;44:291–433.
[17] Phan MH, Peng HX. Giant magnetoimpedance materials: Fundamentals and applications. Prog Mater Sci 2008;53:323–420.
[18] Chang YQ, Guo Q, Zhang J, Chen L, Long Y, Wan FR. Irradiation effects on nanocrystalline materials. Front Mater Sci 2013;7:143–55.
[19] The Chemistry of Nanomaterials. Synthesis, properties and applications. Weinhein: Wiley; 2004.
[20] Koch CC, Ovid'ko IA, Seal S, Veprek S. Structural nanocrystalline materials: fundamentals and applications. Cambridge: Cambridge University Press; 2007.
[21] Bulk Nanostructured Materials. In: Zehetbauer MJ, Zhu YT, editors. Bulk nanostructured materials. Weinheim, Germany: Wiley; 2009.
[22] Nanocrystalline Materials. Their synthesis-structure-property relationships and applications. Amsterdam: Elsevier; 2013.
[23] Valiev RZ, Zhilyaev AP, Langdon TG. Bulk nanostructured materials: fundamentals and applications. Hoboken (NJ), USA: Wiley; 2014.
[24] Wang YM, Ma E. Three strategies to achieve uniform tensile deformation in a nanostructured metal. Acta Mater 2004;52:1699–709.
[25] Ovid'ko IA. Superplasticity and ductility of superstrong nanomaterials. Rev Adv Mater Sci 2005;10:89–104.
[26] Ma E. Eight routes to improve the tensile ductility of bulk nanostructured metals and alloys. JOM 2006;58:49–53.
[27] Ovid'ko IA, Langdon TG. Enhanced ductility of nanocrystalline and ultrafine-grained metals. Rev Adv Mater Sci 2012;30:103–11.
[28] Valiev RZ, Zhu YT. Recent findings in superior strength and ductility of ultrafine-grained materials. Trans MRS Japan 2015;40:309–18.
[29] Zhao YH, Zhu YT, Lavernia EJ. Strategies for improving tensile ductility of bulk nanostructured materials. Adv Eng Mater 2010;12:769–78.
[30] Valiev RZ, Estrin Y, Horita Z, Langdon TG, Zehetbauer MJ, Zhu YT. Fundamentals of superior properties in bulk NanoSPD materials. Mater Res Lett 2016;4:1–21.
[31] Zhao YH, Guo YZ, Wei Q, Dangelewiez AM, Zhu YT, Langdon TG, et al. Influence of specimen dimensions on the tensile behavior of ultrafine-grained Cu. Scripta Mater 2008;59:627–30.
[32] Zhao YH, Guo YZ, Wei Q, Topping TD, Dangelewicz AM, Zhu YT, et al. Influence of specimen dimensions and strain measurement methods on tensile stress-strain curves. Mater Sci Eng A 2009;525:68–77.
[33] Sutton AP, Ballufi RW. Interfaces in crystalline materials. Oxford: Clarendon; 1995.
[34] Ikeda K, Yamada K, Takata N, Yoshida F, Nakashima H, Tsuji N. Grain boundary structure of ultrafine grained pure copper fabricated by accumulative roll bonding. Mater Trans 2008;49:24–30.
[35] Huang JY, Zhu YT, Jiang H, Lowe TC. Microstructures and dislocation configurations in nanostructured Cu processed by repetitive corrugation and straightening. Acta Mater 2001;49:1497–505.
[36] Divinski S, Rösner H, Wilde G. Functional nanostructured materials – microstructure, thermodynamic stability and atomic mobility. In: Wilde G, editor. Frontiers of nanoscience. Elsevier; 2009. p. 1–50.
[37] Kolobov YR, Valiev RZ, Grabovetskaya GP, Zhilyaev A, Dudarev EF. Grain boundary diffusion and properties of nanostructured materials. Cambridge International Science Publishing; 2007.
[38] Priester L, Yu DP. Triple junctions at the mesoscopic, microscopic and nanoscopic scales. Mater Sci Eng A 1994;188:113–9.
[39] Palumbo G, Aust KT. Triple-line corrosion in high-purity nickel. Mater Sci Eng A 1989;113:139–47.
[40] King AH. The geometric and thermodynamic properties of grain boundary junctions. Interface Sci 1999;7:251–71.
[41] Gottstein G, King AH, Shvindlerman LS. The effect of triple-junction drag on grain growth. Acta Mater 2000;48:397–403.
[42] Caro A, Van Swygenhoven H. Grain boundary and triple junction enthalpies in nanocrystalline metals. Phys Rev B 2001;6313:134101.
[43] Zhou Y, Erb U, Aust KT, Palumbo G. The effects of triple junctions and grain boundaries on hardness and Young's modulus in nanostructured Ni-P. Scripta Mater 2003;48:825–30.
[44] Cherkaoui M, Capolungo L. Atomistic and continuum modeling of nanocrystalline materials: deformation mechanisms and scale transition. Springer Ser Mater S 2009;112:1–387.
[45] Volpp T, Goring E, Kuschke WM, Arzt E. Grain size determination and limits to Hall-Petch behavior in nanocrystalline NiAl powders. Nanostruct Mater 1997;8:855–65.
[46] Weertman JR, Sanders PG. Plastic deformation of nanocrystalline metals. Solid State Phenom 1994;35–36:249–62.
[47] Valiev RZ, Estrin Y, Horita Z, Langdon TG, Zehetbauer MJ, Zhu YT. Producing bulk ultrafine-grained materials by severe plastic deformation: ten years later. JOM 2016;68:1216–26.
[48] Hirth JP, Lothe J. Theory of dislocations. 2nd ed. Malabar, FL: Krieger Publishing Company; 1992.
[49] Morris JWJ. Dislocation-controlled plasticity of crystalline materials: Overview. In: Buschow KHJ, Cahn RW, Flemings MC, Ilschner B, Kramer EJ, Mahajan S, et al., editors. Encyclopedia of materials: science and technology. Amsterdam: Elsevier; 2001. p. 2245–55.
[50] Xu G. Dislocation nucleation from crack tip and brittle to ductile transitions in cleavage fracture* Chapter 65. In: Nabarro FRN, Hirth JP, editors. Dislocations in Solids. Amsterdam: Elsevier; 2004. p. 81–145.
[51] Rice JR, Thomson R. Ductile versus brittle behavior of crystals. Philos Mag 1974;29:73–97.

[52] Rice JR. Dislocation nucleation from a crack tip - an analysis based on the peierls concept. J Mech Phys Solids 1992;40:239–71.
[53] Hart EW. Theory of Tensile Test. Acta Metall 1967;15:351–5.
[54] Antolovich SD, Armstrong RW. Plastic strain localization in metals: origins and consequences. Prog Mater Sci 2014;59:1–160.
[55] Considère A. Memoire sur l'emploi du fer et de l'acier dans les constructions. Ann Ponts Chaussées 1885;9:575–775.
[56] Sherby OD, Wadsworth J. Superplasticity - recent advances and future-directions. Prog Mater Sci 1989;33:169–221.
[57] Piling J, Ridley N. Superplasticity in crystalline solids. London: The Institute of Metals; 1989.
[58] Zhu YT, Langdon TG. The fundamentals of nanostructured materials processed by severe plastic deformation. JOM 2004;56(10):58–63.
[59] Langdon TG. Seventy-five years of superplasticity: historic developments and new opportunities. J Mater Sci 2009;44:5998–6010.
[60] Cheng GM, Jian WW, Xu WZ, Yuan H, MIllett PC, Zhu YT. Grain size effect on deformation mechanisms of nanocrystalline bcc metals. Mater Res Lett 2013;1:26–31.
[61] Wei Q, Cheng S, Ramesh KT, Ma E. Effect of nanocrystalline and ultrafine grain sizes on the strain rate sensitivity and activation volume: fcc versus bcc metals. Mater Sci Eng A 2004;381:71–9.
[62] Bay B, Hansen N, Hughes DA, Kuhlmannwilsdorf D. Overview No-96 - evolution of Fcc deformation structures in polyslip. Acta Metall Mater 1992;40:205–19.
[63] Zhu YT, Liao XZ, Srinivasan SG, Lavernia EJ. Nucleation of deformation twins in nanocrystalline face-centered-cubic metals processed by severe plastic deformation. J Appl Phys 2005;98:034319.
[64] Zhu YT, Liao XZ, Srinivasan SG, Zhao YH, Baskes MI, Zhou F, et al. Nucleation and growth of deformation twins in nanocrystalline aluminum. Appl Phys Lett 2004;85:5049–51.
[65] Zhu YT, Huang JY, Gubicza J, Ungar T, Wang YM, Ma E, et al. Nanostructures in Ti processed by severe plastic deformation. J Mater Res 2003;18:1908–17.
[66] Ovid'ko IA, Sheinerman AG. Grain size effect on crack blunting in nanocrystalline materials. Scripta Mater 2009;60:627–30.
[67] Ovid'ko IA, Sheinerman AG. Ductile vs. brittle behavior of pre-cracked nanocrystalline and ultrafine-grained materials. Acta Mater 2010;58:5286–94.
[68] Ovid'ko IA. Review on the fracture processes in nanocrystalline materials. J Mater Sci 2007;42:1694–708.
[69] Zhu YT, Liao XZ. Nanostructured metals - retaining ductility. Nat Mater 2004;3:351–2.
[70] Zhao YH, Liao XZ, Cheng S, Ma E, Zhu YT. Simultaneously increasing the ductility and strength of nanostructured alloys. Adv Mater 2006;18:2280–3.
[71] Weissmuller J, Markmann J. Deforming nanocrystalline metals: new insights, new puzzles. Adv Eng Mater 2005;7:202–7.
[72] Kocks UF, Mecking H. Physics and phenomenology of strain hardening: the FCC case. Prog Mater Sci 2003;48:171–273.
[73] Estrin Y, Vinogradov A. Extreme grain refinement by severe plastic deformation: a wealth of challenging science. Acta Mater 2013;61:782–817.
[74] Mukherjee AK. An examination of the constitutive equation for elevated temperature plasticity. Mater Sci Eng A 2002;322:1–22.
[75] Kumar KS, Suresh S, Chisholm MF, Horton JA, Wang P. Deformation of electrodeposited nanocrystalline nickel. Acta Mater 2003;51:387–405.
[76] Mompiou F, Caillard D, Legros M, Mughrabi H. In situ TEM observations of reverse dislocation motion upon unloading in tensile-deformed UFG aluminium. Acta Mater 2012;60:3402–14.
[77] Mompiou F, Legros M, Boe A, Coulombier M, Raskin JP, Pardoen T. Inter- and intragranular plasticity mechanisms in ultrafine-grained Al thin films: an in situ TEM study. Acta Mater 2013;61:205–16.
[78] Bobylev SV, Gutkin MY, Ovid'ko IA. Transformations of grain boundaries in deformed nanocrystalline materials. Acta Mater 2004;52:3793–805.
[79] Li JCM. Mechanical grain growth in nanocrystalline copper. Phys Rev Lett 2006;96:215506.
[80] Li JCM. Grain boundary impurity and porosity effects on the yield strength of nanocrystalline materials. Appl Phys Lett 2007;90:041912.
[81] Ovid'ko IA, Sheinerman AG, Valiev RZ. Dislocation emission from deformation-distorted grain boundaries in ultrafine-grained materials. Scripta Mater 2014;76:45–8.
[82] Liao XZ, Zhou F, Lavernia EJ, Srinivasan SG, Baskes MI, He DW, et al. Deformation mechanism in nanocrystalline Al: partial dislocation slip. Appl Phys Lett 2003;83:632–4.
[83] Yamakov V, Wolf D, Salazar M, Phillpot SR, Gleiter H. Length-scale effects in the nucleation of extended dislocations in nanocrystalline Al by molecular-dynamics simulation. Acta Mater 2001;49:2713–22.
[84] Yamakov V, Wolf D, Phillpot SR, Gleiter H. Deformation twinning in nanocrystalline Al by molecular dynamics simulation. Acta Mater 2002;50:5005–20.
[85] Murr LE. Dislocation ledge sources: dispelling the myth of frank-read source importance. Metall Mater Trans A 2016;47a:5811–26.
[86] Youssef KM, Scattergood RO, Murty KL, Horton JA, Koch CC. Ultrahigh strength and high ductility of bulk nanocrystalline copper. Appl Phys Lett 2005;87:091904.
[87] Shan ZW, Stach EA, Wiezorek JMK, Knapp JA, Follstaedt DM, Mao SX. Grain boundary-mediated plasticity in nanocrystalline nickel. Science 2004;305:654–7.
[88] Shan ZW, Wiezorek JMK, Stach EA, Follstaedt DM, Knapp JA, Mao SX. Dislocation dynamics in nanocrystalline nickel. Phys Rev Lett 2007;98:095502.
[89] Wu XL, Zhu YT. Partial-dislocation-mediated processes in nanocrystalline Ni with nonequilibrium grain boundaries. Appl Phys Lett 2006;89:031922.
[90] Wu XL, Qi Y, Zhu YT. Partial-mediated slips in nanocrystalline Ni at high strain rate. Appl Phys Lett 2007;90:221911.
[91] Liao XZ, Zhou F, Lavernia EJ, He DW, Zhu YT. Deformation twins in nanocrystalline Al. Appl Phys Lett 2003;83:5062–4.
[92] Liao XZ, Zhao YH, Srinivasan SG, Zhu YT, Valiev RZ, Gunderov DV. Deformation twinning in nanocrystalline copper at room temperature and low strain rate. Appl Phys Lett 2004;84:592–4.
[93] Liao XZ, Srinivasan SG, Zhao YH, Baskes MI, Zhu YT, Zhou F, et al. Formation mechanism of wide stacking faults in nanocrystalline Al. Appl Phys Lett 2004;84:3564–6.
[94] Yamakov V, Wolf D, Phillpot SR, Mukherjee AK, Gleiter H. Deformation-mechanism map for nanocrystalline metals by molecular-dynamics simulation. Nat Mater 2004;3:43–7.
[95] Yamakov V, Wolf D, Phillpot SR, Mukherjee AK, Gleiter H. Dislocation processes in the deformation of nanocrystalline aluminium by molecular-dynamics simulation. Nat Mater 2002;1:45–8.
[96] Van Swygenhoven H, Derlet PM, Hasnaoui A. Atomic mechanism for dislocation emission from nanosized grain boundaries. Phys Rev B 2002;66:024101.
[97] Van Swygenhoven H, Derlet PM, Froseth AG. Stacking fault energies and slip in nanocrystalline metals. Nat Mater 2004;3:399–403.
[98] Van Swygenhoven H, Derlet PM, Froseth AG. Nucleation and propagation of dislocations in nanocrystalline fcc metals. Acta Mater 2006;54:1975–83.
[99] Froseth AG, Derlet PM, Van Swygenhoven H. Dislocations emitted from nanocrystalline grain boundaries: nucleation and splitting distance. Acta Mater 2004;52:5863–70.
[100] Derlet PM, Van Swygenhoven H, Hasnaoui A. Atomistic simulation of dislocation emission in nanosized grain boundaries. Philos Mag 2003;83:3569–75.
[101] Schiotz J, Di Tolla FD, Jacobsen KW. Softening of nanocrystalline metals at very small grain sizes. Nature 1998;391:561–3.
[102] Schiotz J, Jacobsen KW. A maximum in the strength of nanocrystalline copper. Science 2003;301:1357–9.
[103] Bobylev SV, Morozov NF, Ovid'ko IA. Cooperative grain boundary sliding and migration process in nanocrystalline solids. Phys Rev Lett 2010;105:055504.
[104] Bobylev SV, Ovid'ko IA. Grain boundary rotations in solids. Phys Rev Lett 2012;109:175501.
[105] Chinh NQ, Voros G, Szommer P, Horita Z, Langdon TG. Grain boundary sliding as a significant mechanism of low temperature plastic deformation in ECAP aluminum. Nanomater Severe Plastic Deform 2006;503–504:1001–6.
[106] Farkas D, Mohanty S, Monk J. Strain-driven grain boundary motion in nanocrystalline materials. Mater Sci Eng A 2008;493:33–40.
[107] Gutkin MY, Ovid'ko IA. Grain boundary migration as rotational deformation mode in nanocrystalline materials. Appl Phys Lett 2005;87:251916.

[108] Gutkin MY, Ovid'ko IA, Skiba NV. Crossover from grain boundary sliding to rotational deformation in nanocrystalline materials. Acta Mater 2003;51:4059–71.
[109] Ivanov KV, Naydenkin EV. Grain boundary sliding in ultrafine grained aluminum under tension at room temperature. Scripta Mater 2012;66:511–4.
[110] Mungole T, Kumar P, Kawasaki M, Langdon TG. The contribution of grain boundary sliding in tensile deformation of an ultrafine-grained aluminum alloy having high strength and high ductility. J Mater Sci 2015;50:3549–61.
[111] Ovid'ko IA, Skiba NV, Sheinerman AG. Influence of grain boundary sliding on fracture toughness of nanocrystalline ceramics. Phys Solid State 2008;50:1261–5.
[112] Sergueeva AV, Mara NA, Krasilnikov NA, Valiev RZ, Mukherjee AK. Cooperative grain boundary sliding in nanocrystalline materials. Philos Mag 2006;86:5797–804.
[113] Yang KJ, Fecht HJ, Ivanisenko Y. First direct in situ observation of grain boundary sliding in ultrafine grained noble metal. Adv Eng Mater 2014;16:517–21.
[114] Ke M, Hackney SA, Milligan WW, Aifantis EC. Observation and measurement of grain rotation and plastic strain in nanostructured metal thin-films. Nanostruct Mater 1995;5:689–97.
[115] Wang L, Teng J, Liu P, Hirata A, Ma E, Zhang Z, et al. Grain rotation mediated by grain boundary dislocations in nanocrystalline platinum. Nat Commun 2014;5:4402.
[116] Wang YB, Li BQ, Sui ML, Mao SX. Deformation-induced grain rotation and growth in nanocrystalline Ni. Appl Phys Lett 2008;92:011903.
[117] Van Swygenhoven H. Polycrystalline materials - grain boundaries and dislocations. Science 2002;296:66–7.
[118] Wu XL, Zhu YT. Inverse grain-size effect on twinning in nanocrystalline Ni. Phys Rev Lett 2008;101:025503.
[119] Wu XL, Youssef KM, Koch CC, Mathaudhu SN, Kecskes LJ, Zhu YT. Deformation twinning in a nanocrystalline hcp Mg alloy. Scripta Mater 2011;64:213–6.
[120] Han J, Su XM, Jin ZH, Zhu YT. Basal-plane stacking-fault energies of Mg: a first-principles study of Li- and Al-alloying effects. Scripta Mater 2011;64:693–6.
[121] Barnett MR. A rationale for the strong dependence of mechanical twinning on grain size. Scripta Mater 2008;59:696–8.
[122] Jian WW, Cheng GM, Xu WZ, Yuan H, Tsai MH, Wang QD, et al. Ultrastrong Mg Alloy via Nano-spaced Stacking Faults. Mater Res Lett 2013;1:61–6.
[123] Jian WW, Cheng GM, Xu WZ, Koch CC, Wang QD, Zhu YT, et al. Physics and model of strengthening by parallel stacking faults. Appl Phys Lett 2013;103.
[124] Gu P, Zhu YT, Mathaudhu SN. A model for < c plus a & rang; dislocation transmission across nano-spaced parallel basal stacking faults in a HCP alloy. Philos Mag Lett 2015;95:58–66.
[125] Zhou H, Cheng GM, Ma XL, Xu WZ, Mathaudhu SN, Wang QD, et al. Effect of Ag on interfacial segregation in Mg-Gd-Y-(Ag)-Zr alloy. Acta Mater 2015;95:20–9.
[126] Wang WY, Shang SL, Wang Y, Mei ZG, Darling KA, Kecskes LJ, et al. Effects of alloying elements on stacking fault energies and electronic structures of binary Mg alloys: a first-principles study. Mater Res Lett 2014;2:29–36.
[127] Chen KC, Wu WW, Liao CN, Chen LJ, Tu KN. Observation of atomic diffusion at twin-modified grain boundaries in copper. Science 2008;321:1066–9.
[128] Zhu YT, Liao XZ, Wu XL, Narayan J. Grain size effect on deformation twinning and detwinning. J Mater Sci 2013;48:4467–75.
[129] Zhao YH, Bingert JE, Liao XZ, Cui BZ, Han K, Sergueeva AV, et al. Simultaneously increasing the ductility and strength of ultra-fine-grained pure copper. Adv Mater 2006;18:2949.
[130] Zhu YT, Narayan J, Hirth JP, Mahajan S, Wu XL, Liao XZ. Formation of single and multiple deformation twins in nanocrystalline fcc metals. Acta Mater 2009;57:3763–70.
[131] Zhu YT, Liao XZ, Wu XL. Deformation twinning in bulk nanocrystalline metals: experimental observations. JOM 2008;60(9):60–4.
[132] Wu X, Zhu YT, Chen MW, Ma E. Twinning and stacking fault formation during tensile deformation of nanocrystalline Ni. Scripta Mater 2006;54:1685–90.
[133] Ookawa A. On the mechanism of deformation twin in Fcc crystal. J Phys Soc Japan 1957;12:825.
[134] Venables JA. Deformation twinning in face-centred cubic metals. Philos Mag 1961;6:379–96.
[135] Niewczas M, Saada G. Twinning nucleation in Cu-8 at.% Al single crystals. Philos Mag A 2002;82:167–91.
[136] Christian JW, Mahajan S. Deformation twinning. Prog Mater Sci 1995;39:1–157.
[137] Mahajan S, Chin GY. Formation of deformation twins in Fcc crystals. Acta Metall 1973;21:1353–63.
[138] Mahajan S, Green ML, Brasen D. Model for Fcc-]Hcp transformation, its applications, and experimental-evidence. Metall Trans A 1977;8:283–93.
[139] Wang YB, Sui ML, Ma E. In situ observation of twin boundary migration in copper with nanoscale twins during tensile deformation. Philos Mag Lett 2007;87:935–42.
[140] Wang YB, Wu B, Sui ML. Dynamical dislocation emission processes from twin boundaries. Appl Phys Lett 2008;93:041906.
[141] Ovid'ko IA, Skiba NV. Generation of nanoscale deformation twins at locally distorted grain boundaries in nanomaterials. Int J Plast 2014;62:50–71.
[142] Narayan J, Zhu YT. Self-thickening, cross-slip deformation twinning model. Appl Phys Lett 2008;92:151908.
[143] Dregia SA, Hirth JP. A rebound mechanism for lomer dislocation formation in strained layer structures. J Appl Phys 1991;69:2169–75.
[144] Zhu YT, Wu XL, Liao XZ, Narayan J, Mathaudhu SN, Kecskes LJ. Twinning partial multiplication at grain boundary in nanocrystalline fcc metals. Appl Phys Lett 2009;95:031909.
[145] Zhu YT, Liao XZ, Valiev RZ. Formation mechanism of fivefold deformation twins in nanocrystalline face-centered-cubic metals. Appl Phys Lett 2005;86:103112.
[146] Wu F, Zhu YT, Narayan J. Macroscopic twinning strain in nanocrystalline Cu. Mater Res Lett 2014;2:63–9.
[147] Wang J, Anderoglu O, Hirth JP, Misra A, Zhang X. Dislocation structures of Sigma 3 112 twin boundaries in face centered cubic metals. Appl Phys Lett 2009;95:021908.
[148] Wang J, Misra A, Hirth JP. Shear response of Sigma 3{112} twin boundaries in face-centered-cubic metals. Phys Rev B 2011;83:064106.
[149] Liu L, Wang J, Gong SK, Mao SX. High resolution transmission electron microscope observation of zero-strain deformation twinning mechanisms in Ag. Phys Rev Lett 2011;106:175504.
[150] Li BQ, Li B, Wang YB, Sui ML, Ma E. Twinning mechanism via synchronized activation of partial dislocations in face-centered-cubic materials. Scripta Mater 2011;64:852–5.
[151] Ma XL, Zhou H, Narayan J, Zhu YT. Stacking-fault energy effect on zero-strain deformation twinning in nanocrystalline Cu–Zn alloys. Scripta Mater 2015;109:89–93.
[152] Ma XL, Xu WZ, Zhou H, Moering JA, Narayan J, Zhu YT. Alloying effect on grain-size dependent deformation twinning in nanocrystalline Cu-Zn alloys. Philos Mag 2015;95:301–10.
[153] Ovid'ko IA, Skiba NV, Sheinerman AG. Plastic deformation through detwinning and its effect on electric resistivity in ultrafine-grained metals with nanotwinned structures. Rev Adv Mater Sci 2015;43:38–44.
[154] Wang J, Li N, Anderoglu O, Zhang X, Misra A, Huang JY, et al. Detwinning mechanisms for growth twins in face-centered cubic metals. Acta Mater 2010;58:2262–70.
[155] Li N, Wang J, Huang JY, Misra A, Zhang X. Influence of slip transmission on the migration of incoherent twin boundaries in epitaxial nanotwinned Cu. Scripta Mater 2011;64:149–52.
[156] Meyers MA, Vohringer O, Lubarda VA. The onset of twinning in metals: a constitutive description. Acta Mater 2001;49:4025–39.
[157] Zhang JY, Liu G, Wang RH, Li J, Sun J, Ma E. Double-inverse grain size dependence of deformation twinning in nanocrystalline Cu. Phys Rev B 2010;81:172104.

[158] Jiang HG, Zhu YT, Butt DP, Alexandrov IV, Lowe TC. Microstructural evolution, microhardness and thermal stability of HPT-processed Cu. Mater Sci Eng A 2000;290:128–38.
[159] Zhu YT, Wu XL, Liao XZ, Narayan J, Kecskes LJ, Mathaudhu SN. Dislocation-twin interactions in nanocrystalline fcc metals. Acta Mater 2011;59:812–21.
[160] Hosford WF. The mechanics of crystals and textured polycrystals. New York: Oxford University Press; 1993.
[161] Barnett MR, Stanford N, Cizek P, Beer A, Xuebin Z, Keshavarz Z. Deformation mechanisms in Mg alloys and the challenge of extending room-temperature plasticity. JOM 2009;61(8):19–24.
[162] Langdon TG. Grain boundary sliding revisited: developments in sliding over four decades. J Mater Sci 2006;41:597–609.
[163] Mara NA, Sergueeva AV, Mara TD, McFadden SX, Mukherjee AK. Superplasticity and cooperative grain boundary sliding in nanocrystalline Ni3Al. Mater Sci Eng A 2007;463:238–44.
[164] Kawasaki M, Langdon TG. Principles of superplasticity in ultrafine-grained materials. J Mater Sci 2007;42:1782–96.
[165] Valiev RZ, Murashkin MY, Kilmametov A, Straumal B, Chinh NQ, Langdon TG. Unusual super-ductility at room temperature in an ultrafine-grained aluminum alloy. J Mater Sci 2010;45:4718–24.
[166] Markmann J, Bunzel P, Rosner H, Liu KW, Padmanabhan KA, Birringer R, et al. Microstructure evolution during rolling of inert-gas condensed palladium. Scripta Mater 2003;49:637–44.
[167] Valiev RZ, Sergueeva AV, Mukherjee AK. The effect of annealing on tensile deformation behavior of nanostructured SPD titanium. Scripta Mater 2003;49:669–74.
[168] Kumar P, Kawasaki M, Langdon TG. Review: overcoming the paradox of strength and ductility in ultrafine-grained materials at low temperatures. J Mater Sci 2016;51:7–18.
[169] Gutkin MY, Ovid'ko IA. Plastic deformation in nanocrystalline materials. Berlin: Springer; 2004.
[170] Valiev RZ, Kaibyshev OA, Kuznetsov RI, Musalimov RS, Tsenev NK. The low-temperature superplasticity of metallic materials. Doklady Akademii Nauk Sssr 1988;301:864.
[171] McFadden SX, Mishra RS, Valiev RZ, Zhilyaev AP, Mukherjee AK. Low-temperature superplasticity in nanostructured nickel and metal alloys. Nature 1999;398:684–6.
[172] Valiev RZ, Song C, McFadden SX, Mukherjee AK, Mishra RS. TEM/HREM observations of nanostructured superplastic Ni3Al. Philos Mag A 2001;81:25–36.
[173] Fedorov AA, Gutkin MY, Ovid'ko IA. Transformations of grain boundary dislocation pile-ups in nano- and polycrystalline materials. Acta Mater 2003;51:887–98.
[174] Ovid'ko IA, Sheinerman AG. Special strain hardening mechanism and nanocrack generation in nanocrystalline materials. Appl Phys Lett 2007;90:171927.
[175] Ovid'ko IA, Sheinerman AG. Nanocrack generation at dislocation-disclination configurations in nanocrystalline metals and ceramics. Phys Rev B 2008;77:054109.
[176] Ovid'ko IA, Sheinerman AG. Enhanced ductility of nanomaterials through optimization of grain boundary sliding and diffusion processes. Acta Mater 2009;57:2217–28.
[177] Romanov AE, Vladimirov VI. Disclinations in crystals. In: Nabarro FRN, editor. Dislocation in solids. Amsterdam: Elsevier; 1992. p. 191–402.
[178] Kleman M, Friedel J. Disclinations, dislocations, and continuous defects: a reappraisal. Rev Modern Phys 2008;80:61–115.
[179] Romanov AE, Kolesnikova AL. Application of disclination concept to solid structures. Prog Mater Sci 2009;54:740–69.
[180] Gutkin MY, Ovid'ko IA, Skiba NV. Strengthening and softening mechanisms in nanocrystalline materials under superplastic deformation. Acta Mater 2004;52:1711–20.
[181] Padmanabhan KA, Gleiter H. Optimal structural superplasticity in metals and ceramics of microcrystalline- and nanocrystalline-grain sizes. Mater Sci Eng A 2004;381:28–38.
[182] Murayama M, Howe JM, Hidaka H, Takaki S. Atomic-level observation of disclination dipoles in mechanically milled, nanocrystalline Fe. Science 2002;295:2433–5.
[183] Cheng S, Zhao YH, Wang YM, Li Y, Wang XL, Liaw PK, et al. Structure modulation driven by cyclic deformation in nanocrystalline NiFe. Phys Rev Lett 2010;104:255501.
[184] Jang DC, Greer JR. Size-induced weakening and grain boundary-assisted deformation in 60 nm grained Ni nanopillars. Scripta Mater 2011;64:77–80.
[185] Liu P, Mao SC, Wang LH, Han XD, Zhang Z. Direct dynamic atomic mechanisms of strain-induced grain rotation in nanocrystalline, textured, columnar-structured thin gold films. Scripta Mater 2011;64:343–6.
[186] Han XD, Wang LH, Yue YH, Zhang Z. In situ atomic scale mechanical microscopy discovering the atomistic mechanisms of plasticity in nano-single crystals and grain rotation in polycrystalline metals. Ultramicroscopy 2015;151:94–100.
[187] Wang L, Xin T, Kong D, Shu X, Chen Y, Zhou H, et al. In situ observation of stress induced grain boundary migration in nanocrystalline gold. Scripta Mater 2017;134:95–9.
[188] Shimokawa T, Nakatani A, Kitagawa H. Grain-size dependence of the relationship between intergranular and intragranular deformation of nanocrystalline Al by molecular dynamics simulations. Phys Rev B 2005;71.
[189] Schiotz J, Vegge T, Di Tolla FD, Jacobsen KW. Atomic-scale simulations of the mechanical deformation of nanocrystalline metals. Phys Rev B 1999;60:11971–83.
[190] Izadi E, Darbal A, Sarkar R, Rajagopalan J. Grain rotations in ultrafine-grained aluminum films studied using in situ TEM straining with automated crystal orientation mapping. Mater Des 2017;113:186–94.
[191] Ovid'ko IA. Deformation of nanostructures. Science 2002;295:1.
[192] Valiev RZ, Langdon TG. An investigation of the role of intragranular dislocation strain in the superplastic Pb-62-percent Sn eutectic alloy. Acta Metall Mater 1993;41:949–54.
[193] Gutkin MY, Kolesnikova AL, Ovid'ko IA, Skiba NV. Disclinations and rotational deformation in fine-grained materials. Philos Mag Lett 2002;82:651–7.
[194] Gutkin MY, Ovid'ko IA, Skiba NV. Transformations of grain boundaries due to disclination motion and emission of dislocation pairs. Mater Sci Eng A 2003;339:73–80.
[195] Ovid'ko IA, Sheinerman AG. Special rotational deformation in nanocrystalline metals and ceramics. Scripta Mater 2008;59:119–22.
[196] Bobylev SV, Mukherjee AK, Ovid'ko IA. Transition from plastic shear into rotation deformation mode in nanocrystalline metals and ceramics. Rev Adv Mater Sci 2009;19:103–13.
[197] Ovid'ko IA, Sheinerman AG. Free surface effects on rotational deformation in nanocrystalline materials. J Mater Sci 2016;51:6444–51.
[198] Kottada RS, Chokshi AH. Low temperature compressive creep in electrodeposited nanocrystalline nickel. Scripta Mater 2005;53:887–92.
[199] Li JCM. Possibility of subgrain rotation during recrystallization. J Appl Phys 1962;33:2958.
[200] Moldovan D, Yamakov V, Wolf D, Phillpot SR. Scaling behavior of grain-rotation-induced grain growth. Phys Rev Lett 2002;89:206101.
[201] Wang YB, Ho JC, Liao XZ, Li HQ, Ringer SP, Zhu YT. Mechanism of grain growth during severe plastic deformation of a nanocrystalline Ni-Fe alloy. Appl Phys Lett 2009;94:011908.
[202] Jin M, Minor AM, Stach EA, Morris JW. Direct observation of deformation-induced grain growth during the nanoindentation of ultrafine-grained Al at room temperature. Acta Mater 2004;52:5381–7.
[203] Soer WA, De Hosson JTM, Minor AM, Morris JW, Stach EA. Effects of solute Mg on grain boundary and dislocation dynamics during nanoindentation of Al-Mg thin films. Acta Mater 2004;52:5783–90.
[204] Zhang K, Weertman JR, Eastman JA. The influence of time, temperature, and grain size on indentation creep in high-purity nanocrystalline and ultrafine grain copper. Appl Phys Lett 2004;85:5197–9.

[205] Zhang K, Weertman JR, Eastman JA. Rapid stress-driven grain coarsening in nanocrystalline Cu at ambient and cryogenic temperatures. Appl Phys Lett 2005;87:061921.
[206] Sansoz F, Dupont V. Grain growth behavior at absolute zero during nanocrystalline metal indentation. Appl Phys Lett 2006;89:111901.
[207] Farkas D, Froseth A, Van Swygenhoven H. Grain boundary migration during room temperature deformation of nanocrystalline Ni. Scripta Mater 2006;55:695–8.
[208] De Hosson JTM, Soer WA, Minor AM, Shan ZW, Stach EA, Asif SAS, et al. In situ TEM nanoindentation and dislocation-grain boundary interactions: a tribute to David Brandon. J Mater Sci 2006;41:7704–19.
[209] Gianola DS, Van Petegem S, Legros M, Brandstetter S, Van Swygenhoven H, Hemker KJ. Stress-assisted discontinuous grain growth and its effect on the deformation behavior of nanocrystalline aluminum thin films. Acta Mater 2006;54:2253–63.
[210] Gianola DS, Warner DH, Molinari JF, Hemker KJ. Increased strain rate sensitivity due to stress-coupled grain growth in nanocrystalline Al. Scripta Mater 2006;55:649–52.
[211] Liao XZ, Kilmametov AR, Valiev RZ, Gao HS, Li XD, Mukherjee AK, et al. High-pressure torsion-induced grain growth in electrodeposited nanocrystalline Ni. Appl Phys Lett 2006;88:021909.
[212] Pan D, Nieh TG, Chen MW. Strengthening and softening of nanocrystalline nickel during multistep nanoindentation. Appl Phys Lett 2006;88:161922.
[213] Fan GJ, Wang YD, Fu LF, Choo H, Liaw PK, Ren Y, et al. Orientation-dependent grain growth in a bulk nanocrystalline alloy during the uniaxial compressive deformation. Appl Phys Lett 2006;88:171914.
[214] Gai PL, Zhang K, Weertman J. Electron microscopy study of nanocrystalline copper deformed by a microhardness indenter. Scripta Mater 2007;56:25–8.
[215] Pan D, Kuwano S, Fujita T, Chen MW. Ultra-large room-temperature compressive plasticity of a nanocrystalline metal. Nano Lett 2007;7:2108–11.
[216] Dupont V, Sansoz F. Quasicontinuum study of incipient plasticity under nanoscale contact in nanocrystalline aluminum. Acta Mater 2008;56:6013–26.
[217] Ovid'ko IA, Sheinerman AG, Alfantis EC. Stress-driven migration of grain boundaries and fracture processes in nanocrystalline ceramics and metals. Acta Mater 2008;56:2718–27.
[218] Rupert TJ, Gianola DS, Gan Y, Hemker KJ. Experimental observations of stress-driven grain boundary migration. Science 2009;326:1686–90.
[219] Sharon JA, Su P-C, Prinz FB, Hemker KJ. Stress-driven grain growth in nanocrystalline Pt thin films. Scripta Mater 2011;64:25–8.
[220] Gianola DS, Farkas D, Gamarra M, He MR. The role of confinement on stress-driven grain boundary motion in nanocrystalline aluminum thin films. J Appl Phys 2012;112.
[221] Lin YJ, Xu BC, Feng YZ, Lavernia EJ. Stress-induced grain growth during high-temperature deformation of nanostructured Al containing nanoscale oxide particles. J Alloy Compd 2014;596:79–85.
[222] Lin YJ, Wen HM, Li Y, Wen B, Liu W, Lavernia EJ. Stress-induced grain growth in an ultra-fine grained Al alloy. Metall Mater Trans B 2014;45:795–810.
[223] Aramfard M, Deng C. Influences of triple junctions on stress-assisted grain boundary motion in nanocrystalline materials. Model Simulation Mater Sci Eng 2014;22.
[224] Lin YJ, Wen HM, Li Y, Wen B, Liu W, Lavernia EJ. An analytical model for stress-induced grain growth in the presence of both second-phase particles and solute segregation at grain boundaries. Acta Mater 2015;82:304–15.
[225] Ovid'ko IA, Sheinerman AG. Effects of incoherent nanoinclusions on stress-driven migration of low-angle grain boundaries in nanocomposites. J Mater Sci 2015;50:4430–9.
[226] Bobylev SV, Ovid'ko IA. Stress-driven migration of deformation-distorted grain boundaries in nanomaterials. Acta Mater 2015;88:260–70.
[227] Winning M, Gottstein G, Shvindlerman LS. Stress induced grain boundary motion. Acta Mater 2001;49:211–9.
[228] Molodov DA, Ivanov VA, Gottstein G. Low angle tilt boundary migration coupled to shear deformation. Acta Mater 2007;55:1843–8.
[229] Molodov DA, Gorkaya T, Gottstein G. Mechanically driven migration of ⟨100⟩ tilt grain boundaries in Al-bicrystals. Recrystallization and Grain Growth III, Pts 1 and 2. 2007;558–559:927–32.
[230] Gottstein G, Shvindleman LS. Grain boundary migration in metals: thermodynamics, kinetics, applications. Boca Raton: CRC Press; 2010.
[231] Molodov DA, Gorkaya T, Gottstein G. Dynamics of grain boundaries under applied mechanical stress. J Mater Sci 2011;46:4318–26.
[232] Mompiou F, Legros M, Caillard D. Direct observation and quantification of grain boundary shear-migration coupling in polycrystalline Al. J Mater Sci 2011;46:4308–13.
[233] Rajabzadeh A, Mompiou F, Legros M, Combe N. Elementary mechanisms of shear-coupled grain boundary migration. Phys Rev Lett 2013;110.
[234] Cahn JW, Taylor JE. A unified approach to motion of grain boundaries, relative tangential translation along grain boundaries, and grain rotation. Acta Mater 2004;52:4887–98.
[235] Cahn JW, Mishin Y, Suzuki A. Duality of dislocation content of grain boundaries. Philos Mag 2006;86:3965–80.
[236] Cahn JW, Mishin Y, Suzuki A. Coupling grain boundary motion to shear deformation. Acta Mater 2006;54:4953–75.
[237] Molodov DA, Gorkaya T, Gottstein G. Migration of the Σ7 tilt grain boundary in Al under an applied external stress. Scripta Mater 2011;65:990–3.
[238] Wan L, Ishii A, Du J-P, Han W-Z, Mei Q, Ogata S. Atomistic modeling study of a strain-free stress driven grain boundary migration mechanism. Scripta Mater 2017;134:52–6.
[239] Kawasaki M, Langdon TG. Developing superplasticity and a deformation mechanism map for the Zn-Al eutectoid alloy processed by high-pressure torsion. Mater Sci Eng A-Struct Mater Prop Microstruct Process 2011;528:6140–5.
[240] Kawasaki M, Langdon TG. The many facets of deformation mechanism mapping and the application to nanostructured materials. J Mater Res 2013;28:1827–34.
[241] Coble RL. A model for boundary diffusion controlled creep in polycrystalline materials. J Appl Phys 1963;34:1679.
[242] Nabarro FRN. Deformation of crystals by the motion of single lonsin report of a conference on the strength of solids. London; 1948. p. 75–90.
[243] Herring C. Diffusional viscosity of a polycrystalline solid. J Appl Phys 1950;21:437–45.
[244] Bobylev SV, Ovid'ko IA. Anomalous multiplication of lattice dislocations at grain boundaries in nanocrystalline solids. J Phys D 2015;48:035302.
[245] Bobylev SV, Morozov NF, Ovid'ko IA. Generation of deformation twin pairs at grain boundaries in nanomaterials. Rev Adv Mater Sci 2015;41:1–6.
[246] Bobylev SV, Ovid'ko IA. Nucleation of deformation twins on gliding grain-boundary dislocations in nanomaterials. Phys Solid State 2016;58:572–7.
[247] Ovid'ko IA, Sheinerman AG, Aifantis EC. Effect of cooperative grain boundary sliding and migration on crack growth in nanocrystalline solids. Acta Mater 2011;59:5023–31.
[248] Ovid'ko IA, Sheinerman AG. Triple junction nanocracks in deformed nanocrystalline materials. Acta Mater 2004;52:1201–9.
[249] Ovid'ko IA, Skiba NV. Enhanced dislocation emission from grain boundaries in nanocrystalline materials. Scripta Mater 2012;67:13–6.
[250] Li HQ, Ebrahimi F. Transition of deformation and fracture behaviors in nanostructured face-centered-cubic metals. Appl Phys Lett 2004;84:4307–9.
[251] Cheng S, Ma E, Wang YM, Kecskes LJ, Youssef KM, Koch CC, et al. Tensile properties of in situ consolidated nanocrystalline Cu. Acta Mater 2005;53:1521–33.
[252] Youssef KM, Scattergood RO, Murty KL, Koch CC. Nanocrystalline Al-Mg alloy with ultrahigh strength and good ductility. Scripta Mater 2006;54:251–6.
[253] Hohenwarter A, Pippan R. Fracture and fracture toughness of nanopolycrystalline metals produced by severe plastic deformation. Philos Trans Royal Soc A 2015;373:20140366.
[254] Li HQ, Ebrahimi F. Ductile-to-brittle transition in nanocrystalline metals. Adv Mater 2005;17:1969.
[255] Padilla HA, Boyce BL. A review of fatigue behavior in nanocrystalline metals. Exp Mech 2010;50:5–23.
[256] Moser B, Hanlon T, Kumar KS, Suresh S. Cyclic strain hardening of nanocrystalline nickel. Scripta Mater 2006;54:1151–5.
[257] Asaro RJ, Suresh S. Mechanistic models for the activation volume and rate sensitivity in metals with nanocrystalline grains and nano-scale twins. Acta Mater 2005;53:3369–82.

[258] Farkas D, Van Swygenhoven H, Derlet PM. Intergranular fracture in nanocrystalline metals. Phys Rev B 2002;66:060101.
[259] Mirshams RA, Mao CH, Whang SH, Yin WM. R-curve characterization of the fracture toughness of nanocrystalline nickel thin sheets. Mater Sci Eng A 2001;315:21–7.
[260] Zhao YS, Qian J, Daemen LL, Pantea C, Zhang JZ, Voronin GA, et al. Enhancement of fracture toughness in nanostructured diamond-SiC composites. Appl Phys Lett 2004;84:1356–8.
[261] Pei YT, Galvan D, De Hosson JTM. Nanostructure and properties of TiC/a-C: H composite coatings. Acta Mater 2005;53:4505–21.
[262] Kaminskii AA, Akchurin MS, Gainutdinov RV, Takaichi K, Shirakava A, Yagi H, et al. Microhardness and fracture toughness of Y2O3- and Y3Al5O12-based nanocrystalline laser ceramics. Crystallogr Rep+ 2005;50:869–73.
[263] Dominguez-Rodriguez A, Gomez-Garcia D, Zapata-Solvas E, Shen JZ, Chaim R. Making ceramics ductile at low homologous temperatures. Scripta Mater 2007;56:89–91.
[264] Bobylev SV, Mukherjee AK, Ovid'ko IA, Sheinerman AG. Effects of intergrain sliding on crack growth in nanocrystalline materials. Int J Plast 2010;26:1629–44.
[265] Ovid'ko IA, Skiba NV, Mukherjee AK. Nucleation of nanograins near cracks in nanocrystalline materials. Scripta Mater 2010;62:387–90.
[266] Morozov NF, Ovid'ko IA, Sheinerman AG, Aifantis EC. Special rotational deformation as a toughening mechanism in nanocrystalline solids. J Mech Phys Solids 2010;58:1088–99.
[267] Ovid'ko IA, Sheinerman AG. Nanoscale rotational deformation near crack tips in nanocrystalline solids. J Phys D 2012;45:335301.
[268] Ovid'ko IA, Sheinerman AG. Grain boundary rotations near crack tips in deformed nanomaterials. Rev Adv Mater Sci 2014;37:97–104.
[269] Ovid'ko IA. Micromechanics of fracturing in nanoceramics. Philos Trans Royal Soc A 2015;373:20140129.
[270] Yang F, Yang W. Brittle versus ductile transition of nanocrystalline metals. Int J Solids Struct 2008;45:3897–907.
[271] Yang F, Yang W. Crack growth versus blunting in nanocrystalline metals with extremely small grain size. J Mech Phys Solids 2009;57:305–24.
[272] Gutkin MY, Ovid'ko IA, Skiba NV. Crack-stimulated generation of deformation twins in nanocrystalline metals and ceramics. Philos Mag 2008;88:1137–51.
[273] Liu YG, Zhou JQ, Wang L, Zhang S, Wang Y. Grain size dependent fracture toughness of nanocrystalline materials. Mater Sci Eng A 2011;528:4615–9.
[274] Fang QH, Feng H, Liu YW, Lin S, Zhang N. Special rotational deformation effect on the emission of dislocations from a crack tip in deformed nanocrystalline solids. Int J Solids Struct 2012;49:1406–12.
[275] Feng H, Fang QH, Zhang LC, Liu YW. Special rotational deformation and grain size effect on fracture toughness of nanocrystalline materials. Int J Plast 2013;42:50–64.
[276] Feng H, Fang QH, Zhang LC, Liu YW. Effect of cooperative grain boundary sliding and migration on emission of dislocations from a crack tip in nanocrystalline materials. Mech Mater 2013;61:39–48.
[277] Yu M, Fang QH, Feng H, Liu YW. Effect of cooperative grain boundary sliding and migration on dislocation emitting from a semi-elliptical blunt crack tip in nanocrystalline solids. Acta Mech 2014;225:2005–19.
[278] Zhao YX, Fang QH, Liu YW. Effect of cooperative nanograin boundary sliding and migration on dislocation emission from a blunt nanocrack tip in nanocrystalline materials. Philos Mag 2014;94:700–30.
[279] Yu M, Fang QH, Feng H, Liu YW. Effect of special rotational deformation on dislocation emission from interface collinear crack tip in nanocrystalline bi-materials. Acta Mech 2016;227:2011–24.
[280] Valiev RZ, Salimonenko DA, Tsenev NK, Berbon PB, Langdon TG. Observations of high strain rate superplasticity in commercial aluminum alloys with ultrafine grain sizes. Scripta Mater 1997;37:1945–50.
[281] Langdon TG. Twenty-five years of ultrafine-grained materials: achieving exceptional properties through grain refinement. Acta Mater 2013;61:7035–59.
[282] Kawasaki M, Langdon TG. Review: achieving superplastic properties in ultrafine-grained materials at high temperatures. J Mater Sci 2016;51:19–32.
[283] Edalati K, Masuda T, Arita M, Furui M, Sauvage X, Horita Z, et al. Room-temperature superplasticity in an ultrafine-grained magnesium alloy. Sci Rep-Uk 2017;7.
[284] Ivanisenko Y, Darbandi A, Dasgupta S, Kruk R, Hahn H. Bulk nanostructured materials: non-mechanical synthesis. Adv Eng Mater 2010;12:666–76.
[285] Witkin DB, Lavernia EJ. Synthesis and mechanical behavior of nanostructured materials via cryomilling. Prog Mater Sci 2006;51:1–60.
[286] Valiev RZ, Langdon TG. Report of international NanoSPD steering committee and statistics on recent NanoSPD activities. IOP Conf Series: Mater Sci Eng 2014;63:011002.
[287] Valiev RZ, Estrin Y, Horita Z, Langdon TG, Zehetbauer MJ, Zhu YT. Producing bulk ultrafine-grained materials by severe plastic deformation. JOM 2006;58(4):33–9.
[288] Islamgaliev RK, Yunusova NF, Sabirov IN, Sergueeva AV, Valiev RZ. Deformation behavior of nanostructured aluminum alloy processed by severe plastic deformation. Mater Sci Eng A 2001;319:877–81.
[289] Edalati K, Horita H. A review on high-pressure torsion (HPT) from 1935 to 1988. Mater Sci Eng A 2016;652:325–52.
[290] Valiev RZ, Langdon TG. Principles of equal-channel angular pressing as a processing tool for grain refinement. Prog Mater Sci 2006;51:881–981.
[291] Zhilyaev AP, Langdon TG. Using high-pressure torsion for metal processing: fundamentals and applications. Prog Mater Sci 2008;53:893–979.
[292] Bachmaier A, Pippan R. Generation of metallic nanocomposites by severe plastic deformation. Int Mater Rev 2013;58:41–62.
[293] Wongsa-Ngam J, Kawasaki M, Langdon TG. A comparison of microstructures and mechanical properties in a Cu-Zr alloy processed using different SPD techniques. J Mater Sci 2013;48:4653–60.
[294] Production of multifunctional materials using severe plastic deformation. In: Horita Z, editor. Int sym giant straining process for advanced materials (GSAM2010). Fukuoka, Japan: Kyushu University Press; 2010.
[295] Sauvage X, Wilde G, Divinski SV, Horita Z, Valiev RZ. Grain boundaries in ultrafine grained materials processed by severe plastic deformation and related phenomena. Mater Sci Eng A 2012;540:1–12.
[296] Sabirov I, Enikeev NA, Murashkin MY, Valiev RZ. Bulk nanostructured materials with multifunctional properties. Springer; 2015. p. 64.
[297] Zhao YH, Zhu YT, Liao XZ, Horita Z, Langdon TG. Tailoring stacking fault energy for high ductility and high strength in ultrafine grained Cu and its alloy. Appl Phys Lett 2006;89:121906.
[298] Wang YB, Liao XZ, Zhao YH, Cooley JC, Horita Z, Zhu YT. Elemental separation in nanocrystalline Cu-Al alloys. Appl Phys Lett 2013;102:231912.
[299] Gleiter H. Nanocrystalline materials. Prog Mater Sci 1989;33:223–315.
[300] Valiev RZ. On grain boundary engineering of UFG metals and alloys for enhancing their properties. Mater Sci Forum 2008;584–586:22–8.
[301] Grabski MW. Mechanical-properties of internal interfaces. J Phys 1985;46:567–79.
[302] Valiev RZ, Gertsman VY, Kaibyshev OA. Grain-boundary structure and properties under external influences. Phys Stat Sol A 1986;97:11–56.
[303] Nazarov AA, Romanov AE, Valiev RZ. On the structure, stress-fields and energy of nonequilibrium grain-boundaries. Acta Metall Mater 1993;41:1033–40.
[304] Nazarov AA, Romanov AE, Valiev RZ. Incorporation model for the spreading of extrinsic grain-boundary dislocations. Scripta Metall Mater 1990;24:1929–34.
[305] Romanov AE, Kolesnikova AL, Orlova TS, Hussainova I, Bougrov VE, Valiev RZ. Non-equilibrium grain boundaries with excess energy in graphene. Carbon 2015;81:223–31.
[306] Horita Z, Smith DJ, Furukawa M, Nemoto M, Valiev RZ, Langdon TG. An investigation of grain boundaries in submicrometer-grained Al-Mg solid solution alloys using high-resolution electron microscopy. J Mater Res 1996;11:1880–90.
[307] Rosner H, Boucharat N, Padmanabhan KA, Markmann J, Wilde G. Strain mapping in a deformation-twinned nanocrystalline Pd grain. Acta Mater 2010;58:2610–20.
[308] Dinda GP, Rosner H, Wilde G. Synthesis of bulk nanostructured Ni, Ti and Zr by repeated cold-rolling. Scripta Mater 2005;52:577–82.

[309] Wilde G, Dinda GP, Rosner H. Synthesis of bulk nanocrystalline materials by repeated cold rolling. Adv Eng Mater 2005;7:11–5.
[310] Divinski SV, Reglitz G, Rosner H, Estrin Y, Wilde G. Ultra-fast diffusion channels in pure Ni severely deformed by equal-channel angular pressing. Acta Mater 2011;59:1974–85.
[311] Hytch MJ, Snoeck E, Kilaas R. Quantitative measurement of displacement and strain fields from HREM micrographs. Ultramicroscopy 1998;74:131–46.
[312] Wilde G, Ribbe J, Reglitz G, Wegner M, Rosner H, Estrin Y, et al. Plasticity and grain boundary diffusion at small grain sizes. Adv Eng Mater 2010;12:758–64.
[313] Bobylev SV, Ovid'ko IA. Thickening of deformation-distorted high-angle grain boundaries in nanomaterials. Phys Solid State 2015;57:2059–65.
[314] Ni S, Wang YB, Liao XZ, Li HQ, Figueiredo RB, Ringer SP, et al. Effect of grain size on the competition between twinning and detwinning in nanocrystalline metals. Phys Rev B 2011;84:235401.
[315] Zhang HW, Huang X, Pippan R, Hansen N. Thermal behavior of Ni (99.967% and 99.5% purity) deformed to an ultra-high strain by high pressure torsion. Acta Mater 2010;58:1698–707.
[316] Rajgarhia RK, Saxena A, Spearot DE, Hartwig KT, More KL, Kenik EA, et al. Microstructural stability of copper with antimony dopants at grain boundaries: experiments and molecular dynamics simulations. J Mater Sci 2010;45:6707–18.
[317] Nurislamova G, Sauvage X, Murashkin M, Islamgaliev R, Valiev R. Nanostructure and related mechanical properties of an Al-Mg-Si alloy processed by severe plastic deformation. Philos Mag Lett 2008;88:459–66.
[318] Sha G, Wang YB, Liao XZ, Duan ZC, Ringer SP, Langdon TG. Influence of equal-channel angular pressing on precipitation in an Al-Zn-Mg-Cu alloy. Acta Mater 2009;57:3123–32.
[319] Liddicoat PV, Liao XZ, Zhao YH, Zhu YT, Murashkin MY, Lavernia EJ, et al. Nanostructural hierarchy increases the strength of aluminum alloys. Nat Commun 2010;1:63.
[320] Sauvage X, Murashkin MY, Valiev RZ. Atomic scale investigation of dynamic precipitation and grain boundary segregation in a 6061 aluminium alloy nanostructured by ECAP. Kovove Materialy-Metallic Mater 2011;49:11–5.
[321] Valiev RZ, Enikeev NA, Murashkin MY, Kazykhanov VU, Sauvage X. On the origin of the extremely high strength of ultrafine-grained Al alloys produced by severe plastic deformation. Scripta Mater 2010;63:949–52.
[322] Sha G, Tugcu K, Liao XZ, Trimby PW, Murashkin MY, Valiev RZ, et al. Strength, grain refinement and solute nanostructures of an Al-Mg-Si alloy (AA6060) processed by high-pressure torsion. Acta Mater 2014;63:169–79.
[323] Trimby PW. Orientation mapping of nanostructured materials using transmission Kikuchi diffraction in the scanning electron microscope. Ultramicroscopy 2012;120:16–24.
[324] Murayama M, Horita Z, Hono K. Microstructure of two-phase Al-1.7 at% Cu alloy deformed by equal-channel angular pressing. Acta Mater 2001;49:21–9.
[325] Sha G, Wang YB, Liao XZ, Duan ZC, Ringer SP, Langdon TG. Microstructural evolution of Fe-rich particles in an Al-Zn-Mg-Cu alloy during equal-channel angular pressing. Mater Sci Eng A-Struct Mater Prop Microstruct Process 2010;527:4742–9.
[326] Xu C, Furukawa M, Horita Z, Langdon TG. Influence of ECAP on precipitate distributions in a spray-east aluminum alloy. Acta Mater 2005;53:749–58.
[327] Cai M, Field DP, Lorimer GW. A systematic comparison of static and dynamic ageing of two Al-Mg-Si alloys. Mater Sci Eng A 2004;373:65–71.
[328] Roven HJ, Liu MP, Werenskiold JC. Dynamic precipitation during severe plastic deformation of an Al-Mg-Si aluminium alloy. Mater Sci Eng A 2008;483–84:54–8.
[329] Sha G, Li JH, Xu W, Xia K, Jie WQ, Ringer SP. Hardening and microstructural reactions in high-temperature equal-channel angular pressed Mg-Nd-Gd-Zn-Zr alloy. Mater Sci Eng A 2010;527:5092–9.
[330] Valiev RZ, Murashkin MY, Bobruk EV, Raab GI. Grain refinement and mechanical behavior of the Al alloy, subjected to the new SPD technique. Mater Trans 2009;50:87–91.
[331] Valiev RZ, Murashkin MY, Sabirov I. A nanostructural design to produce high-strength Al alloys with enhanced electrical conductivity. Scripta Mater 2014;76:13–6.
[332] Murashkin MY, Sabirov I, Kazykhanov VU, Bobruk EV, Dubravina AA, Valiev RZ. Enhanced mechanical properties and electrical conductivity in ultrafine-grained Al alloy processed via ECAP-PC. J Mater Sci 2013;48:4501–9.
[333] Kim WJ, Wang JY, Choi SO, Choi HJ, Sohn HT. Synthesis of ultra high strength Al-Mg-Si alloy sheets by differential speed rolling. Mater Sci Eng A 2009;520:23–8.
[334] Gryaznov VG, Kaprelov AM, Romanov AE. Size effect of dislocation stability in small particles and microcrystallites. Scripta Metall 1989;23:1443–8.
[335] Gryaznov VG, Polonsky IA, Romanov AE, Trusov LI. Size effects of dislocation stability in nanocrystals. Phys Rev B 1991;44:42–6.
[336] Evans AG, Hirth JP. Deformation of nanoscale cermets. Scripta Metall Mater 1992;26:1675–80.
[337] Koch CC, Ovid'ko IA, Seal S, Veprek S. Structural nanocrystalline materials fundamentals and applications introduction. Structural nanocrystalline materials: fundamentals and applications; 2007. p. 1–24.
[338] Valiev RZ, Alexandrov IV, Zhu YT, Lowe TC. Paradox of strength and ductility in metals processed by severe plastic deformation. J Mater Res 2002;17:5–8.
[339] Valiev R. Materials science - nanomaterial advantage. Nature 2002;419:887.
[340] Dalla Torre F, Lapovok R, Sandlin J, Thomson PF, Davies CHJ, Pereloma EV. Microstructures and properties of copper processed by equal channel angular extrusion for 1–16 passes. Acta Mater 2004;52:4819–32.
[341] Kumar P, Xu C, Langdon TG. Influence of strain rate on strength and ductility in an aluminum alloy processed by equal-channel angular pressing. J Mater Sci 2009;44:3913–6.
[342] Mungole T, Kumar P, Kawasaki M, Langdon TG. A critical examination of the paradox of strength and ductility in ultrafine-grained metals. J Mater Res 2014;29:2534–46.
[343] Semenova I, Salimgareeva G, Da Costa G, Lefebvre W, Valiev R. Enhanced strength and ductility of ultrafine-grained Ti processed by severe plastic deformation. Adv Eng Mater 2010;12:803–7.
[344] Polyakov AV, Semenova IP, Valiev RZ, Huang Y, Langdon TG. Influence of annealing on ductility of ultrafine-grained titanium processed by equal-channel angular pressing-Conform and drawing. MRS Comm 2013;3:249–53.
[345] Suo T, Li YL, Zhao F, Xie K. Influence of short time annealing on strain hardening rate and flow stress of ultrafine grained material processed by severe plastic deformation. Mater Res Innov 2011;15:S69–92.
[346] Andreau O, Gubicza J, Zhang NX, Huang Y, Jenei P, Langdon TG. Effect of short-term annealing on the microstructures and flow properties of an Al-1% Mg alloy processed by high-pressure torsion. Mater Sci Eng A 2014;615:231–9.
[347] Maury N, Zhang NX, Huang Y, Zhilyaev AP, Langdon TG. A critical examination of pure tantalum processed by high-pressure torsion. Mater Sci Eng A 2015;638:174–82.
[348] Lu L, Shen YF, Chen XH, Qian LH, Lu K. Ultrahigh strength and high electrical conductivity in copper. Science 2004;304:422–6.
[349] Wang ZW, Wang YB, Liao XZ, Zhao YH, Lavernia EJ, Zhu YT, et al. Influence of stacking fault energy on deformation mechanism and dislocation storage capacity in ultrafine-grained materials. Scripta Mater 2009;60:52–5.
[350] Wang YB, Sui ML. Atomic-scale in situ observation of lattice dislocations passing through twin boundaries. Appl Phys Lett 2009;94:021909.
[351] Ovid'ko IA, Sheinerman AG. Mechanical properties of nanotwinned metals: a review. Rev Adv Mater Sci 2016;44:1–25.
[352] Jin ZH, Gumbsch P, Albe K, Ma E, Lu K, Gleiter H, et al. Interactions between non-screw lattice dislocations and coherent twin boundaries in face-centered cubic metals. Acta Mater 2008;56:1126–35.
[353] Yamakov V, Wolf D, Phillpot SR, Gleiter H. Dislocation-dislocation and dislocation-twin reactions in nanocrystalline Al by molecular dynamics simulation. Acta Mater 2003;51:4135–47.

[354] Lu K, Lu L, Suresh S. Strengthening materials by engineering coherent internal boundaries at the nanoscale. Science 2009;324:349–52.
[355] Xiao GH, Tao NR, Lu K. Strength-ductility combination of nanostructured Cu-Zn alloy with nanotwin bundles. Scripta Mater 2011;65:119–22.
[356] Zhang X, Misra A, Wang H, Nastasi M, Embury JD, Mitchell TE, et al. Nanoscale-twinning-induced strengthening in austenitic stainless steel thin films. Appl Phys Lett 2004;84:1096–8.
[357] Wu F, Zhu YT, Narayan J. Grain size effect on twin density in as-deposited nanocrystalline Cu film. Philos Mag 2013;93:4355–63.
[358] Zhao YH, Liao XZ, Horita Z, Langdon TG, Zhu YT. Determining the optimal stacking fault energy for achieving high ductility in ultrafine-grained Cu-Zn alloys. Mater Sci Eng A 2008;493:123–9.
[359] Ungar T, Balogh L, Zhu YTT, Horita Z, Xu C, Langdon TG. Using X-ray microdiffraction to determine grain sizes at selected positions in disks processed by high-pressure torsion. Mater Sci Eng A 2007;444:153–6.
[360] Sun PL, Zhao YH, Cooley JC, Kassner ME, Horita Z, Langdon TG, et al. Effect of stacking fault energy on strength and ductility of nanostructured alloys: an evaluation with minimum solution hardening. Mater Sci Eng A 2009;525:83–6.
[361] Fang XT, Ma XL, Zhang LW, Zhu YT. Nucleation of deformation twins in nanocrystalline fcc alloys. Philos Mag 2016;96:3790–802.
[362] Huang CX, Hu WP, Wang QY, Wabg C, Yang G, Zhu YT. An ideal ultrafine-grained structure for high strength and high ductility. Mater Res Lett 2015;3:88–94.
[363] Chan HL, Ruan HH, Chen AY, Lu J. Optimization of the strain rate to achieve exceptional mechanical properties of 304 stainless steel using high speed ultrasonic surface mechanical attrition treatment. Acta Mater 2010;58:5086–96.
[364] Chen AY, Li DF, Zhang JB, Song HW, Lu J. Make nanostructured metal exceptionally tough by introducing non-localized fracture behaviors. Scripta Mater 2008;59:579–82.
[365] Zhu LL, Ruan HH, Li XY, Dao M, Gao HJ, Lu J. Modeling grain size dependent optimal twin spacing for achieving ultimate high strength and related high ductility in nanotwinned metals. Acta Mater 2011;59:5544–57.
[366] Wei YJ, Li YQ, Zhu LC, Liu Y, Lei XQ, Wang G, et al. Evading the strength- ductility trade-off dilemma in steel through gradient hierarchical nanotwins. Nat Commun 2014;5.
[367] Wang YM, Ma E, Valiev RZ, Zhu YT. Tough nanostructured metals at cryogenic temperatures. Adv Mater 2004;16:328.
[368] Wang YM, Ma E. Temperature and strain rate effects on the strength and ductility of nanostructured copper. Appl Phys Lett 2003;83:3165–7.
[369] Huang Z, Gu LY, Weertman JR. Temperature dependence of hardness of nanocrystalline copper in low-temperature range. Scripta Mater 1997;37:1071–5.
[370] Dalla Torre F, Van Swygenhoven H, Victoria M. Nanocrystalline electrodeposited Ni: microstructure and tensile properties. Acta Mater 2002;50:3957–70.
[371] Reed RP, Clark AF. Materials at low temperatures. Metals Park (OH): ASM; 1983.
[372] Wang YM, Ma E, Chen MW. Enhanced tensile ductility and toughness in nanostructured Cu. Appl Phys Lett 2002;80:2395–7.
[373] Wang YM, Chen MW, Zhou FH, Ma E. High tensile ductility in a nanostructured metal. Nature. 2002;419:912–5.
[374] Weertman JR, Farkas D, Hemker K, Kung H, Mayo M, Mitra R, et al. Structure and mechanical behavior of bulk nanocrystalline materials. Mrs Bull. 1999;24:44–50.
[375] Wang YM, Wang K, Pan D, Lu K, Hemker KJ, Ma E. Microsample tensile testing of nanocrystalline copper. Scripta Mater 2003;48:1581–6.
[376] Jia D, Wang YM, Ramesh KT, Ma E, Zhu YT, Valiev RZ. Deformation behavior and plastic instabilities of ultrafine-grained titanium. Appl Phys Lett 2001;79:611–3.
[377] Bengus VZ, Tabachnikova ED, Natsik VD, Mishkuf I, Chakh K, Stolyarov VV, et al. Low-temperature deformation and fracture of bulk nanostructural titanium obtained by intense plastic deformation using equal channel angular pressing. Low Temp Phys+. 2002;28:864–74.
[378] Reed-Hill RE, Abbaschian R. Physical Metallurgy Principles. 3rd ed. Boston, MA: PWS Publishing Company; 1994.
[379] Wu XL, Yang MX, Yuan FP, Chen L, Zhu YT. Combining gradient structure and TRIP effect to produce austenite steel with high strength and ductility. Acta Mater 2016;112:337–46.
[380] Chen AY, Ruan HH, Wang J, Chan HL, Wang Q, Li Q, et al. The influence of strain rate on the microstructure transition of 304 stainless steel. Acta Mater 2011;59:3697–709.
[381] Wu XL, Zhu YT, Wei YG, Wei Q. Strong Strain Hardening in Nanocrystalline Nickel. Phys Rev Lett 2009;103:205504.
[382] Wu XL, Jiang P, Chen L, Yuan FP, Zhu YT. Extraordinary strain hardening by gradient structure. Proc Natl Acad Sci USA 2014;111:7197–201.
[383] Wu XL, Jiang P, Chen L, Zhang JF, Yuan FP, Zhu YT. Synergetic Strengthening by Gradient Structure. Mater Res Lett 2014;2:185–91.
[384] Lu K. Making strong nanomaterials ductile with gradients. Science 2014;345:1455–6.
[385] Fang TH, Li WL, Tao NR, Lu K. Revealing Extraordinary Intrinsic Tensile Plasticity in Gradient Nano-Grained Copper. Science 2011;331:1587–90.
[386] Roumina R, Embury JD, Bouaziz O, Zurob HS. Mechanical behavior of a compositionally graded 300M steel. Mater Sci Eng A 2013;578:140–9.
[387] Wu XL, Yang MX, Yuan FP, Wu GL, Wei YJ, Huang XX, et al. Heterogeneous lamella structure unites ultrafine-grain strength with coarse-grain ductility. Proc Natl Acad Sci USA 2015;112:14501–5.
[388] Yang MX, Pan Y, Yuan FP, Zhu YT, Wu XL. Back stress strengthening and strain hardening in gradient structure. Mater Res Lett 2016;4:145–51.
[389] Moering J, Ma XL, Chen GZ, Miao PF, Li GZ, Qian G, et al. The role of shear strain on texture and microstructural gradients in low carbon steel processed by Surface Mechanical Attrition Treatment. Scripta Mater 2015;108:100–3.
[390] Chakravarthy SS, Curtin WA. Stress-gradient plasticity. Proc Natl Acad Sci USA 2011;108:15716–20.
[391] Hirth JP. Dislocation pileups in the presence of stress gradients. Philos Mag 2006;86:3959–63.
[392] Tian YZ, Wu SD, Zhang ZF, Figueiredo RB, Gao N, Langdon TG. Microstructural evolution and mechanical properties of a two-phase Cu-Ag alloy processed by high-pressure torsion to ultrahigh strains. Acta Mater 2011;59:2783–96.
[393] Valiev RZ, Langdon TG. The Art and Science of Tailoring Materials by Nanostructuring for Advanced Properties Using SPD Techniques. Adv Eng Mater 2010;12:677–91.
[394] Horita Z, Ohashi K, Fujita T, Kaneko K, Langdon TG. Achieving high strength and high ductility in precipitation-hardened alloys. Adv Mater 2005;17:1599.
[395] Zhao YH, Bingert JF, Zhu YT, Liao XZ, Valiev RZ, Horita Z, et al. Tougher ultrafine grain Cu via high-angle grain boundaries and low dislocation density. Appl Phys Lett 2008;92:081903.
[396] Tian YZ, Wu SD, Zhang ZF, Figueiredo RB, Gao N, Langdon TG. Comparison of microstructures and mechanical properties of a Cu-Ag alloy processed using different severe plastic deformation modes. Mater Sci Eng A 2011;528:4331–6.
[397] Horita Z, Fujinami T, Nemoto M, Langdon TG. Equal-channel angular pressing of commercial aluminum alloys: Grain refinement, thermal stability and tensile properties. Metall Mater Trans A 2000;31:691–701.
[398] Zhu YT, Valiev RZ, Langdon TG, Tsuji N, Lu K. Processing of nanostructured metals and alloys via plastic deformation. Mrs Bull 2010;35:977–81.
[399] An XH, Wu SD, Zhang ZF, Figueiredo RB, Gao N, Langdon TG. Enhanced strength-ductility synergy in nanostructured Cu and Cu-Al alloys processed by high-pressure torsion and subsequent annealing. Scripta Mater 2012;66:227–30.
[400] Zhu YT, Lowe TC, Langdon TG. Performance and applications of nanostructured materials produced by severe plastic deformation. Scripta Mater 2004;51:825–30.
[401] Zhao YH, Topping T, Bingert JF, Thornton JJ, Dangelewicz AM, Li Y, et al. High tensile ductility and strength in bulk nanostructured nickel. Adv Mater 2008;20:3028–33.
[402] Zhao YH, Liao XZ, Zhu YT, Valiev RZ. Enhanced mechanical properties in ultrafine grained 7075 Al alloy. J Mater Res 2005;20:288–91.
[403] Ashby MF. Deformation of plastically non-homogeneous materials. Philos Mag 1970;21:399.
[404] Gao H, Huang Y, Nix WD, Hutchinson JW. Mechanism-based strain gradient plasticity – I. Theory. J Mech Phys Solids 1999;47:1239–63.
[405] Huang Y, Gao H, Nix WD, Hutchinson JW. Mechanism-based strain gradient plasticity – II. Analysis. J Mech Phys Solids 2000;48:99–128.

[406] Hughes DA, Hansen N, Bammann DJ. Geometrically necessary boundaries, incidental dislocation boundaries and geometrically necessary dislocations. Scripta Mater 2003;48:147–53.
[407] Lapovok R, Dalla Torre FH, Sandlin J, Davies CHJ, Pereloma EV, Thomson PF, et al. Gradient plasticity constitutive model reflecting the ultrafine microstructure scale: the case of severely deformed copper. J Mech Phys Solids 2005;53:729–47.
[408] Estrin Y, Molotnikov A, Davies CHJ, Lapovok R. Strain gradient plasticity modelling of high-pressure torsion. J Mech Phys Solids 2008;56:1186–202.
[409] Tsuji N, Ito Y, Saito Y, Minamino Y. Strength and ductility of ultrafine grained aluminum and iron produced by ARB and annealing. Scripta Mater 2002;47:893–9.
[410] Huang XX, Kamikawa N, Hansen N. Increasing the ductility of nanostructured Al and Fe by deformation. Mater Sci Eng A 2008;493:184–9.
[411] Huang XX, Kamikawa N, Tsuji N, Hansen N. Nanostructured aluminum and IF steel produced by rolling - a comparative study. Isij Int 2008;48:1080–7.
[412] Purcek G, Saray O, Karaman I, Maier HJ. High strength and high ductility of ultrafine-grained, interstitial-free steel produced by ECAE and annealing. Metall Mater Trans A 2012;43A:1884–94.
[413] Hazra SS, Pereloma EV, Gazder AA. Microstructure and mechanical properties after annealing of equal-channel angular pressed interstitial-free steel. Acta Mater 2011;59:4015–29.
[414] Wu XL, Yang MX, Yuan FP, Chen L, Zhu YT. Combining gradient structure and TRIP effect to produce austenite stainless steel with high strength and ductility. Acta Mater 2016;112:337–46.
[415] Zhang Z, Vajpai SK, Orlov D, Ameyama K. Improvement of mechanical properties in SUS304L steel through the control of bimodal microstructure characteristics. Mater Sci Eng A 2014;598:106–13.
[416] Sawangrat C, Kato S, Orlov D, Ameyama K. Harmonic-structured copper: performance and proof of fabrication concept based on severe plastic deformation of powders. J Mater Sci 2014;49:6579–85.
[417] Vajpai SK, Ota M, Watanabe T, Maeda R, Sekiguchi T, Kusaka T, et al. The development of high performance Ti-6Al-4V alloy via a unique microstructural design with bimodal grain size distribution. Metall Mater Trans A 2015;46:903–14.
[418] Han QH, Asgari A, Hodgson PD, Stanford N. Strain partitioning in dual-phase steels containing tempered martensite. Mater Sci Eng A 2014;611:90–9.
[419] Kadkhodapour J, Schmauder S, Raabe D, Ziaei-Rad S, Weber U, Calcagnotto M. Experimental and numerical study on geometrically necessary dislocations and non-homogeneous mechanical properties of the ferrite phase in dual phase steels. Acta Mater 2011;59:4387–94.
[420] Calcagnotto M, Adachi Y, Ponge D, Raabe D. Deformation and fracture mechanisms in fine- and ultrafine-grained ferrite/martensite dual-phase steels and the effect of aging. Acta Mater 2011;59:658–70.
[421] Calcagnotto M, Ponge D, Demir E, Raabe D. Orientation gradients and geometrically necessary dislocations in ultrafine grained dual-phase steels studied by 2D and 3D EBSD. Mater Sci Eng A 2010;527:2738–46.
[422] Ryu JH, Kim DI, Kim HS, Bhadeshia HKDH, Suh DW. Strain partitioning and mechanical stability of retained austenite. Scripta Mater 2010;63:297–9.
[423] Tasan CC, Diehl M, Yan D, Zambaldi C, Shanthraj P, Roters F, et al. Integrated experimental-simulation analysis of stress and strain partitioning in multiphase alloys. Acta Mater 2014;81:386–400.
[424] Ma XL, Huang CX, Xu WZ, Zhou H, Wu XL, Zhu YT. Strain hardening and ductility in a coarse-grain/nanostructure laminate material. Scripta Mater 2015;103:57–60.
[425] Ma XL, Huang CX, Moering J, Ruppert M, Höppel HW, Göken M, et al. Mechanical properties in copper/bronze laminates: role of interfaces. Acta Mater 2016;116:43–52.
[426] Fan GJ, Choo H, Liaw PK, Lavernia EJ. Plastic deformation and fracture of ultrafine-grained Al-Mg alloys with a bimodal grain size distribution. Acta Mater 2006;54:1759–66.
[427] Zhao MC, Hanamura T, Yin FX, Qiu H, Nagai K. Formation of bimodal-sized structure and its tensile properties in a warm-rolled and annealed ultrafine-grained Ferrite/Cementite steel. Metall Mater Trans A 2008;39A:1691–701.
[428] Khoddam S, Estrin Y, Kim HS, Bouaziz O. Torsional and compressive behaviours of a hybrid material: Spiral fibre reinforced metal matrix composite. Mater Des 2015;85:404–11.
[429] Bouaziz O, Kim HS, Estrin Y. Architecturing of metal-based composites with concurrent nanostructuring: a new paradigm of materials design. Adv Eng Mater 2013;15:336–40.
[430] Beygelzimer Y, Estrin Y, Kulagin R. Synthesis of hybrid materials by severe plastic deformation: a new paradigm of SPD processing. Adv Eng Mater 2015;17:1853–61.
[431] Latypov MI, Beygelzimer Y, Kulagin R, Varyukhin V, Kim HS. Toward architecturing of metal composites by twist extrusion. Mater Res Lett 2015;3:161–8.
[432] Koch CC. Optimization of strength and ductility in nanocrystalline and ultrafine grained metals. Scripta Mater 2003;49:657–62.
[433] Zhao YH, Liao XZ, Jin Z, Valiev RZ, Zhu YT. Microstructures and mechanical properties of ultrafine grained 7075 Al alloy processed by ECAP and their evolutions during annealing. Acta Mater 2004;52:4589–99.
[434] Cheng S, Zhao YH, Zhu YT, Ma E. Optimizing the strength and ductility of fine structured 2024 Al alloy by nano-precipitation. Acta Mater 2007;55:5822–32.
[435] Thostenson ET, Ren ZF, Chou TW. Advances in the science and technology of carbon nanotubes and their composites: a review. Compos Sci Technol 2001;61:1899–912.
[436] Lee C, Wei XD, Kysar JW, Hone J. Measurement of the elastic properties and intrinsic strength of monolayer graphene. Science 2008;321:385–8.
[437] Ovid'ko IA. Mechanical properties of graphene. Rev Adv Mater Sci 2013;34:1–11.
[438] Bakshi SR, Lahiri D, Agarwal A. Carbon nanotube reinforced metal matrix composites - a review. Int Mater Rev 2010;55:41–64.
[439] Tjong SC. Recent progress in the development and properties of novel metal matrix nanocomposites reinforced with carbon nanotubes and graphene nanosheets. Mater Sci Eng R 2013;74:281–350.
[440] Silvestre ME, Franzreb M, Weidler PG, Shekhah O, Woll C. Magnetic cores with porous coatings: growth of metal-organic frameworks on particles using liquid phase epitaxy. Adv Funct Mater 2013;23:1210–3.
[441] Ovid'ko IA. Metal-graphene nanocomposites with enhanced mechanical properties: a review. Rev Adv Mater Sci 2014;38:190–200.
[442] Li HQ, Misra A, Horita Z, Koch CC, Mara NA, Dickerson PO, et al. Strong and ductile nanostructured Cu-carbon nanotube composite. Appl Phys Lett 2009;95:071907.
[443] Li HQ, Misra A, Zhu YT, Horita Z, Koch CC, Holesinger TG. Processing and characterization of nanostructured Cu-carbon nanotube composites. Mater Sci Eng A 2009;523:60–4.
[444] Greer JR, Nix WD. Nanoscale gold pillars strengthened through dislocation starvation. Phys Rev B 2006;73.
[445] Yu Q, Shan ZW, Li J, Huang XX, Xiao L, Sun J, et al. Strong crystal size effect on deformation twinning. Nature 2010;463:335–8.
[446] Choi HJ, Shin JH, Bae DH. Grain size effect on the strengthening behavior of aluminum-based composites containing multi-walled carbon nanotubes. Compos Sci Technol 2011;71:1699–705.
[447] Asgharzadeh H, Joo SH, Kim HS. Consolidation of carbon nanotube reinforced aluminum matrix composites by high-pressure torsion. Metall Mater Trans A 2014;45a:4129–37.
[448] Nguyen J, Holland TB, Wen H, Fraga M, Mukherjee A, Lavernia E. Mechanical behavior of ultrafine-grained Ni-carbon nanotube composite. J Mater Sci 2014;49:2070–7.
[449] Wang JY, Li ZQ, Fan GL, Pan HH, Chen ZX, Zhang D. Reinforcement with graphene nanosheets in aluminum matrix composites. Scripta Mater 2012;66:594–7.
[450] Chen LY, Konishi H, Fehrenbacher A, Ma C, Xu JQ, Choi H, et al. Novel nanoprocessing route for bulk graphene nanoplatelets reinforced metal matrix nanocomposites. Scripta Mater 2012;67:29–32.

[451] Nasibulin AG, Koltsova T, Nasibulina LI, Anoshkin IV, Semencha A, Tolochko OV, et al. A novel approach to composite preparation by direct synthesis of carbon nanomaterial on matrix or filler particles. Acta Mater 2013;61:1862–71.
[452] Hwang J, Yoon T, Jin SH, Lee J, Kim TS, Hong SH, et al. Enhanced mechanical properties of graphene/copper nanocomposites using a molecular-level mixing process. Adv Mater 2013;25:6724–9.
[453] Kuang D, Xu LY, Liu L, Hu WB, Wu YT. Graphene-nickel composites. Appl Surf Sci 2013;273:484–90.
[454] Pavithra CLP, Sarada BV, Rajulapati KV, Rao TN, Sundararajan G. A new electrochemical approach for the synthesis of copper-graphene nanocomposite foils with high hardness. Sci Rep-Uk 2014;4.
[455] Shin SE, Choi HJ, Shin JH, Bae DH. Strengthening behavior of few-layered graphene/aluminum composites. Carbon 2015;82:143–51.
[456] Zhang DD, Zhan ZJ. Strengthening effect of graphene derivatives in copper matrix composites. J Alloy Compd 2016;654:226–33.
[457] Zhang DD, Zhan ZJ. Preparation of graphene nanoplatelets-copper composites by a modified semi-powder method and their mechanical properties. J Alloy Compd 2016;658:663–71.
[458] Yolshina LA, Muradymov RV, Korsun IV, Yakovlev GA, Smirnov SV. Novel aluminum-graphene and aluminum-graphite metallic composite materials: synthesis and properties. J Alloy Compd 2016;663:449–59.
[459] Kim Y, Lee J, Yeom MS, Shin JW, Kim H, Cui Y, et al. Strengthening effect of single-atomic-layer graphene in metal-graphene nanolayered composites. Nat Commun 2013;4:2114.
[460] Kim JK, Kim HK, Park JW, Kim WJ. Large enhancement in mechanical properties of the 6061 Al alloys after a single pressing by ECAP. Scripta Mater 2005;53:1207–11.
[461] Chua BW, Lu L, Lai MO. Deformation behaviour of ultrafine and nanosize-grained Mg alloy synthesized via mechanical alloying. Philos Mag 2006;86:2919–39.
[462] Billard S, Fondere JP, Bacroix B, Dirras GF. Macroscopic and microscopic aspects of the deformation and fracture mechanisms of ultrafine-grained aluminum processed by hot isostatic pressing. Acta Mater 2006;54:411–21.
[463] Han BQ, Lavernia EJ. Deformation mechanisms of nanostructured Al alloys. Adv Eng Mater 2005;7:457–65.
[464] Hockauf M, Meyer LW, Zillmann B, Hietschold M, Schulze S, Kruger L. Simultaneous improvement of strength and ductility of Al-Mg-Si alloys by combining equal-channel angular extrusion with subsequent high-temperature short-time aging. Mater Sci Eng A 2009;503:167–71.
[465] Huang JY, Zhu YT, Liao XZ, Valiev RZ. Amorphization of TiNi induced by high-pressure torsion. Philos Mag Lett 2004;84:183–90.
[466] Valiev R, Gunderov D, Prokofiev E, Pushin V, Zhu YT. Nanostructuring of TiNi alloy by SPD processing for advanced properties. Mater Trans 2008;49:97–101.
[467] Song M, Zhu R, Foley DC, Sun C, Chen Y, Hartwig KT, et al. Enhancement of strength and ductility in ultrafine-grained T91 steel through thermomechanical treatments. J Mater Sci 2013;48:7360–73.
[468] Koseki T, Inoue J, Nambu S. Development of multilayer steels for improved combinations of high strength and high ductility. Mater Trans 2014;55:227–37.
[469] Wu XL, Zhu YT. Heterogeneous materials: a new class of materials with unprecedented mechanical properties. Mater Res Lett 2017;5:527–32.
[470] Gleiter H, Marquardt P. Nanocrystalline structures - an approach to new materials. Zeitschrift Fuer Metallkunde 1984;75:263–7.
[471] Nieman GW, Weertman JR, Siegel RW. Microhardness of nanocrystalline palladium and copper produced by inert-gas condensation. Scripta Metall 1989;23:2013–8.
[472] Sanders PG, Fougere GE, Thompson LJ, Eastman JA, Weertman JR. Improvements in the synthesis and compaction of nanocrystalline materials. Nanostruct Mater 1997;8:243–52.
[473] Saber M, Koch CC, Scattergood RO. Thermodynamic grain size stabilization models: an overview. Mater Res Lett 2015;3:65–75.
[474] Weissmuller J. Alloy effects in nanostructures. Nanostruct Mater 1993;3:261–72.
[475] Weissmuller J. Alloy thermodynamics in nanostructures. J Mater Res 1994;9:4–7.
[476] Kirchheim R. Grain coarsening inhibited by solute segregation. Acta Mater 2002;50:413–9.
[477] Liu F, Kirchheim R. Grain boundary saturation and grain growth. Scripta Mater 2004;51:521–5.
[478] Liu F, Kirchheim R. Nano-scale grain growth inhibited by reducing grain boundary energy through solute segregation. J Crystal Growth 2004;264:385–91.
[479] Darling KA, Tschopp MA, VanLeeuwen BK, Atwater MA, Liu ZK. Mitigating grain growth in binary nanocrystalline alloys through solute selection based on thermodynamic stability maps. Comp Mater Sci 2014;84:255–66.
[480] Trelewicz JR, Schuh CA. Grain boundary segregation and thermodynamically stable binary nanocrystalline alloys. Phys Rev B 2009;79.
[481] Saber M, Kotan H, Koch CC, Scattergood RO. Thermodynamic stabilization of nanocrystalline binary alloys. J Appl Phys 2013;113.
[482] Saber M, Kotan H, Koch CC, Scattergood RO. A predictive model for thermodynamic stability of grain size in nanocrystalline ternary alloys. J Appl Phys 2013;114.
[483] Kirchheim R. Reducing grain boundary, dislocation line and vacancy formation energies by solute segregation II. Experimental evidence and consequences. Acta Mater 2007;55:5139–48.
[484] Chookajorn T, Murdoch HA, Schuh CA. Design of stable nanocrystalline alloys. Science 2012;337:951–4.
[485] Murdoch HA, Schuh CA. Stability of binary nanocrystalline alloys against grain growth and phase separation. Acta Mater 2013;61:2121–32.
[486] Chookajorn T, Schuh CA. Nanoscale segregation behavior and high-temperature stability of nanocrystalline W-20 at.% Ti. Acta Mater 2014;73:128–38.
[487] Murdoch HA, Schuh CA. Stability of binary nanocrystalline alloys against grain growth and phase separation. Acta Mater 2013;61:2121–32.
[488] Darling KA, VanLeeuwen BK, Koch CC, Scattergood RO. Thermal stability of nanocrystalline Fe-Zr alloys. Mater Sci Eng A 2010;527:3572–80.
[489] Darling KA, Chan RN, Wong PZ, Semones JE, Scattergood RO, Koch CC. Grain-size stabilization in nanocrystalline FeZr alloys. Scripta Mater 2008;59:530–3.
[490] Saber M, Kotan H, Koch CC, Scattergood RO. Thermal stability of nanocrystalline Fe-Cr alloys with Zr additions. Mater Sci Eng A 2012;556:664–70.
[491] Xu WZ, Li LL, Saber M, Koch CC, Zhu YT, Scattergood RO. Nano ZrO2 particles in nanocrystalline Fe-14Cr-1.5Zr alloy powders. J Nucl Mater 2014;452:434–9.
[492] Talin AA, Marquis EA, Goods SH, Kelly JJ, Miller MK. Thermal stability of Ni-Mn electrodeposits. Acta Mater 2006;54:1935–47.
[493] da Silva M, Wille C, Klement U, Choi P, Al-Kassab T. Electrodeposited nanocrystalline Co-P alloys: microstructural characterization and thermal stability. Mater Sci Eng A 2007;445:31–9.
[494] Mehta SC, Smith DA, Erb U. Study of grain growth in electrodeposited nanocrystalline nickel-1.2 wt% phosphorus alloy. Mater Sci Eng A 1995;204:227–32.
[495] Xu WZ, Li LL, Saber M, Koch CC, Zhu YT, Scattergood RO. Microstructures and stabilization mechanisms of nanocrystalline iron-chromium alloys with hafnium addition. Metall Mater Trans A 2015;46a:4394–404.
[496] Haslam AJ, Phillpot SR, Wolf H, Moldovan D, Gleiter H. Mechanisms of grain growth in nanocrystalline fcc metals by molecular-dynamics simulation. Mater Sci Eng A 2001;318:293–312.
[497] Haslam AJ, Moldovan D, Yamakov V, Wolf D, Phillpot SR, Gleiter H. Stress-enhanced grain growth in a nanocrystalline material by molecular-dynamics simulation. Acta Mater 2003;51:2097–112.
[498] Ni S, Wang YB, Liao XZ, Alhajeri SN, Li HQ, Zhao YH, et al. Grain growth and dislocation density evolution in a nanocrystalline Ni-Fe alloy induced by high-pressure torsion. Scripta Mater 2011;64:327–30.
[499] Fan GJ, Fu LF, Wang YD, Ren Y, Choo H, Liaw PK, et al. Uniaxial tensile plastic deformation of a bulk nanocrystalline alloy studied by a high-energy x-ray diffraction technique. Appl Phys Lett 2006;89:101918.
[500] Fan GJ, Fu LF, Qiao DC, Choo H, Liaw PK, Browning ND. Grain growth in a bulk nanocrystalline Co alloy during tensile plastic deformation. Scripta Mater 2006;54:2137–41.

[501] Fan GJ, Fu LF, Choo H, Liaw PK, Browning ND. Uniaxial tensile plastic deformation and grain growth of bulk nanocrystalline alloys. Acta Mater 2006;54:4781–92.
[502] Zhang Y, Sharon JA, Hu GL, Ramesh KT, Hemker KJ. Stress-driven grain growth in ultrafine grained Mg thin film. Scripta Mater 2013;68:424–7.
[503] Rottmann PF, Hemker KJ. Experimental quantification of mechanically induced boundary migration in nanocrystalline copper films. Acta Mater 2017;140:46–55.
[504] Zhang Y, Tucker GJ, Trelewicz JR. Stress-assisted grain growth in nanocrystalline metals: grain boundary mediated mechanisms and stabilization through alloying. Acta Mater 2017;131:39–47.
[505] Prasad MJNV, Chokshi AH. Deformation-induced thermally activated grain growth in nanocrystalline nickel. Scripta Mater 2012;67:133–6.
[506] Li L, Ungar T, Wang YD, Fan GJ, Yang YL, Jia N, et al. Simultaneous reductions of dislocation and twin densities with grain growth during cold rolling in a nanocrystalline Ni-Fe alloy. Scripta Mater 2009;60:317–20.
[507] Legros M, Gianola DS, Hemker KJ. In situ TEM observations of fast grain-boundary motion in stressed nanocrystalline aluminum films. Acta Mater 2008;56:3380–93.
[508] Hemker KJ, Nix WD. Nanoscale deformation - seeing is believing. Nat Mater 2008;7:97–8.
[509] Hu J, Shi YN, Sauvage X, Sha G, Lu K. Metallurgy grain boundary stability governs hardening and softening in extremely fine nanograined metals. Science 2017;355:1292.
[510] Stolyarov VV, Valiev RZ, Zhu YT. Enhanced low-temperature impact toughness of nanostructured Ti. Appl Phys Lett 2006;88:041905.
[511] Pippan R, Hohenwarter A. The importance of fracture toughness in ultrafine and nanocrystalline bulk materials. Mater Res Lett 2016;4:127–36.